UNIVERSITY OF SOUTHAMPTON

Faculty of Engineering and Physical Sciences

Engineering Materials, Mechanical Engineering

Influences of microstructure and oxidation processes on fatigue failure mechanisms in advanced turbine disc Ni-based superalloy

by

Donghyuk Kim

Thesis for the degree of Doctor of Philosophy

November 2021

Abstract

Most in-service Ni-based turbine disc alloys have a bi-modal or tri-modal γ′ size distribution, where primary γ′ size (or presence) is linked to the duration and temperature of the solution heat treatment (e.g. super or sub-solvus) whilst secondary γ′ and tertiary γ′ size are linked to the ageing temperature and the cooling rates. The effect and relative balance of these different γ′ size populations on slip character is a matter of continuing debate. Therefore it is necessary to establish the role of γ′ size on slip character for unimodal distributions to allow a deeper understanding of deformation behaviour. The accumulation of damage is intrinsically affected by the degree of slip heterogeneity at both low and high temperatures and this can affect both crack initiation and growth processes. In this work, a non-commercial heat treatment has been used on RR1000 alloy to produce two different unimodal γ′ size distributions. The heat treatments also caused a varying carbide distribution on grain boundary, with more continuous grain boundary carbides observed in the coarse γ′ variant. These carbides on grain boundaries also play a key role in strengthening and weakening damage mechanisms over a range of temperatures.

Short fatigue crack tests (uninterrupted and interrupted tests) have been conducted on polished plain bend bars of both fine and coarse γ′ variants under three point bending, with a sine waveform (20Hz) and trapezoidal waveform (90s dwell time) loading applied at room temperature and 650 ^{o}C in air, respectively. At room temperature, in terms of deformation and slip character, it is seen that the fine γ′ variant exhibits more γ′ shearing and heterogeneous slip character (relatively higher planar slip and intense slip bands), which is more linked to less resistance to crack initiation while the coarse γ′ variant is apt to show more Orowan looping and homogeneous slip character. In both γ′ variants fatigue cracks mainly initiated at pores at the surface or sub-surface, slip bands or along twin boundary presenting a crystallographic faceting. High strain levels and more diffuse strain localisation take place in the vicinity of crack initiation areas such as pore and slip bands. Crack initiation along the twin boundary occurs with relatively high Schmid factor (SF) and further propagation is inclined to follow high SFs of adjacent grains with the activated slip systems. Short fatigue crack growth rates in both γ′ variants show a high extent of scatter at low ΔK level as a distinctive short crack behaviour, which is significantly linked to the complexity of local microstructure and intrinsic shielding effects. Under the testing conditions in this study, the lifetimes appear to be strongly connected to the number of crack initiation sites (partly linked to initiation resistance), which seems more associated with the defect distribution or grain misorientation than γ′ alone. More crack initiation sites generally lead to the multi-site coalescence events that contribute to enhanced fatigue crack growth rates and reduced lifetime. Three dimensional (3D) evaluation (sub-surface) of early crack growth processes by X-ray CT scanning has also been conducted on micro-tensile samples of the coarse γ′ variant at room temperature. Internal microstructure has been investigated from a series of tomographically reconstructed two dimensional (2D) slices assessing

porosity distribution and complex morphology of the early crack, showing the crack propagated along slip bands slanted at around 45°.

Overall, the lifetimes at 650 °C are significantly shortened by the effect of dwell time and consequent oxidation damage. At elevated temperature, fatigue crack initiation mechanisms are influenced by synergistic effects of the microstructural features and oxidation processes. Cross slip and homogenous slip character are promoted in both γ′ variants due to the effects of elevated temperature. On applying a 90s dwell time, a large amount of grain boundary cracking at bulging Co-rich oxides can be seen on the surface in both γ′ variants. Such plentiful intergranular cracking promotes frequent crack coalescences and results in significantly accelerated fatigue crack growth rates, leading to shortened lifetime. The bulged oxides at particular grain boundaries are associated with enhanced mismatch strain and stress concentration, resulting in oxide cracking. Cracks also initiate at the interface between oxidised carbides and grain boundaries due to volume expansion and concomitant strain localisation.

The complex influences of microstructural variation, loading frequency (linked to diffusion time), temperature and oxidation on long fatigue crack growth behaviour have also been assessed. Long fatigue crack tests on single edge notched bend samples of both γ′ variants have been carried out under three point bend and a trapezoidal waveform loading with dwell times of 1s and 90s at peak load at 650 °C and 725 °C in air. Overall, in both γ′ variants, intergranular failure modes are dominant and even more marked with longer dwell time and higher temperature. The fine γ′ variant shows a better fatigue resistance at 650 °C and 725 °C for both dwell times, and this is more marked with longer dwell time and higher temperature. The coarse γ′ variant exhibits more time dependent crack growth and distinctly more intergranular fracture modes, which can ascribed to the more continuous carbide distribution on grain boundaries. Oxidation damage zones ahead of the crack tip in both γ′ variants were investigated by switching between low and high loading frequencies at 650 °C, showing that the coarse γ′ variant exhibited the most significant oxidation damage zone in the transition. Such damage zones are linked to embrittlement cracking and accelerated crack growth rates. 3D analysis by X-ray CT scanning as well as 2D observation showed that the crack path at low frequency (longer diffusion time per cycle) is relatively more tortuous and contains greater secondary crack formation, with a discontinuous crack path and uncracked ligaments seen due to significant oxidation damage and embrittled zones formed which is more marked in the coarse γ′ variant.

Table of Contents

Table of Tables

Table of Figures

Research Thesis: Declaration of Authorship

Print name: Donghyuk Kim

Title of thesis: Influences of microstructure and oxidation processes on fatigue failure mechanisms in advanced turbine disc Ni-based superalloy

I declare that this thesis and the work presented in it are my own and has been generated by me as the result of my own original research.

I confirm that:

1. This work was done wholly or mainly while in candidature for a research degree at this University;
2. Where any part of this thesis has previously been submitted for a degree or any other qualification at this University or any other institution, this has been clearly stated;
3. Where I have consulted the published work of others, this is always clearly attributed;
4. Where I have quoted from the work of others, the source is always given. With the exception of such quotations, this thesis is entirely my own work;
5. I have acknowledged all main sources of help;
6. Where the thesis is based on work done by myself jointly with others, I have made clear exactly what was done by others and what I have contributed myself;
7. Parts of this work have been published as:
   - D. Kim, R. Jiang, A. Evangelou, I. Sinclair, P.A.S. Reed, Effects of γ′ size and carbide distribution on fatigue crack growth mechanisms at 650 °C in an advanced Ni-based superalloy, Int. J. Fatigue. 145 (2021). doi:10.1016/j.ijfatigue.2020.106086.

Signature: Date: 03-01-2022

Acknowledgements

First and foremost, I would like to express my sincere gratitude to my supervisor Professor Philippa Reed for the continuous support, guidance, enthusiasm and patience in all the time of research and writing of this thesis. She has given me a significant motivation as a researcher and as a person for that I will be forever grateful. I could not imagine I am able to come this far in my PhD without having her as my supervisor. I also would like to thank my second supervisor Professor Ian Sinclair who offered valuable knowledge and experience in X-ray CT analysis in the μ-VIS laboratory at the University of Southampton. My thanks also go to Dr. Rong Jiang who is a previous researcher in our group (and who has acted as my third PhD supervisor) Dr Jiang left extensive work that I can refer to and with whom I have had many valuable discussions on my research and in writing a journal paper.

Beside my supervisors, Dr. Nong Gao and Dr. Andrew Hamilton are greatly thanked for the insightful comments from my progression VIVAs offering various perspectives as examiners. I would also like to thank Dr. Angelos Evangelou for his help in conducting fatigue tests and helpful discussion and suggestions in terms of the results. Thanks go to Dr. Shuncai Wang for SEM, EDX and EBSD training. I must also thank Dr. Dan Bull for his help in analysis by X-ray CT scanning. Dr. Andy Robinson at TSRL at the University of Southampton for teaching me how to use the mechanical testing machines including Instron 1 and Instron 2 is gratefully acknowledged. In addition the assistance from Dr. Geoff Howell, technical lead in the materials laboratory, is gratefully acknowledged.

I am also greatly indebted to past and present members of the research group, in no particular order, Diego, Ara, Ben, Alvaro, Yuanguo, Anqi, Mike, Corentin, Talha, Songsong, Som. Most importantly, not only the valuable discussions and help with various aspects of my work but also the time away from our work make me go this far by sharing laughs and concerns. Also I wish much luck to new group members to Yeajin and Joe. I am grateful for the support and sharing similar concerns at all stages of the PhD, which comfort and cheer me up in my own language by my Korean friends at the University of Southampton.

Finally, I would like to thank deeply my parents and sister for their unconditional support and encouragement. I will be always grateful for your love which is shaping me into the person I am today.

Abbreviations

2D	Two dimensional
3D	Three dimensional
AOI	Area of interest
APB	Antiphase boundary
BEI	Backscatter electron imaging
CRSS	Critical resolved shear stress
CSS	Cyclic stress strain
CT	Computed tomography
DCPD	Direct current potential drop
DIC	Digital image correlation
EBSD	Electron backscattered diffraction
ECCI	Electron channelling contrast imaging
EDM	Electrostatic discharge machining
EDX	Energy dispersive X-ray
EPFM	Elastic plastic fracture mechanics
ESR	Electro-slag remelting
FCC	Face centred cubic
FCG	Fatigue crack growth
FIB	Focused ion beam
HCF	High cycle fatigue
HR	High resolution
KW	Kear Wilsdorf
LCF	Low cycle fatigue
LEFM	Linear elastic fracture mechanics
ND	Normal direction
NDT	Non-destructive testing

OM Optical microscope

P/M Powder metallurgy

PBB Plain bend bar

PSB Persistent slip band

RD Rolling direction

RR Rolls-Royce

SAGBO Stress-assisted grain boundary oxidation

SENB Single edge-notched bend

SEI Secondary electron imaging

SEM Scanning electron microscope

SFE Stacking fault energy

TEM Transmitting electron microscope

TIT Turbine inlet temperatures

VAR Vacuum arc remelting

VIM Vacuum induction melting

WD Working distance

Chapter 1 Introduction

1.1 Background

Gas turbines are power generation turbomachinery used in a variety of industrial fields since their emergence in the middle of the 19th century. Gas turbines containing turbine disc and blade components are a type of heat engine operated by the gas combustion with high temperature and high pressure passing through a fan, which then converts the power into mechanical or electric work. Nowadays, turbine inlet temperatures (TIT) of the modern gas turbines for aeroengines have risen beyond 1600 °C with extensive developments of materials, manufacture and processing techniques and engine design [1]. The higher temperatures achieved in gas turbine engines are critical factors for the enhanced fuel efficiency and thrust linked to the performance as well as reduced pollutant emissions [2].

The severe service environment of aeroengines inevitably allows turbine discs to experience elevated temperatures of around 650 °C (higher in more advanced aeroengines) and relatively high cyclic mechanical stresses. Synergistic influences of high temperatures and cyclic loads particularly during the service cycles between start-up and shut-down result in damage such as fatigue and creep leading to mechanical degradation combined with oxidation and corrosion under the operating environment [3]. The combination of mechanical and environmental degradation is closely related to the critical performance and lifetime of turbine discs. Consequently, research has been carried out on turbine disc materials to improve their properties against the degradation in service. Research on material composition, manufacturing, heat treatment technique and processing focusses on developments in disc materials aiming at optimisation and better performance under increasing temperature demands.

Polycrystalline Ni-base superalloys have been the choice of high temperature materials for turbine disc applications because of their excellent combined properties such as high temperature strength, superior mechanical and environmental damage tolerance (i.e. fatigue, creep, oxidation and corrosion) [4–6]. However, the fatigue failure risk in mechanical components has been of particular significance as their failure mechanisms are not fully understood yet. It is therefore necessary to understand the fatigue failure mechanisms under relevant operating environments in order to direct appropriate alloying and processing developments of turbine disc applications. The properties and performance of disc alloys are closely associated with their microstructural characteristics [6–9]. Considerable previous work therefore has critically assessed how microstructural features in these systems are linked to their mechanical properties and failure mechanisms over a range of temperatures. Primary

microstructural factors in polycrystalline disc alloys include: strengthening precipitate (γ′), grain distribution and grain boundary characteristics. At elevated temperatures, oxidation and creep damage processes are significantly linked to the time dependent intergranular cracking observed in Ni-based superalloys, causing accelerated crack propagation rates and subsequently reduced fatigue lifetime. Such time-dependent fatigue behaviour is considerably assisted by the complex effects of oxidation, loading condition (dwell time), temperature as well as microstructure. Understanding the complex interaction between these controlling factors and fatigue failure mechanisms at a range of service temperatures is an ongoing area of research.

RR1000 is an advanced polycrystalline Ni-based superalloy for turbine disc applications produced by Rolls-Royce (RR) using a powder metallurgical (P/M) route, which is employed for many modern turbine disc alloys. RR1000 is a precipitation-strengthened alloy and developed for better strength, damage tolerance and creep resistance than Udimet 720Li alloy [10]. Commercial disc alloys normally exhibit a bi- or tri-modal size distribution of γ′ precipitate, thus somewhat obscuring the respective role of γ′ precipitate size. Size distribution of the γ′ precipitate is often linked to the variation in slip character as this affects the damage accumulation (at both low and high temperature) and further fatigue crack initiation and propagation behaviour in Ni-based superalloys. In this study, model RR1000 alloys with two different unimodal distributions of γ′ precipitate size have been produced by non-commercial heat treatment processes from an initial disc supplied by RR. As a consequence, not only γ′ size distribution but also carbide distribution on the grain boundaries appears to be another variant. Carbide distribution on grain boundaries can act as an effective barrier to crack growth at room temperature while it can weaken the grain boundary strength in an oxidising environment at elevated temperature. Study of the interplay of these different microstructural variants and oxidation on fatigue behaviour of RR1000 at varying temperatures will contribute to further development of microstructural optimisation, lifetime assessment approaches and inform processing techniques, and therefore lead to better lifetime and performance of these alloys in turbine disc applications. The materials and their fatigue behaviour under the testing conditions studied are characterised by high resolution imaging techniques using both traditional 2D observations and 3D X-ray computed tomography (CT). This provides a deeper understanding of fatigue crack initiation and propagation mechanisms in this model turbine disc alloy under a range of service relevant applications by these imaging techniques.

1.2 Research objectives and aims

The following objectives were established to develop our understanding of the fatigue failure mechanisms of the RR1000 alloys at a range of temperatures. This aims to contribute to improved

lifetime and performance of turbine discs and to direct an appropriate material optimisation and comprehensive life assessment method. The following objectives are:

1) Characterise the microstructural and mechanical features of the model RR1000 alloy under non-commercial heat treatment processes at a range of temperatures by high resolution image analysis.
2) Study the microstructural influences (such as varying γ′ precipitate size and carbide distribution on grain boundaries) on slip character, fatigue crack initiation and early propagation behaviour in polycrystalline turbine disc material at room temperature.
3) Investigate the role of oxidation in fatigue crack initiation and propagation mechanisms in conjunction with microstructural effects at elevated temperatures.
4) Understand the synergies of microstructure, temperature, oxidation and loading condition on oxygen-related fatigue failure mechanism at elevated temperatures.

1.3 Thesis structure

This thesis begins with **Chapter 1,** an introduction that describes the background, aims and objectives of this study. **Chapter 2** represents a literature review regarding fundamentals and existing knowledge of Ni-based superalloys and fatigue mechanisms focussing on polycrystalline turbine disc materials. Background on 3D image analysis approaches applied to microstructural characterisation and fatigue mechanism evaluation of metallic materials using X-ray CT is also discussed. After these background chapters, Chapters 3-6 present the materials characterisation and experimental testing results. In **Chapter 3**, material characterisation and baseline mechanical testing of the RR1000 alloy is described to establish the microstructural features in the heat treated variants. Then **Chapter 4** presents the effects of these microstructural features on fatigue crack initiation and early crack propagation behaviour at room temperature where environmental effects are limited. **Chapter 5** describes fatigue crack initiation and resultant lifetimes at high temperature where the failure mechanisms are assisted by significant oxidation effects. The results are compared to the fatigue behaviour at room temperature. In **Chapter 6**, long fatigue crack growth (FCG) behaviour at elevated temperature is discussed in detail. The combined effects of microstructure variants, temperature, loading condition (including frequency and dwell) on long fatigue crack propagation are systematically presented. **Chapter 7** summarises the primary findings and conclusions from this PhD and **Chapter 8** comprises suggestions for further work based on the results of this study.

The research work in these chapters is schematically summarised in the flow diagram (Figure 1.1) in the following page. It is divided into four sections including experiments, methodology, results and contributions to the field of this study.

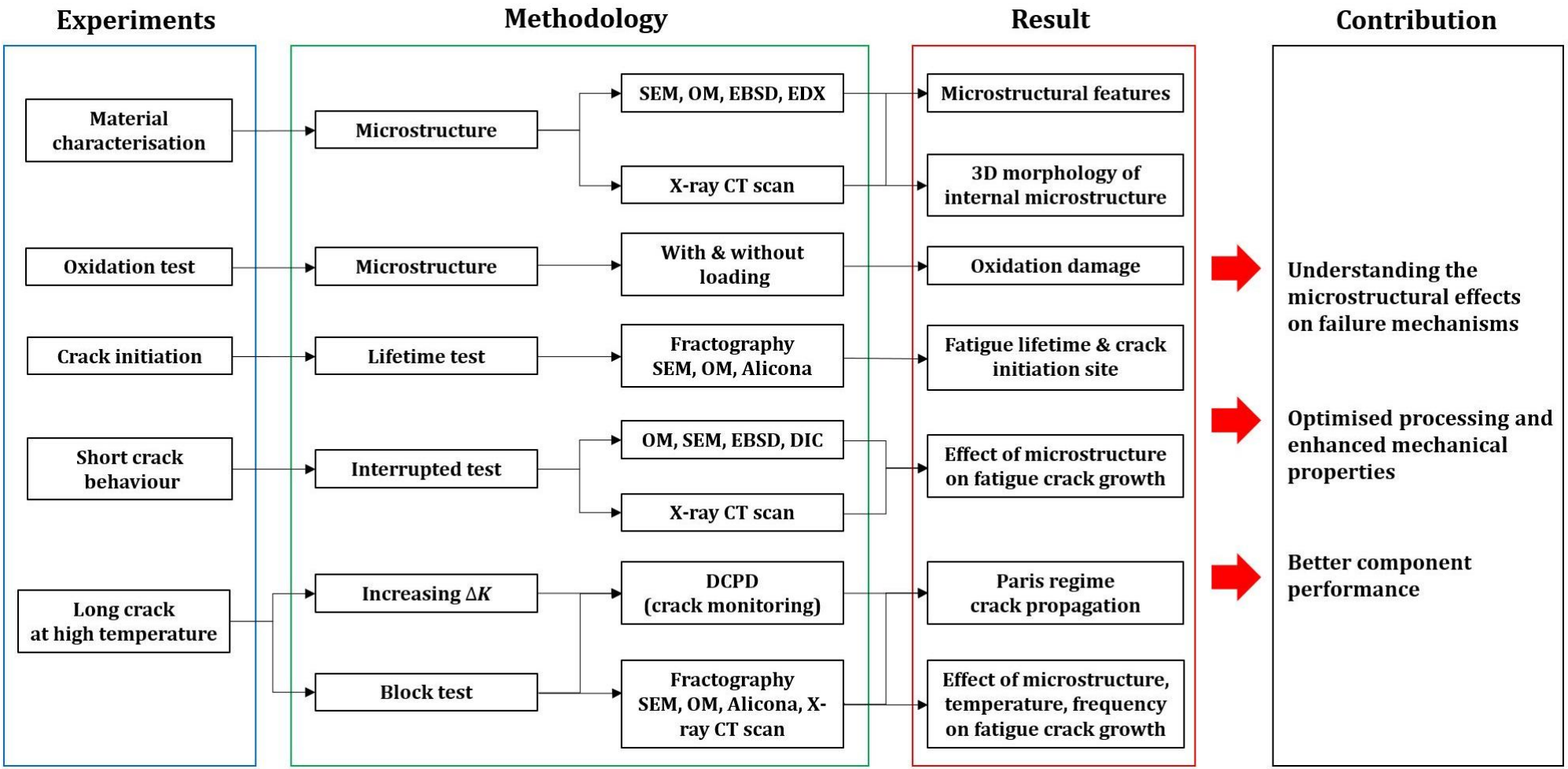

Figure 1.1: Flow diagram of the research work in the thesis representing experiments, methodology, results and their contribution.

Chapter 2 Literature review

2.1 Ni-based superalloys for turbine disc application

Turbine discs widely used in aeroengine and power generation turbomachinery experience elevated temperatures of around 650 °C (higher in more advanced aeroengines) together with cyclic loading at high stress levels. Such a harsh service environment has required superior mechanical properties and the enhanced damage tolerance of Ni-based superalloys which exhibit excellent high temperature strength, resistance to fatigue and creep as well as oxidation and corrosion [4–6,11]. This has led to their wide-spread use in disc applications since the first commercial application of Waspaloy in the 1950s. The alloys primarily consist of γ phase and strengthening γ′ phase with a face centred cubic (FCC) crystal structure seen in both phases. Figure 2.1 represents the development of Ni-based superalloys in turbine disc applications showing the increase in their temperature capability and the different processing routes used to achieve this. Initially, cast and wrought were the established processing routes P/M has recently become the more dominant processing route. P/M processing avoids the issue of elemental segregation in these increasingly highly alloyed systems and hence further enhances the mechanical properties [4]. The development of such manufacturing processes, combined with alloying developments, contribute to the improved high temperature strength and performance required to enable increased TITs with high thrust to weight ratios of modern aeroengines.

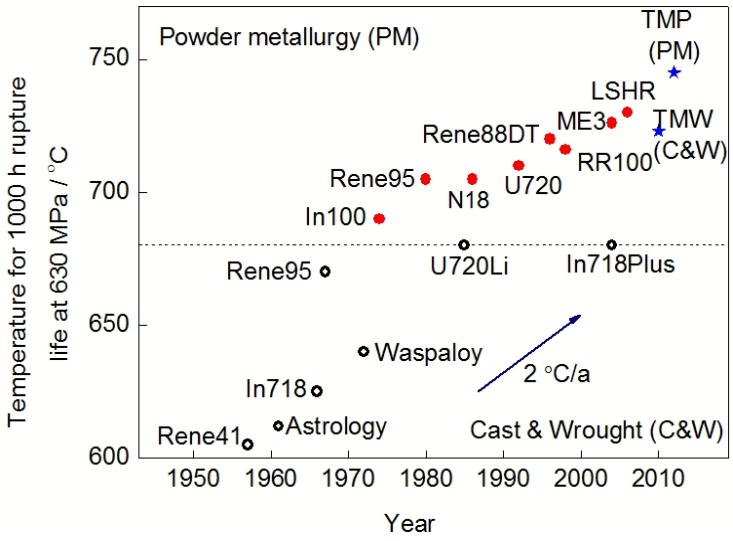

Figure 2.1: Evolution in temperature capability of Ni-based superalloys for turbine disc applications [12].

2.1.1 Composition: alloying elements and phase formation

Alloy	Cr	Co	Mo	W	Nb	Al	Ti	Ta	Fe	Hf	C	B	Zr	Ni
Alloy 10	11.5	15	2.3	5.9	1.7	3.8	3.9	0.75	-	-	0.030	0.020	0.05	Bal
Astroloy	15.0	17.0	5.3	-	-	4.0	3.5	-	-	-	0.06	0.030	-	Bal
Inconel 706	16	-	-	-	2.9	0.2	1.8	-	40.0	-	0.03	-	-	Bal
Inconel 718	19.0	-	3.0	-	5.1	0.5	0.9	-	18.5	-	0.04	-	-	Bal
ME3	13.1	18.2	3.8	1.9	1.4	3.5	3.5	2.7	-	-	0.030	0.030	0.050	Bal
MERL-76	12.4	18.6	3.3	-	1.4	0.2	4.3	-	-	0.35	0.050	0.03	0.06	Bal
N18	11.5	15.7	6.5	0.6	-	4.35	4.35	-	-	0.45	0.015	0.015	0.03	Bal
Rene 88DT	16.0	13.0	4.0	4.0	0.7	2.1	3.7	-	-	-	0.03	0.015	0.03	Bal
Rene 95	14.0	8.0	3.5	3.5	3.5	3.5	2.5	-	-	-	0.15	0.010	0.05	Bal
Rene 104	13.1	18.2	3.8	1.9	1.4	3.5	3.5	2.7	-	-	0.030	0.030	0.050	Bal
RR 1000	15.0	18.5	5.0	-	1.1	3.0	3.6	2.0	-	0.5	0.027	0.015	0.06	Bal
Udimet 720	17.9	14.7	3.0	1.25	-	2.5	5.0	-	-	-	0.035	0.033	0.03	Bal
Udimet 720Li	16.0	15.0	3.0	1.25	-	2.5	5.0	-	-	-	0.025	0.018	0.05	Bal
Waspaloy	19.5	13.5	4.3	-	-	1.3	3.0	-	-	-	0.08	0.006	-	Bal

Table 2.1: Chemical composition of turbine disc alloys (wt.%) [4].

Ni-based superalloys mainly consist of an FCC γ matrix phase as the main constituent with a strengthening ordered FCC γ′ phase. The alloying elements and their amount in the total composition play different and important roles in the formation of the phases and the subsequent alloy properties [6,13]. Table 2.1 illustrates the alloying elements widely used in Ni-based superalloys in terms of weight percentage (wt.%). Nickel is the major element among the 14 different alloy elements (typically 60-70 wt.%) and it has a melting point of 1455 ^{o}C that provides much of the temperature capability of Ni-based superalloys. The other alloying elements can be generally categorised depending on their contribution to a range of phase formations such as a γ phase, a strengthening γ′ phase, carbides and borides etc. [4,14–16]. A variety of elements exert influence on the stability of each phase, resulting in different contributions to the service performance of the alloys. Overall roles of the alloying elements are summarised in Figure 2.2.

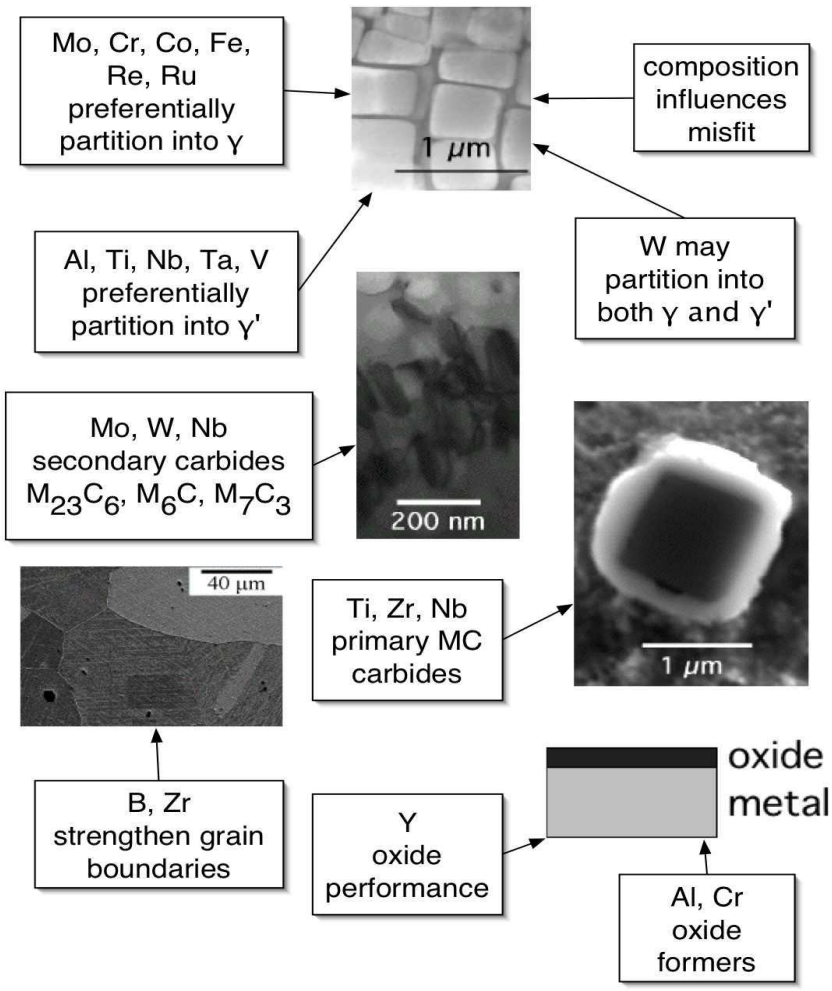

Figure 2.2: Role of alloying elements in Ni-based superalloys [17].

First of all, the γ phase which exhibits a FCC crystal structure forms a continuous matrix phase (Ni-based austenitic phase). It normally includes high levels of solid solution strengthening elements such as cobalt (Co), chromium (Cr), molybdenum (Mo), tungsten (W) and rhenium (Re). Co is likely to promote high temperature strength by making cross-slip more difficult since it contributes to lower stacking fault energy (SFE) which is also linked to creep resistance [18]. Cr forms a coherent Cr_2O_3 layer which enhances resistance to corrosion and oxidation process.

Secondly, the coherent strengthening gamma prime (γ′) precipitate has an ordered $L1_2$ (FCC) crystal structure and is preferentially formed by hardening elements including aluminium (Al), titanium (Ti), tantalum (Ta) and niobium (Nb), i.e. $Ni_3(Al,Ta,Ti)$ [19]. The ordered γ′ phase strengthens the alloy by acting as barriers to dislocation motion. The γ′ precipitate can be characterised by parameters such as phase volume fraction, size distribution and morphology. The volume fraction of γ′ precipitate is closely associated with the amount of Al and Ti, resulting in high volume fraction around 70 % in some modern blade alloys. With respect to the size distribution of γ′ precipitate, it can be primarily

tailored by not only relevant alloying elements but also heat treatment processes such as choice of solvus temperature or cooling process as well as ageing temperatures and times. For instance, it has been observed that a slower cooling rate from solution heat treatment and subsequent ageing process generally leads to a larger size distribution of spherical γ′ precipitate [20,21]. The detailed interaction between γ′ precipitate size and heat treatment will be covered in more detail in section 2.1.4. In terms of morphology, the typical shape of the coherent small γ′ precipitates is spherical while their shapes become cuboidal, arrays of cubes or solid-state dendrites in turn as they coarsen (e.g. with significant degrees of ageing). These morphology transitions are linked to the value of γ matrix/γ′ precipitate lattice misfit [16,22]. The coherent γ′ precipitate in the γ matrix (and the varying alloying elements in each phase) produce different lattice constants and lead to a resultant lattice misfit around a coherent γ′ precipitate. A close match in γ matrix/γ′ precipitate lattice constants along with chemical compatibility allows spherical γ′ precipitate phases to be coherent in the matrix and to have long-time stability, while a larger lattice misfit (such as over ~3 %) results in precipitates which may form as semi-coherent or incoherent plates [15]. Coarsening of γ′ precipitates promotes a loss of coherency and an increasing magnitude of the lattice misfit. High lattice misfit gives rise to an enhanced stress field around the γ′ precipitate, which promotes lower dislocation mobility and consequently can offer considerable strengthening.

Carbon accounts for up to 0.2 wt.% in some Ni-based superalloys and forms primary metal MC carbides (where M is metal element) from the melt during solidification combined with reactive elements such as titanium (Ti), tantalum (Ta) and hafnium (Hf). $M_{23}C_6$ and M_6C are secondary carbides formed by decomposing of primary MC carbides during heat treatment process or in service and these carbides preferentially reside on the γ-grain boundaries [22]. These grain boundary carbides can offer significant grain boundary strengthening but may be both advantageous or disadvantageous to Ni-based superalloy properties. However, it is generally believed that a fine distribution can restrain grain boundary sliding, reducing creep contributions to high temperature strength [16]. Borides are also likely to reside on the γ-grain boundaries, and are formed by the combination of boron (B), chromium (Cr) or molybdenum (Mo) [23]. These are associated with the higher amounts of C and B elements seen in polycrystalline Ni-based superalloys (where grain boundary strengthening is desirable).

2.1.2 Strengthening mechanisms in Ni-based superalloys

In Ni-based superalloys, strengthening mechanisms contribute considerably to the excellent mechanical properties including the distinctive high yield stress retained at elevated temperatures. The strengthening mechanisms can be categorised depending on the alloying elements and

processing routes as described in section 2.1.1, which includes solid solution strengthening, precipitate strengthening and the action of other particle formers (e.g. carbides and borides).

2.1.2.1 Solid solution strengthening

Plastic deformation of metallic alloys is closely linked to the dislocation movement. In Ni-based superalloys, solid solutions resulting from substitutional solute atoms contribute to strengthening in materials by inhibiting the dislocation motion on the basis of solid solution strengthening elements such as Co, Cr, W, Mo and Re (and their relative amounts) which are typically seen in Ni-based superalloys [15]. The difference in atomic diameters between these alloying elements and nickel produce lattice distortion and hence constrain dislocation motion, promoting the strengthening of the alloys. These elements in solid solution are expected to induce different elastic moduli in the crystal lattice and therefore requires additional energy for dislocation motions to traverse, contributing to the strengthening. Furthermore, solid solution strengthening elements may induce a decrease in SFE in the parent crystal lattice, which leads to an increase in the separation of dissociated dislocations into partial dislocations, and hence more planar slip. The lowered SFE is related to a bigger "barrier" to make the partial dislocations reassociated [24]. This is related to the strengthening observed at high temperature in these alloys by making cross slip more difficult.

2.1.2.2 Precipitation strengthening

As the distinctive principal strengthening mechanism in Ni-based superalloys, γ′ precipitates formed by alloying hardening elements such as Ni, Al, Ta and Ti generally play a significant role in the achievement of overall strength at elevated temperature. Precipitation strengthening is also linked to enhanced creep resistance which is an important mechanism to consider in high temperature applications. The primary strengthening mechanism by γ′ precipitates is achieved by hindering the dislocation movement. During plastic deformation dislocations either cut through smaller coherent γ′ precipitates or bow around larger γ′ precipitates then leaving a dislocation loop behind precipitates (Orowan looping) [15,25–27]. Other dislocation behaviours of climb or cross-slip can also be activated at elevated temperature. The deformation mechanisms of dislocation cutting and looping precipitates are controlled by several factors such as size and volume fraction of the precipitates, coherency between γ matrix and γ′ precipitate phase as well as the antiphase boundary (APB) energy in ordered precipitates.

The coherent precipitation of a γ′ precipitate in the γ matrix results in different lattice constants and a resultant lattice misfit around γ′ precipitate. A higher extent of the lattice misfit is linked to a greater stress field. Consequently, this constrains dislocation motion and offers strengthening. The ABP energy is indicative of the unstable high energy required for a dislocation to cut through an ordered precipitate. This distorts the periodic ordered atomic arrangement in its slip plane leaving behind a

distorted plane (known as the APB), often leading to pairing of dislocations cutting [28] the γ′ to minimise the APB. The first leading dislocation induces the APB and the second trailing dislocation interacts with the distorted precipitates then promote rearrangement of the chemical bond between precipitates back to the ordered structure, contributing to strengthening. Figure 2.3 schematically describes the interaction between precipitate size and dislocation cutting processes, indicating ordered γ′ particles being cut by different pairings of dislocations (i.e. 'weak' and 'strong' pair coupling) on the basis of the size of γ′ particles. [29].

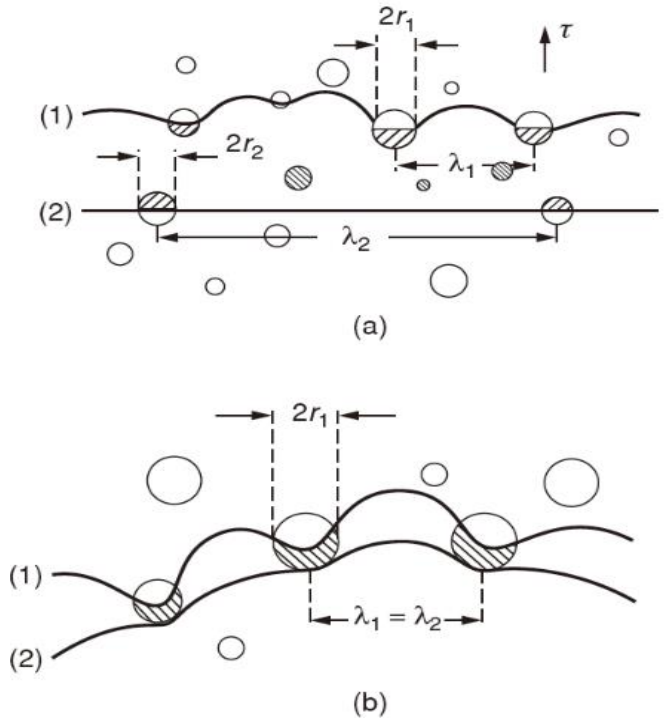

Figure 2.3: Particles of ordered γ′ being sheared by pairs of dislocations: (a) weak pair-coupling (b) strong pair-coupling [29].

In the first case shown in Figure 2.3 (a), a weak pair coupling occurs when the spacing between two paired dislocations is relatively large compared to the precipitate diameters, causing the second trailing dislocation to be some way behind the first, leaving faulted precipitates between two dislocations. In the second case, strong pair coupling seen in Figure 2.3 (b) occurs when the spacing between two paired dislocations is comparable to the particle diameter, causing γ′ particles to include a pair of dislocations which are now 'strongly coupled'. The cross-over between the two mechanisms is dependent on size, volume fraction of γ′ particles and APB energy. The critical resolved shear stress τ_c (CRSS) for precipitate cutting by weak and strong pair coupling dislocation can be proportionally estimated by the following equations respectively [29–31]:

$$\tau_{weak.c} \propto {\gamma_{APB}}^{3/2} \sqrt{\frac{rf}{G}} \qquad (2.1)$$

$$\tau_{strong.c} \propto \sqrt{\frac{\gamma_{APB} G f}{r}} \qquad (2.2)$$

where γ_{APB} is APB energy and G is the shear modulus, *f* is the volume fraction of precipitates and *r* is the radius of a uniform distribution of particles.

With an increasing particle size, the cutting stress of weak pair coupling in order to force dislocations through the precipitates increases while that of strong pair coupling decreases. This leads the two cases to intersect at the transition precipitate size as seen in Figure 2.4. When the fine γ′ precipitate size increases and reaches a certain size, it is observed that the strength starts decreasing and the dislocation mechanism changes from weak pair coupling to strong pair coupling. The critical γ′ size of transition hence contributes to an optimum hardening. When γ′ precipitates become even larger, the deformation mechanism is likely to switch from dislocation cutting to looping around precipitates (Orowan looping) as described in Figure 2.4. The Orowan looping process is schematically illustrated in the Figure 2.5 and the interaction between strength and Orowan looping is shown in the equation given below [32]:

$$\tau_0 = \frac{Gb}{l-2r} \qquad (2.3)$$

where G is the shear modulus, b is the Burgers vector, 2*r* is the particle diameter and *l* is the average particle spacing between particle centres.

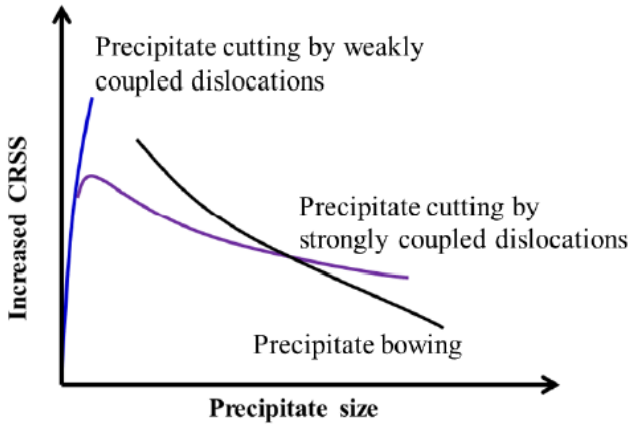

Figure 2.4: Schematic graph of the relation between increased CRSS and precipitate size and different dislocation-precipitate interactions [4].

These two dislocation mechanisms are associated with different slip characteristics seen in Ni-based superalloys. The γ′ particles that are cut by dislocations become less resistant to subsequent deformation on the same plane especially when particles are small, due to dislocation coupling (linked to the APB effect) and the reduced cross-sectional area of the precipitate as it is repeatedly cut. This together with the typical low SFE, which leads to dislocation dissociation, also constraining dislocation motion to the same cutting plane, can cause significant strain localisation and preferential

slip remaining on the same cutting plane. Such preferential slip results in an overall planar slip characteristic. On the other hand, dislocation looping around particles induces much more wavy slip that is linked to a more homogeneous dislocation behaviour. These different deformation behaviours under cyclic loading will be discussed further in section 2.2.3.

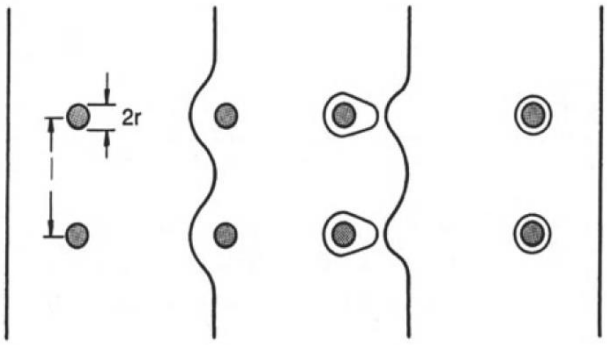

Figure 2.5: Schematic different stages of the Orowan looping mechanism [33].

One of the distinguishing features that Ni-based superalloys possess, is that yield stress sustains or even slightly increases with increasing temperature up to around 800 ºC (Figure 2.6). This phenomena is widely ascribed to the anisotropic property of an APB energy [34]. This anomalous yielding increase with elevated temperatures is related to the formation of Kear Wilsdorf (KW) locking typically seen in $L1_2$ structured alloys [35]. A brief explanation of this is that, upon deformation, coupled dislocations are inclined to dissociate into a superpartial dislocation with an APB. As temperature increases (allowing additional thermal energy), cross slip of the γ' superpartial dislocations from the (111) slip planes to the (001) slip planes is promoted by the applied stress and the anisotropy of APB energy. Such thermally activated cross slip segments promote microstructural locks by hindering deformation since they resist deformation, inducing increased the CRSS for dislocation motion and a subsequent increase in strength with increasing temperature [4].

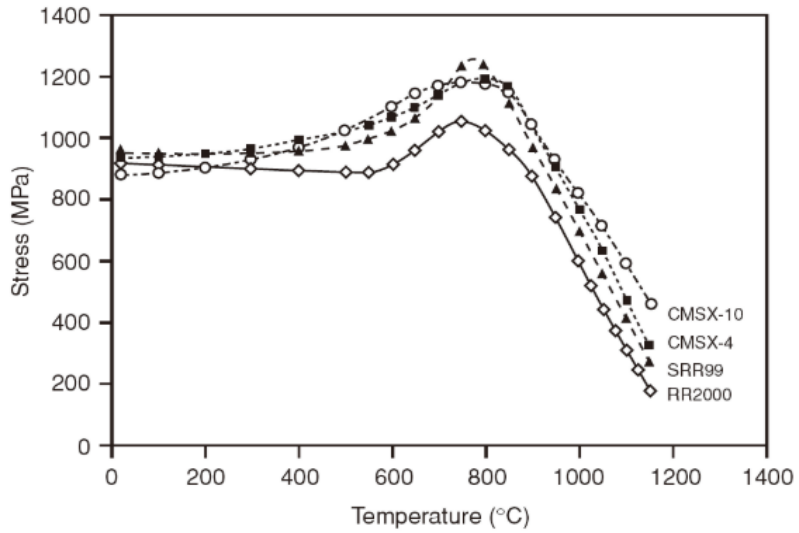

Figure 2.6: Variation of the yield stress at increasing temperature of several Ni-based superalloys [4].

2.1.3 Processing of turbine disc alloys: cast & wrought and powder metallurgy

The performance and characteristics of turbine disc alloys can be optimised by controlling the manufacturing processing (and resultant microstructure). The disc alloys for gas turbines are typically produced via two distinct methods: a) controlling the ingot metallurgy and subsequent forming (cast and wrought), and b) powder metallurgy (P/M) for highly alloyed powders. Both processes can be selected based on the chemistry of the superalloys to be produced [36].

Ingot metallurgy is the first stage of the cast and wrought process. The ingots are produced by vacuum induction melting (VIM), electro-slag remelting (ESR) and vacuum arc remelting (VAR). Significant alloying element segregation (and subsequent variable mechanical properties after VIM), has led to secondary melting processes (e.g. ESR and VAR) being employed in order to alleviate them. The cast and wrought process is schematically described in Figure 2.7, which begins with VIM, ESR and VAR to produce the initial ingot, followed by annealing the ingot to homogenise compositions, subsequent thermal mechanical work and a series of forging operations of the final turbine component [4]. Waspaloy and IN718 are typically produced by cast and wrought processes.

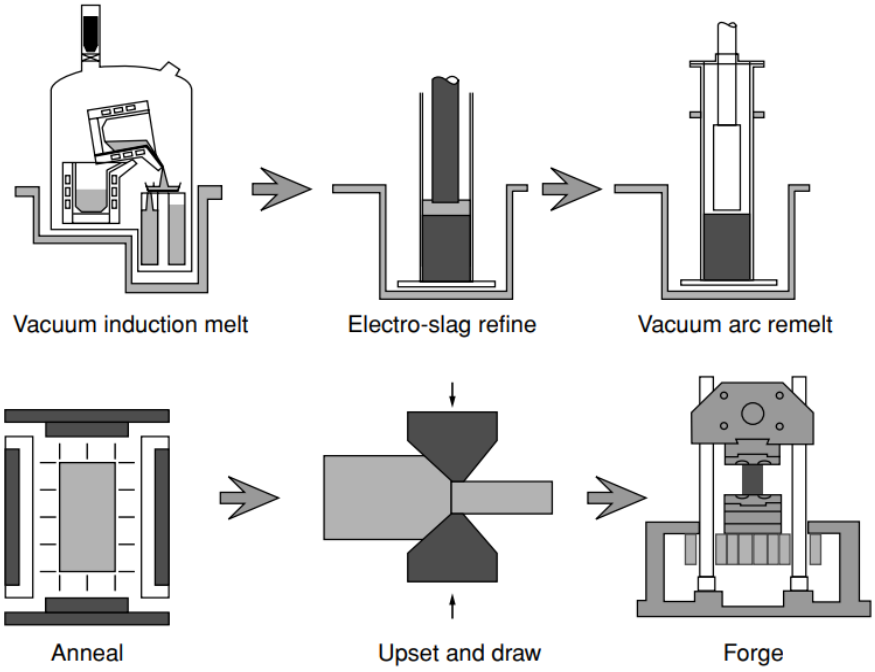

Figure 2.7: Ingot metallurgy casting processes and subsequent thermomechanical processing in production of cast and wrought turbine disc alloys [4].

For heavily alloyed grades such as Rene 95 and RR1000, the cast and wrought route is not an appropriate process due to cracking caused by the considerable segregation produced in producing the ingot and high level of flow stress. **Powder metallurgy (P/M)** is an approach used for these more highly alloyed systems, which provides excellent combined properties such as high strength at high

temperature, superior resistance to fatigue, creep, oxidation and corrosion, when produced by P/M processes [4,37]. The sequence of processes for P/M is illustrated in Figure 2.8 showing VIM as the initial process corresponding to the ingot production method. Remelting and atomising is then used to produce the powder followed by processes of sieving which is a critical step in P/M as it removes large non-metallic inclusions and promotes significant cleanliness. The powder attained is consolidated, degassed and then sealed before hot isostatic pressing or extrusion. Despite the more complex processing and greater cost of P/M than those of ingot metallurgy, enhanced cleanliness of P/M can be achieved by the removal of large non-metallic inclusions. In addition, the property uniformity can be enhanced by the alleviation of macrosegregation and the production of the fine grain structure.

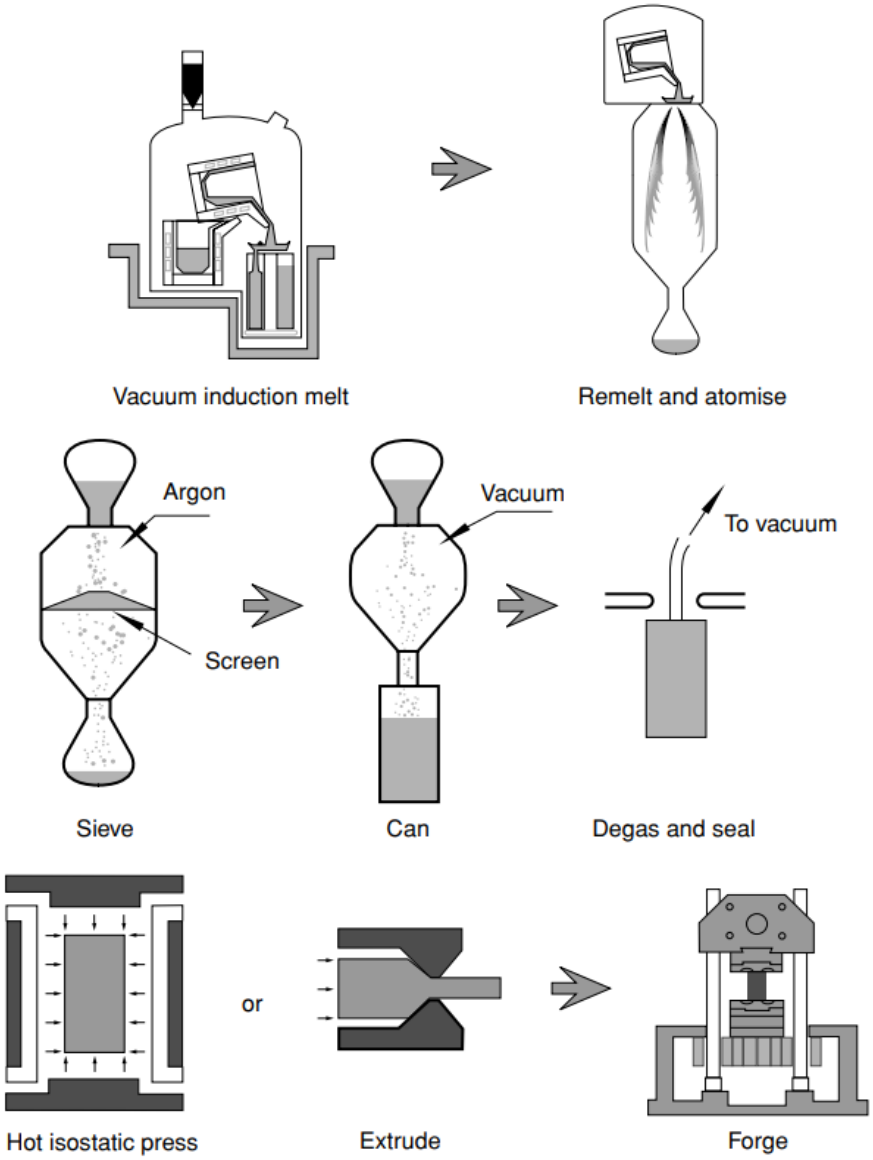

Figure 2.8: P/M processes of production of turbine disc alloys [4].

2.1.4 Heat treatment and microstructure

In polycrystalline Ni-based superalloys, the microstructure exerts significant influences on the material and mechanical properties. The microstructure varies with chemical composition, materials processing, and especially heat treatment condition. In Ni-based superalloys, the proportion, morphology, size and distribution of various phases including γ phase, γ′ precipitates as well as carbides and borides can be tailored typically by heat treatment process including solution heat treatment and subsequent ageing heat treatments used to achieve desirable microstructures [6,38,39]. Figure 2.9 schematically illustrates the key microstructural features of turbine disc alloys indicating the distribution of γ grains, grain boundaries and varying size distribution of γ′ precipitates. The size distribution of strengthening γ′ precipitates correlates to the yield stress of turbine disc alloys as it is related to dislocation interactions as discussed in section 2.1.2.2, which is significantly dependent on the heat treatment. It is well known that heat treatment processing has a controlling effect on the size distribution of γ′ precipitates (i.e. primary, secondary and tertiary γ′ precipitates) and grain size depends on different solution heat treatment (i.e. sub or super solvus) and ageing with varying cooling process. The heat treatment can also decompose MC carbides produced by solidification process into a different type of carbides such as $M_{23}C_6$ and M_6C [22,40].

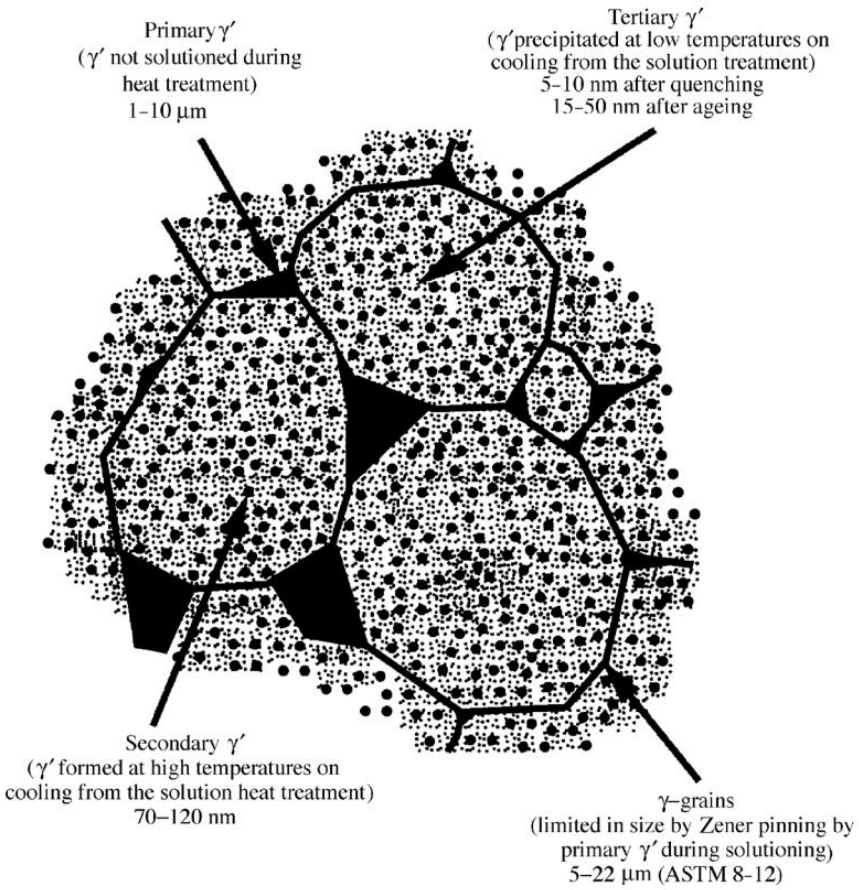

Figure 2.9: Schematic illustration of different phases formed in turbine disc alloys [4].

Commercial heat treatment processes in disc alloys commonly comprise a solution treatment (annealing) normally as a first part of the process, followed by two different ageing treatments [4,41]. In particular the temperature and duration of solution and ageing treatments as well as their cooling rates are critical parameters for tailoring microstructures. It is widely known that the temperature of solution heat treatment primarily influences grain size variation via controlling the distribution of primary γ′ precipitates (which pin the grain boundaries and restrict grain growth during the solution heat treatment). The γ′ solvus for most turbine disc alloys is between 1050 °C and 1200 °C. Solution treatment above (super-) or below (sub-) the γ′ solvus can achieve loss or retention of primary γ′ precipitates and concomitant varying grain size distributions. Grain sizes in Ni-based superalloys can be approximately classified based on ASTM as: fine grain (4-11μm), midi grain (11-32μm) or coarse grain (32-125μm) [42] while grain size is not a variant in this study. It has been established that a fine grained microstructure can be produced with sub γ′ solvus solution heat treatment while a coarse grained microstructure can be achieved by super γ′ solvus solution heat treatments [42–44]. Sub-solvus solution heat treatment retains typically 10-20 % of undissolved primary γ′ precipitates, which constrains grain boundary motion and grain growth and consequently retains a finer grain structure. On the other hand, super-solvus solution heat treatment causes all γ′ precipitate to be dissolved and hence grain boundaries to be relatively unrestricted, leading to a coarse grain size distribution.

In turbine disc applications, the characteristics of a fine grained microstructure are likely to be required for the bore region where tensile and fatigue strength are significant at relatively lower service temperatures while a coarse grained microstructure exhibits distinctive features of greater resistance to creep and dwell fatigue behaviour in the rim region that normally experiences higher temperature [42,45]. As a consequence, dual microstructure heat treatments have been developed to produce different microstructure (i.e. fine and coarse grain size) in different parts of a turbine disc for better component performance [43,44].

Solution temperature (°C)	**Grain size (μm)**	**Primary γ′**		**Secondary γ′**		**Tertiary γ′**	
		Volume fraction	Size (μm)	Volume fraction	Size (nm)	Volume fraction	Size (nm)
1100	4.00 ± 0.45	0.189	2.65 ± 0.24	0.304	72.87 ± 17.99	0.0019	16.0 ± 2.66
1150	40.5 ± 9.6	0.040	2.77 ± 0.31	0.405	93.17 ± 37.22	0.0331	15.1 ± 4.35
1180	413 ± 87			0.455	97.82 ± 27.25	0.0509	15.4 ± 4.39

Table 2.2: Microstructure features in a disk alloy TMW-4M3. Note that the solvus temperature is 1162°C; aging: 650°C/24h/air cooled & 760°C/16h/air cooled [12,46].

Heat treatment parameters result in varying microstructure including grain and precipitate size distributions despite of the same alloy. For instance, different solution temperatures of 1100 °C, 1150 °C and 1180 °C during heat treatment process provide different microstructures (Table 2.2) in disc alloys where the solvus temperature is 1162 °C. A temperature of 1150 °C retains relatively larger grain size and smaller volume fraction of primary γ′ precipitates compared to that of 1100 °C. This is ascribed to slightly higher solution temperature although they are below the solvus temperature. On the other hand, at 1180 °C beyond the solvus temperature, all primary γ′ is dissolved, consequently representing a significantly larger grain size distribution and a bi-modal size distribution comprising secondary and tertiary γ′ precipitates. Figure 2.10 shows clear difference in grain size distribution by electron backscattered diffraction (EBSD) maps and relevant distributions of γ′ precipitates are observed by transmitting electron microscopes (TEM) images [46]. A slightly higher solution heat treatment temperature of 1150 °C offers larger size distribution of secondary γ′ size distribution compared to 1100 °C while tertiary γ′ sizes are similar from the same aging processes.

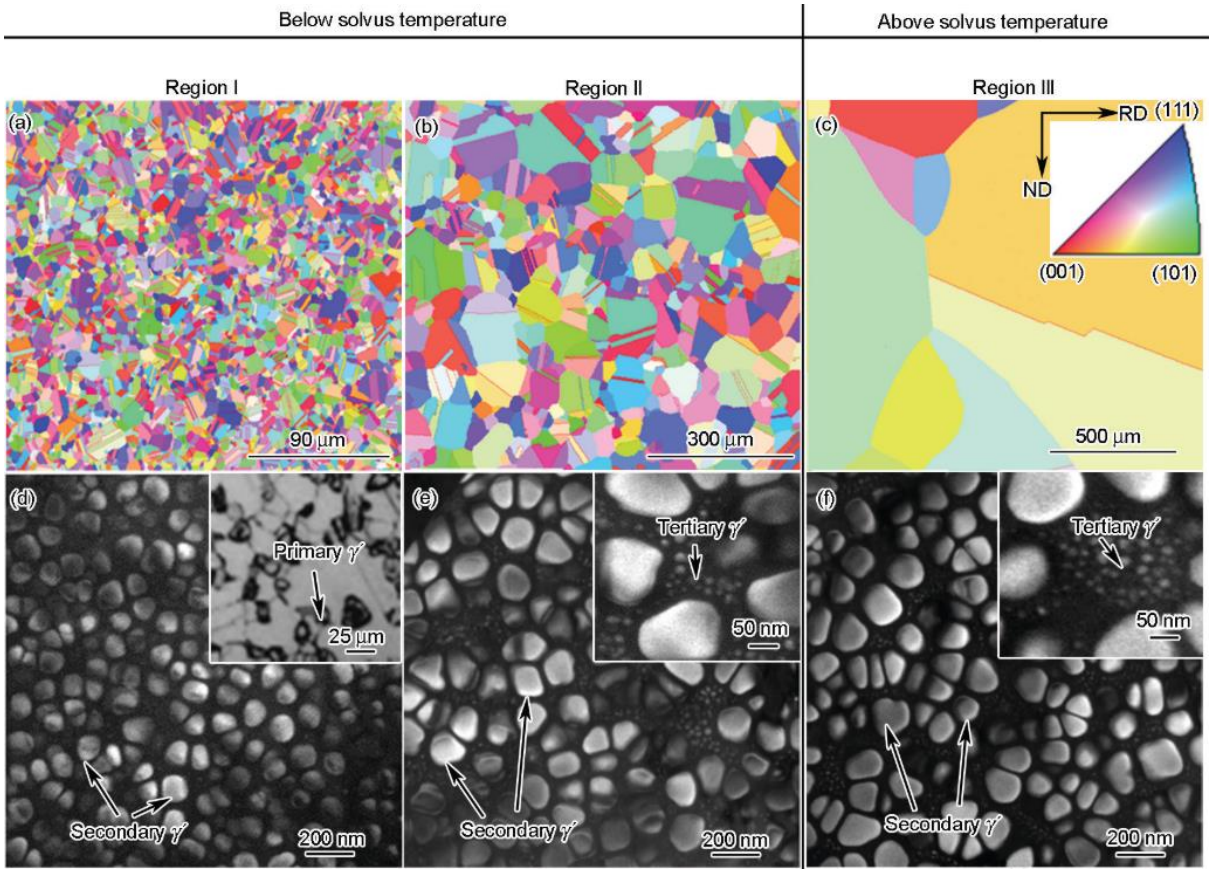

Figure 2.10: (a-c) EBSD maps and (d-f) TEM images of a disc alloy TMW-4M3 after solid solution treatment (a) and (d) at 1100°C; (b) and (e) at 1150 °C; (c) and (f) at 1180 °C; ageing treatment of 650°C/24h/air cooled & 760°C/16h/air cooled (RD-rolling direction, ND-normal direction) [12,46].

It is known that the size, volume fraction, shape and distribution of secondary and tertiary γ′ precipitates have an influence on the mechanical properties of turbine disc alloys, which is achieved by different parameters of the heat treatment process [20,21,45,47–50]. It is generally agreed that the size of secondary γ′ precipitates in typical commercial heat treatments are related to the cooling rate and they tend to exhibit coarsening as the cooling rate decreases. The size of tertiary γ′ precipitates is controlled by the temperature and duration of ageing heat treatment (normally around 700 °C for several hours) with minor effects from the cooling rate of solution heat treatment. The morphology of secondary and tertiary γ′ is generally cuboidal or circular except for the case of considerably slow cooling after solution treatment resulting in a dendritic shape. Figure 2.11 (a)-(c) shows size distributions of γ′ precipitate caused by different cooling rates after solution annealing in turbine disc alloys and Figure 2.11 (d) represent the relation between γ′ precipitate size and cooling rate. It is observed that slower cooling rate is inclined to produce a larger size distribution of secondary γ′ precipitates with cuboidal morphology while faster cooling rate tend to promote a smaller size distribution and more spherical secondary and some extent of tertiary γ′ precipitates are also observed [48].

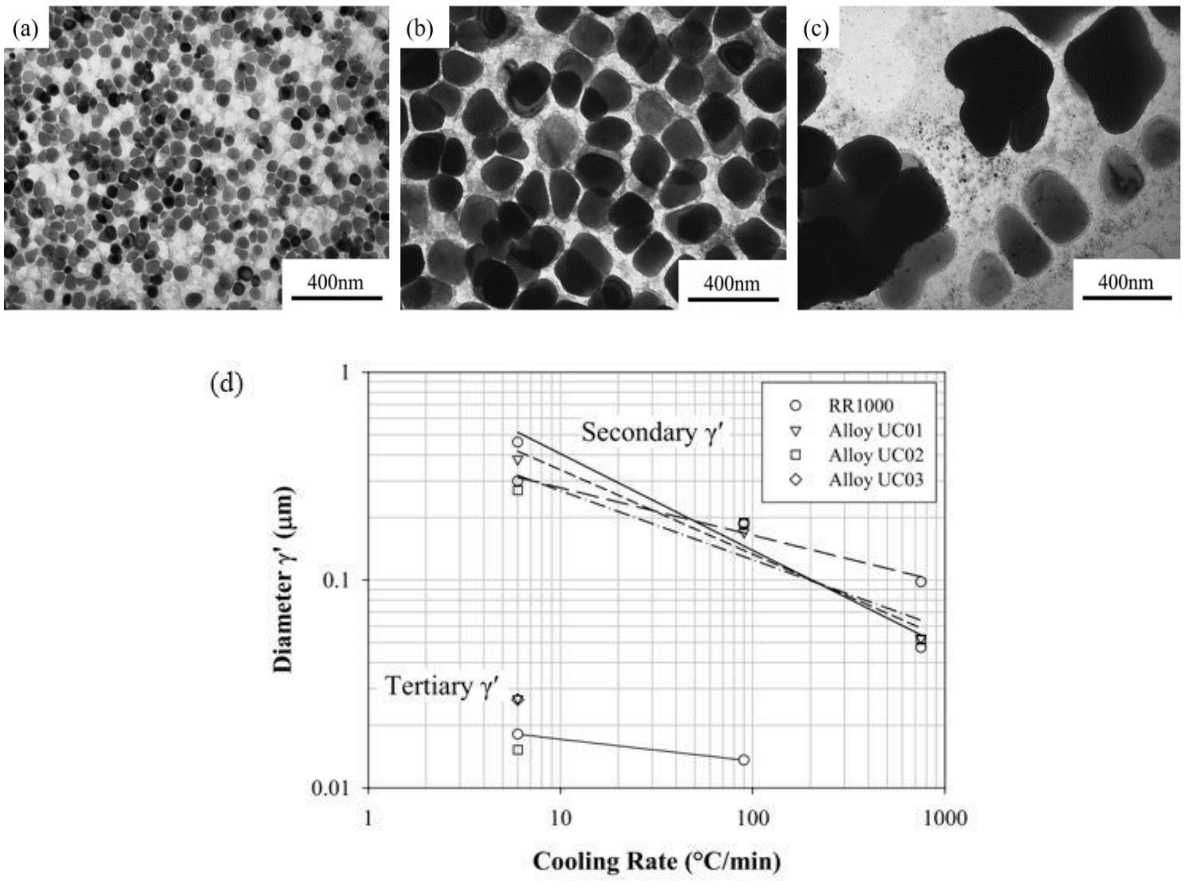

Figure 2.11: (a) Fine secondary γ′ (50 nm) air cooling at 600-900 °C/min (b) secondary γ′ (170 nm) intermediate cooling at 60-120 °C/min (c) secondary γ′ (370 nm) and some tertiary γ′ observed (15 nm) at slow cooling at 6 °C/min (d) effect of cooling rate on secondary and tertiary γ′ size [48]

2.2 Fatigue mechanisms of Ni-based superalloys

2.2.1 Introduction: fatigue of metallic materials

Fatigue refers to damage and failure caused in materials or components by cyclic and fluctuating service loading that is normally less than the yield strength of material. Fatigue damage can be defined as progressive localised permanent structural change occurring in materials subjected to service conditions that produce fluctuating stresses and strains at some point or points and that may culminate in cracks or complete fracture after a sufficient number of fluctuations [51]. Fatigue failure is widely observed in various structural components and therefore it is necessary to investigate its mechanism. Fatigue behaviour is influenced by a range of relevant parameters such as loading condition, geometry, microstructure of materials and environments and can occur in different ways. In elevated temperature environments, the synergistic effects of cyclic loading and elevated temperature can cause creep-fatigue or thermomechanical fatigue. Oxidation or corrosion related fatigue can be attributed to a chemically aggressive or oxidising environment with high stress level in service. Therefore, it is important to understand the mechanisms of fatigue failure under these combined service conditions to develop improved the performance in a variety of materials and components. The entire process of fatigue mechanism typically comprises the fatigue crack initiation (or nucleation), and slow crack propagation, crack coalescence and final fast fracture.

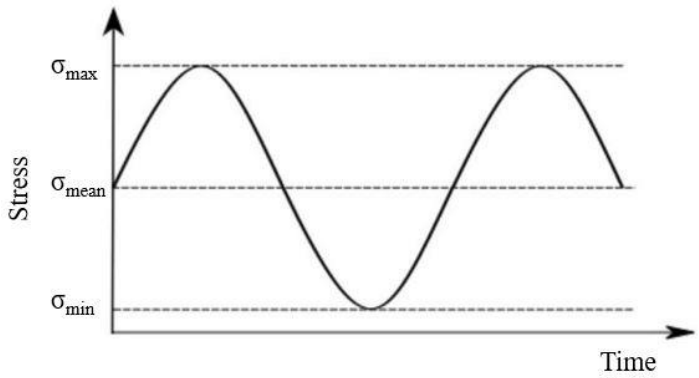

Figure 2.12: A schematic sinusoidal loading cycle of fatigue [52].

Figure 2.12 schematically illustrates simple features of a fatigue loading case presenting fluctuating stresses (or strains) under a sinusoidal loading. σ_{max} and σ_{min} denote a maximum and minimum and a mean load and load amplitude are described by σ_{mean} (= σ_{max} + σ_{min})/2 and σ_{amp} (= σ_{max} - σ_{min})/2, respectively [52]. A load ratio can be represented by an R-ratio (σ_{min} / σ_{max}), which is a distinct parameter of fatigue loading. The fatigue loads can be categorised by the type of loading mode applied to cracks as shown in Figure 2.13. These loading modes are termed Mode I, II and III applied in particular loading directions including tension, in-plane shear and out-of-plane shear, respectively.

The corresponding stress intensity factors for these three loading modes are denoted by $K_{\mathrm{I}}, K_{\mathrm{II}}$ and K_{III} in fracture mechanics terminology. It is worth noting that a mixed mode of such loading conditions is commonly seen in service loading cases.

- Mode I: Separation of the crack surface by tension loading perpendicular to the surfaces denotes an opening mode. It is the most commonly applied and studied loading mode
- Mode II: Sliding of two-crack surfaces over each other by in-plane shear in a normal direction to the crack front known as a sliding mode.
- Mode III: Moving in opposite directions of two crack surfaces, resulting from out-of-plane shear parallel to the crack front is known as a tearing mode.

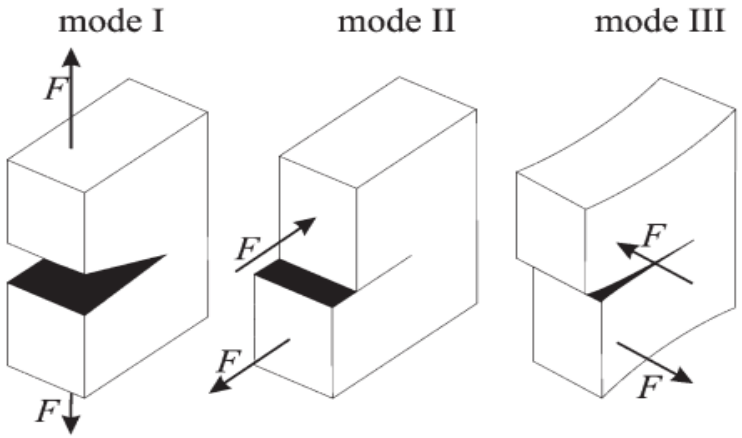

Figure 2.13: Definition of loading modes; mode I (tension), mode II (in-plane shear) and mode III (out of plane shear) [53].

2.2.2 Fatigue life approaches

Much work has focused on the lifetimes of a variety of engineering components to predict their failure and identify what defect levels need to be checked and repaired in service. Two main approaches widely used for the development of fatigue life prediction are the total life approach and damage-tolerant approach. They are outlined in this section with respect to understanding the different stages of fatigue.

2.2.2.1 Total life approach

The first systematic approach to assess the fatigue behaviour was introduced by Wohler (known for Wohler curve or S-N curve), which has become the most common in fatigue life prediction method. The S-N curve as shown in Figure 2.14 describes the relation between applied stress or strain amplitude (S) and loading cycles (N) to fracture. The total life approach comprises two main methods, which are stress-life (S-N curve) and strain-life (ε-N) approaches. The stress-life method is typically used for high cycle fatigue (HCF) regime where elastic deformation is dominant in a component

caused by low amplitude stresses. As a distinct feature of this approach, fatigue limit (or endurance limit) can be defined through the S-N curve (Figure 2.14). The fatigue limit refers to a stress amplitude below which materials appear to have an infinite lifetime without failure (or to a specific long lifetime, e.g. $>10^7$ cycles). On the other hand, the strain-life approach is normally employed for low cycle fatigue (LCF) regime where plastic deformation predominantly occurs from cyclic loading at high stress amplitudes and where the strain range controls the lifetime.

For a simple relationship between stress amplitude with loading cycle to failure proposed by Basquin (known as the Basquin relation [54]), a linear line of the S-N curve applied in the logarithmic plot was defined as:

$$\frac{\Delta\sigma}{2} = \sigma_a = \sigma_f'(2N_f)^b \qquad (2.4)$$

where σ_f' is the fatigue strength coefficient and b is the fatigue strength exponent, which are material constants.

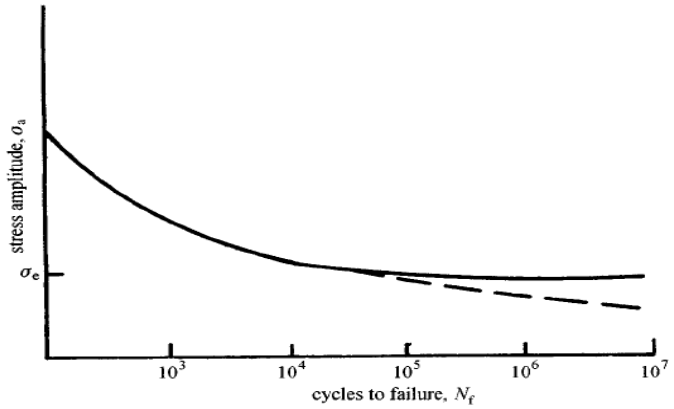

Figure 2.14: Typical S-N diagram [52].

In a similar way to the Basquin relation, Coffin and Manson introduced a relation between the strain amplitude with loading cycle to failure, which is known as the Coffin-Manson equation [55,56]

$$\frac{\Delta\varepsilon_p}{2} = \varepsilon_a = \varepsilon_f'(2N_f)^c \qquad (2.5)$$

where ε_f' is the fatigue ductility coefficient and c is the exponent of fatigue ductility.

The total strain amplitude, $\Delta\varepsilon/2$ can be expressed to the sum of both elastic strain amplitude ($\Delta\varepsilon_p/2$) and plastic strain amplitude ($\Delta\varepsilon_p/2$) followed by:

$$\frac{\Delta\varepsilon}{2} = \frac{\Delta\varepsilon_e}{2} + \frac{\Delta\varepsilon_p}{2} \qquad (2.6)$$

and by using the Basquin and Coffin-Manson equations as well as the total strain amplitude, the total fatigue life can be characterised by total strain amplitude (elastic and plastic):

$$\frac{\Delta\varepsilon}{2} = \frac{\sigma_f'}{E}(2N_f)^b + \varepsilon_f'(2N_f)^c \qquad (2.4)$$

where the constants σ_f', b, ε_f' and c are material properties.

It is generally known that the fatigue life assessment using the total life approach of the stress-life or strain-life is examined on defect-free specimens and essentially associated with the fatigue life in a system which is mostly dominated by factors that control the crack initiation process (i.e. most of the lifetime is dominated by fatigue initiation processes). However, on occasion, structural components containing notches or defects mean it is necessary to take into account the effects of the notches and defects where a crack propagation process is normally dominant. In a case where pre-existing defects are embodied, total life approaches are expected to be unreliable when the main controlling factor in service life is a crack propagation process from pre-existing defects.

2.2.2.2 Damage-tolerant approach

The damage-tolerant approach assumes flaws such as geometric discontinuities and non-linear sections already exist in engineering components, which can lead to a stress concentration. The size of the existing flaw (an initial size, a_0) is normally determined from the non-destructive testing (NDT) methods including visual, X-ray techniques and ultrasonic methods [57]. This approach aims to understand the FCG behaviour of these inevitable defects until the failure takes place once a flaw size reaches a critical size (a_c). In other words, the components should be safe and stable as long as the existing flaws do not reach a critical value (a_c) beyond the design tolerance. The usable fatigue life is then defined as the number of fatigue cycles or time for the crack growth from the initial defect size (a_0) to reach the critical defect size (a_c). The critical defect size for the fatigue crack can be calculated based on the fracture toughness of the material, limit load and allowable strain or change in the compliance of the component. The determination of fatigue propagation life based on a damage tolerant approach is often based on theories of Linear Elastic Fracture Mechanics (LEFM) or Elastic Plastic Fracture Mechanics (EPFM).

In fracture mechanics, LEFM is widely used to describe the local stress characteristics in the vicinity of the crack tip in terms of applied loading and defect size when the plastic zone ahead of the crack tip is sufficiently smaller than the defect size. LEFM can be typically applied in components embodying a sharp crack with a length of 2a passing through the middle of the component under Mode I loading as shown in Figure 2.15 (a). The local stress state near the crack tip in an elastic material is schematically illustrated in Figure 2.15 (b)

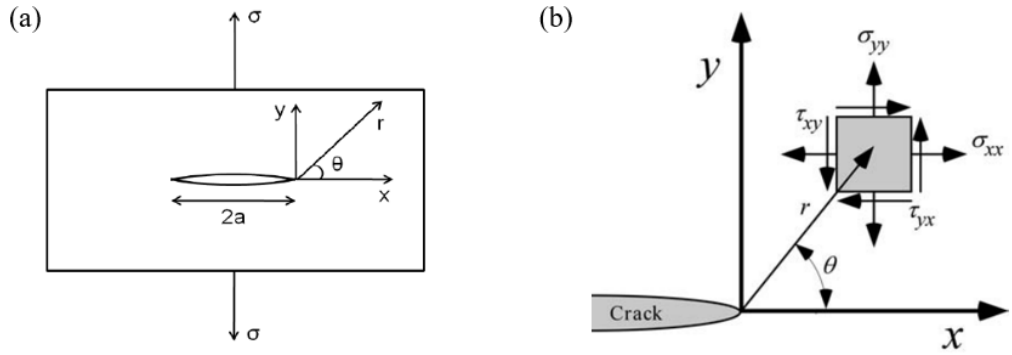

Figure 2.15: (a) A thin elastic plate containing a sharp crack (b) stresses near the crack tip in an elastic material [52,58].

The local stresses at coordinates (r,θ) close to the crack tip can be expressed by the following equations:

$$\sigma_{xx} = \frac{K_I}{\sqrt{2\pi r}}\left[cos\frac{\theta}{2}\left(1 - sin\frac{\theta}{2}cos\frac{3\theta}{2}\right)\right] \quad (2.7)$$

$$\sigma_{yy} = \frac{K_I}{\sqrt{2\pi r}}\left[cos\frac{\theta}{2}\left(1 + sin\frac{\theta}{2}cos\frac{3\theta}{2}\right)\right] \quad (2.8)$$

$$\sigma_{zz} = \frac{K_I}{\sqrt{2\pi r}}\left[cos\frac{\theta}{2}sin\frac{\theta}{2}cos\frac{3\theta}{2}\right] \quad (2.9)$$

where K_I is the stress intensity factor of Mode I, mainly affected by shape, location and size of a defect and the remote load on the structure as:

$$K = \sigma\sqrt{\pi a}\, f\left(\frac{a}{w}\right) \quad (2.10)$$

where σ is applied stress, a is the size of crack and $f\left(\frac{a}{w}\right)$ is the compliance function varying with geometry and shape.

The stress intensity factor *K* plays a major role in the characterisation of fracture dominated by crack propagation [59]. A stress intensity criterion using the parameter *K* is a way of taking into account the stress state in the vicinity of the crack tip and hence the driving force for the crack growth. This is straightforward to use, where the value of *K* as expressed in equation 2.10 can be defined in terms of the crack size, applied stress and the compliance function reflecting the dimensions of a component. The stress state near the crack tip area where an annular zone ahead of the crack tip can be characterised by *K* is also known as the region of *K*-dominance (Figure 2.16). When considering the parameter *K* near the crack tip, however, the stress intensity is predicted to increase infinitely as *r* approaches to zero where the crack tip exists (a stress singularity), as shown in Figure 2.17. In reality, the area near the crack tip experiences plastic yielding in the inner radius zone of the region of *K*-

dominance, and LEFM will be invalid in this local plastic deformation zone. In the *K*-dominance region further away from plastic zone, *K* appears to provide a good description of the stress state around the crack. If the plastic zone size is sufficiently small compared with the size of the specimen and crack, *K* can still be a reasonable descriptor of the overall crack driving force. The area outside of the outer radius of *K*-dominance zone can be described as far-field stresses influenced by the sample geometry.

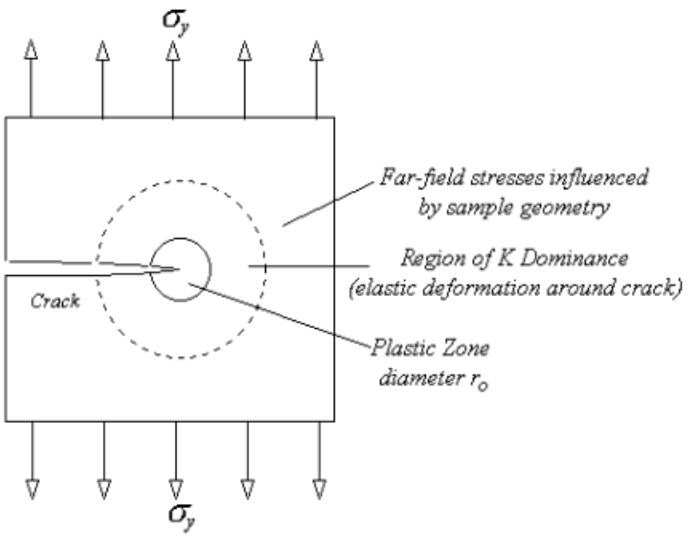

Figure 2.16: Schematic *K*-dominance and plastic zones [60].

Crack growth behaviour (the ability of a material to resist fracture) is characterised by the critical value of the stress intensity factor K_c which is a function of the mode of loading, material microstructure, strain rate, stress state (plane stress or strain), environment and temperature. The critical stress intensity factor (K_c) generally denotes the fracture toughness of materials. The stress intensity factor range, ΔK is derived from the applied stress range $\Delta\sigma$ and characterises fatigue crack growth.

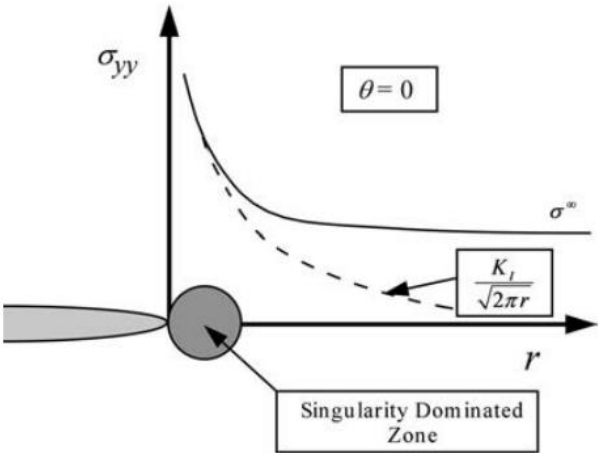

Figure 2.17: A schematic plot of stress vs distance from the crack tip in Mode I [58].

Specimens with pre-existing long cracks are often experimentally tested and FCG rate (*da/dN*) vs stress intensity range (ΔK) curves are commonly obtained for a given material. The plot of *da/dN* vs ΔK represented on a log-log scale generally shows a sigmoid shape curve indicating three distinct areas referred to as region A, B and C as distinguished in Figure 2.18. In region A where a low ΔK is dominant and cracks propagate slowly, crack growth behaviour is strongly influenced by the local microstructure of materials, mean stress levels or environment. A threshold of stress intensity factor (ΔK_{th}) in region A is the point below which a fatigue crack will not grow significantly, indicating the critical driving force to obtain a detectable crack growth rate (for a pre-existing crack). Region-B is characterised by the Paris' law, describing the stable crack growth and power law relationship between stress intensity factor range and fatigue crack propagation rate as shown in the equation below:

$$\frac{da}{dN} = C\Delta K^m \qquad (2.11)$$

where *C* and *m* are material constants determined by experimental testing.

Finally, region C represents rapid crack growth until the final fracture which occurs at the high degree of ΔK levels (where K_{max} is approaching fracture toughness) and which exhibits bursts of monotonic fracture mechanisms often with a large amount of plasticity. This regime is also influenced by the microstructure and mean stress levels. The crack size when final fracture occurs in this regime denotes the critical crack size (a_f).

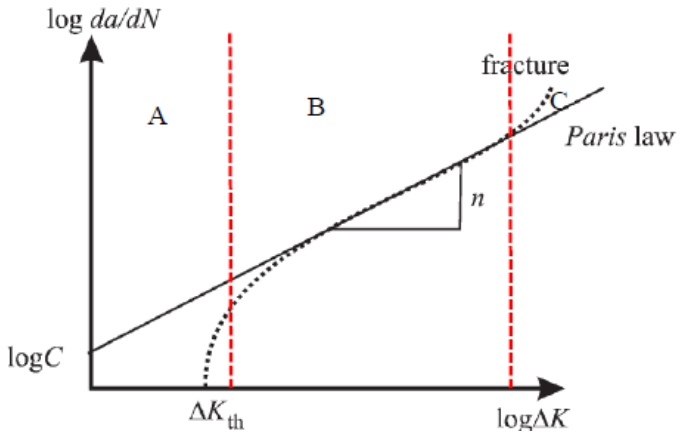

Figure 2.18: A schematic diagram of FCG rate (*da/dN*) vs stress intensity factor (ΔK) on a log-log plot showing three different regions of the crack propagation [53].

2.2.3 Cyclic deformation behaviour

2.2.3.1 Overview of cyclic deformation

Deformation processes under cyclic loading in metallic materials give rise to a critical understanding of the whole spectrum of fatigue behaviour, particularly as precursors to fatigue crack initiation. Cyclic loading leads to changes in materials with hardening, softening or stabilised behaviour developing depending on their microstructure, mechanical stress level, loading frequency, temperature and environment, etc. The mechanism of cyclic deformation correlates with the nature and stability of the dislocation substructures produced, linking to any decrease in the intensity of the cyclic hardening or softening until no further changes in material properties occur (a saturation point) [52,61]. Such behaviour can be categorised under two different characteristics as soft and hard materials. Soft materials exhibit a low dislocation density at the start of cycling while there is an increase in the dislocation density during cyclic straining which induces cyclic hardening. On the other hand, hard materials possess an initial high dislocation density at first, followed by a decrease in the dislocation density by the rearrangement and annihilation of dislocation substructures during cyclic straining. This results in cyclic softening. The presence of hardening precipitates can also contribute to the evolution of such behaviours under cyclic loading [62].

Materials generally experience softening and hardening during cyclic loading. Such cyclic hardening and softening deformation is characterised by a relation between cyclic stress and strain amplitude which is known as a stress-strain hysteresis loop as shown in Figure 2.19 (a). A curve connecting maximum stress or strain points of saturated stress-strain hysteresis loops is known as the cyclic stress strain (CSS) curve seen in Figure 2.19 (b). The CSS curve basically plays a crucial role in characterising the stress-strain relation of a material for the fatigue initiation behaviour and consequent overall fatigue life. The cyclic deformation behaviour also varies with the microstructure of materials, e.g. polycrystalline alloys have different grain orientations in individual grains, differing grain sizes and their complex interactions with cyclic loading, particularly in terms of the resolved shear stress applied, which associated with overall slip behaviour response.

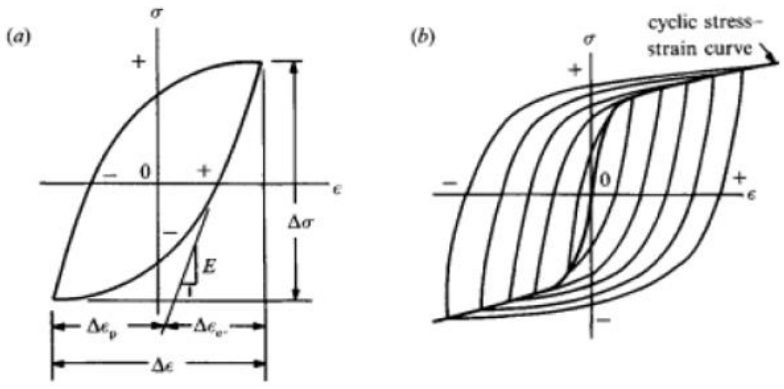

Figure 2.19: Schematic graphs of (a) a typical hysteresis loop (b) a CSS curve [52].

2.2.3.2 Deformation behaviour of Ni-based superalloys

It is widely recognised that the deformation behaviour during cyclic loading of Ni-based superalloys is closely linked to the dislocation motion and concomitant slip behaviour. The dislocation motion is influenced by a variety of factors such as elemental composition (related to strengthening mechanism), microstructural features, temperature and strain rate and amplitude [63–67]. In this study, the effects of microstructure (i.e. γ′ precipitates) and temperature on deformation behaviour in polycrystalline Ni-based superalloys are mainly examined. Particularly, the slip behaviour (linked to dislocation motion) interacting with the size of precipitates contributes to fatigue crack initiation process of the alloy [4]. As aforementioned in section 2.1.2.2, dislocation motion in Ni-based superalloys (i.e. whether cutting or looping of γ′ precipitates) is closely linked to the size distribution of the strengthening precipitate. These deformation processes result in homogeneity or heterogeneity of slip behaviour characterised by various features including slip planarity, density of slip bands or average spacing between slip bands. The γ′ precipitate shearing process is linked to more planar slip and heterogeneous deformation, featured by a low slip band density with intense slip bands formed. Such shearing processes contribute to the advanced cyclic softening in γ′ strengthened superalloys by reducing the γ′ precipitate cross sectional area that the dislocations have to traverse [63]. It is observed that Ni-based superalloys with a microstructure of coarse grains and small γ′ particles predominantly experience such deformation behaviour [49,65,68]. The Orowan looping mechanism exhibits different features of deformation behaviour presenting more wavy slip and homogeneous deformation, with cross-slip allowed. In Ni-based superalloys with a microstructure of fine grains and large γ′ particles, these deformation features are of significance, showing a relatively high slip band density but with less intense slip bands [65,68]. Overall, precipitate cutting is likely to occur at finer precipitate sizes and represent more planar slip, whereas precipitate cutting takes place relatively less at coarser precipitate sizes thus indicating the dislocation mechanism is inclined to switch to a looping process and more homogeneous deformation while slip bands can still be observed [69].

Heterogeneous slip in the shearable γ′ precipitate size results from dislocation motion concentrated in planar slip bands, which is also related to low SFE and formation of an APB. SFE can be lowered by some alloying elements and subsequently lead to further dissociation of screw dislocations into partial dislocations separated by the stacking fault. Such partial dislocations formed can no longer cross slip, then contributing to more planar slip. As mentioned previously, an APB of an unstable structure possessing a high energy is formed when a/2 <110>{111} dislocation cut through ordered γ′ precipitates. In the process of precipitate shearing, paired dislocations are therefore activated to minimise the APB and the paired dislocations (whether strongly or weakly coupled) repeatedly cut the γ′ precipitates in the same slip plane, which decrease the cross sections of γ′ precipitates [70].

This makes it easier for subsequent paired dislocations to penetrate the γ′ precipitates at a lower stress level promoting softening in the slip direction and leading to the concentration of slip, which again results in dominant planar slip. As the size of γ′ precipitate becomes too large to be sheared, Orowan dislocation looping becomes a more dominant mechanism and thereby promotes homogeneous deformation although some slip bands are still observed. [68]. Homogeneous deformations is normally linked to more strain hardening and attributed to a higher response stress under a given strain range.

At elevated temperature, cross slip appears more dominant (as sufficient thermal energy allows dissociated dislocations to recombine and cross-slip) and promotes a more homogeneous slip character. KW locking is also thermally activated (as mentioned in section 2.1.2.2) as a distinct feature of Ni-based superalloys [35]. The process can contribute to an enhancement in high temperature strength by hindering deformation behaviour on account of thermally activated locking of cross slipping screw dislocations in γ′ precipitates and thereby a hardening effect. Coarsening of γ′ precipitates may also take place at high temperature and result in a hardening effect by causing dislocations to loop more and consequently deformation to be hindered. In addition, the formation of carbides, borides or other precipitates or segregation of solutes at dislocations can also promote hardening by acting as a barrier to further dislocation motion [71,72]. However, cyclic softening can also take place at the beginning of cyclic loading exhibiting less localised slip bands and lower dislocation density within the slip bands as the increased mobility of dislocations at high temperature can result in the applied plastic strain being accommodated by fewer dislocations [70]. In addition, some formation of planar slip bands and resultant γ′ precipitate cutting can be observed even at high temperatures, which also results in a softening effect. It appears that the effects of γ′ size distribution on dislocation behaviour and hence slip character is a complex mechanism, especially at varying temperatures.

2.2.4 Fatigue crack initiation behaviour

2.2.4.1 Overview of fatigue crack initiation

Fatigue crack initiation, the first stage of fatigue mechanism, is widely understood to be a microscopic nucleation of a crack that can be detected at the size scale of observation. The main sources of fatigue crack initiation in metallic materials generally relate to the sites where stress concentration occurs, followed by local plastic deformation. The mechanism of crack initiation at a surface is closely associated with dislocation motion under shear stress at an atomic level. The dislocations keep moving along slip bands (the intensity of which may vary with overall slip character) and then pile up when they are interrupted by microstructural barriers such as inclusions, precipitates and grain boundaries. At a surface, the slip band may experience irreversible slip (either

mechanically irreversible due to slipping back on a different plane or due to physical/chemical absorption processes blocking reversed slip on the same plane) [73]. Cyclic loading repeatedly builds on the irreversible slip and then forms persistent slip bands (PSBs) - an assembly of slip planes due to these slip irreversibility processes, followed by strain localisation [74]. Once the intensity of dislocation increases within the PSBs, localised work hardening and softening arise, resulting in local plastic deformation that includes intrusions and extrusions on a surface as shown in Figure 2.20 [75]. This promotes roughening of the surface. Such characteristics of irregularity on a surface act a localised stress concentrator which can initiate a crack on the surface and thereby induce further surface roughening processes and crack initiation [76].

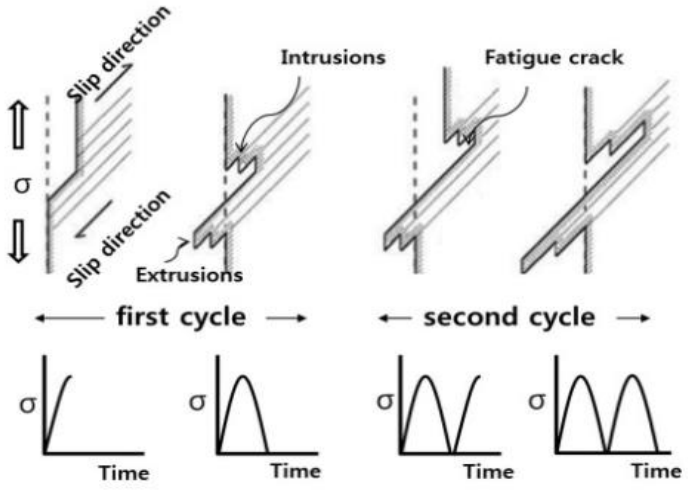

Figure 2.20: Schematic illustration of fatigue crack initiation mechanism at a surface [75].

2.2.4.2 Microstructural effects on fatigue crack initiation

In polycrystalline Ni-based superalloys, it is widely known that fatigue cracks generally initiate at various microstructural heterogeneities including slip bands, precipitates, porosities, grain boundaries, twin boundaries and other defects where stress concentration arises in the absence of environmental effects [8,20,43,49,77–79]. For instance, microstructural features such as porosity distribution, γ′ precipitate size, grain size and carbide formation exert considerable influences on the crack initiation process.

Slip band cracking caused by cyclic strain localisation is primarily observed as the fatigue crack initiation mechanism in Ni-based superalloys at room and intermediate temperatures. Crack initiation from slip bands is closely associated with the intrinsic microstructure of the alloys. The size distribution of γ′ precipitates is connected to the slip planarity resulting from different dislocation motions of precipitate cutting or Orowan looping during cyclic deformation, which leads to the crack initiation behaviour. Microstructures with coarse grains and fine γ′ precipitates appear to promote

stage-I cracking along PSB promoted by heterogeneous and planar slip at room and low temperatures, considerably contributing to slip band crack initiation [49,65,68,80]. Slip band crack initiation is also promoted by environmentally assisted slip irreversibility as the absorption of oxygen at the fresh formed slip steps can make reversed slip difficult as schematically illustrated in Figure 2.21. During cyclic loading, the damage is gradually accumulated due to such slip irreversibility, causing local decohesion along the slip band. This mechanism can promote enhanced surface roughening, which results in the crack initiation process. It appears that intense slip bands are also promoted adjacent to twin boundaries in Ni-based superalloys as twin boundaries are linked to strain localisation due to high elastic incompatibility stress, which give rise to crack initiation at low temperature [79,81].

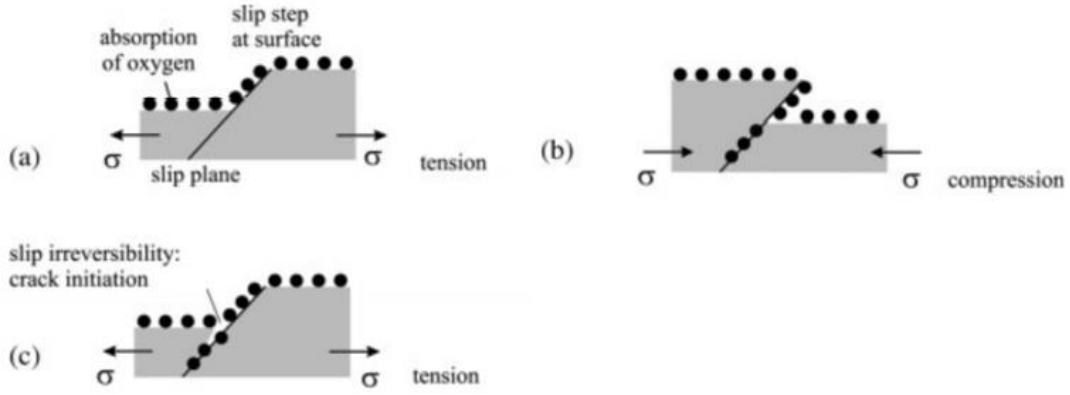

Figure 2.21: Crack initiation due to environmentally assisted slip irreversibility: (a) exposure of fresh metal surface; (b) absorption of oxygen; (c) local decohesion [53].

Grain boundaries are known as preferable fatigue crack initiation sites in polycrystalline Ni-based superalloys, which is associated with different crystallographic grain orientations (related to elastic anisotropic material property and plastic incompatibility of the grains) [53]. Different crystallographic orientation of the grains causes heterogeneously distributed local stress and consequently anisotropic properties as illustrated in Figure 2.22. This can promote stress peaks at the grain boundaries and triple points that may exceed locally the yield strength, which can result in fatigue crack initiation [53]. Plastic incompatibility of adjacent grains is another critical parameter in the crack initiation process for high strain amplitudes (i.e. LCF and high misorientation angles) while elastic anisotropy becomes more significant during crack initiation at low strain amplitudes (i.e. HCF) [82–87]. High angled grain boundaries are likely to result in a significant amount of slip band impingement due to dislocation pile-ups at the grain boundaries. On the other hand, it is seen that slip bands can transmit through low angled grain boundaries, which is linked to better intergranular crack resistance. It is also observed that the crack initiation preferentially initiates within grains or in grain boundaries neighbouring larger grains than average [88].

It is commonly seen that cracks tend to initiate from pores which are a significant controlling factor of the initiation mechanism of the alloys together with slip bands impinging on, or emanating from

the pores due to the local stress concentration they offer [49]. This is marked at low temperatures. Highly faceted areas indicating planar slip behaviour and stage-I cracking along slip bands are seen near the pore, showing slip band cracking at the initiation point. In addition, cracks are likely to initiate at the interface between inclusions and the matrix as their different elastic properties can also promote an increase in stress concentration near the interface, leading to enhanced crack initiation behaviour.

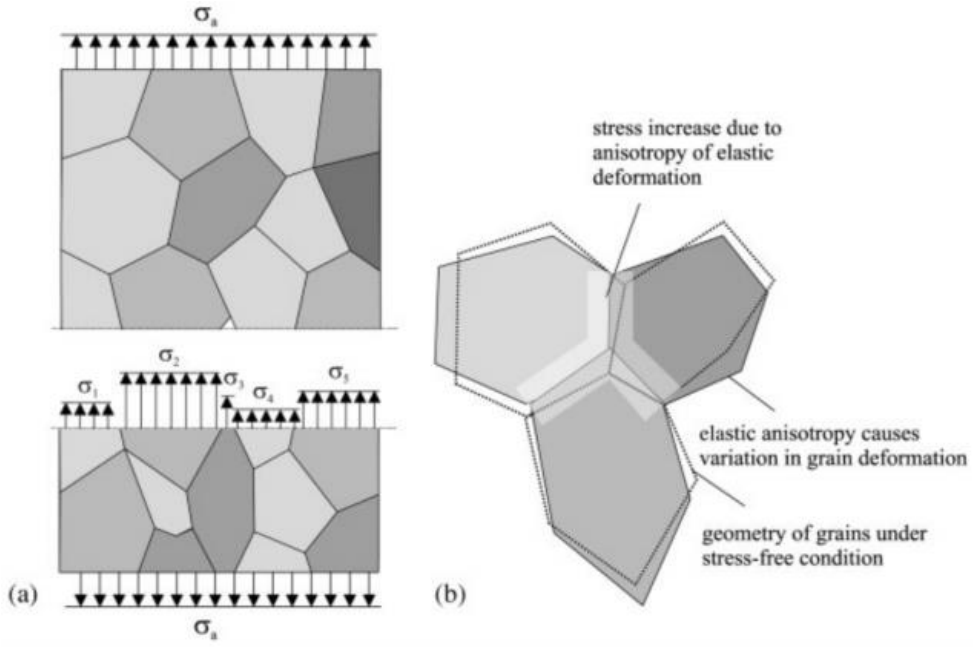

Figure 2.22: Schematic representation of the influence of crystallographically anisotropic materials properties: (a) inhomogeneous stress distribution (simplified for normal stresses only); (b) resulting anisotropy of elastic deformation [53].

At elevated temperatures thermally activated processes promote multiple slip processes. Slip band cracking is less prevalent while fatigue crack initiation at the grain boundaries (intergranular cracking) is promoted more by the reduced grain boundary strength due to the diffusion of oxygen and concomitant oxidation process on the grain boundaries [89–91]. It is observed that a finer grain size is closely related to a greater extent of intergranular crack initiation as more grain boundaries act as diffusion paths for oxidising and embrittling species and are environmentally attacked. The stress increase from oxide formation and difference in the volumes between the oxides formed and regions of grain boundaries under applied loading contributes to enhanced intergranular crack initiation, which results from the embrittlement behaviour of oxides. In turbine disc superalloys, NiO, Cr_2O_3, CoO, Al_2O_3 and TiO_2 are the oxides commonly seen at elevated temperatures [92,93]. Oxidised carbides (particularly at grain boundaries) are also seen at elevated temperatures and they are expected to promote crack initiation in Ni-based superalloys due to the volume expansion assisted by the oxidising environment and loading applied [94,95]. Consequently, this also promotes short

crack propagation along the grain boundaries after any fatigue crack initiation process. Creep can also have an influence on crack initiation at the grain boundaries as porosities form at triple points at grain boundaries due to the combination of grain boundary sliding and vacancy diffusion towards areas of high hydrostatic tension [53].

2.2.5 Fatigue crack growth behaviour

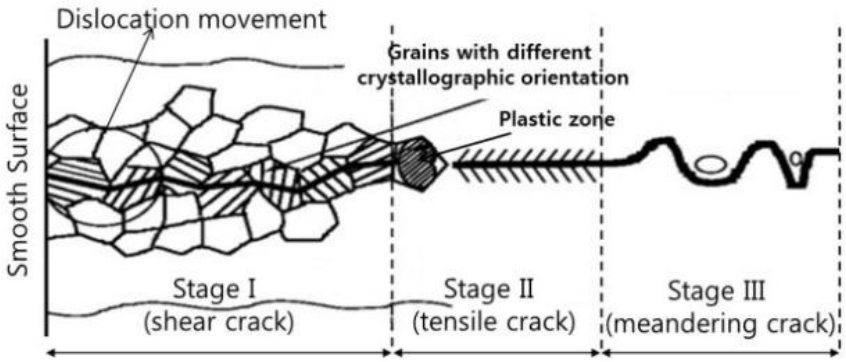

Figure 2.23: A schematic diagram of fatigue crack propagation showing the three different stages [75].

The usable fatigue life of the majority of engineering components comprises the time to propagate a flaw from its initial dimension to a critical size under cyclic loading. Fatigue crack propagation is characterised by the FCG rate in terms of the crack length increment per cycle (*da/dN*). The mechanism of the FCG is generally dominated by the slip characteristics of materials, dimensions of microstructural features, applied stress level, the extent of plasticity ahead of the crack tip and environmental effects. The microscopic FCG is schematically divided into three different stages as described in Figure 2.23. Firstly, stage-I is dominated by shear stresses or strains in the direction of the primary slip system at low stress intensity range levels when the crack and plastic deformation zone around a crack tip accounts for only a few grain diameters. The mechanism of single shear promotes micro-crack propagation exhibiting a zig-zag crack path along activated slip planes across grains, which is closely linked to local microstructural features such as the crystallographic orientation of the grains. Consequently, fracture surfaces show characteristics of crystallographic facets or serrated crack growth as the resultant of more planar slip processes (Figure 2.24 (a)), which is pronounced at low temperatures.

Sequentially, at higher stress intensity range levels, a crack tip plastic zone now extends over several grains, with a more widespread yielding and crack propagation will transmit into stage-II growth which is driven by tensile stresses or strains perpendicular to the crack path, although it is still somewhat influenced by the local microstructures. This stage can involve simultaneous or alternating

deformation behaviour along two slip systems propagating the crack overall normal to the far field stress as shown in Figure 2.24 (b). This stage can exhibit the formation of fatigue 'striations' as characteristic ripples on the fracture surface. It is observed that the spacing between adjacent striations indicates the average crack growth rate per cycle in the Paris' regime of the crack propagation process. Finally, stage-III indicates that cracks propagate rapidly with an unstable rapid crack growth rate as K_{max} approaches the fracture toughness of the material and catastrophic failure takes place in the end of this stage (which has the shortest lifetime of the three stages). Stage-III fatigue fracture surfaces generally show fibrous and rough features as well as an extensive extent of plastic deformation (e.g. large shear lips) due to the bursts of monotonic behaviour.

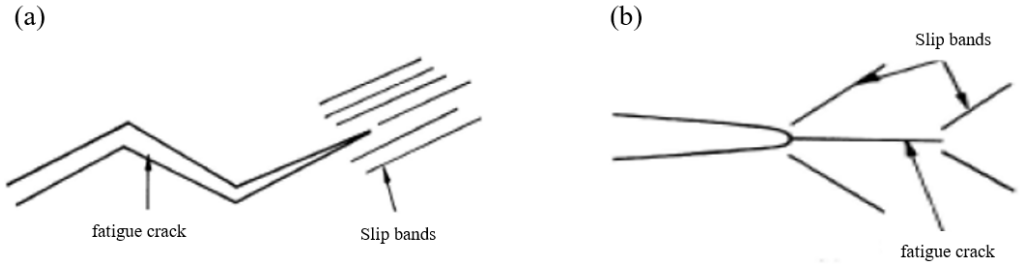

Figure 2.24: Schematic of an idealisation of (a) stage-I crack growth with a zig-zag crack path (b) stage-II crack growth [52].

2.2.5.1 Overview of short fatigue crack growth

The short crack growth regime occurs just after the crack initiation process, followed by a transition to the long crack growth regime. The majority of the fatigue life of turbine discs is spent in the early stages of lifetime such as crack initiation and short crack growth regime due to their high overall service stresses. In this regime, LEFM application is not strictly appropriate as the size of the short crack is comparable to the crack tip plastic zone size and thereby cannot be considered to be described as being controlled by the *K* dominance zone. Such short cracks are often termed "mechanically short". It is also not easy to detect such short cracks due to their size, therefore high resolution observations are usually used. A widely used common method is the regular replication of the surface containing short cracks during interrupted testing, using silicone compounds which are later observed with optical microscope (OM) or scanning electron microscope (SEM). One explicit characteristic of short FCG behaviour is that it exhibits significant scattered and irregular FCG rate and typically experiences stage-I crack growth. At similar levels of ΔK, short fatigue cracks normally experience highly scattered FCG rates compared to the averaged long crack behaviour [96,97]. This scatter is closely related to the varying effects of local microstructural features. In addition, this can also be partly linked to the lack of closure developing in the wake of so-called "physically small" cracks compared to a longer crack, as well as the possible invalidity of LEFM and the fact that the crack is growing under mixed mode conditions rather than pure Mode I loading. Due to the concentration of

deformation into intense slip bands, short cracks in polycrystalline Ni-based superalloys appear to propagate in a crystallographic manner parallel to the {111} planes along the <011> direction at low temperatures that promote planar slip processes [4]. These short cracks forming along the primary slip system in each grain typically exhibit a zig-zag crack path and crystallographically faceted fracture surface, followed by stage-II crack growth at longer crack lengths when the faceted features become less evident [8,49].

2.2.5.2 Microstructural effects on short crack behaviour

In Ni-based superalloys, early stage FCG mechanisms are strongly influenced by local microstructural features such as grain boundary features, grain orientation, twin boundaries and precipitates ahead of the crack tip and are also affected by extrinsic influential factors such as temperature and loading conditions [3,49,78,81,98–101]. Microstructural parameters including γ′ precipitate size, grain size and carbide distribution at grain boundaries are tailorable by heat treatment processes and exert an influence on the mechanical properties and FCG behaviour.

The γ′ precipitates provide some benefits in the crack propagation resistance as slip bands are likely to terminate at grain boundaries or interfaces of γ matrix/γ′ precipitate in Ni-based superalloys [49,99]. In addition, a short fatigue crack can be arrested when it encounters γ′ precipitates, consequently hindering crack propagation. The γ′ precipitate size is expected to influence dislocations' travel whether by precipitate shearing or looping mechanisms as aforementioned in section 2.2.3. This is linked to slip planarity and slip reversibility, which influences transgranular crack growth behaviours [6,64]. The finer γ′ precipitate size is more associated with shearing mechanisms and therefore heterogeneous slip character indicating enhanced slip reversibility or planar slip, which can result in lower FCG rates in P/M disc alloys [49,80]. On the other hand, less precipitate shearing takes place as γ′ precipitate size increases whereas the dislocation process is transferred to precipitate looping related to less planar slip and more homogeneous slip character. At elevated temperature, the effect of γ′ precipitate becomes less marked due to environmental damage. Moreover, the interfaces of γ matrix/γ′ precipitate (or carbides) are preferential fatigue crack paths due to oxidation damage and subsequent degradation of boundary properties, which promotes short FCG along the interfaces [20,94,95,102]. At elevated temperature, cross slip and multiple slip are activated and result in reduced CRSS, promoting less crystallographic short FCG.

In terms of grains and grain boundaries, it is believed that highly planar slip promotes more intense impingement of slip bands at grain boundaries, resulting from significant pile up of dislocations in the slip bands. This contributes to reduced crack growth resistance due to easier nucleation of dislocation sources near grain boundaries and weakens their effectiveness as a crack growth barrier. The effect of grain size on short FCG is linked to the free slip length for dislocation motion under cyclic deformation, which promotes an increase in the degree of pile up of dislocations expected at grain boundaries as grain size increases. This causes the grain boundary to be a less effective barrier

for dislocations and this, combined with the fact that fewer such barriers are offered as grain size increases, resulting in poor FCG resistance. On the other hand, a coarse grained microstructure is likely to exhibit more tortuous crack paths and highly planar slip character (linked to increased slip reversibility) due to the intense slip bands extending across the grain [9,80]. This can then provide an enhanced resistance to FCG due to increased crack tip deflection and hence intrinsic shielding with a more tortuous crack path [49,103]. At elevated temperature, a transition from transgranular fracture to intergranular fracture can be discerned due to oxygen-related damage at the grain boundary. This phenomenon is less frequently seen when the grain size become greater due to fewer embrittled grain boundaries, resulting in enhanced FCG resistance and fatigue lifetime [103]. It is also observed that a distribution of secondary phases such as carbides formed at grain boundaries can contribute to enhanced fatigue crack initiation and short FCG [104,105]. Generally, metallic carbides (MC or $M_{23}C_6$) on grain boundaries inhibit the grain boundary sliding and consequent crack growth along the grain boundary. However carbides continuously formed at a grain boundary can reduce the binding force of the grain boundary, which promotes fatigue crack initiation and intergranular crack growth behaviour under applied stress [106]. Elevated temperature also gives rise to significant volume expansion of carbides (that oxidise) especially on the grain boundaries and also contributes to reduced grain boundary properties, which induces preferential short crack paths.

The crystallographic orientation of the grains (misorientation) adjacent to the crack path can also affect activated primary slip systems and short FCG behaviour in polycrystalline Ni-based superalloys. This can be assessed by a combination of EBSD and digital image correlation (DIC) by providing strain accumulation and slip character analysis on the grains containing short crack segments [100,107,108]. It is known that the highest Schmid factor is related to the highest resolved shear stress activating the slip system and thereby leads to enhanced crack initiation and short FCG processes, although short FCG does not always follow the highest Schmid factors [8,79]. It is known that larger crack deflections (linked to crack arrest) and consequent decelerated FCG rate occur when grain boundaries possess higher misorientations whilst lower grain misorientations are less effective in providing FCG resistance [81,109,110]. It is observed that high angle misorientations or large differences in Schmid factor of the active primary slip systems between neighbouring grains is related to a significant extent of dislocation pile-ups and strain accumulation. The primary slip systems can be also activated parallel to twin boundaries with relatively high Schmid factors [8]. This is linked to strain localisation and slip band cracking, promoting crack initiation and early crack growth at low temperature [79,108].

The effects of microstructural features become less dominant at elevated temperature where environmental impacts are more significant. The elevated temperatures can be associated with slip behaviour such as secondary activated slip and cross slip, which contributes to homogeneous slip characteristics (decreased slip reversibility) and subsequent enhanced short FCG rates. It is observed

that the early stage of crack propagation has undergone mainly crystallographic slip band cracking at lower temperatures while an intergranular fracture mode becomes more dominant at higher temperature. Elevated temperature also promotes a number of intergranular short fatigue cracks and consequently crack coalescences due to the oxygen-related intergranular damage, resulting in enhanced short FCG rates [111,112].

2.2.5.3 Overview of long fatigue crack growth

After the early stages of crack propagation, a long FCG regime is discerned with less irregular and scattered crack growth behaviour compared to the short crack regime at comparable ΔK level. Long fatigue cracks propagate through several grains or grain boundaries via stage-II crack growth driven by tensile stresses or strains perpendicular to the crack path. In this regime, the basic LEFM assumption that the plastic zone size ahead of the crack tip is significantly smaller than the crack itself and the uncracked ligament is applicable. This FCG behaviour is affected by microstructure, environment, temperature and loading conditions and the synergistic effects between them. However, the local microstructure variations less significantly impact long FCG behaviour than in short FCG behaviour. In turbine disc alloys, the relevant fracture modes of the long crack growth appear to be transgranular, intergranular or mixed fracture mode [69,113–115]. The crack growth regimes can be subsequently characterised as cycle dependent or time dependent crack growth behaviour depending on the extent of interaction between time and fatigue crack propagation [116]. Generally, fatigue testing at a high loading frequency and low temperature (in vacuum or inert environment) exhibits cycle dependent crack growth and a transgranular fracture mode. On the other hand, fatigue testing under a low loading frequency and high temperature (in air) is apt to show time dependent crack growth and intergranular fracture modes where oxidation and/or creep effects start to interact with failure mechanisms under cyclic loading. It appears that at a given frequency an intergranular fracture may occur at low ΔK level whereas transgranular fracture takes place at high ΔK level, which is associated with the crack propagation rate outstripping oxygen diffusion ahead of a crack tip per loading cycle [113].

2.2.5.4 Microstructural effects on long crack behaviour

Effects of the γ′ precipitate and grain size

Microstructural features such as a size distribution of γ′ precipitates and grains have an influence on slip character and resultant FCG behaviour while it is difficult to untangle the sole effect of variants including grain size, primary, secondary and tertiary γ′ precipitate in turbine disc alloys [47,113,117,118]. As aforementioned, finer γ′ precipitate structures are likely to exhibit heterogeneous slip with enhanced slip reversibility or planar slip, which can decrease the degree of fatigue damage accumulation and contribute better resistance to FCG [6,119–121]. On the other hand, more homogeneous slip character with wavy slip and reduced slip reversibility is predominantly

observed in coarser γ′ precipitate structures, resulting in decreased FCG resistance as seen in Figure 2.25. Finer γ′ precipitate structures exhibit cutting of γ′ precipitates as a main mechanism and some dislocation looping around precipitates can be seen at elevated temperature while looping mechanisms are normally seen in coarser γ′ precipitate structures and these are more marked at elevated temperature [122]. It appears that finer secondary and tertiary γ′ precipitate sizes are linked to improved yield strength and thereby FCG resistance [123]. It is also observed that fine γ′ variants contribute to enhanced resistance to cycle dependent FCG compared to coarse γ′ variants [124]. However, it is seen that the effects of γ′ precipitate size become less dominant while the intergranular cracking process is significant due to oxidation damage at elevated temperatures.

With respect to grain size, a coarser grained microstructure contributes to enhanced slip reversibility and resultant less fatigue damage accumulation, indicating better resistance to long crack propagation than a fine grained microstructure [69,80,113,119]. More roughness-induced crack closure may also result in crack deviations with coarse grains, promoting enhanced resistance to long crack propagation at a low ΔK level. In a time dependent FCG regime, it is believed that a coarse grained microstructure provides better resistance to oxidation-assisted FCG resulting from less grain boundary area where oxygen diffusion is favoured. In this study, however, a similar grain size is produced and grain size influence is therefore likely to be minimal.

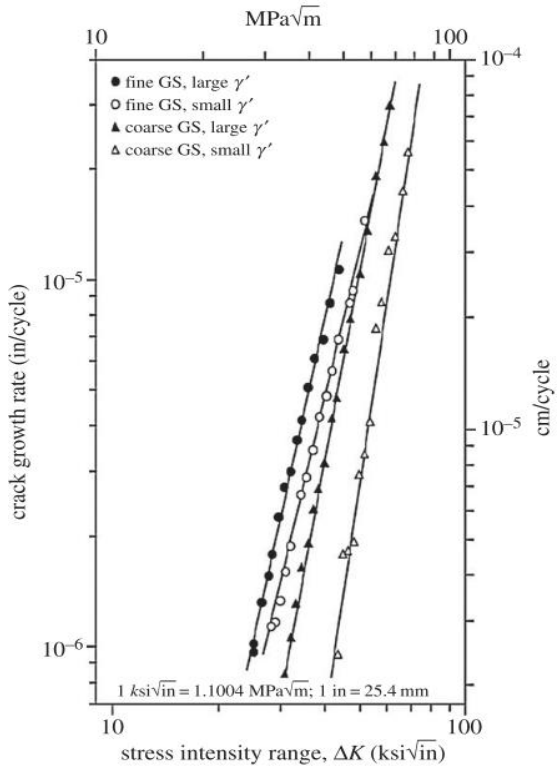

Figure 2.25: Fatigue crack propagation of turbine disc alloy of Waspaloy with different microstructures at constant load at room temperature (GS stands for grain size) [119].

Effects of precipitates at grain boundary

Generally, $M_{23}C_6$ or M_6C carbides on grain boundaries inhibit grain boundary sliding and consequent crack growth along grain boundary. However, such carbides continuously formed at a grain boundary can reduce the cohesive force of the grain boundary, which promotes enhanced intergranular fatigue crack propagation under applied stress [104,105,124]. At elevated temperature, oxidised carbides ahead of the crack tip appears to cause a favoured crack growth path along the oxidised carbides on grain boundaries and consequently enhanced intergranular FCG. Cyclic fatigue loading plays a role in promoting the kinetics of matrix oxidation and effects on preferential oxidation of carbides in an interface region. Fatigue crack branching along grain boundaries in fatigue tests at high temperature is observed more in air compared to vacuum, which can be ascribed to preferential carbide oxidation [125]. Volume expansion of the carbides in an oxidising environment at grain boundaries is also related to surface fatigue cracking at erupted carbides.

Effects of temperature and dwell time

An increase in the temperature can cause microstructural changes such as coarsening of the strengthening precipitates. Elevated temperature can contribute to active dislocation mobility and a change in slip character (cross slip and climb), exhibiting a more homogeneous slip and consequent reduced localised stress concentration [70]. However, the pronounced homogeneous slip results in less slip reversibility and consequently more damage accumulation, which may cause deterioration in crack growth resistance, particularly in the cycle dependent regime. It is also well known that elevated temperature promotes diffusivity of aggressive species and resultant degradation ahead of the crack tip and at grain boundary, which results in accelerated intergranular FCG behaviour [112,117,126]. The effect of elevated temperature (oxidation damage) on enhanced FCG rates is more significant in the time dependent crack growth regime compared to the cycle dependent crack growth regime. In addition, the extent of thermally activated processes such as creep and environment degradation as characteristics of time dependent growth behaviour can increase with an elevated temperature [114,127]. The thermally activated processes can also give rise to the transition from a transgranular fracture mode (cycle dependent crack growth) to an intergranular fracture mode (time dependent crack growth) or a mixed trans-intergranular mode [65,127,128].

Testing frequency does not significantly impact FCG rates at room temperature while enhanced FCG rates are promoted by an introduction of dwell time at elevated temperature [129–132]. This is more marked in air compared to vacuum testing conditions, which is ascribed to the effects of an oxidising environment and environmental degradation. Dwell time at the peak load in an oxidising environment is linked to the diffusion time of oxygen in the vicinity of crack tip and associated advanced FCG rates. In general, enhanced FCG rates are seen under longer dwell (lower frequency), which promotes more intergranular and time dependent crack propagation [126] although stress

relaxation and lowered stress at the crack tip may sometimes cause a decrease in FCG rate. The degree of time dependent crack growth behaviour potentially depends on either oxidation or creep (or some combination of these) along the grain boundary. However, it appears that creep damage exerts a limited influence in time dependent FCG under dwell in turbine disc applications, particularly in aggressive environments and at high FCG rate (high ΔK levels) [133,134]. Creep damage effects can be distinguished from those due to environmental damage by conducting fatigue tests in vacuum or inert conditions. On the other hand, a shorter dwell time with insufficient diffusion time (i.e. a higher frequency) often shows more transgranular and cycle dependent crack propagation [135].

Effects of oxidation and dynamic embrittlement

In fatigue testing at elevated temperature in air, oxidation is the dominant thermal damage mechanism particularly occurring at grain boundary, crack tip or at interfaces such as carbide/grain boundary in turbine disc superalloys. Oxygen-related damage promotes a deteriorated resistance to FCG and intergranular fracture processes that cracks propagate along grain boundary particularly under dwell fatigue conditions [112,117,136,137]. The mechanisms of the process are often attributed to stress-assisted grain boundary oxidation (SAGBO) [3,113,138–142] or dynamic embrittlement [143–146]. In brief, SAGBO is achieved by diffusion of oxygen and oxides formed at grain boundary due to the assistance of the local stress/strain applied to accommodate the volume expansion needed for oxide formation. Subsequent crack propagation involves cracking of oxides formed or at the oxide/matrix interface, contributing to enhanced intergranular FCG. Dynamic embrittlement is related to diffusion of oxygen along preferential paths such as slip bands and grain boundaries, which can result in consequent decohesion of the grain boundary (without necessarily forming any oxide). The stress at the crack tip in dynamic embrittlement mechanism plays a role in assisting the diffusion of these embrittling atoms along grain boundaries [145].

Figure 2.26 schematically illustrates the oxidation process of a RR1000 disc alloy at the crack wake and ahead of the crack tip along grain boundary, which is one of the dominant factors in time dependent FCG behaviour. The oxidation process of Ni-based superalloys varies with the chemical composition of different alloys as oxidation layers are formed in a thermodynamic sequence, i.e. a sequence of CoO, NiO, Cr_2O_3, TiO_2 and Al_2O_3 formed in turbine disc alloys [111,138,140]. The oxides formed ahead of the crack tip include external layers of NiO/CoO and internal layers of $Cr_2O_3/TiO_2/Al_2O_3$ in RR1000 alloy [140]. The oxides formed promote degradation of grain boundaries and act as a local stress concentration, resulting in accelerated FCG rates. The brittle nature of these oxides can give rise to weakening of the grain boundary and act as stress concentrators. The extent of oxidation ahead of the crack tip varies with the testing condition including applied loading and local inelastic strain [138,140]. The load applied to the materials

promotes the oxidation process by forming a thicker layer of oxidation compared to the unloaded condition, which is related to accelerated diffusion of oxidation forming elements under loading whereas the load does not influence the nature of oxidising products [147]. The enhanced oxidation process is also often ascribed to high densities of dislocations and vacancies caused by accumulated inelastic strain. These combined effects of oxidation with cyclic loading at elevated temperatures are likely to produce a deterioration in FCG resistance.

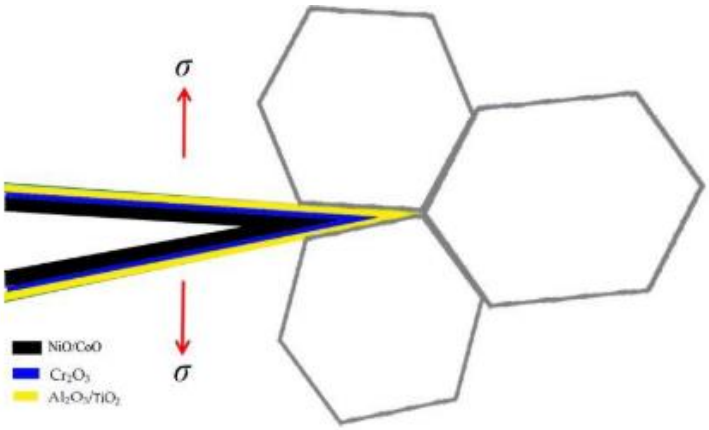

Figure 2.26: A schematic representation of the formation of oxides at the crack wake and ahead of the crack tip along a grain boundary in a RR1000 disc alloy [140].

The dynamic embrittlement process also deteriorates grain boundary properties by the penetration of embrittler diffusion elements (i.e. oxygen) at nanometre scale, particularly along the grain boundary and slip bands aided by the driving force from the applied stress [143–145]. The oxygen is available to react with materials at grain boundaries, precipitates or inclusions. It has been reported that the process results in decohesion of the grain boundary and deteriorated resistance to intergranular FCG [144,145]. Accordingly, the grain boundary character is critical in determining in the susceptibility to cracking process by dynamic embrittlement. Intergranular fracture is therefore a distinctive feature which can result from stress-assisted grain-boundary diffusion of the embrittler atoms followed by interfacial decohesion as schematically described by Figure 2.27 [53].

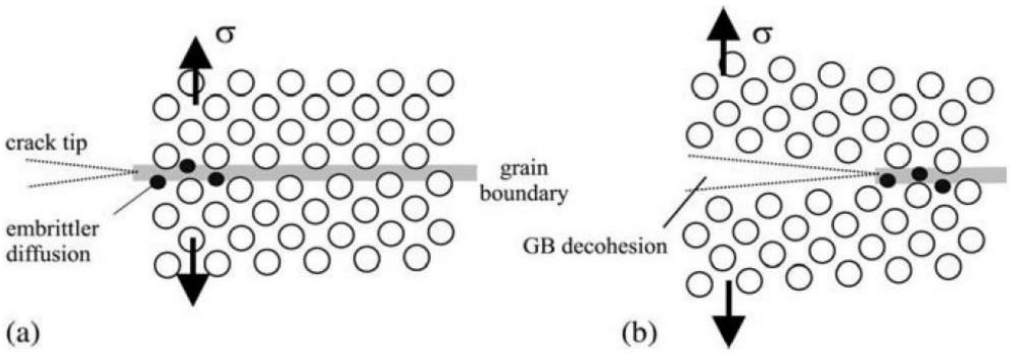

Figure 2.27: Schematic processes of the dynamic embrittlement mechanism (a) embrittler diffusion on grain boundary in the elastically stretched cohesive zone ahead of crack tip (b) consquent decohesion [53].

These oxygen-related FCG behaviours measured in conventional ways (i.e. surface based 2D microscopic observation and/or direct current potential drop (DCPD) method) may not include the true effect of oxygen by underestimating the crack length due to their limitations (more details in the following section). This can be ascribed to complex 3D crack growth process including crack branching at the crack tip during intergranular crack growth and interlinking of the crack tip with uncracked ligaments [137,148]. The 3D assessment of the crack propagation by X-ray or synchrotron radiation CT will provide a deeper understanding in terms of local crack propagation behaviours and 3D complex crack morphology. The fundamentals of X-ray CT assessment approaches on metallic materials will be discussed more in section 2.3.

2.3 3D image analysis in metallic materials

2.3.1 Introduction

Analysis of FCG behaviour in metallic materials has generally been conducted by conventional approaches such as replication methods by using 2D microscopes or DCPD method. The replication approach widely employed in short FCG analysis allows an acetate block or silicone compound to periodically capture information on the surface where cracks exist and hence to investigate crack evolution with a series of snapshots of cracks. The DCPD method continuously evaluates a long FCG in specimens containing a pre-existing defect by monitoring the change in a potential difference (V) due to a crack growth and comparing the change with a reference value. However, replication only gives 2D surface information although the fatigue crack propagation process of a surface breaking crack is a 3D complex process. The crack area estimation offered by the potential drop (PD) approach for through thickness cracks likewise only captures rather generalised projected crack growth information. Recently significant development and research has been carried out by using 3D imaging techniques at higher resolution to assess FCG behaviour where fatigue cracks initiate or propagate with a more complex propagation process such as crack coalescence and secondary crack formation, assessing true crack morphology and interaction with other microstructural features in three dimension [137,149–153].

In 3D analysis approaches for short FCG, the interaction between microstructure and FCG behaviour has been studied by several different techniques such as synchrotron micro tomography, heat tinting, serial-section polishing and combination of focused ion beam (FIB), SEM or EBSD [149,154]. These techniques can be categorised as destructive techniques (e.g. serial sectioning approaches) which can induce damage or contaminate samples and non-destructive methods that are able to maintain raw materials without any damage on samples such as X-ray CT scanning and ultrasonic testing. In this

project, 3D X-ray together with traditional 2D methods such as OM, SEM and EBSD have been conducted to gain a better insight of fatigue crack initiation and growth mechanisms.

2.3.2 Fundamentals of X-ray CT imaging

X-ray CT is a radiographic imaging technique to reconstruct a 3D image of the internal structure of a variety of materials at high spatial resolution used as a non-destructive technique. The mechanism of 3D reconstruction through X-ray CT of an object is schematically illustrated in sequence in Figure 2.28. The X-ray source scans a specimen on a rotation stage, which generates a series of 2D projection radiographs captured by the detector for different orientations of the specimen. The 3D image is represented by each voxel from the X-ray absorption at each point from a tomographic reconstruction of the 2D slices. The 3D internal structures of materials can then be resolved due to the relationship between X-ray absorption and material density. X-ray attenuation in the samples is characterised by the grey scale value of images, which is the measurement of the absorbed or deflected energy. In terms of image analysis, image processing and segmentation are commonly used in image quantification. Image processing retrieves the improvement of images by the grey scale modification including brightness and contrast adjustment and normalisation and filtering such as noise removal or by subtracting the background. Segmentation aims to define different phases of images in the materials based on the grey scale value allocated to certain discrete groups such as microstructural features, materials or air. Internal microstructure can then be segmented by a threshold method based on a range or gradient of grey scale value although more sophisticated threshold methods are required when the boundaries between phases are unclear. Visualisation through 3D rendering based on a series of 2D slices produced by the imaging software can provide a more in-depth analysis than can be achieved by surface based 2D analysis approaches.

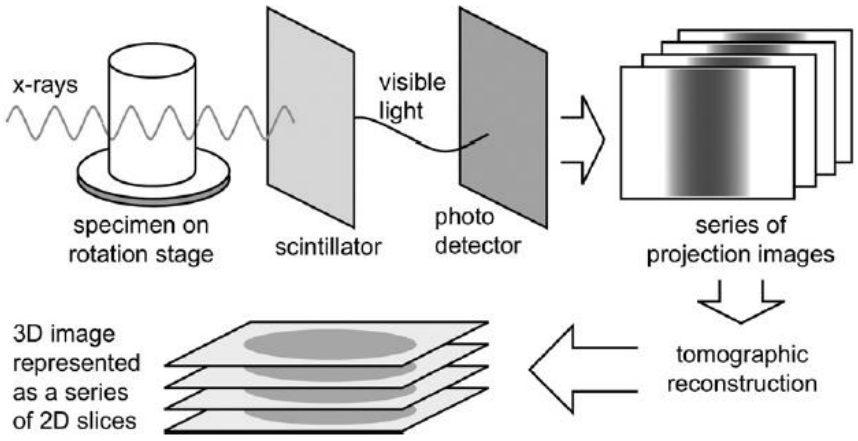

Figure 2.28: Sequence of X-ray CT acquisition and reconstruction processes [152].

X-ray tomography has sub-micron range in spatial resolution that can be utilised for a range of structural materials with an acquisition time range from a few minutes to several days depending on various factors such as the material of samples, spatial resolution, source intensity, etc. [152,155,156]. X-ray CT has been increasingly used for the microstructural characterisation of polycrystalline materials including fatigue crack morphology, internal microstructure and interaction between them in 3D by static or in-situ CT imaging [8,137,149,157]. For instance, Figure 2.29 represents the 3D morphology of short fatigue crack which is initiated from the matrix-inclusion interface by in-situ fatigue testing a range of views of a RR1000 turbine disc alloy [158]. The 3D crack morphology over applied cycles is segmented and reconstructed, which show the direction of crack propagation. In Figure 2.30, a 3D reconstruction of long FCG following the crack path on a surface of turbine disc material is visualised by X-ray CT scanning, showing a complex morphology such as nature of crack tortuosity, crack coalescence process, secondary crack formation and crack depth from the surface of Ni-based superalloys. This represents the tortuous nature of the crack plane in 3D and the events of crack coalescences at surface and depth, which is linked to geometrical comparability of the overall 3D crack path. The interaction between fatigue crack and microstructure can also be achieved with a combination of X-ray CT scan and EBSD [149,157]. This provides a 3D complex crack morphology and relation between crystallographic orientation of individual grain and crack propagation along the crack path. Such combination of traditional methods and 3D X-ray CT scan can provide a deeper understanding of the mechanisms of fatigue crack initiation and propagation behaviour of turbine disc alloys.

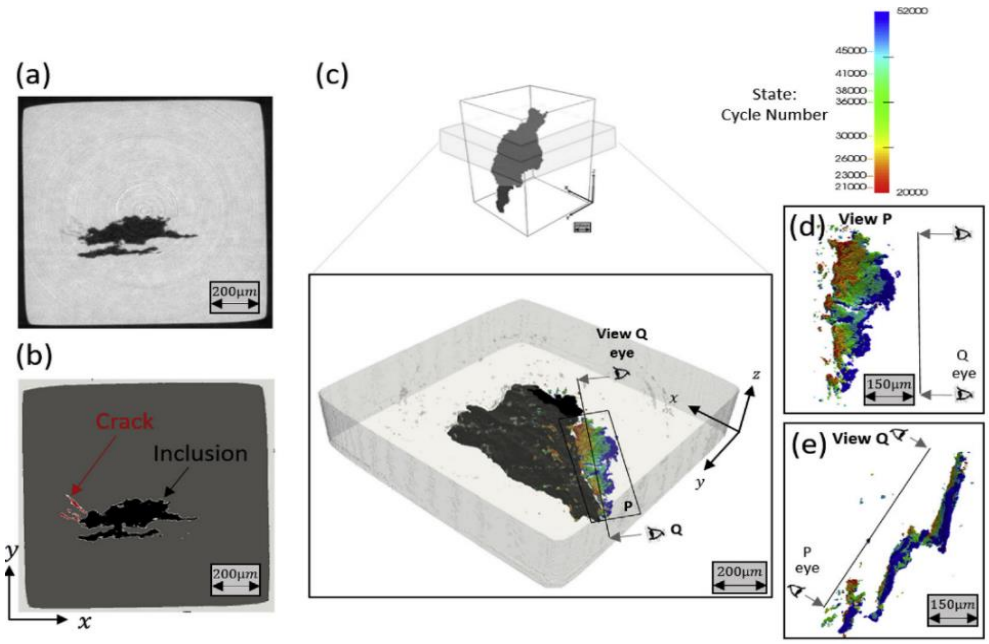

Figure 2.29: (a) Cross-section from μ-CT reconstruction juxtaposed with (b) results of segmentation of the different phases: matrix, inclusion, and crack. (c) specimen with inset showing the crack growing from the inclusion between 20k and 52k cycles. (d) view of the crack along plane P (as defined in c), displaying crack growth relative to the cycle number. (e) view of the crack from vantage point Q (as defined in c), showing a bridge in the crack structure[158].

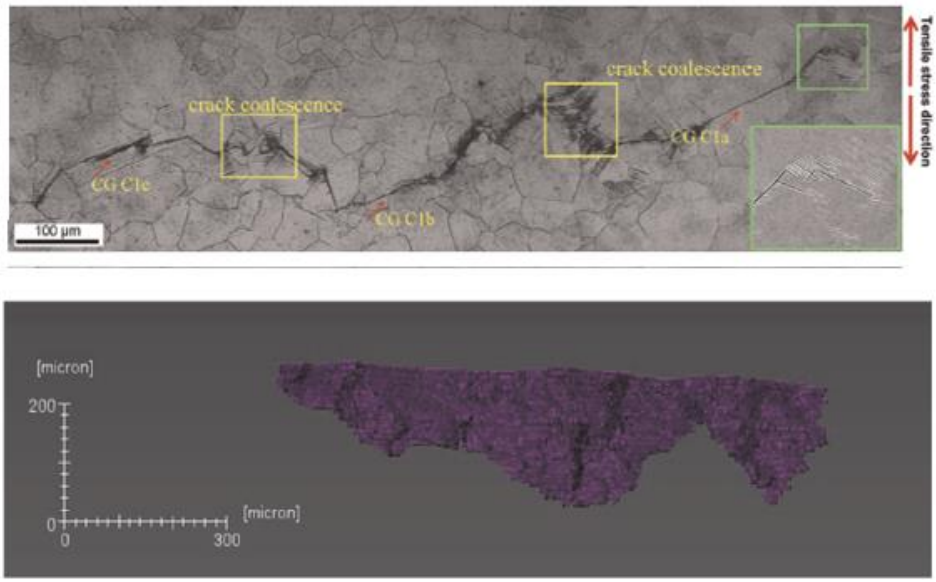

Figure 2.30: A 3D image reconstruction of the fatigue crack path and coalescences on the surface of the turbine disc material by CT scanning [8].

2.4 Summary of literature review

The excellent mechanical properties of turbine disc alloys are closely related to optimised alloying, processing and resultant microstructures and result in their wide spread applications in aeroengines as well as industrial power generation, where gas turbines are required to deal with rising and variable demands on the power infrastructure. P/M Ni-based superalloys are increasingly used for turbine disc applications due to elimination of segregation which can cause cracking during processing and allow the achievement of excellent mechanical properties for heavily alloyed systems. The distinctive microstructural features of Ni-based superalloy consist of a γ phase and strengthening ordered γ′ precipitate which typically exhibits a tri-modal distribution comprising primary, secondary and tertiary γ′ precipitates. Such microstructural features are tailorable for optimisation and improvement in overall properties of the alloy by heat treatment process. This is linked to superior mechanical properties and resistance to aggressive environments and cyclic loading conditions. Extensive work has assessed the relation between microstructural features and corresponding mechanical behaviour including fatigue, creep and strength at high temperature.

In the operating environment, much of fatigue life is controlled by fatigue crack initiation and the early stages of crack growth, which is linked to their slip character and associated damage accumulation mechanisms. The deformation mechanism and slip character under cyclic loading significantly interact with a given size distribution of γ′ precipitate, controlling the transition of dislocation motion between shearing and looping mechanisms. It is known that fine γ′ precipitate size is linked to more precipitate shearing with more planar slip (heterogeneous deformation) and

enhanced slip reversibility while coarse γ′ precipitate size tends to exhibit more looping mechanism with more wavy slip (homogeneous deformation) and reduced slip reversibility. At elevated temperature, KW locking, which is a distinctive feature of Ni-based superalloy, is activated by thermal energy, promoting a homogeneous slip character by hindering the deformation behaviour and having a hardening effect. This contributes to an excellent high temperature strength.

In polycrystalline Ni-based superalloys, fatigue cracks are mainly initiated at microstructural heterogeneities such as slip bands, porosity, precipitates, grain boundaries, twin boundaries and the interface of matrix/precipitates where stress concentration and strain localisation take place. At elevated temperatures, multiple slip processes are activated and therefore slip band cracking become less significant. Also an oxidising environment gives rise to degradation in grain boundary strength and volume expansion of oxidised phases on the grain boundary, resulting in crack initiation processes.

Local microstructure including grain boundaries, twin boundaries, grain orientation and precipitates exert a significant influence on short FCG behaviour. This is closely related to the high extent of scattered FCG behaviour compared to long FCG behaviour at similar ΔK levels. Size distribution of the γ′ precipitate can impact slip character and thereby damage accumulation, resulting in varying short FCG behaviour. Short FCG can also be hindered by precipitates such as γ′ particles or carbides, which provides somewhat enhanced resistance to crack propagation. At elevated temperature, these microstructural effects become less critical due to the competing effects of environmental damage. Long FCG behaviour is linked to the synergistic effects of microstructure, temperature, dwell time and oxygen-related damage. In general, shorter dwell times at peak load and lower temperature exhibit cycle dependent crack growth, related to more transgranular fracture modes. Longer dwell times at peak load and higher temperature appears to present time dependent crack growth with more intergranular fracture modes.

Based on the literature, it is important to understand the relative role of γ′ precipitate size to allow further optimisation of turbine disc alloys to enable better component performance and fatigue lifetime. Due to the bi- or tri-modal γ′ size distributions typical in commercial turbine disc alloys, it is complex to dis-entangle the effects of varying γ′ population on slip character, and hence on fatigue crack initiation and growth behaviour. The effect and relative balance of these different γ′ size populations on slip character is still a matter of continuing debate. In this study, fatigue crack initiation and propagation behaviour of a RR1000 (a polycrystalline Ni-based superalloy produced by a P/M method) with two different unimodal secondary γ′ size distribution produced by non-commercial heat treatment processes will be investigated. The effects of any variation in slip character and microstructural features resulting from heat treatment process on fatigue crack initiation and growth will be examined at a range of temperatures. Unimodal γ′ ‘model’ systems may

allow a more explicit understanding to be developed, where grain size is not a variable, and variations in temperature will also change slip character. Moreover, the effect of grain boundary character (i.e. carbide distribution on grain boundaries) as well as the variations in γ' precipitate size associated on deformation mechanisms, crack initiation and FCG behaviour and in RR1000 alloy in both cycle and time dependent regimes will be assessed. For a better understanding, 3D evaluations of the FCG by X-ray CT scan to complement traditional 2D observations will be conducted by providing a variety of information such as internal microstructure, crack morphology, crack tortuosity and secondary crack formation.

Chapter 3 Material characterisation

3.1 Introduction

Microstructural features of materials are directly linked with mechanical properties and fatigue behaviour as discussed in the literature review sections. In this chapter, the microstructural features such as the distribution of γ′ precipitates, grain and carbide size distributions of the RR1000 alloys was investigated by traditional metallographic methodologies and 2D image analysis. The material processing route to produce two different γ′ distributions is presented as well as the procedure of material preparation for subsequent characterisation and mechanical testing. Proof stresses at a range of temperatures of the alloys were obtained by collaborators and the results are discussed to help understand the fatigue testing at elevated temperatures presented in the following chapters. The effects of oxidation behaviour on the microstructure of the materials with two different γ′ distributions were also systematically examined and compared by isothermal oxidation testing with and without loading as the oxidation behaviour is also closely linked to the high temperature fatigue behaviour. Much of work presented in this chapter has also been published in the following paper:

D. Kim, R. Jiang, A. Evangelou, I. Sinclair, P.A.S. Reed, Effects of γ′ size and carbide distribution on fatigue crack growth mechanisms at 650 °C in an advanced Ni-based superalloy, Int. J. Fatigue. 145 (2021). doi:10.1016/j.ijfatigue.2020.106086.

3.2 Materials

The material used for this study is a model RR1000 alloy (a polycrystalline Ni-based superalloy) which was provided by Rolls Royce in the form of a disc and is a third generation alloy used for turbine disc applications. The alloy was produced by P/M route, followed by various proprietary thermomechanical treatments and it normally exhibits a tri-modal γ′ size distribution. The chemical composition is shown in Table 3.1. Heat treatment blanks of 40 mm x 40 mm x 110 mm were extracted from the disc provided. The specimens for this PhD study including characterisation and fatigue testing samples were cut from the blanks. Further heat treatments on the alloys were performed to produce a unimodal size distribution of γ′ precipitates at the University of Manchester. This is a non commercial heat treatment that is quite different from the typical heat treatment used for turbine disc applications. A super-solvus solution treatment followed by different ageing treatments at different temperatures and cooling rates was carried out to ensure the unimodal fine

and coarse γ′ size distribution as described in Table 3.2. The super-solvus solution treatment was conducted at 1180 °C (20 °C higher than the γ′ solvus of 1160 °C) for 2 hours to dissolve primary γ′ precipitates in both γ′ variants of the RR1000 alloy and was subsequently cooled by oil quench. Subsequent ageing treatments at different temperatures of 800 °C and 1050 °C for an hour were carried out to produce the fine and coarse secondary γ′ precipitates, respectively. Finally, the alloy with coarse γ′ was rapidly cooled at -1 °C/min down from 1050 °C to 800 °C and then at -0.1 °C/min for the remainder of the cooling while the alloy with fine γ′ was cooled at -0.1 °C/min from 800°C. This slow cooling stage from 800 °C was performed to avoid any tertiary γ′ formation.

Cr	**Co**	**Mo**	**Nb**	**Al**	**Ti**	**Ta**	**Hf**	**C**	**B**	**Zr**	**Ni**
15	18.5	5.0	1.1	3.0	3.6	2.0	0.5	0.027	0.015	0.06	Bal

Table 3.1: Composition of RR1000 alloy (wt.%).

Solution treatment	Fine/Coarse γ′	1180 °C for 2 hrs	→	Oil quench cooled
Ageing treatment	Fine γ′	800 °C for 1 hr	→	-0.1 °C /min cooled
	Coarse γ′	1050 °C for 1 hr	→	-1 °C /min cooled to 800 °C -0.1 °C /min cooled for the rest

Table 3.2: Heat treatment processes applied to the model RR1000 alloy conducted at University of Manchester (Note: γ′ -solvus is approximately 1160 °C).

The tests to obtain the proof stress of the RR1000 alloys at a range of temperatures were also carried out at the University of Manchester (where the heat treatments were carried out). Figure 3.1 shows that the proof stress of the fine γ′ variant shows a slight decrease between 1100 to 1000 MPa until the temperature approaches 800 °C and then it drops significantly. The coarse γ′ variant follows a similar trend while a significant decrease is seen at temperatures between 500 °C and 600 °C. The data point at 600 °C requires further checking as it seems somewhat anomalous. A distinct feature of Ni-based superalloys, is that yield stress does not significantly decrease with increasing temperatures until higher temperatures (e.g. 800 °C). At temperatures below 300 °C the proof stress values are comparable between the two γ′ variants while a slightly higher proof stress can be seen for the fine γ′ variant overall. It is worth noting that both fine and coarse γ′ variants experience a significant drop in the proof stress at temperatures beyond 800 °C.

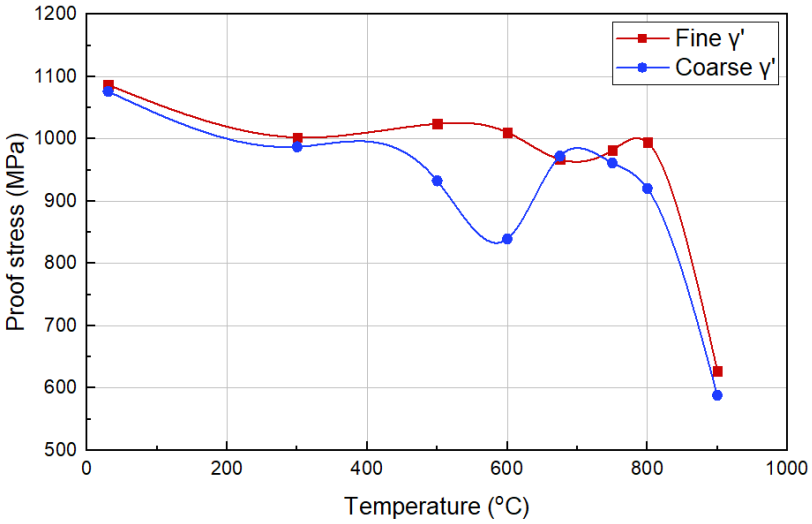

Figure 3.1: Proof stress vs temperature of RR1000 with fine and coarse γ′ microstructures conducted at University of Manchester [159].

3.3 Experimental methodology

3.3.1 Metallographic characterisation

Offcuts of fine and coarse γ′ variant materials were employed for the microstructural characterisation and were cut into rectangular cross sections around 15 mm x 20 mm using a diamond cut-off wheel suitable for hard and brittle materials (M1D15). The samples were then mounted in Bakelite, followed by a process of successively manually grinding and polishing to produce an optimized surface condition for characterisation through the following steps:

120 grit paper → 800 grit paper → 1200 grit paper → 4000 grit paper → 1 µm Diamond suspension → (0.02 µm OPA solution)

Final polishing to a 1 µm finish can normally provide good resolution for surface images captured by the replica method for short fatigue crack test. Subsequently, etching by Kalling's reagent (80ml HCl + 40ml CH_3OH + 40g $CuCl_2$) for approximately 3 seconds was carried out to reveal the grain boundaries and γ′ distributions of the RR1000 alloys. Following the specimen preparation, the samples were characterised with an Olympus BH2 microscope and JSM 6500F field emission gun (FEG) SEM. The characterisation in the SEM has employed both secondary electron imaging (SEI) and backscatter electron imaging (BEI) modes to examine the microstructure in detail including morphology of grains, grain boundary character, γ′ precipitates and carbide distribution at a typical working distance (WD) of around 10mm and an accelerating voltage of 15kV.

EBSD mappings were then performed to investigate microstructural features such as the distribution of grains, grain boundaries, grain orientations and twin boundaries using a JSM 6500F FEG-SEM. For the EBSD analysis, a further final polishing stage using OPA with 0.02 µm resolution was carried out on the RR1000 samples with both γ′ distributions, followed by etching with Kalling's reagent (80 ml HCl + 40 ml CH_3OH + 40 g $CuCl_2$). Step size of 1 µm and grain boundary tolerance angle of 2^o were employed for EBSD mapping. The average grain size and grain/twin boundary distribution on EBSD mapping was analysed by the post processing software of HKL Channel 5 software provided by Oxford Instruments.

3.3.2 Isothermal oxidation testing - microstructural features at high temperature

In order to investigate the microstructural characteristics at elevated temperature, particularly focusing on grain boundary oxidation and the precipitate behaviour (i.e. carbides or borides) formed at the grain boundary, both γ′ variants were thermally exposed in a furnace at 650 ^{o}C. Both γ′ alloys were exposed for 1, 5, 10 and 20 hours and systematically characterised to examine any microstructural features related to oxidation behaviour. The samples for this microstructural characterisation stage were extracted from off-cut samples and cut into 8 mm x 4 mm x 2 mm dimensions, followed by grinding and polishing up to 0.02 µm OPA on the top surface. To ensure the sample was heated to the required temperature, a thermocouple was also used to check the temperature in the area where the sample was positioned in the furnace. After the tests, the samples were examined by OM and SEM. An energy dispersive X-ray (EDX) analysis on the precipitates on the grain boundary was conducted to investigate the elemental composition after oxidation on the SEM images.

A static three point bending test with a maximum stress of 90% of yield stress was also carried out at 650 ^{o}C for 10 hours to assess the effect of stress/strain compared to the unloaded condition under an oxidising environment. The set up for the test is presented in Figure 3.2. The test was carried out in the Instron 8501 servo-hydraulic testing machine with an ESH Ltd. high temperature chamber attached with four high intensity quartz IR lamps. The temperatures of the specimens were monitored by a Eurotherm 815 thermo-controller and R-type (platinum + 13%rhodium/platinum) thermocouple spot-welded to the specimens. A plain bend bar (PBB) sample with a dimension of 9.31 mm x 3.83 mm x 55 mm was used in the test and ground and polished to 0.02 µm of OPA finish. The test was conducted on the on the coarse γ′ variant as it has a distinctive feature of a continuous carbide distribution on the grain boundary. An overview of the isothermal oxidation testing is presented in Table 3.3.

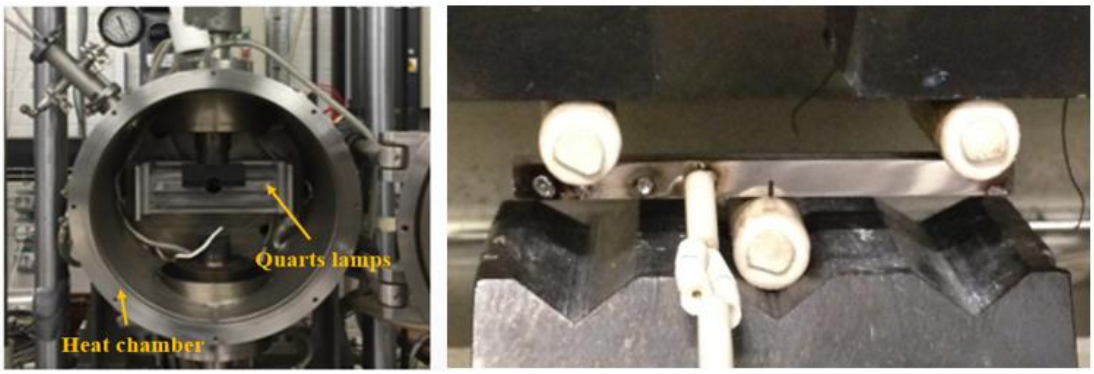

Figure 3.2: A servo-hydraulic testing machine with a high temperature chamber and the setup of the three point bending test on a PBB sample under a static loading test at 650 °C.

	Fine γ′ variant	**Coarse γ′ variant**
Without loading	√	√
With loading	-	√

Table 3.3: The test matrix for microstructural characterisation in an oxidising environment at 650 °C.

3.4 Results

3.4.1 Microstructure

At high magnification on the SEM, Figure 3.3 (a) and (b) illustrate the morphology of both fine and coarse γ′ distribution produced by the different heat treatment processes. The morphology of the fine and coarse γ′ tends to show a mostly circular shape. The very slow cooling rates post ageing should have avoided the formation of any tertiary γ′. Figure 3.3 (c) and (d) show a more quantitative analysis of the size distribution of fine and coarse γ′ particles. The graph of the number of particles vs particle size is presented with the mean particle size and standard deviation of both γ′ variants, which are 73.2 ± 16.3 SD nm and 161.4 ± 43.0 SD nm, respectively. It is notable that the mean value of the coarse γ′ size is approximately three times greater than that of the fine γ′.

The surface of the fine γ′ variant polished by OPA solution and etched by Kalling's reagent are shown in Figure 3.4 (a) and (b), respectively. It was observed that the sample shows limited porosity on the surface and clearly defined grain boundaries after etching. The coarse γ′ structure exhibits similar features as shown in the image in Figure 3.4.

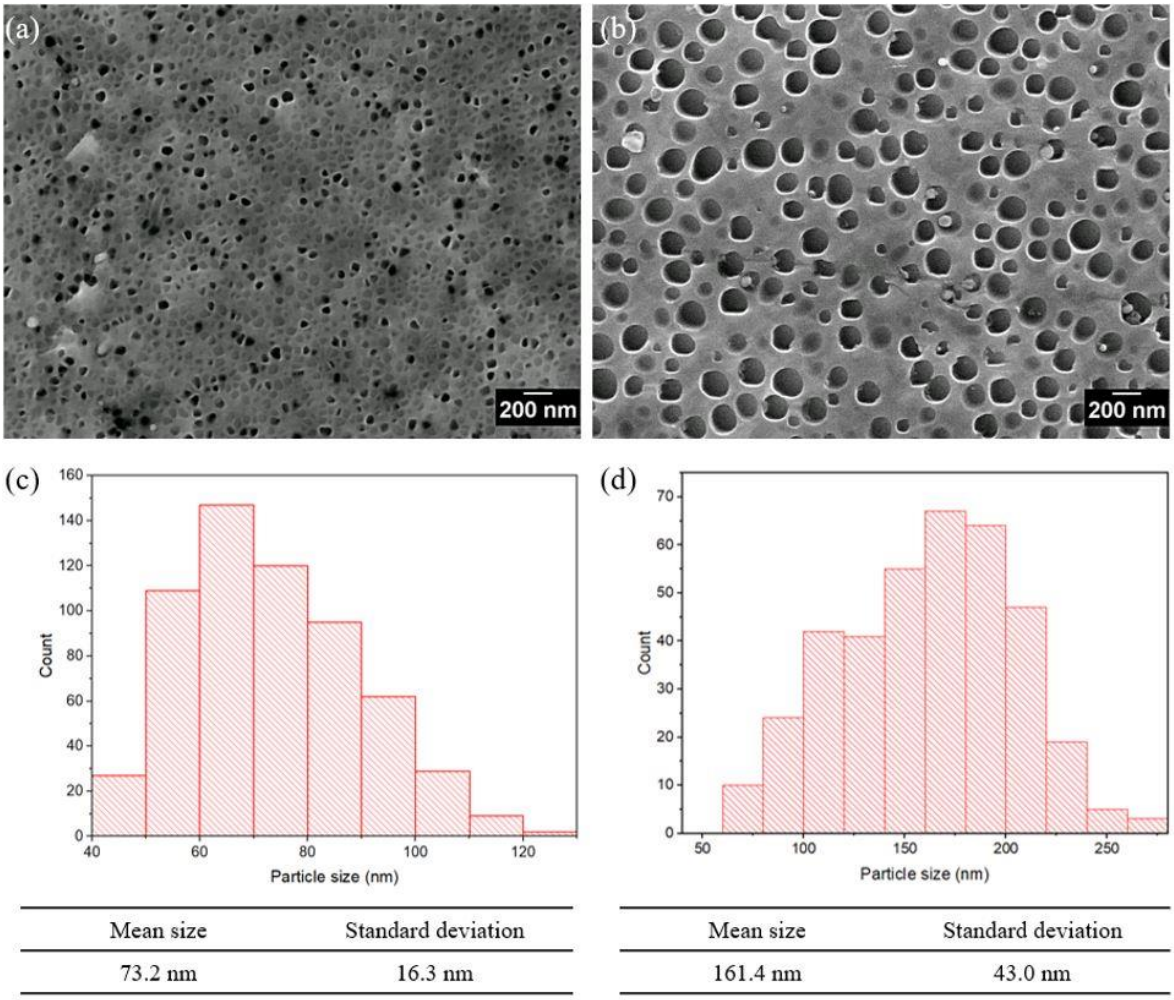

Mean size	Standard deviation
73.2 nm	16.3 nm

Mean size	Standard deviation
161.4 nm	43.0 nm

Figure 3.3: Morphology of γ′ particles of RR1000 (a) fine γ′ (b) coarse γ′; statistics of size distribution of (c) fine γ′ and (d) coarse γ′ with mean value and standard deviation.

Figure 3.5 (a) and (b) captured by the SEM at higher magnification delineates the microstructure of both etched alloys showing well decorated grain boundaries and evidence of twins at higher magnifications. It was seen that the grain boundaries of the coarse γ′ variant were more highlighted by etching, indicating a heavier distribution of grain boundary phases and carbide distributions. Higher magnification SEM images in Figure 3.5 (c) and (d) of the grain boundaries of both γ′ variants have illustrated the distribution of γ′ particles residing within the grains and carbides within the grains and on the grain boundaries. EDX analysis of the particles on the grain boundary supports the evidence of carbide formation by representing a considerable ratio of carbon as shown in Figure 3.6 although the concentration may be influenced by the surrounding matrix due to larger sampling volume of the EDX. It is noted that RR1000 with fine γ′ precipitates tends to exhibit a discrete carbide distribution while RR1000 with coarse γ′ precipitates is likely to show a more continuous carbide formation along the grain boundary. The more continuous distribution of the carbides along the grain boundary of the coarse γ′ variant is linked to the higher temperature ageing during the non-commercial heat treatment process in this study. In RR1000 alloys, the formation of the lower carbide

($M_{23}C_6$, Cr-Mo rich carbide) is commonly observed in the grain boundary as unstable primary carbide (MC) is expected to react with the γ matrix during the heat treatment process [160].

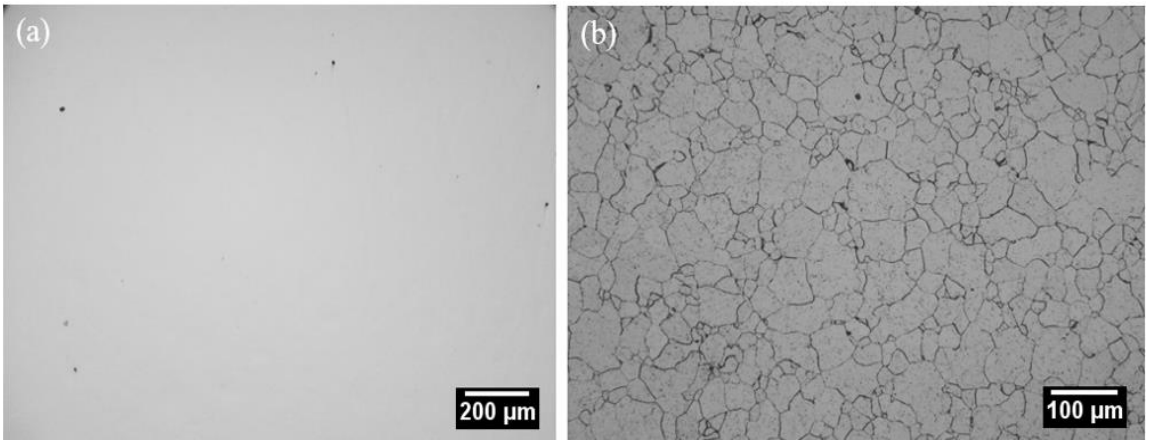

Figure 3.4: OM images of the fine γ′ variant (a) plain polished surface with OPA finish to reveal low porosity level (b) etched surface by revealing grain boundaries. Note that the images of the coarse γ′ variant are very similar to these figures.

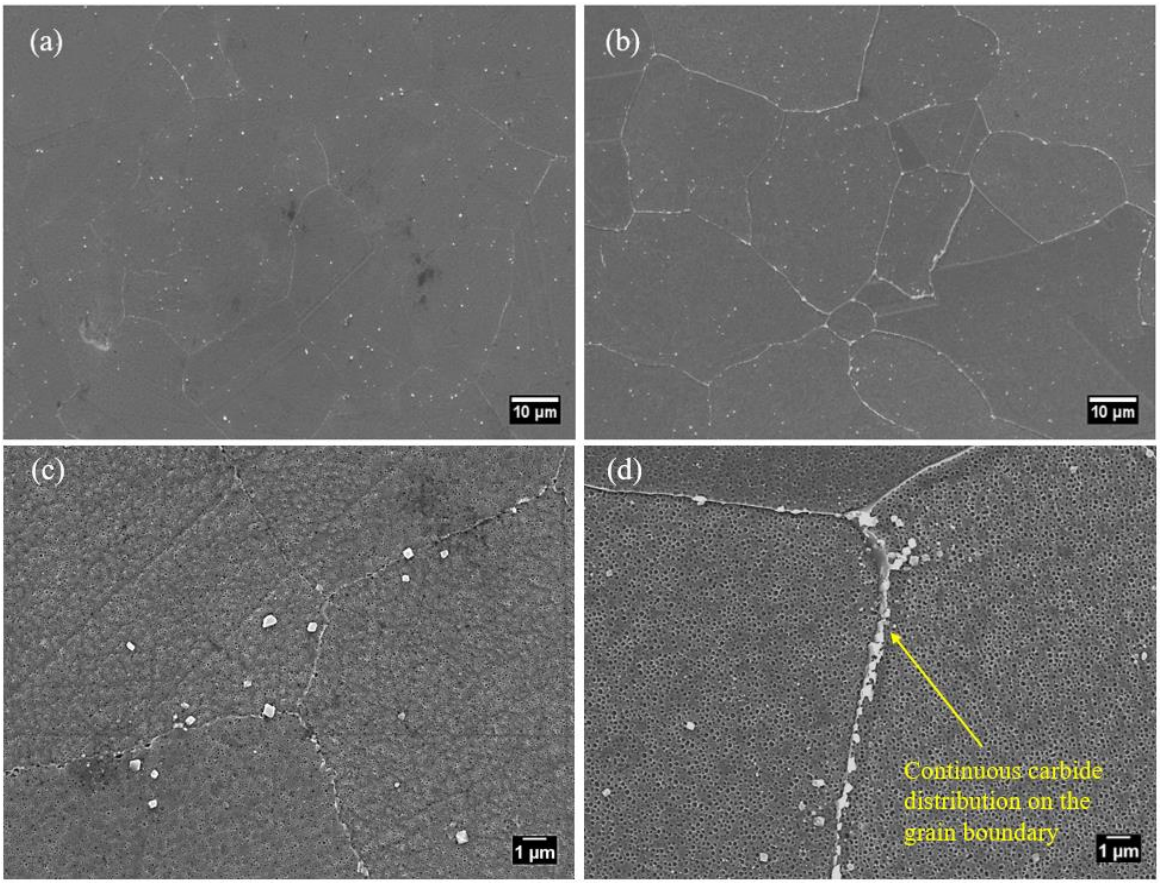

Figure 3.5: SEI images of the microstructure of etched surface of (a) the fine γ′ structure and (b) the coarse γ′ structure. Microstructural features on the etched surface captured by SEM at higher magnification (c) the fine γ′ structure and (d) the coarse γ′ structure with a continuous carbide distribution on the grain boundary.

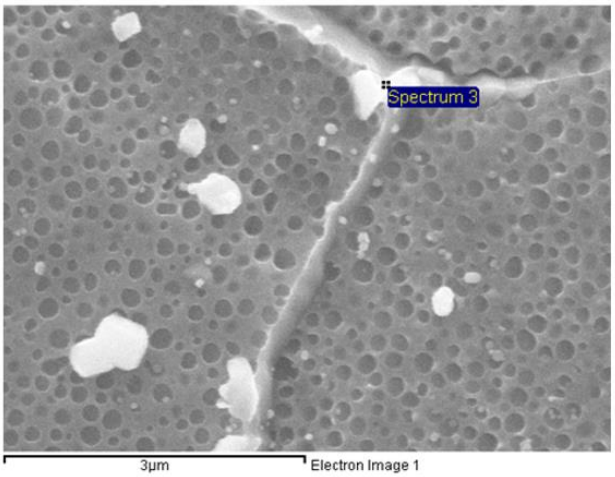

Element	Weight%	Atomic%
C K	15.01	45.32
Al K	2.11	2.84
Si K	0.58	0.74
Ti K	2.57	1.95
Cr K	14.06	9.81
Co K	16.66	10.25
Ni K	44.05	27.22
Mo L	4.96	1.88
Totals	100.00	

Figure 3.6: EDX analysis of the precipitate on the grain boundary of the coarse γ′ variant.

Grain distributions assessed by EBSD mapping (carried out by R. Jiang, previous researcher at University of Southampton) for both fine and coarse γ′ variants were previously investigated. A preliminary EBSD map (Figure 3.7) with a small-scale microstructure on the fine γ′ variant was also examined on the same material but from a different batch in the current project to compare directly with R. Jiang's work as shown in Figure 3.8. The EBSD map represents grain boundaries (black lines) and twin boundaries (red lines) in the figures. The twin boundaries are a distinctive feature of turbine disc alloys and form during recrystallization processes due to hot disc manufacturing processes such as forging and extrusion. In terms of grain size analysis, twin boundaries were ignored and grain sizes under 5 µm were not considered as they are too small to be confidently identified as grains by this technique. 353 and 286 grains were measured in the alloys with fine and coarse γ′ precipitates respectively via the previously obtained EBSD maps. Both received a super-solvus solution treatment at a temperature higher than the γ′ solvus, thus removing all primary γ′ and yielding a similar grain size distribution in both γ′ variants. It was observed that they showed similar quantitatively assessed grain size distributions as expected, with 32.4 ± 24.0 SD µm and 32.9 ± 25.1 SD µm for fine and coarse γ′ precipitate variants, respectively. The smaller scale EBSD map including 28 grains in the fine γ′ variant studied in this PhD also illustrated a similar grain size of 32.2 ± 20.9 SD µm although it has assessed a smaller number of grains. Further analysis of grain orientations and twin boundaries with respect to the crack initiation and short crack path in both fine and coarse γ′ variants will be discussed in Chapter 4.

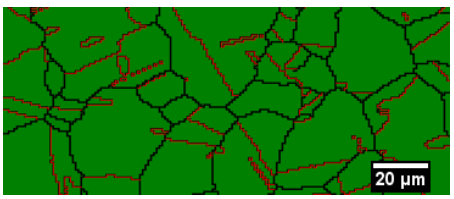

Figure 3.7: A trial EBSD map of the fine γ′ variant describing grain distribution, grain boundaries and twin boundaries obtained as part of this PhD study to compare with Figure 3.8.

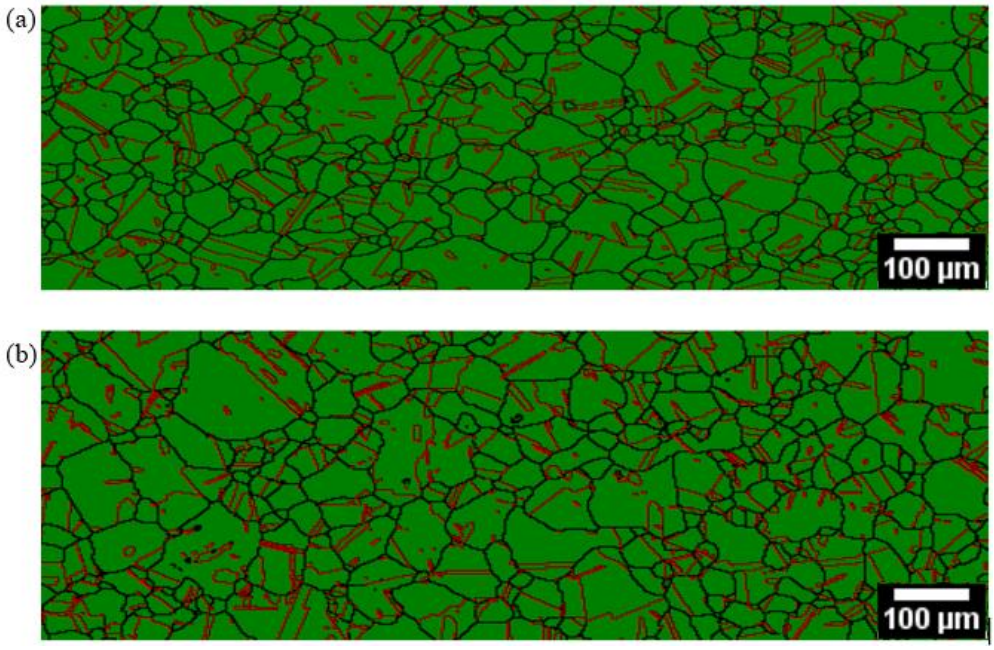

Figure 3.8: EBSD map of (a) the fine γ′ variant (b) the coarse γ′ variant describing grain distribution, grain boundaries and twin boundaries (captured by R. Jiang).

3.4.2 Effect of oxidation behaviour on the microstructure

Figure 3.9 shows SEM images illustrating the microstructural features observed in the oxidation tests on RR1000 in both γ′ variants thermally exposed in the furnace at 650 ^{o}C without loading for various testing times. Grain boundaries are oxidised and revealed via this "thermal etching", indicating the segregation on the grain boundary has occurred preferentially more in the coarse γ′ variant than the fine γ′ variant. It is observed that the carbides on the grain boundary are likely to exhibit cuboidal or bulky shapes before the thermal exposure and after a short time of thermal exposure. Carbides with a more "flower" or broken/ex-foliated shape are observed with increasing exposure time to high temperature, which is related to volume expansion due to oxidation of the carbide [95]. This can indicate that the interface of carbide/oxide and expanded carbide/grain boundary becomes a preferential oxygen diffusion path and contributes to marked oxidation damage. This can promote weakening of grain boundary strength and thereby fatigue crack initiation or intergranular fatigue crack propagation. Note that not all carbides were revealed by the thermal effect (via carbide oxidation processes) as were seen in the etching studies as seen in Figure 3.5. It is interesting to note that grain boundaries of the coarse γ′ variant seem more clearly delineated by the oxidation than those of the fine γ′ variant as described with yellow arrows in Figure 3.9. EDX analysis (Figure 3.10 and Figure 3.11) conducted on the precipitates on the grain boundary give evidence of carbide formation and subsequent oxidation process. It is observed that the ratio of oxygen increased with longer testing

durations as expected, which is linked to more oxygen diffusion time and further progression of the oxidation reaction.

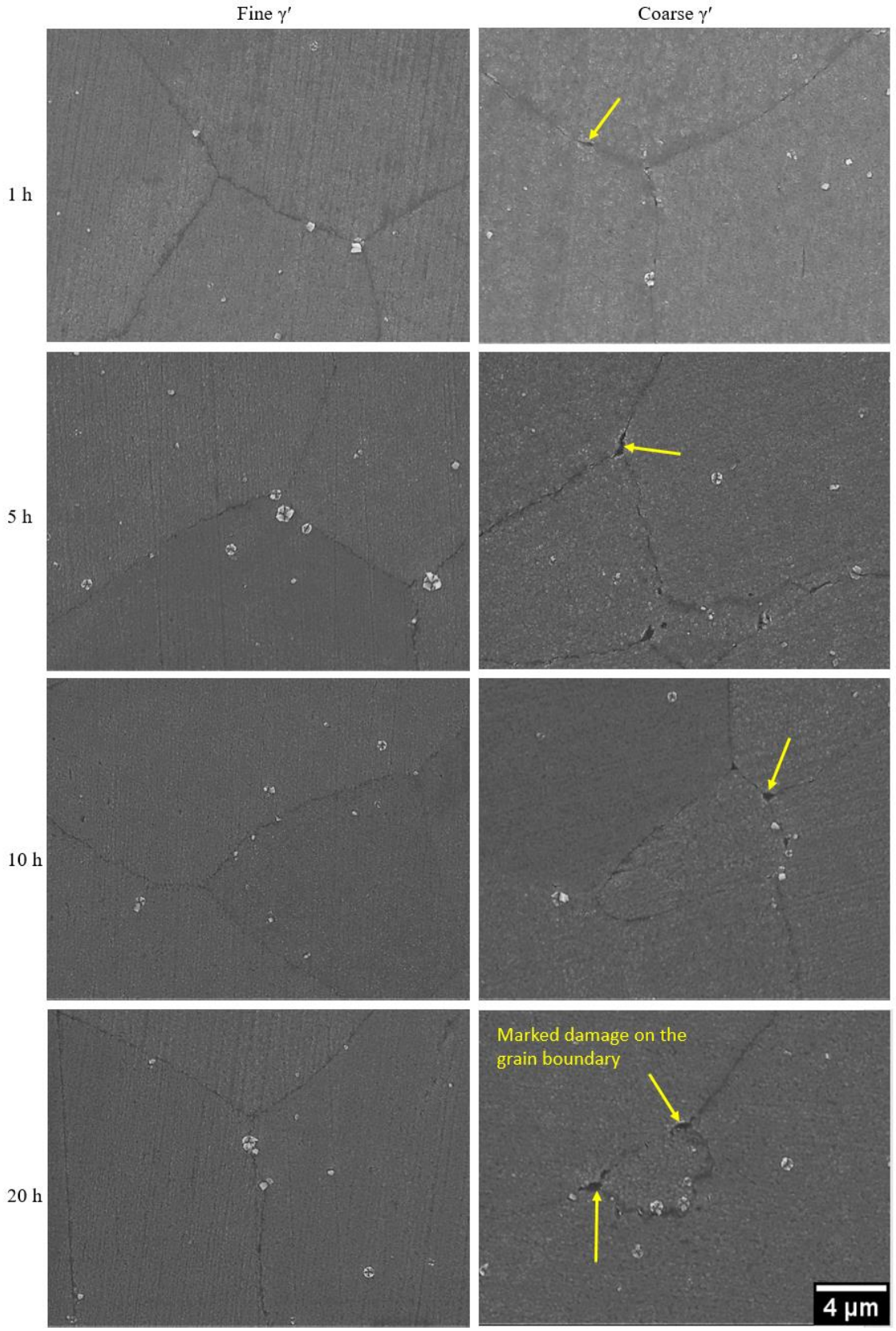

Figure 3.9: Microstructures thermally exposed at 650 ºC for various times without loading for the fine and coarse γ′ variants.

(a)

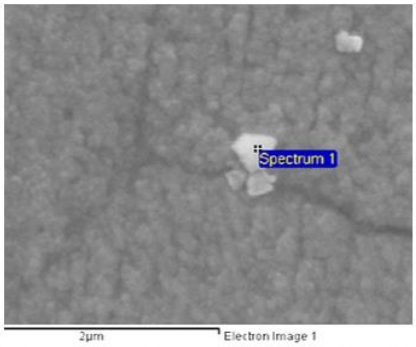

Element	Weight%	Atomic%
C K	7.91	24.44
O K	9.87	22.91
Al K	2.44	3.36
Ti K	4.03	3.12
Cr K	12.78	9.12
Co K	14.72	9.27
Ni K	39.79	25.17
Mo L	4.71	1.82
Ta M	3.75	0.77
Totals	100.00	

(b)

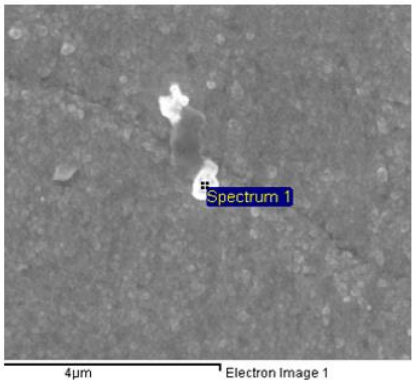

Element	Weight%	Atomic%
C K	3.65	8.98
O K	24.36	45.00
Al K	15.91	17.42
Si K	0.49	0.51
Ti K	2.38	1.47
Cr K	9.86	5.61
Co K	10.67	5.35
Ni K	28.59	14.40
Mo L	4.11	1.27
Totals	100.00	

Figure 3.10: EDX analysis on the precipitate on the grain boundary exposed at 650 ºC for 1 hour (a) the fine γ′ structure (b) the coarse γ′ structure.

(a)

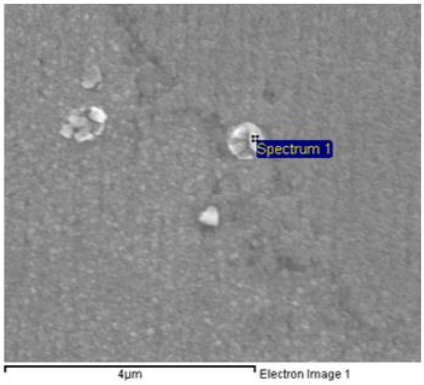

Element	Weight%	Atomic%
C K	3.46	9.77
O K	24.40	51.74
Al K	1.84	2.32
Ti K	7.25	5.13
Cr K	11.64	7.60
Co K	10.82	6.23
Ni K	22.94	13.26
Mo L	3.93	1.39
Hf M	2.95	0.56
Ta M	10.77	2.02
Totals	100.00	

(b)

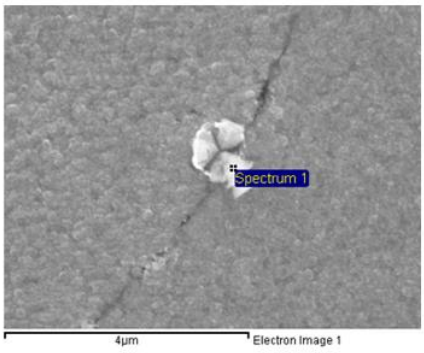

Element	Weight%	Atomic%
C K	3.76	10.28
O K	28.61	58.70
Al K	1.09	1.32
Ti K	9.92	6.80
Cr K	6.59	4.16
Co K	7.74	4.31
Ni K	16.63	9.30
Mo L	2.77	0.95
Hf M	6.67	1.23
Ta M	16.22	2.94
Totals	100.00	

Figure 3.11: EDX analysis on the precipitate on the grain boundary exposed at 650 ºC for 10 hours (a) the fine γ′ structure (b) the coarse γ′ structure.

The grain boundary character of the coarse γ′ variant which has oxidised under loading is presented in Figure 3.12. The coarse γ′ variant was assessed further under load due to its distinctive grain boundary features such as greater segregation and more severe oxidation. A comparison with the fine γ′ variant oxidation would be interesting as future work. It appears that a heavily damaged grain boundary can be discerned, with the formation of slip bands due to the stress/strain applied. It can be discerned that the grain boundary character of the coarse γ′ variant is relatively more vulnerable to an oxidising environment as seen in Figure 3.9-Figure 3.12. Especially the more continuous distribution of carbides oxidised on the grain boundary (linked to the higher temperature ageing) can contribute to the weakened grain boundary strength.

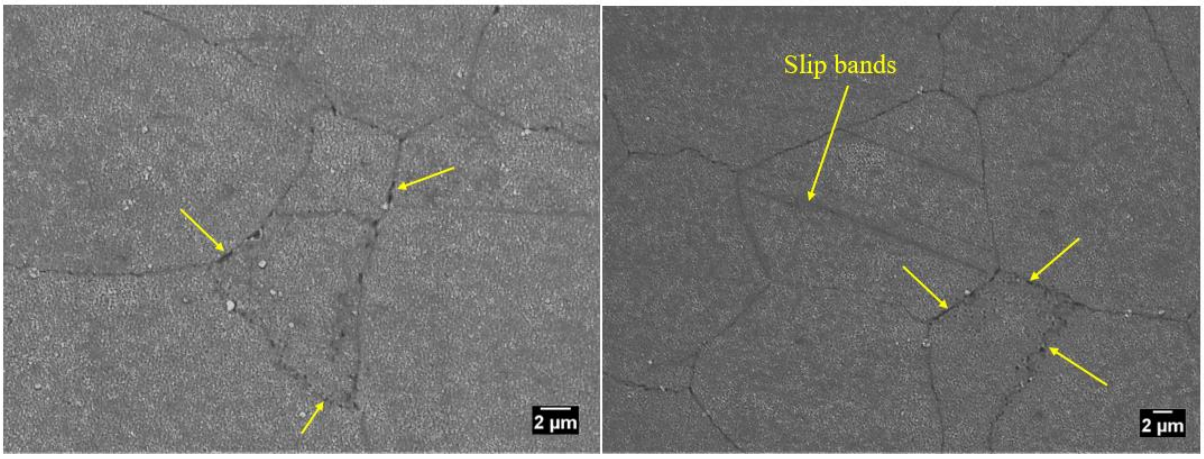

Figure 3.12: Microstructures of samples thermally exposed at 650 ºC at 90 % yield stress for 10 hours for the coarse γ′ variant. Yellow arrows represent slip bands and marked damage on the grain boundary.

3.5 Discussion

It is well known that microstructural features such as γ′ size and grain boundary features are tailorable by the heat treatment in turbine disc alloys. In this study, a non-commercial heat treatment has produced the two different unimodal distributions of secondary γ′ precipitate (Figure 3.3) to allow clearer understanding of just this effect on the failure mechanisms. The heat treatment process here consists of a solution treatment and different ageing treatments with different temperatures and cooling rates as described in Table 3.2, which leads to the model RR1000 alloys with fine and coarse γ′ microstructures. The solution heat treatment at a temperature higher or lower than γ′ solvus can achieve loss or retention of the primary γ′ precipitates and concomitant varying grain size as the primary γ′ precipitates can constrain the grain boundary and grain growth. The grain size of both γ′ variants here is achieved by the same super solvus solution treatment, which results in dissolved primary γ′ precipitates and similar grain size. Therefore, the grain size is *not* a variant in this study although it exerts a significant influence on mechanical and environment damage tolerance. The

different temperatures and cooling processes of ageing treatments contributed to the size distribution of secondary γ′ precipitates. The lower ageing temperature is linked to the fine γ′ microstructure while the higher ageing temperature promotes the coarse γ′ microstructure. The ageing temperature differences also resulted in somewhat different carbide distributions along the grain boundary as assessed by the material characterisation in this chapter.

It is widely known that Ni-based superalloys have excellent high temperature strength making them suitable for turbine disc applications. Proof stresses at a range of temperatures in both γ′ variants obtained by University of Manchester testing show the typical retention of superior high temperature strength of Ni-based superalloys until the temperature reaches around 800 ^{o}C, followed by a significant drop in yield stress. It is interesting to note that the yield stress of the fine γ′ variant is marginally higher than that of the coarse γ′ variant. This can be ascribed to the more continuous carbide distribution of the coarse γ′ variants and consequently weakened grain boundary strength in an oxidising environment at higher temperature.

Grain boundary strengthening phases such as carbides and borides are commonly observed in Ni-based superalloys. In this study, carbide formation on grain boundaries is seen in both γ′ variants, interestingly more continuous grain boundary carbides have formed in the coarse γ′ variant. It is believed that primary MC carbides become unstable during the heat treatment process and are expected to react with the γ matrix and form lower carbides such as $M_{23}C_6$ or M_6C (normally Cr-Mo rich carbide in RR1000 alloy) within the grains and on the grain boundaries [160]. Grain boundary carbides normally contribute to constrain grain boundary sliding and creep behaviour effects in high temperature fatigue. The volume expansion of carbides observed due to oxidation processes when the alloys are exposed at high temperature can induce broken/ex-foliated carbides on the grain boundary and this may weaken the grain boundary, which becomes more serrated during the oxidation process. It is seen that such features of carbide oxidation are more marked in the coarse γ′ variant where more carbides have formed on the grain boundaries.

3.6 Summary

Detailed microstructure analysis of the model RR1000 alloys is presented in this chapter. Non-commercial heat treatment processes were employed to produce a unimodal γ′ size distribution and concomitant different carbide distributions on the grain boundaries. Isothermal oxidation testing with and without loading on both γ′ variants was conducted to understand the effect of oxidation behaviour on the microstructures. Based on the results and discussion in this chapter, the following conclusions can be made:

1. Microstructural features such as grain size, grain boundary particles and γ′ size distribution (fine and coarse sizes) can be tailored by heat treatment process. Consequently, the average γ′ size of the coarse γ′ variant is around three times larger than that of the fine γ′ variant. The heat treatment also results in different carbide distributions on the grain boundary. A more continuous carbide distribution is seen in the coarse γ′ variant while discrete carbide distribution is observed in the fine γ′ variant.
2. Due to the same solution heat treatment process, the grain size of both γ′ variants is similar. Therefore, the grain size is not a variant in this study although it is an important microstructural feature controlling mechanical and environmental damage tolerance, but is not a focus of this study.
3. Isothermal oxidation testing indicates that the coarse γ′ variant exhibits more serrated clearly defined grain boundaries. Volume expansion of carbides on the grain boundary due to oxidation processes at high temperature is likely to be associated with decrease of grain boundary strength, which is more marked in the coarse γ′ variant.

Chapter 4 Fatigue crack initiation and the early stage propagation behaviour at room temperature

4.1 Introduction

In service, the performance of disc alloys and much of their fatigue life are controlled by fatigue crack initiation processes and the early stages of FCG. The mechanisms of fatigue crack initiation and short FCG in polycrystalline Ni-based superalloys are closely associated with microstructural characteristics including size distribution of strengthening precipitate (γ′), grain boundary character as well as grain orientation. The effect of varying γ′ size on crack initiation and growth in Ni-based superalloys is often linked to variation in slip character. In this chapter, fatigue lifetime tests and short fatigue crack tests on RR1000 alloys have been conducted to understand the effect of microstructure on fatigue mechanisms at room temperature. The uninterrupted tests for PBB specimens allow an investigation of fatigue lifetime and crack initiation sites followed by assessment of crack propagation features in both γ′ variants. In the interrupted tests, a replica method is employed for the incremental measurement of the crack evolution with intervals of loading cycles and allows observation of the surface crack evolution at a high resolution. The lifetime and short fatigue crack tests on microtensile specimens in both γ′ variants were conducted to understand sub-surface fatigue mechanisms and the interaction with internal microstructure by X-ray CT scanning approaches. Traditional 2D observations together with 3D evaluations should provide a better understanding of fatigue mechanisms in this advanced disc alloy. The testing procedure and results for these fatigue tests are described in detail in the following sections. It should be noted that much of the work in this chapter is linked to (and so extensively compared with) a previous EPSRC project conducted in collaboration with Rolls Royce, Alstom, DSTL, and Universities of Manchester and Loughborough in UK. Any work from this prior collaboration, conducted by other researchers (including a previous researcher, R. Jiang, at the University of Southampton) is clearly mentioned or marked (by red colour) throughout this chapter while the work carried out as part of the current PhD is presented as new data (hence unattributed).

4.2 Experimental methodology

4.2.1 Fatigue testing and fractography analysis

Material (RR1000)	Nominal maximum applied stress	Room temperature, frequency 20Hz, R-ratio=0.1			
		Uninterrupted test		Interrupted test	
Fine γ′ variant	90% yield stress	√	-	√	-
	110% yield stress	√	o	√	o
Coarse γ′ variant	90% yield stress	√	-	√	-
	110% yield stress	√	-	√	-

Table 4.1: The test matrix for uninterrupted and interrupted tests ('√' and 'o' denote the tests done by R.Jiang and myself, respectively).

The test matrix includes uninterrupted (fatigue lifetime) and interrupted tests (short fatigue crack behaviour) carried out by R.Jiang and myself as presented in Table 4.1. The fatigue tests on PBB samples of both fine and coarse γ′ variants have been carried out under a range of testing conditions. Sample dimension and setup for this fatigue testing are comparable to the isothermal oxidation testing in Chapter 3 (as shown in Figure 3.2) using three ceramic rollers: two located on the top surface and one on the bottom. The samples were manually ground and polished up to 1 μm finish on top surface prior to the tests. Such a polished condition can ensure a high resolution in the replica observations of the crack evolution. The fatigue tests were performed under three point bending on an Instron 8502 servo-hydraulic testing machine. The alignment between the specimen and rollers during test set-up were carefully considered to avoid asymmetric loading being applied.

Uninterrupted fatigue tests on RR1000 alloys were carried out at nominal maximum load of 90% and 110% yield stress, an R-ratio of 0.1 and frequency of 20Hz at room temperature. The results convey information about fatigue lifetime and fracture surface features including fatigue crack initiation and propagation. Interrupted fatigue tests employed a replica method on RR1000 alloys under the same test conditions at cycling intervals. Replication method using a silicone compound (provided by Struers Ltd) was used on the top surface of the samples to monitor the crack evolution of short cracks until the detectable nucleation of short cracks was seen. Then the intervals between replica records

were decreased as crack growth rate increased to allow a thorough evaluation of surface crack length (a) versus number of cycles (N). To ensure the cracks were clear and visible when monitored, crack opening was induced by holding samples at the mean load level during the process of replication.

The assessment of crack evolution by the replica record was conducted with OM images using ImageJ software. The crack length was measured in terms of the projected crack length perpendicular to the tensile axis as schematically shown in Figure 4.1. Then, crack growth rates were obtained by the secant method and da/dN versus stress intensity factor range (ΔK) was plotted on log-log scales. The stress intensity factor range was evaluated from the empirical equation for surface breaking semi-elliptical cracks by Scott and Thorpe [161] by considering the crack to be semi-elliptical. The equations and details for the stress intensity factor range evaluation are illustrated in Appendix A, which shows a schematic of crack shape assumptions and various parameter definitions. Fractography analysis has been carried out as a post analysis process. A Wild optical macroscope was employed to examine the fracture surface overviews and pinpoint interesting features on the fracture surface. OM was then used to assess microscopic features on the fracture surface. To examine the morphology of fractured features and identify the nature of fatigue failure including crack initiation sites and short crack propagation behaviour in RR1000, a JEOL JSM 6500 FEG SEM was used with WD of around 10 mm and accelerating voltage of 15kV.

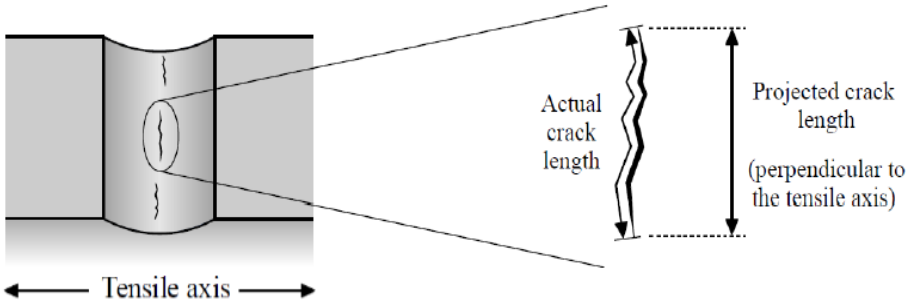

Figure 4.1: Schematic crack measurement in terms of definition of actual and projected crack length perpendicular to tensile axis [109].

4.2.2 EBSD characterisation of the crack path

EBSD mapping was carried out around various areas of interest (e.g. crack path of Crack 2 of the coarse γ′ variant and neighbouring grains as seen in Figure 4.2) containing the region of crack initiation and short crack growth after the fatigue testing. For EBSD characterisation, RR1000 alloys were polished up to 0.02 µm finish by OPA before fatigue testing. Step size of 1 µm and grain boundary tolerance angle of 2° were employed for EBSD mapping by using HKL Channel 5 software provided by Oxford Instruments. For the slip trace analysis, the parameters including the {111} slip

plane, the calculated inclination angle (α_c), measured inclination angle (α_m) and calculated Schmid factor (μ_c) were examined. The α_c can be used as a reference to identify the active slip systems associated with the actual crack segment within each cracked grain. Schmid factor represents the slip system and critically resolved shear stress, which is related to the active slip system. In order to calculate the Schmid factors of grains of interest, Euler angles ($\varphi_1, \emptyset, \varphi_2$) were obtained from EBSD crystal orientation for the coordinate transformation between sample and crystal frame. The rotation matrix $\boldsymbol{g}$ to transform from the sample to the crystal coordinates can be calculated with Euler angles as represented in the equation:

$$\boldsymbol{g} = \begin{bmatrix} cos\varphi_1 cos\varphi_2 - sin\varphi_1 sin\varphi_2 cos\emptyset & sin\varphi_1 cos\varphi_2 + cos\varphi_1 sin\varphi_2 cos\emptyset & sin\varphi_2 sin\emptyset \\ -cos\varphi_1 sin\varphi_2 - sin\varphi_1 cos\varphi_2 cos\emptyset & -sin\varphi_1 sin\varphi_2 + cos\varphi_1 cos\varphi_2 cos\emptyset & cos\varphi_2 sin\emptyset \\ sin\varphi_1 sin\emptyset & -cos\varphi_1 sin\emptyset & cos\emptyset \end{bmatrix} \quad (1)$$

By using the rotation matrix, the coordinate transformation of the loading direction (L) between the crystal and sample frame can be made using the following equation [108]:

$$L_{\text{crystal}} = \boldsymbol{g} L_{\text{sample}} \quad (2)$$

where L_{crystal} and L_{sample} are the vectors indicating the loading direction written in crystal and sample coordinates, respectively.

Then, the Schmid factor for the primary slip systems of the grains of interest can be calculated by the equation:

$$Schmid\ Factor = |(L_{\text{crystal}} \cdot n^{\varepsilon})(L_{\text{crystal}} \cdot l^{\varepsilon})| \quad (3)$$

where n^{ε} is the slip plane normal and l^{ε} is the slip direction for the slip system ε.

The calculated angle (α_c) between the slip trace and loading direction can be calculated using the equation [162]:

$$cos\alpha = (n^{\varepsilon} \times Z_{crystal}) \cdot L_{crystal} \quad (4.4)$$

where $Z_{crystal}$ is the direction perpendicular to the specimen surface written in crystal coordinates.

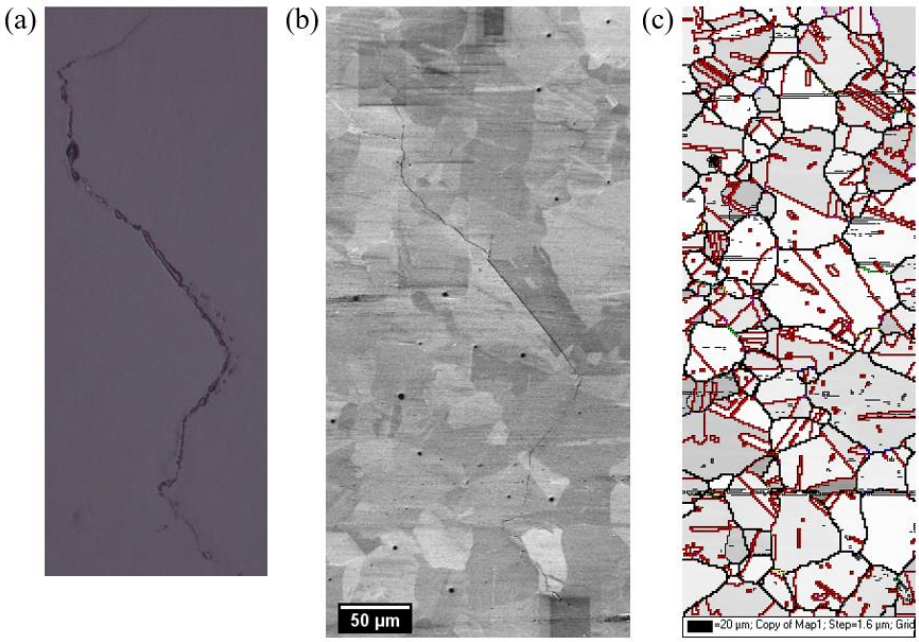

Figure 4.2: (a) OM image showing morphology of Crack 2 of the coarse γ′ variant (b) SEM image of crack path (c) EBSD mapping indicating grain boundaries (black lines) and twin boundaries (red lines).

4.2.3 Characterisation of strain localisation under cyclic loading

Tension-tension fatigue tests were conducted on micro-tensile specimens on an Instron Electro-plus testing machine at room temperature with a 20 Hz sine waveform and an R-ratio of 0.1 as shown in Figure 4.3 (a). A maximum nominal stress of 90% yield stress which was calculated based on the measured cross-section determined from optical measurements at the narrowest region in the gauge section was applied. The gauge section in the micro-tensile specimens was ground and polished up to 1 µm finish, followed by etching in Kalling's reagent to reveal the γ' which provided the speckle pattern for ex-situ SEM-DIC investigation of strain localisation under cyclic loading (this is all prior work [163]). Reference images were taken at two areas of interest (AOIs) within the gauge section using a JEOL JSM 6500 FEG SEM under SEI mode before the fatigue tests. The SEM images taken from the AOIs were stitched together using ImageJ software, and the stitched images are shown in Figure 4.3 (b) and (c). Once the reference images were taken, fatigue tests were conducted and interrupted after further loading cycles to capture the SEM images in the ex-situ (unloaded) deformed gauge section. The observation history of this SEM-DIC specimen is taken sequentially at 10 cycles → 1,000 cycles → 10,000 cycles → 95,000 cycles. DIC analysis was carried out using MatchID commercial software, and the detailed parameters used for DIC analysis is shown in Table 4.2 based on our previous study [100].

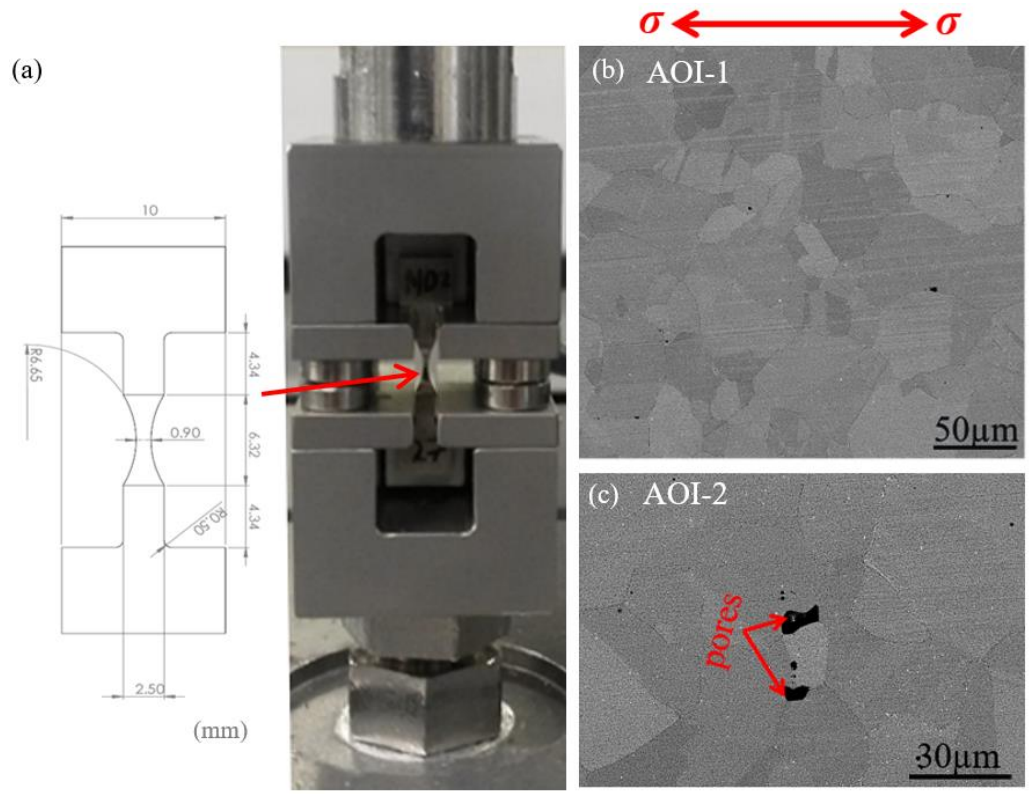

Figure 4.3: (a) Schematic dimension for a micro-tensile sample and set up of tension-tension tests with the sample. (b) AOI-1 and (c) AOI-2 at the gauge section. Images taken previously in prior work [163].

Subset	Stepsize	Correltation algorithm	Interpolation	Shape functions	Pre-smoothing	Strain window
27 × 27 pixels	7 pixels	ZNSSD	Bicubic spline	Quadratic	Gaussian 5	3

Table 4.2 Parameters used for DIC analysis.

4.2.4 3D morphology of crack path by X-ray CT scan

X-ray CT analysis on the coarse γ′ variant was carried out to examine internal microstructural features and short FCG behaviour in three dimensions. In this report, micro-tensile specimens with a small gauge section (cross section of ~ 0.9 mm x 0.9 mm as presented in Figure 4.4 (a)) were employed for the X-ray CT scanning evaluation due to the high degree of attenuation of Ni-based superalloys. The lifetime was assessed by the micro-tensile fatigue testing (Figure 4.4 (a)) under testing conditions of 85% yield stress, sine waveform loading of 20Hz frequency and an R-ratio of 0.1 at room temperature by R.Jiang. The interrupted fatigue testing was then conducted up to 95,000 cycles at nominal maximum load of 90% yield stress under the same testing condition done by

R.Jiang. X-ray CT scanning was carried out on the coarse γ′ variant containing a short fatigue crack by using the Zeiss 160 kVp Versa 510 at μ-VIS Imaging Centre of University of Southampton. Testing parameters of the CT scanning is presented in Table 4.3. 3D evaluation of internal microstructure (i.e. pore distribution) and short FCG was conducted by several software packages such as VG studio, Avizo and ImageJ. Post image processing after the X-ray CT scan was conducted on an AOI particularly focusing on the gauge section where the crack exists as shown in Figure 4.4 (b). Two scans in the gauge section from the mid plane to +450 μm and -450 μm were conducted and allocated for the position A and B as seen in Table 4.3. After two scans, the series of 2D raw images were obtained and stitched for the whole AOI using the aforementioned image software packages.

The series of 2D raw images were then processed by the segmentation for the pore distribution and short fatigue crack based on the different greyscale of the material, pores, crack and air assessed by ImageJ. During the segmentation, it is found that there was some noise, which is a common and typical issue in this imaging process. There are a several ways of alleviating such noise issues such as pixel control including dilation, erosion, despeckle or volume thresholds. In this study, the volume threshold approach was employed for the segmentation process on the pores while the crack itself was manually segmented as this was found to be most effective in terms of quantification and precision.

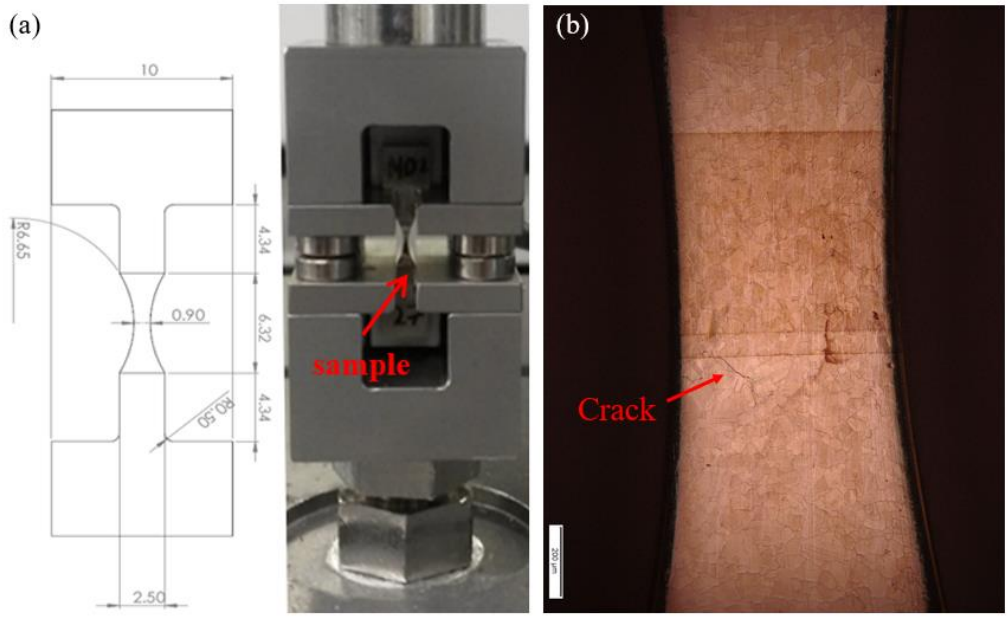

Figure 4.4: (a) Dog-bone shape microtensile sample with dimension for X-ray CT scanning (b) AOI of the microtensile sample of the coarse γ′ variant for X-ray CT scanning representing the microstructure and short fatigue crack.

Parameter	
Voltage	160kV
Power	9W
Pixel size	0.9461µm
Exposure time	50s
Binning	x2
Imaging angle range	-180 º to 180 º
Scan time	49 hrs
Number of projection	973 (Pos A) + 974 (Pos B)

Table 4.3: Parameters for X-ray CT scanning carried out at University of Southampton.

4.3 Results

4.3.1 Fatigue lifetime and crack initiation behaviour

Uninterrupted tests of both γ′ variants have been carried out to investigate the effect of microstructure such as the distribution of γ′ precipitates and carbides on fatigue crack initiation and lifetime at room temperature. Fatigue lives of both γ′ variants with their slightly different room temperature yield stresses are presented in Table 4.4 in terms of the proportion of yield stress applied. The lifetimes generally show the scatter in data seen over this range of testing conditions (i.e. the lifetime of the coarse γ′ variant can be either lower or higher than that of the fine γ′ variant). It can be seen that the lifetime of the fine γ′ variant is clearly greater than the for the coarse γ′ variant when tested at 90% yield stress while it is perhaps only slightly higher when tested at 110% yield stress. The lifetime of the fine γ′ variant was however found to be slightly lower in the dog-bone samples when tested at 85% yield stress (possibly linked to the one test interruption). Statistical evaluations of the true lifetime scatter would require multiple tests, but that is not the focus of this study. Overall, the crack initiation of both γ′ variants is likely to occur at pores and/or slip bands. The fractography analysis to establish this is further discussed in the section 4.3.3.

Uninterrupted test	Sample	Loading conditions	Fatigue life (Cycle)	Crack initiation sites
Room temperature, frequency 20HZ, R-ratio=0.1	Fine γ′ variant (PBB)	90% yield stress	757,135	Pores/slip bands
			632,513	
		*110% yield stress	176,566	
			*113,874	
	Coarse γ′ variant (PBB)	90% yield stress	320,805	
			483,731	
		110% yield stress	148,485	
	Fine γ′ variant (dog-bone)	*85% yield stress	*105,908 (interrupted at 40,000)	
	Coarse γ′ variant (dog-bone)	85% yield stress	132,244	

Table 4.4: The test matrix of uninterrupted fatigue tests carried out on RR1000 alloys (tests done as part of this PhD are marked by '*' and the remainder were done by R.Jiang for the previous EPRSC project).

A stress range (*S*) versus loading cycles (*N*) curve of these fatigue tests is presented in Figure 4.5. Comparison of the PBB samples indicate a fairly typical *S-N* curve trend where lower stress ranges result in higher lifetimes. However, scatter in lifetime data is observed even in tests with same specimen geometry and test condition. The lifetime of the small dog-bone specimens (tested under uniaxial tension) is generally lower than in the PBB even at lower stress ranges. It is difficult to directly compare tests with such different geometry and size as the PBB and dog bone samples, as different sample geometry can affect loading distribution on samples, sampling volumes, distribution of defects and varying surface finishes.

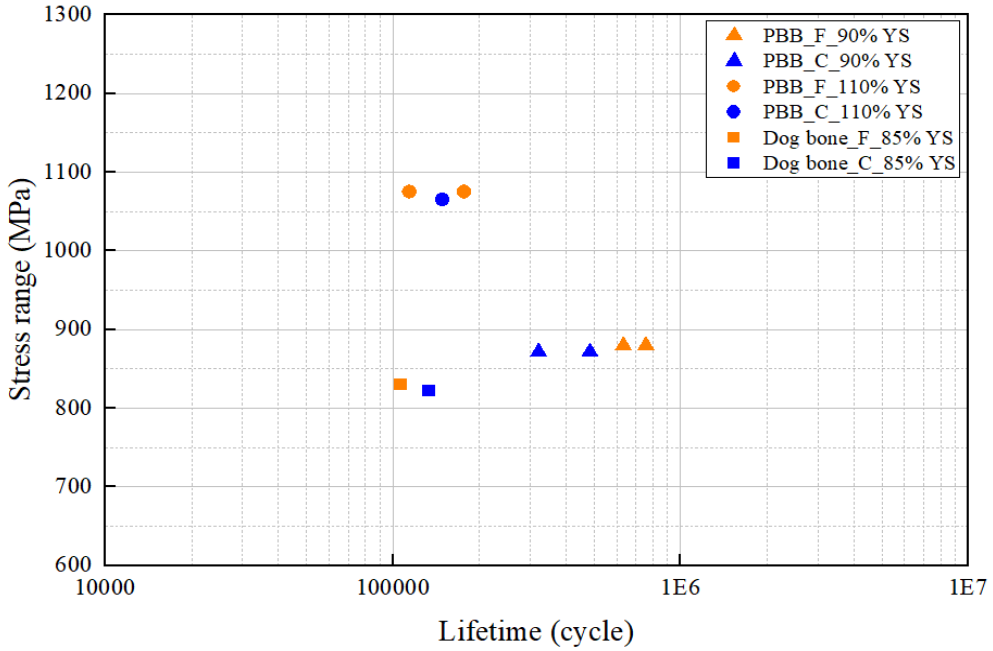

Figure 4.5: S-N curve of data tested on PBB and dog-bone samples with varying test condition (F and C denote fine and coarse γ′ variant, respectively).

Macroscopic images of the fracture surface of the fine γ′ variant tested at 110% yield stress is presented in Figure 4.6. It is seen that there are distinct features where cracks have initiated on the top surface. Fracture surfaces were then examined with SEM imaging and showed cracks have initiated from pores or/and slip bands at different loading conditions at room temperature. Figure 4.7 (a) and (b) shows surface pore crack initiation in fine γ′ variant at 90% yield stress and Figure 4.7 (c) and (d) represent crystallographic faceted crack initiation at 110% yield stress. The pore distribution (position as well as size/shape) is related to the degree of stress concentration that occurs, which can then result in a favourable fatigue crack initiation site and thereby contribute to the scatter in the lifetime although the amount of porosity is expected to be very low in these alloys. This is a more marked at room temperature where oxidation effects are absent and pores and slip bands in favourably oriented large grains are the main fatigue initiation sites. In the coarse γ′ variant, cracks at both proportions of yield stress have initiated at slip bands showing crystallographic facets that are indicative of stage-I crack growth as seen in Figure 4.8.

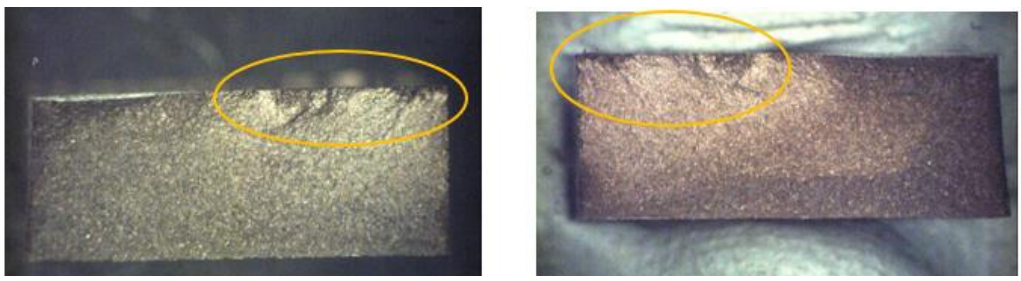

Figure 4.6: Macroscopic overview of fracture surface of the fine γ′ variant and AOI showing the initiation sites.

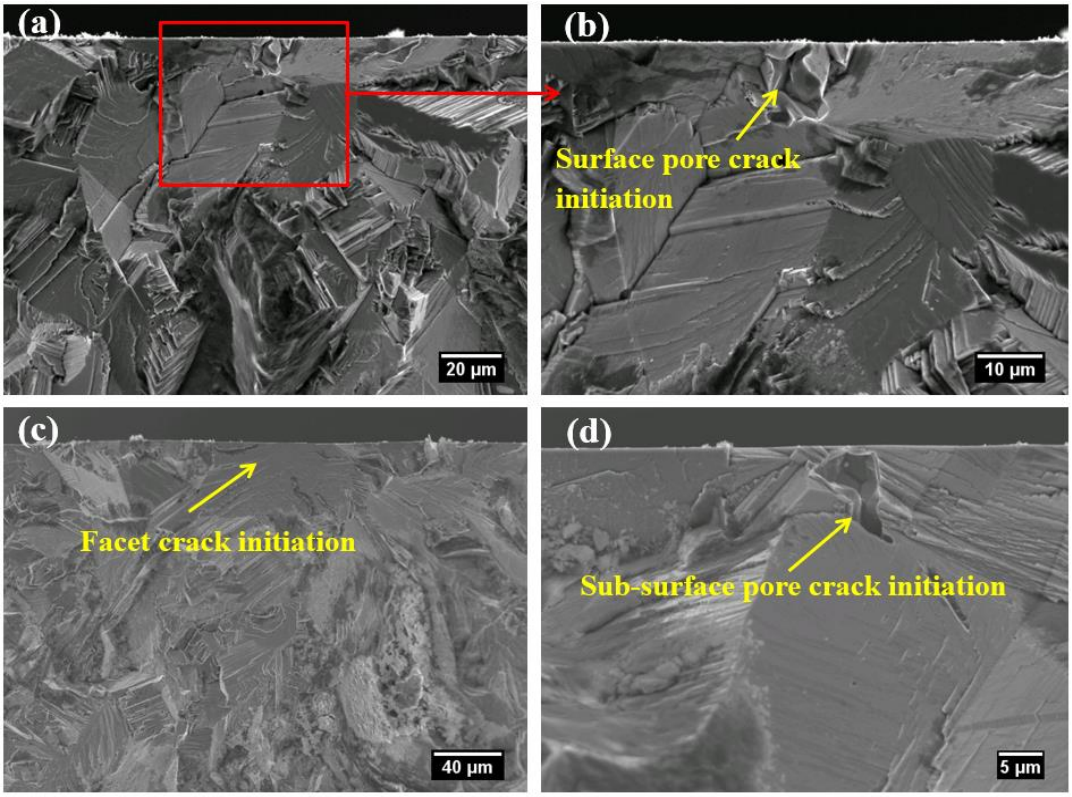

Figure 4.7: Fracture surfaces showing crack initiation area of the fine γ′ variant (a) and (b) at 90% yield stress (presented by R.Jiang); (c) and (d) at 110% yield stress.

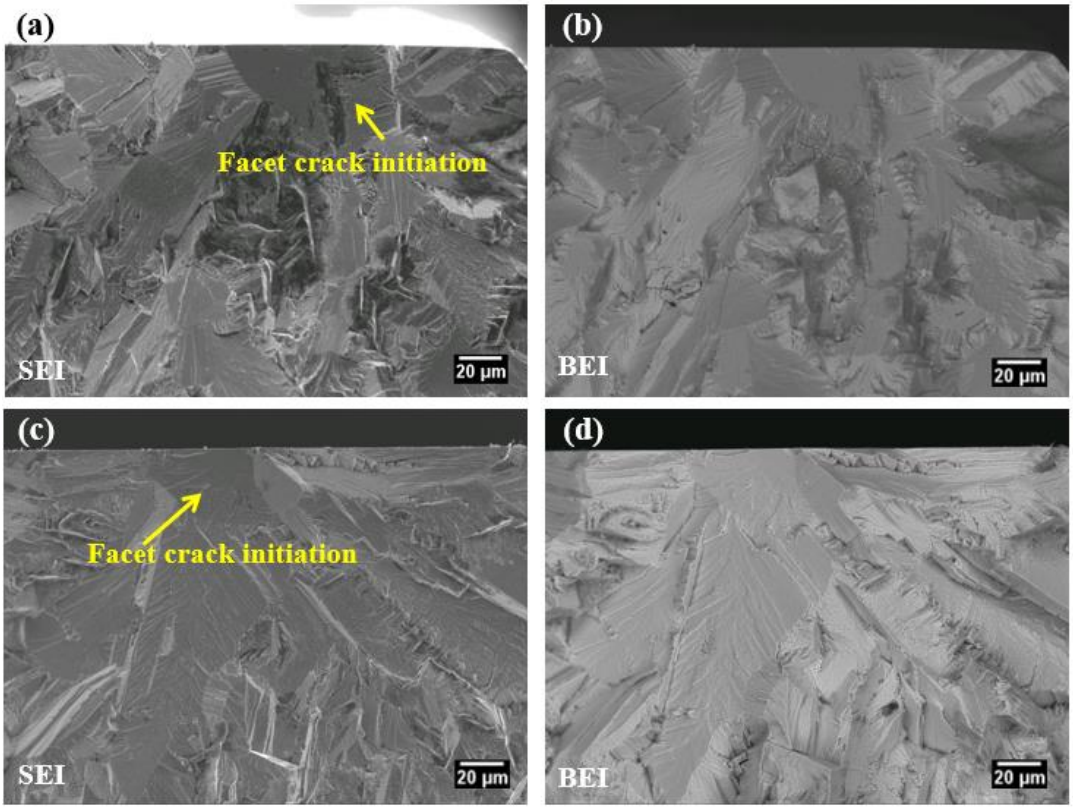

Figure 4.8: Fracture surfaces showing crack initiation area of the coarse γ′ variant (a) SEI image (b) BEI image at 90% yield stress; (c) SEI image and (d) BEI image at 110% yield stress (by R.Jiang).

4.3.2 Short fatigue crack growth behaviour

Interrupted test	Sample	Loading conditions	Number of cracks
Room temperature, frequency 20HZ, R-ratio=0.1	RR1000 with fine γ′ (PBB)	90% yield stress	270K cycles, long crack seen, failed to capture early stage crack propagation
			>2M cycles, long crack was observed
		110% yield stress	Fine γ′ _1) 4 cracks were measured (stopped at 108k)
			*Fine γ′ _2) 10 cracks were measured (failed at 85,603)
	RR1000 with coarse γ′ (PBB)	90% yield stress	No crack initiation after 3M cycles
		110% yield stress	10 cracks were measured (stopped at 115k)

Table 4.5: The test matrix of interrupted short FCG tests on RR1000 alloys (tests carried out as part of this PhD are marked by '*' and the rest were carried out by R.Jiang).

The test matrix for the group of interrupted tests where the silicone replica compound has been used to obtain a series of snapshots of the crack evolution is presented in Table 4.5. Crack initiation is somewhat unpredictable in terms of the position and the number of cycles to initiate so that early stage crack propagation is often hard to capture. In the tests on both fine and coarse γ′ variants at 90% yield stress, it was difficult to observe early stages of crack propagation for the HCF regime via replica records. The fine γ′ variant appeared to offer less crack initiation resistance at 90% yield stress as the first crack was observed earlier than in the coarse γ′ variant as described in Table 4.5. Only one crack was observed for each test of the fine γ′ variant at 270k and 2M cycles and no crack initiation up to 3M cycles for the coarse γ′ variant was observed, which indicates better crack initiation resistance in the coarse γ′ variant. On the other hand, at the higher yield stress level of 110% yield stress, 4 and 10 cracks for the fine γ′ variant and 10 cracks for the coarse γ′ variant were captured and measured through OM. It can be inferred that the fewer crack initiation sites in fine γ′_1 is associated with the observed enhanced fatigue lifetime as seen in the interrupted tests. Figure 4.9 indicates the first crack in the fine γ′ variant was observed at 20,000 and 60,000 cycles in each test under the same conditions while the first crack in the coarse γ′ variant was seen at around 43,000 cycles. The later observation of the first crack and fewer number of cracks are related to better fatigue crack initiation resistance and consequently enhanced fatigue lifetime. In contrast, earlier observation

of the first crack and overall a greater number of cracks gives a rise to inferior crack initiation resistance and reduced fatigue lifetime.

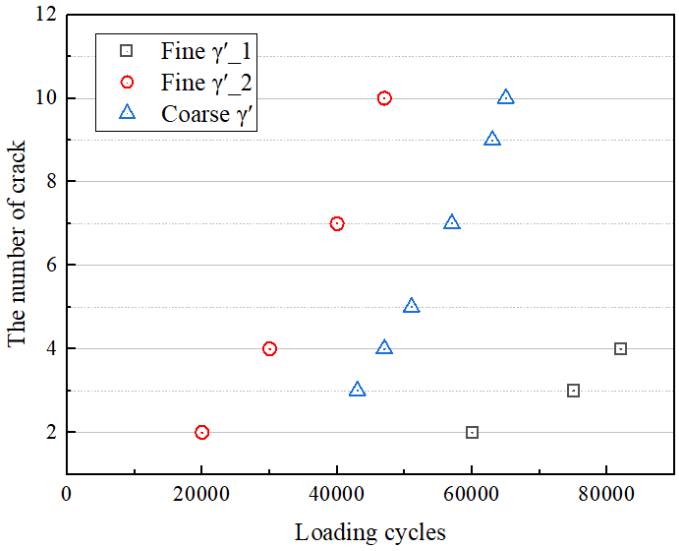

Figure 4.9: The number of cracks initiated during the lifetime at 110% yield stress of RR1000 alloys.

Consistency of crack length measurement

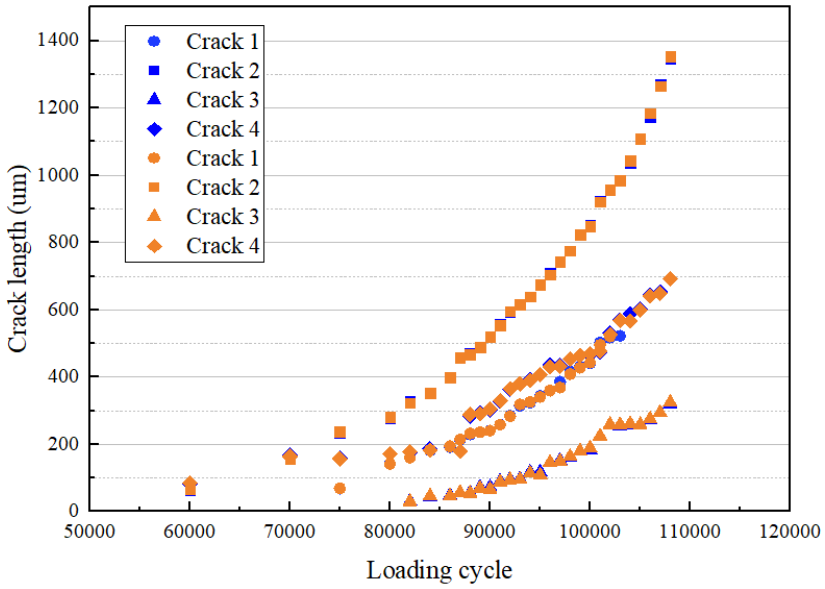

Figure 4.10: Reanalysis of the crack length measurement of four cracks from replicas of the fine γ′ variant for the reproducibility of the measurement technique. Blue and orange colours denote re-measurement and original data respectively.

Reanalysis of crack length measurement from replica images that had been previously taken by R.Jiang was conducted to ensure the reproducibility of the measurement technique. The four cracks of the fine γ′_1 test were measured by Image J software with respect to the projected crack length to

the loading direction applied (as described in Figure 4.1). At the stage after the immediate crack initiation when the crack opening distance is small, it was hard to measure the crack length clearly, which leads to difficulty in unambiguously identifying the start and end point for the crack measurement. It is found that the reanalysed measurement was extremely similar to the original measurement with only marginal differences as shown in Figure 4.10. The results showed the difference in this analysis between different operators was generally less than around 1 %, representing good consistency of the measurement. The maximum percentage difference was found to be around 8.6 % for Crack 3 at 90,000 cycles, indicating around 5 µm difference between two different measurements of 72.7 µm and 67 µm. Such marginal differences as seen in Figure 4.10 gives a confidence in the reproducibility of the measurement technique between different observers and allows valid comparisons to be made with previously obtained data.

Crack evolution

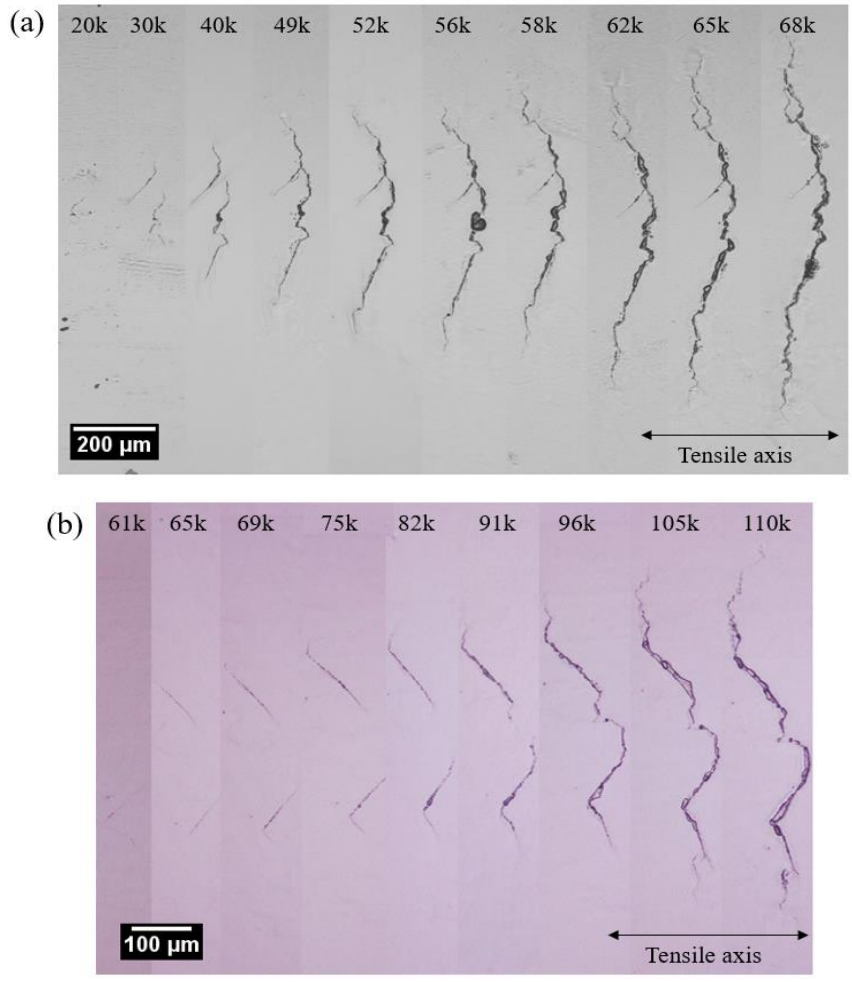

Figure 4.11: Primary crack evolution process over applied loading cycles of the interrupted test (a) in the fine γ′_2 variant (b) in the coarse γ′ variant at 110% yield stress.

Evolution of the primary crack in the interrupted tests in RR1000 alloys with fine and coarse γ′ can be seen in Figure 4.11 respectively. The primary crack in the fine γ′ variant in Figure 4.11 (a) propagates from a pore on the surface. It is interesting to note that two cracks were initiated, showing initiation/early propagation to be along what appear to be locally angled directions of 45° to the loading applied, likely to be linked to slip band cracking but as the crack grows it turns to adopt an overall direction normal to the loading condition and crack coalescence is observed in both γ′ variants. It is found that there was crack coalescence at early stage of crack growth which is related to reduced lifetime in fine γ′_2 while it occurred late in the coarse γ′ variant, linked to longer lifetime. Crack evolution from the replica images of the fine γ′ variants is available as a video to help visualise crack growth during loading cycles (Figure 4.12 below, click on link to Youtube video).

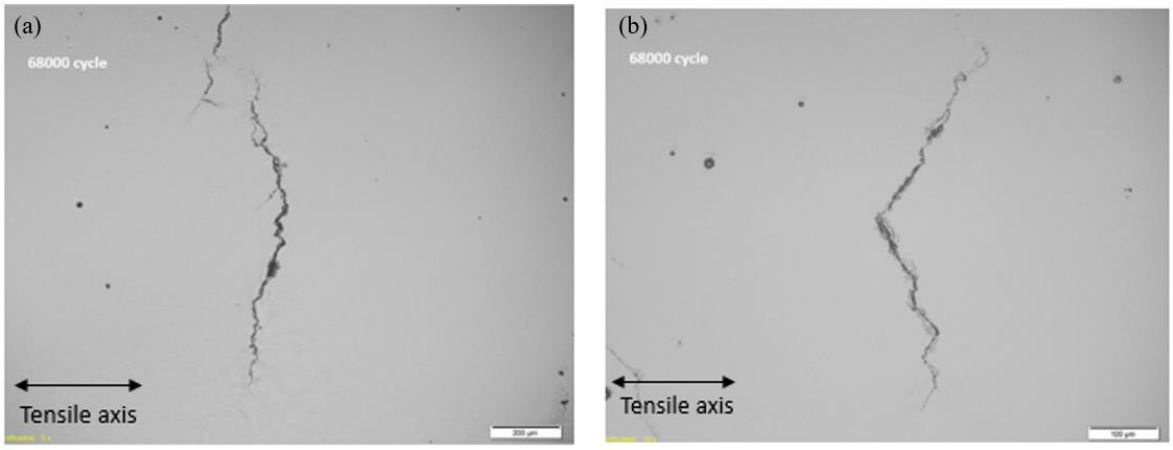

Figure 4.12: Video of primary and second largest crack evolution of the fine γ′ variant (a) https://youtu.be/dBubvlIHnuM and (b) https://youtu.be/0auDDgMYJHE.

FCG rates versus Loading cycles

Figure 4.13 represents the crack length variation with loading cycles for two tests in the fine γ′ variant and one test in the coarse γ′ variant. It can be seen that the primary crack which is most critical to final failure propagated noticeably faster than other cracks. It should be noted that crack coalescence took place at an early stage in life and two other cracks of the fine γ′_1 (crack 8a and 8b in Figure 4.13 (b)) have propagated close to each other and coalesced later, leading to accelerated FCG rate and consequently reduced lifetime. The primary crack (crack number 5 of the coarse γ′ variant) in Figure 4.13 (c) emerged as a result of the coalescence of two cracks and thereby propagated fast. The FCG rate observed in both fine and coarse γ′ variants as a function of the ΔK is plotted in Figure 4.14. It can be seen that FCG rates of the fine γ′ variant occupy a slightly higher overall envelope of FCG rates than that of the coarse γ′ variant, both showing considerable overlapping scatter, particularly at lower ΔK levels, which is a characteristic of short crack growth.

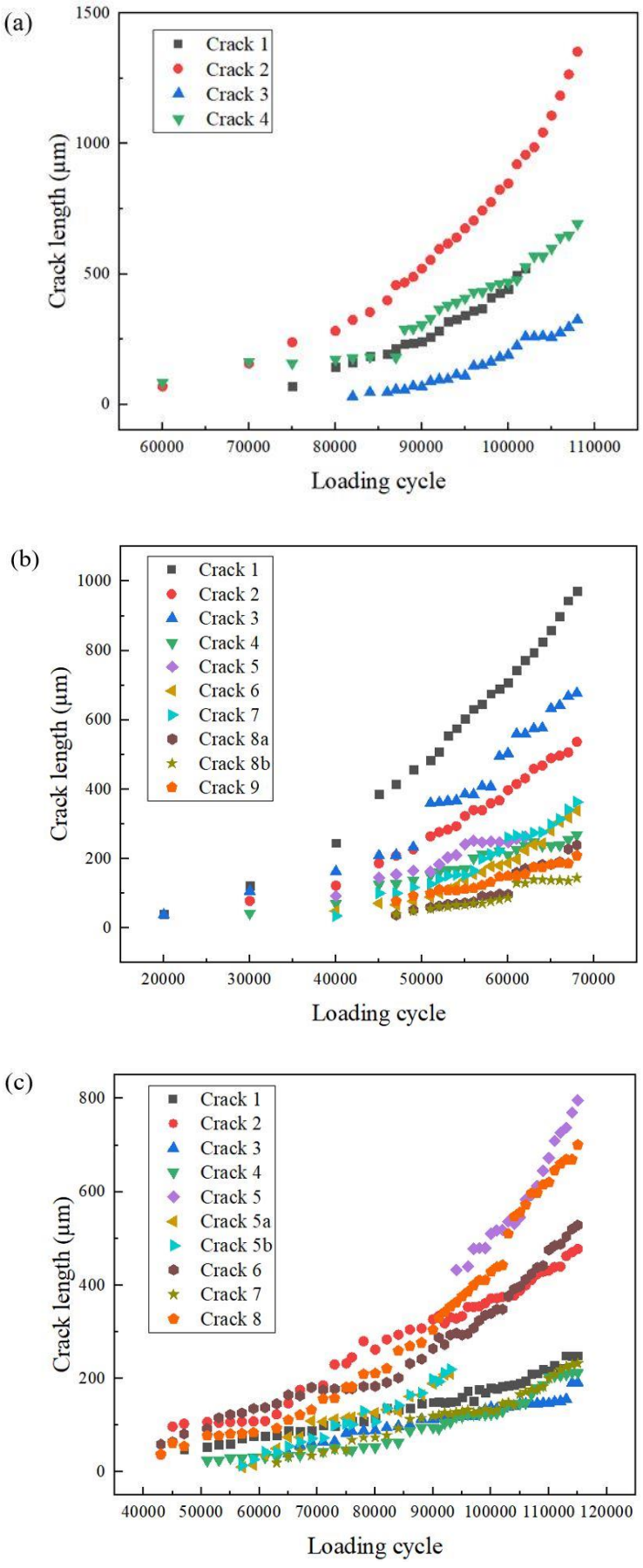

Figure 4.13: Crack length (a) versus loading cycles (N) tested at 110% yield stress for (a) fine γ′_1 (b) fine γ′_2 (c) coarse γ′ (note: fine γ′_1 and 2 denote two different tests).

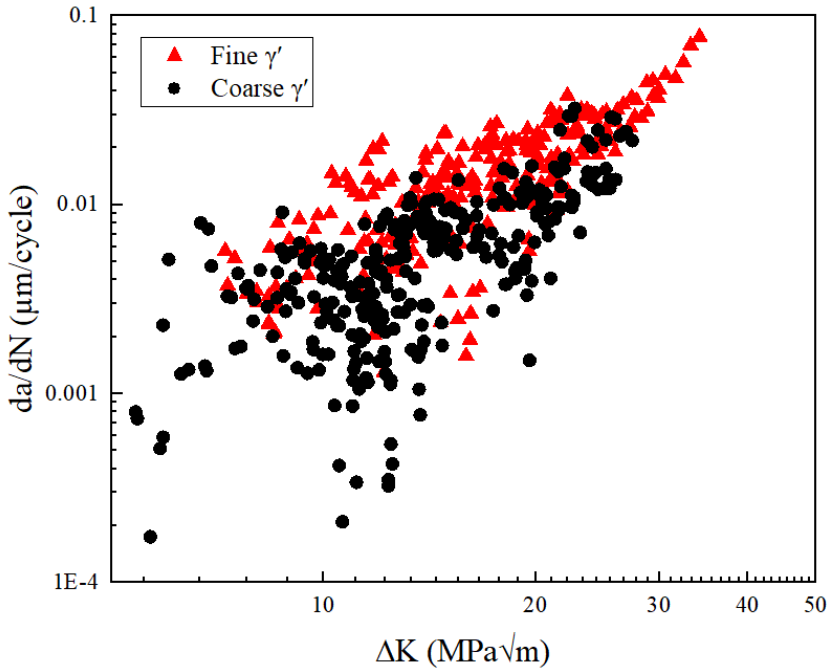

Figure 4.14: FCG rate (*da/dN*) vs Δ*K* of short FCG tests on the both γ′ variants (fine γ′ variant consists of fine γ′_1 and fine γ′ _2).

Slip trace analysis by EBSD mapping

EBSD analysis on the top surface of an interrupted test of the coarse γ′ variant was conducted to investigate in detail the effect of grain orientation on fatigue crack initiation and short FCG behaviour. Figure 4.15 (a) shows the crack path together with neighbouring grains examined by SEM and the crack path overlaid with EBSD mapping including grains and grain boundaries. It is shown that the crack has initiated along a twin boundary in a relatively large grain as marked in the figure, which is commonly observed as a crack initiation site of P/M Ni-based superalloys. Neighbouring grains overlapping with the crack initiation site and crack path are labelled to conduct a slip trace analysis. The calculated slip trace of the crack segment in each grain is presented with different colour legend bars. Table 4.6 summarises the slip trace analysis for the {111} slip plane on Crack 2 of the coarse γ′ variant including the calculated inclination angle (α_c), measured inclination angle (α_m) and calculated Schmid Factor (μ_c). It is found that crack propagation in each grain usually follows one of the calculated slip traces although there is a slight deviation between the calculated slip trace and actual crack segment. It is interesting to note that the Schmid Factor of the activated primary slip system is generally the highest but in some cases is not the highest.

As seen in Figure 4.15 (a), the crack initiated along a twin boundary area between grain 7 and 8 which is at an angle of around 45° to the applied loading. There was a noticeable deflection as one crack tip propagated “upwards” into grain 6 by following the twin boundary, then splitting and one branch was deflected again when it turned into grain 5 and its grain boundary. The other crack tip

direction propagated “downwards” into grain 9, the crack has propagated along the primary active slip system of grain 8 by accommodating grain 9 and then propagated into grain 10 with a similar inclination angle to that seen in the initiation area with the highest Schmid Factor. When the crack propagated through grains from 10 to 12, a small zig-zag crack growth was observed. There was a significant deflection from grain 12, which propagated at a similar inclination angle in grain 13 which is a relatively large grain by following its primary active slip system. Figure 4.15 (b) and (c) represent a graph of crack length vs loading cycle applied and FCG rate vs ΔK, respectively. It is interesting to note there was crack temporary arrest and a decelerated FCG rate at the beginning of crack propagation although it propagated gradually back later. The zig-zag deflection from the ends of crack initiation and significant deflection can be related to the crack arrest and then corresponding slow crack propagation, showed in a scattered FCG rate.

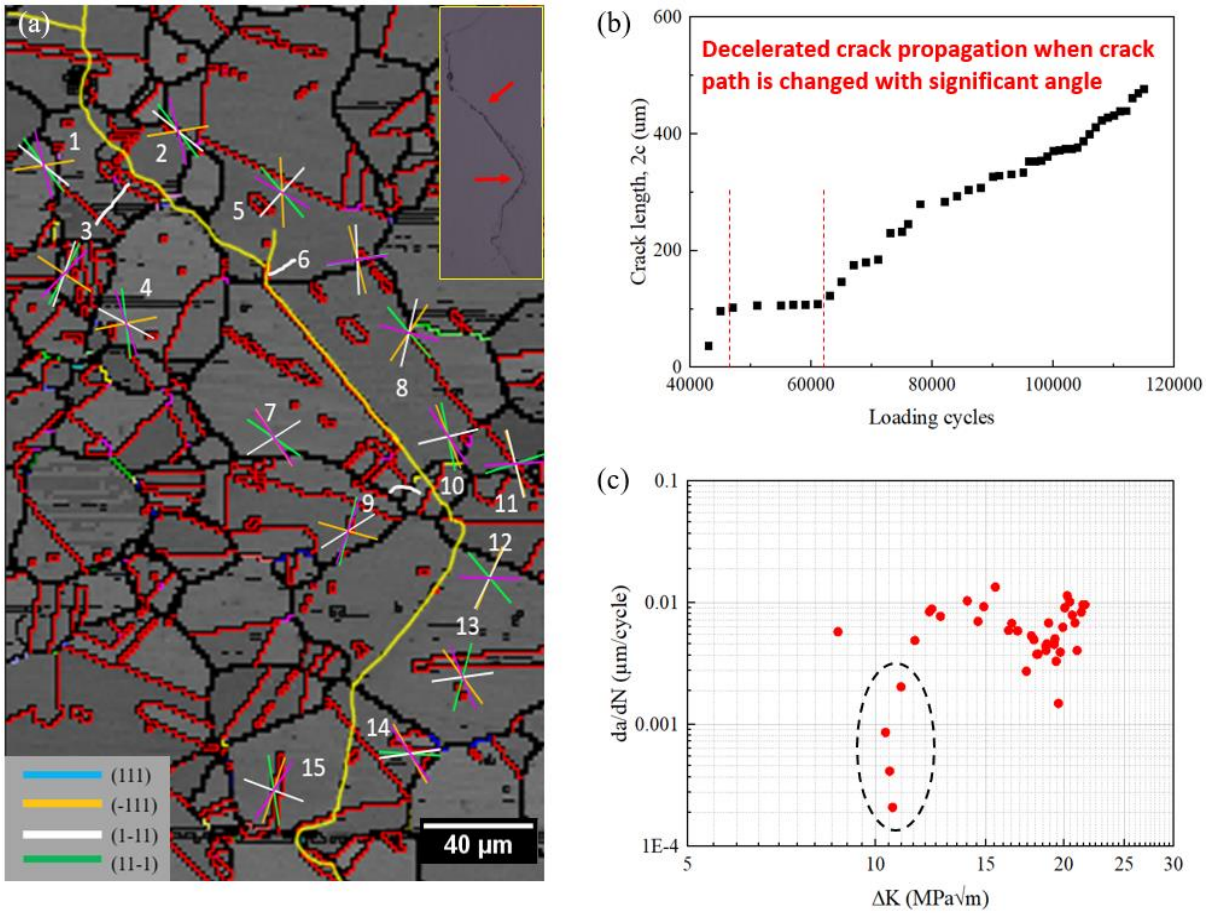

Figure 4.15: (a) Band contrast map by EBSD (obtained by R.Jiang) overlaying the crack path including crack initiation site of Crack 2 of the coarse γ′ variant. Black and red lines represent high angle grain boundaries and twin boundaries. The calculated slip trace in the grains containing the crack path is labelled and the legend of {111} slip planes is described. (b) crack length over loading cycle of Crack 2. (c) FCG rate vs ΔK of Crack 2 of the coarse γ′ variant indicating decelerated crack propagation.

Grain	Slip system	μ_c	α_c	α_m	Grain	Slip system	μ_c	α_c	α_m
Grain 1	(111)[01-1]	0.294	**49.280**	**43.2**	**Grain 8**	(111)[1-10]	0.147	**46.359**	**47**
	(-111)[01-1]	0.091	**172.182**			(-111)[01-1]	0.490	**127.548**	
	(1-11)[110]	0.427	**35.132**			(1-11)[011]	0.460	**105.091**	
	(11-1)[1-10]	0.263	**74.131**			(11-1)[1-10]	0.228	**13.728**	
Grain 2	(111)[01-1]	0.294	**49.280**	**36.8**	**Grain 9**	(111)[01-1]	0.498	**106.663**	**47.2**
	(-111)[01-1]	0.091	**172.182**			(-111)[110]	0.199	**14.430**	
	(1-11)[110]	0.427	**35.132**			(1-11)[110]	0.339	**151.584**	
	(11-1)[1-10]	0.263	**74.131**			(11-1)[011]	0.455	**112.419**	
Grain 3	(111)[01-1]	0.335	**120.179**		**Grain 10**	(111)[10-1]	0.129	**77.238**	**45.2**
	(-111)[01-1]	0.396	**30.261**	**36.8**		(-111)[110]	0.458	**66.311**	
	(1-11)[110]	0.468	**111.142**			(1-11)[-101]	0.178	**168.339**	
	(11-1)[1-10]	0.479	**138.318**			(11-1)[1-10]	0.478	**52.412**	
Grain 4	(111)[01-1]	0.495	**82.224**	**53.8**	**Grain 11**	(111)[1-10]	0.127	**164.900**	**71.5**
	(-111)[110]	0.132	**170.529**			(-111)[101]	0.453	**71.037**	
	(1-11)[110]	0.299	**25.349**			(1-11)[-101]	0.380	**74.426**	
	(11-1)[011]	0.436	**69.772**			(11-1)[1-10]	0.028	**177.766**	
Grain 5	(111)[1-10]	0.234	**46.188**	**23.2**	**Grain 12**	(111)[1-10]	0.157	**46.440**	**111.5**
	(-111)[101]	0.448	**87.059**			(-111)[01-1]	0.410	**115.037**	
	(1-11)[-101]	0.489	**136.648**			(1-11)[011]	0.467	**119.076**	
	(11-1)[1-10]	0.394	**26.269**			(11-1)[1-10]	0.027	**1.617**	
Grain 6	(111)[1-10]	0.095	**171.221**	**98.1**	**Grain 13**	(111)[10-1]	0.432	**107.513**	**122.53?**
	(-111)[01-1]	0.449	**74.535**			(-111)[110]	0.432	**50.849**	
	(1-11)[011]	0.450	**87.078**			(1-11)[-101]	0.082	**173.918**	
	(11-1)[1-10]	0.093	**173.651**			(11-1)[1-10]	0.331	**65.096**	
Grain 7	(111)[10-1]	0.303	**31.508**	**47**	**Grain 14**	(111)[10-1]	0.024	**3.024**	**86.99?**
	(-111)[110]	0.492	**53.002**			(-111)[110]	0.418	**57.787**	
	(1-11)[-101]	0.305	**151.002**			(1-11)[011]	0.039	**173.015**	
	(11-1)[1-10]	0.493	**51.254**			(11-1)[1-10]	0.443	**51.830**	
					Grain 15	(111)[10-1]	0.427	**80.863**	**122.5**
						(-111)[110]	0.475	**111.726**	
						(1-11)[-101]	0.271	**18.639**	
						(11-1)[1-10]	0.443	**127.798**	

Table 4.6: Summary of μ_c, α_c and α_m in the grains neighbouring Crack 2 of the coarse γ′ variant on {111} slip planes.

4.3.3 Strain localisation and evolution

Strain localisation which is closely related to fatigue cracking was characterised in the coarse γ′ variant under cyclic loading by SEM-DIC. The DIC analysis was conducted on only the coarse γ′ variant by R.Jiang as there was no evident difference in strain localisation in both γ′ variants as seen in [164]. Figure 4.16 presents strain (i.e. ε_{xx}) distribution at 10, 1000, 10000 and 95000 cycles, and grain boundaries obtained by EBSD are overlaid on the strain map to better reveal the influence of microstructure on the strain localisation. As shown in DIC images in Figure 4.16, strain mainly occurs within the slip bands due to dislocation movement on the {111} slip plane. In certain grains, multiple sets of strain bands can be observed, indicating more than one slip system is activated. Observing the morphology of the slip band by SEM, sheared secondary γ′ precipitates can be discerned as shown in Figure 4.16 (c). As loading cycles increased from 10 to 1,000, the slip band density and the strain value in the slip band increases significantly, and it seems strain saturation may occur in 1,000 cycles as there is little strain increase observed in the following loading up to 10,000 and 95,000 cycles. Moreover, observation of the slip band with high strain value shows micro-cracking in the slip band as shown in Figure 4.16 (f).

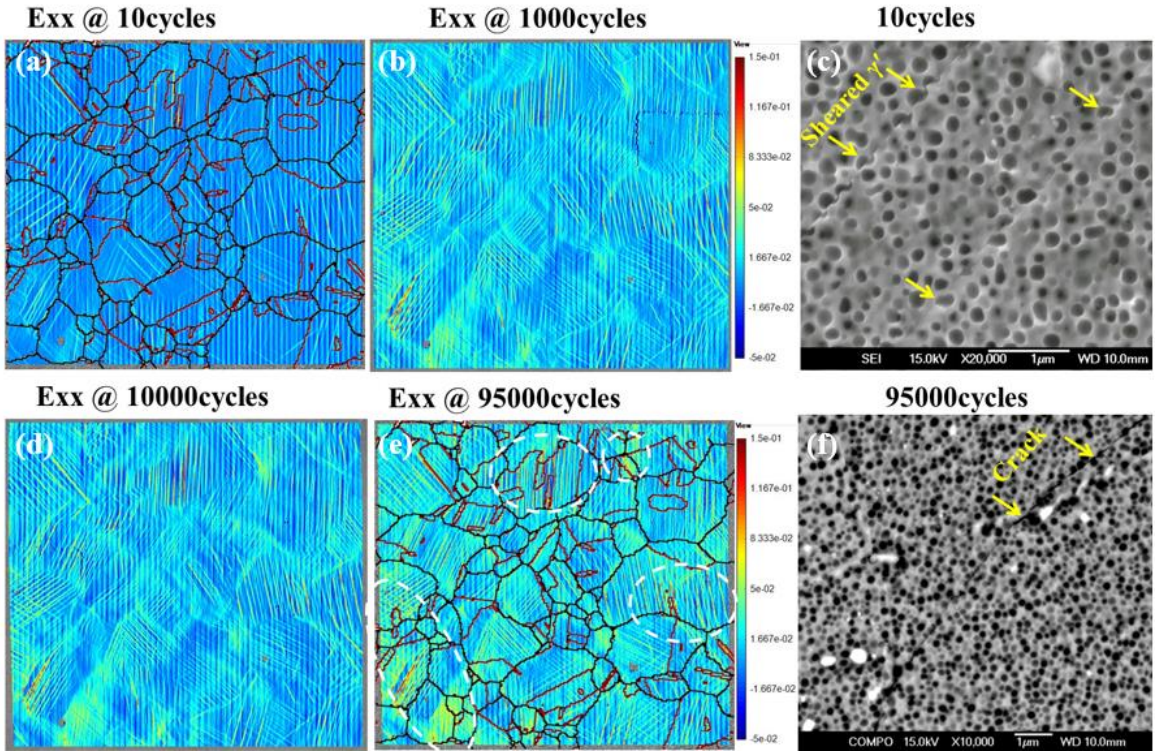

Figure 4.16: SEM-DIC analysis conducted by R.Jiang of AOI-1 of Figure 4.3 (a) strain localisation at 10 cycles and (b) at 1,000 cycles. (c) SEM image at 10 cycles showing sheared γ′. (d) strain localisation at 10000 cycles and (e) at 95,000 cycles. (f) SEM image at 95,000 cycles showing fatigue cracking.

Figure 4.17 shows strain localisation and fatigue cracking in another AOI containing pores. In general, similar strain localisation and evolution can be seen as shown in Figure 4.17, and the micro-

cracking in the slip band is associated with relatively high strain value. However, the strain distribution seems to be more diffused around the pores rather than localised in the slip bands. Due to the stress concentration and strain localisation around the pores, micro-crack forms adjacent to the pores as shown in Figure 4.17 (c). In addition, zig-zag crack path is observed when micro-crack propagates through the grain boundaries (Figure 4.17 (d)), which is associated with intense strain accumulation in the slip bands.

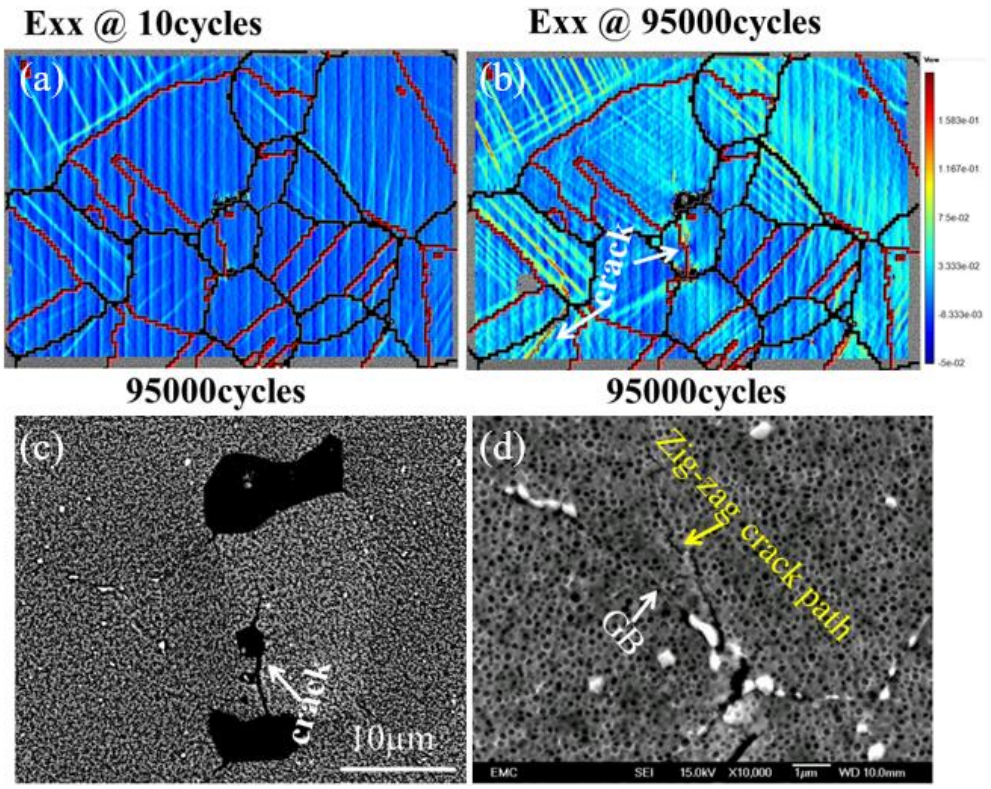

Figure 4.17: SEM-DIC analysis conducted by R.Jiang of AOI-2 of Figure 4.3 (a) strain localisation at 10 cycles and (b) at 95,000 cycles. (c) SEM image at 95,000 cycles showing micro cracking. (d) SEM image at 95000 cycles showing zig-zag crack path.

4.3.4 3D evaluation of internal microstructure and short fatigue crack by X-ray CT scan

X-ray CT scanning was conducted on the microtensile sample of the coarse γ′ variant after interrupted fatigue testing containing a short crack. Internal microstructure including the areas of air, material, pores and short fatigue crack can be discerned by a series of 2D raw images as shown in Figure 4.18. A series of raw images were examined by the plot profile in terms of the grey scale to conduct the segmentation process. It can be seen that each region of air, pores, crack and material exhibits different grey values, some differences are sufficient to allow easy segmentation while some show a

marginal difference in grey values, as seen in Figure 4.19. The volume threshold for the porosity distribution was employed based on the pixel size by a particle analyser via ImageJ software. Approximately 360,000 particles were analysed with a range of volume size from 1 to 5,154 pixels, as shown in Figure 4.20. The minimum volume size of pores was set to a 27 pixel^3 cube (3 pixel x 3 pixel x 3 pixel) and smaller volume sizes were considered as possible noise.

After the segmentation process, a 3D rendering was reconstructed by a series of 2D raw slices using VG studio and ImageJ software, as shown from Figure 4.21 to Figure 4.23. The crack morphology was manually segmented from a series of 2D slices, which describes the overall complicated geometry of the short crack with a dimension of approximate 140 µm x 100 µm. Porosity distribution inside the material is presented in Figure 4.23. It is observed that the volume fraction of pores accounts for around 0.011% in the scanned area, which is low. This can be ascribed to the P/M process of the alloy, which minimises the extent of porosity formation in the material. The 3D morphology of an early stage crack propagating about 100 µm inwards into the material is observed near one corner of the material along with the neighbouring pores, as shown in Figure 4.23. The short crack appears to be slanted at 45^o to the loading applied on the sample, indicating initiation has occurred along the slip band as also seen in the surface results of the fatigue tests on PBB samples (section 4.3.1).

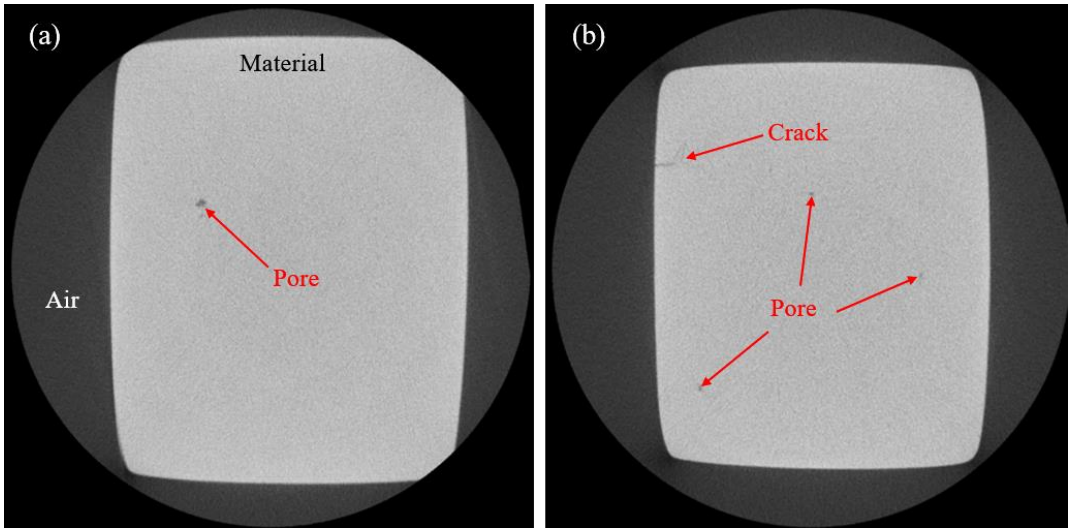

Figure 4.18: 2D image slices by X-ray CT scan indicating regions of pores, crack, material and air.

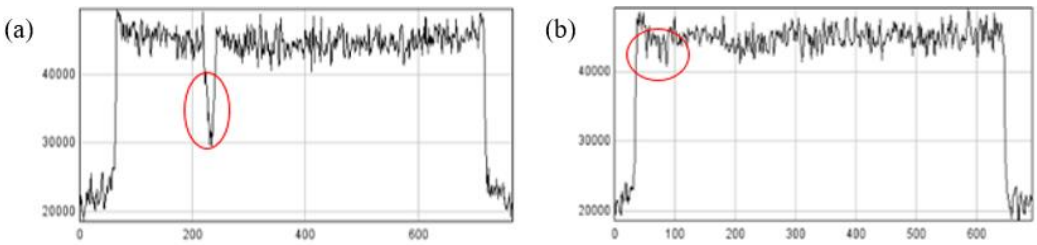

Figure 4.19: Plot profile (grey value vs distance (pixels)) of Figure 4.18 (a) and (b) respectively indicating the change in grey value associated with (a) pore (b) crack as marked with the red circles.

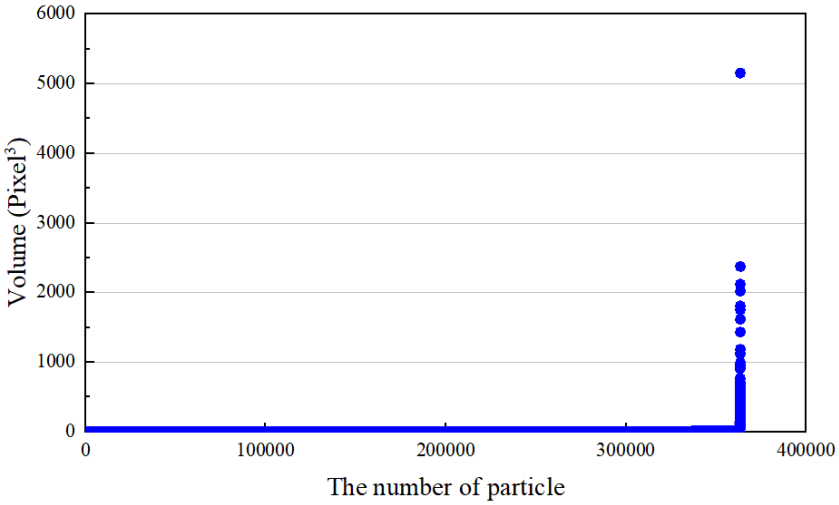

Figure 4.20: Quantitative data of voxel sizes in terms of allocated particles by the particle analyser.

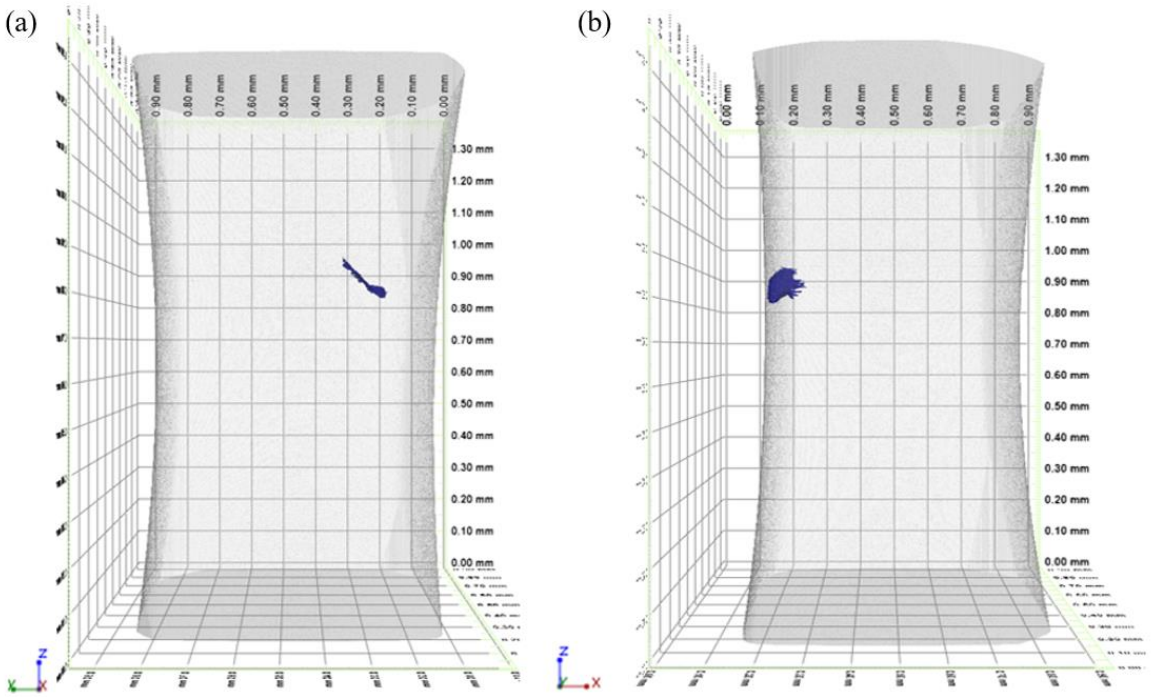

Figure 4.21: Different 3D views of the crack geometry in the dog-bone sample of the coarse γ′ variant (a) front view (b) side view.

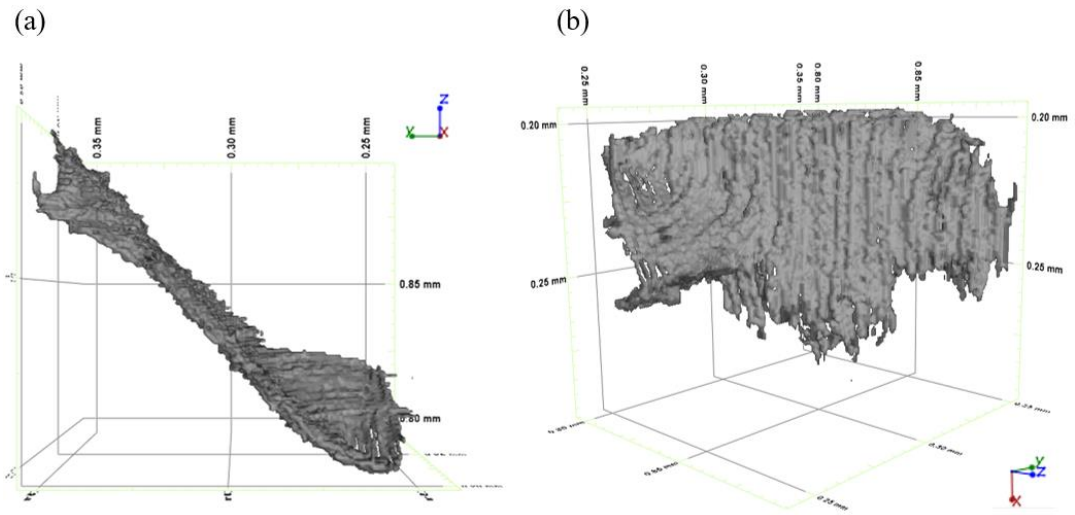

Figure 4.22: 3D image reconstruction of the short crack observed in the coarse γ′ variant with different perspective views.

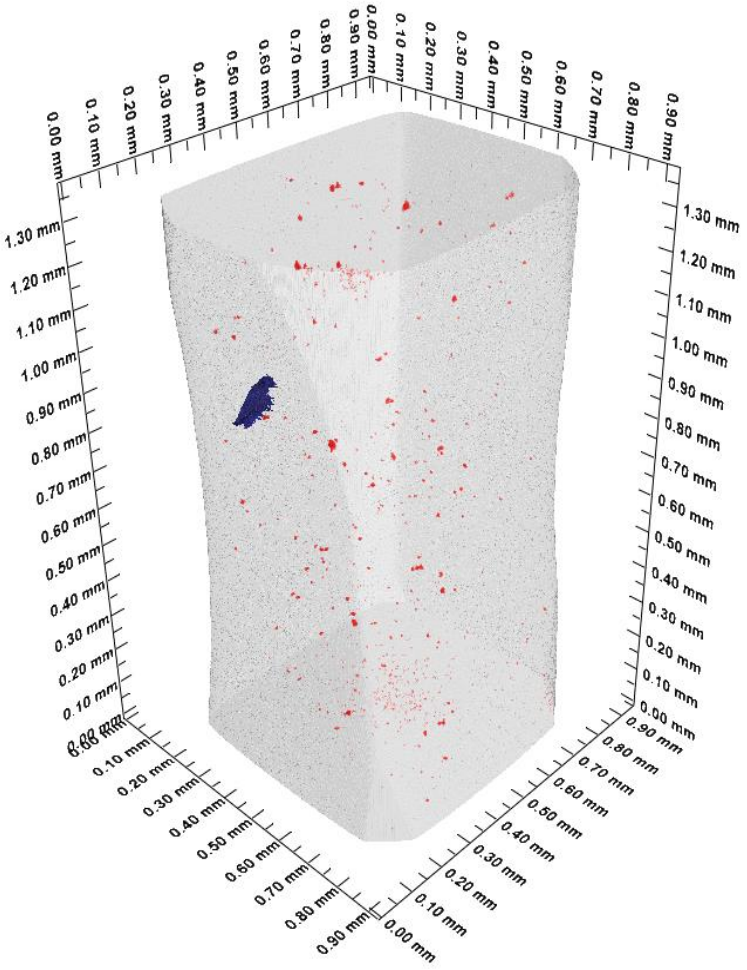

Figure 4.23: 3D reconstruction image including areas of pores, material and short crack observed in the coarse γ′ variant.

4.4 Discussion

4.4.1 Slip deformation behaviour (recap of prior EPSRC collaborative project results relevant to this PhD)

In Ni-based superalloys, the γ′ precipitates are considered to have a significant effect on the fatigue crack initiation and propagation behaviour, linked to different dislocation interactions during cyclic deformation and the resulting planarity of slip in the materials system. It is known that γ′ size distribution can give rise to different dislocation motions. As to whether cutting or looping of the γ′ precipitate occurs [4], smaller γ′ precipitates are easier to shear while larger γ′ precipitates are likely to exhibit looping. The γ′ cutting or looping contributes to planar or wavy slip behaviour respectively, which can affect both crack initiation and crack growth processes. Precipitate cutting tends to show more planar (heterogeneous) slip which leads to less resistance to crack initiation while Orowan looping is likely to exhibit less planar (homogeneous) slip which contributes to better crack initiation resistance. The critical precipitate size where the transition of dislocation motion between dislocation cutting and bowing occurs will therefore be associated with the different deformation behaviour of γ′ precipitates. H.T.Pang [9] estimated the critical precipitate size to be approximately 32 nm based on information for several Ni-base superalloys such as UDIMET 720Li and Inconel 718 from the literature. Precipitate cutting tends to be observed in precipitate sizes under the critical size while precipitate bowing occurs in precipitates above the critical size in Ni-based superalloys such as Waspaloy and Nimonic 90 [64,65]. It was noted that a γ′ particle size around 32 nm can induce both precipitate cutting and looping. It is notable that even our fine γ′ variant particle size is larger than this critical size.

As a part of collaborative EPSRC project, high resolution (HR)-DIC analysis on RR1000 with similar distribution of fine and coarse γ′ variants was carried out to investigate slip character by University of Manchester [165]. HR-DIC is a non-contact optical technique for measuring strain and displacement by tracking blocks of pixels and can show local strains and surface displacement with high resolution. Figure 4.24 indicates that both γ′ microstructures exhibit similar slip character of predominant planar slip at a low overall strain level (1 %). Nonetheless, the coarse γ′ variant is likely to exhibit relatively wider slip bands than the fine γ′ variant as seen in Figure 4.25. In a large area by stitching 800 images captured by HR-DIC (Figure 4.26), it appears that both γ′ variants represent both diffuse and well-defined slip characteristics at the same applied strain (note in this characterisation a higher strain level of 3 % was applied).

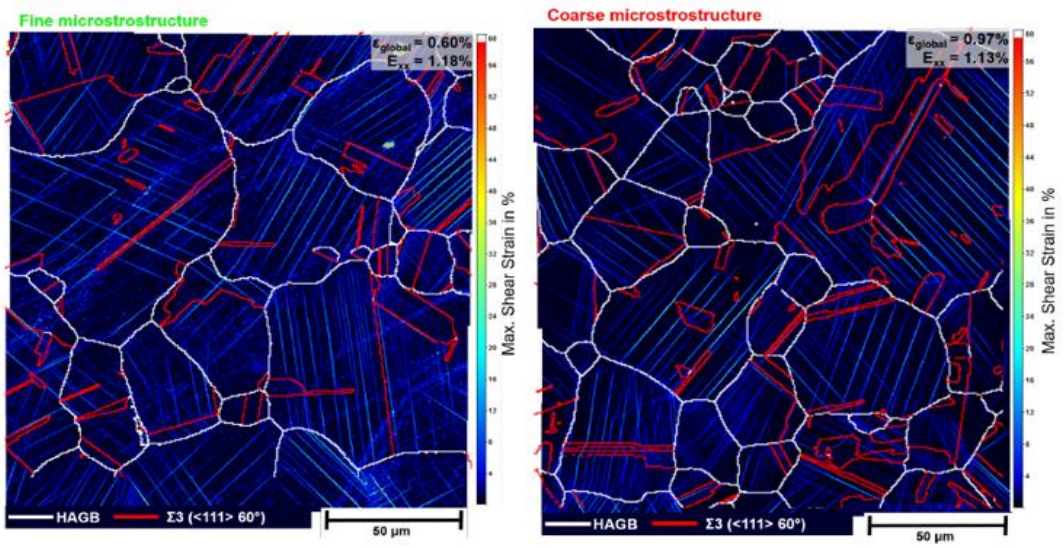

Figure 4.24: HR-DIC of RR1000 with fine and coarse γ′ structure at low strain (1 %) conducted by University of Manchester [165].

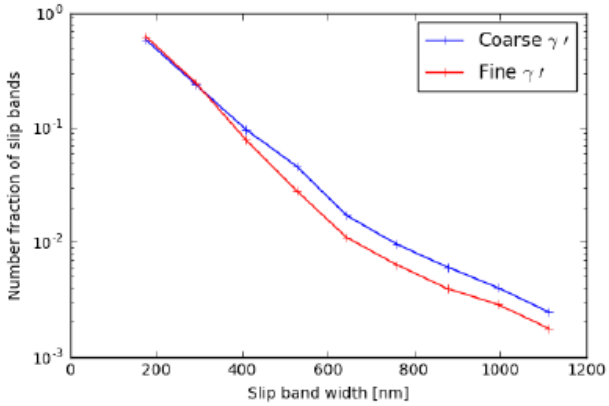

Figure 4.25: A graph of number fraction of slip bands vs slip band width, showing the coarse γ′ variant has relatively wider slip bands conducted by University of Manchester [165].

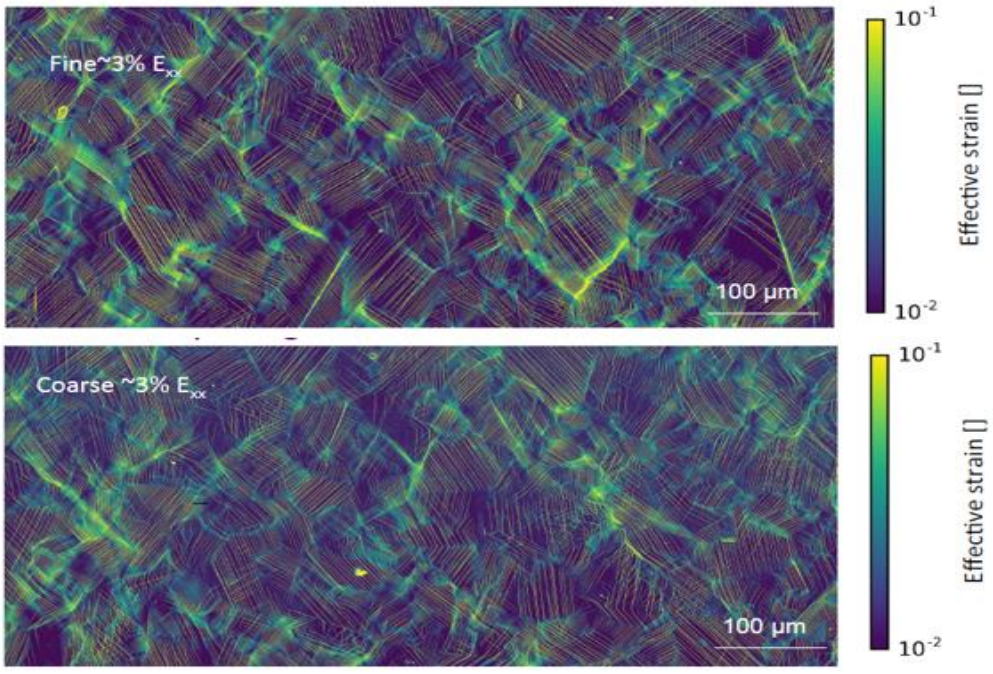

Figure 4.26: Extended map of both γ′ variants at 3 % ε_{xx} conducted by University of Manchester[165].

Electron Channelling Contrast Imaging (ECCI) is an imaging technique in the SEM based on electron channelling applying a backscatter electron detector and therefore shows deformation structures such as dislocation or stacking faults in-situ at high resolution. Figure 4.27 (a) and (b) of ECCI images carried out at University of Manchester show similar sharp slip band regions of both γ′ variants while it is seen that multiple parallel planes have slipped in the coarse γ′ variant. The ECCI analysis indicates that the slip lines consist of dislocations concentrated between the coarse γ′ particles and some dislocations have looped around the coarse γ′ particles as seen in Figure 4.27 (c) and (d). In the fine γ′ variant, both sharp slip bands and smaller line defects exist, which exhibits a different apparent defect structure compared to that seen in the coarse γ′ variant. Such defects appear to be stacking faults, linked to the precipitate shearing of the fine γ′ precipitate. It can be deduced that the larger γ′ precipitates (~230 nm) are likely to show more Orowan looping while the smaller γ′ precipitates (~75 nm) exhibit more pronounced cutting processes.

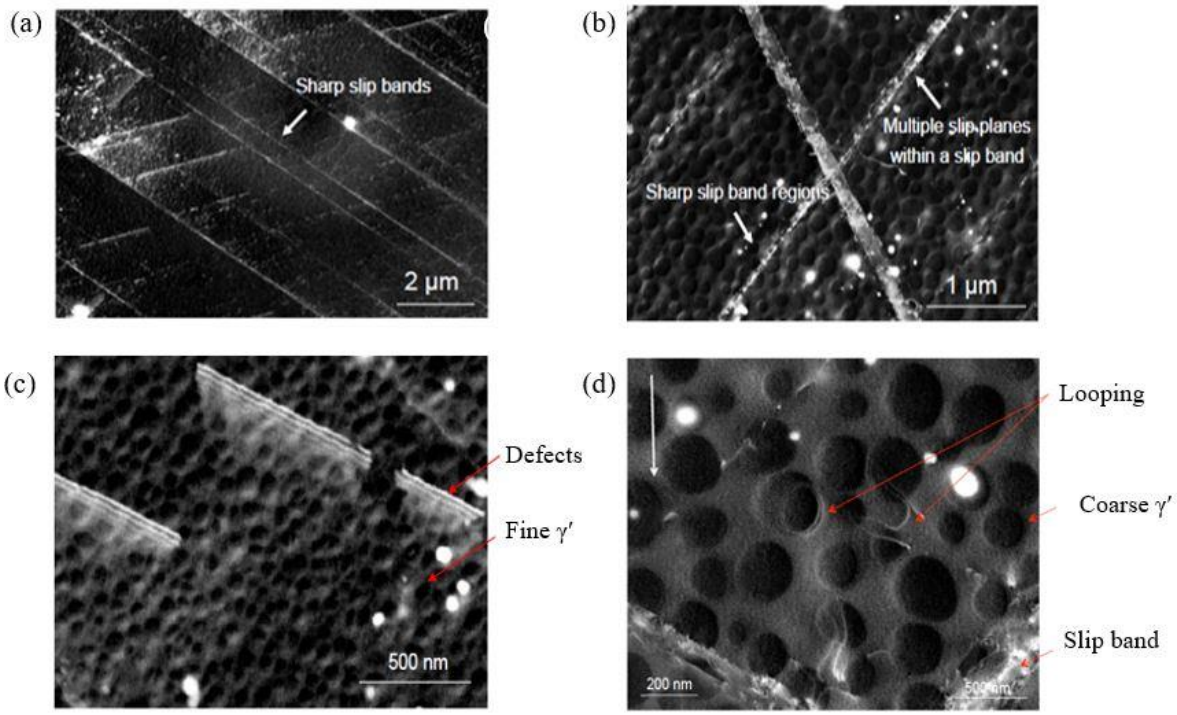

Figure 4.27: ECCI images showing deformation microstructure showing slip bands and dislocation (a) the fine γ′ variant (b) the coarse γ′ variant (c) the fine γ′ variant (d) the coarse γ′ variant done by University of Manchester [165].

4.4.2 Effect of the microstructural features on lifetime and fatigue behaviour

The effect of microstructure such as γ′ size distribution and grain boundary orientation on lifetime and fatigue behaviour at room temperature in RR1000 alloy has been investigated. It is observed that fatigue cracks in Ni-based superalloys generally initiate where stress concentration and strain

localisation occurs such as pores, slip bands, twin boundaries, precipitates and grain boundary [8,20,43,49,77,78]. In this study, fatigue cracks have initiated mostly from slip bands, twin boundaries and pores at the surface or sub-surface followed by crystallographic facet growth indicative of stage-I propagation in both γ' variants. Crystallographic faceting then becomes less marked as the crack propagates, followed by the transition to stage-II crack growth. Porosity is expected to produce protrusions and locally stress concentrations and strain localisation, promoting crack initiation along crystallographic slip planes.

In the work on RR1000 alloys exhibiting a similar average grain size to that seen in this study [30], the fine γ' variant is likely to exhibit more highly planar slip with intense slip bands and subsequent heterogeneous slip character, which can be linked to less crack initiation resistance. Both the number of cracks observed and the number of cycles until the first crack is observed can indicate the level of fatigue crack initiation resistance. Although scatter in both these measures is to be expected as they are both dependent on the local microstructure and defect distribution in small gauge region of the specimens. The interrupted tests at 90% yield stress indicated that the coarse γ' variant showed better crack initiation resistance as the first crack is seen later than in the fine γ' variant (in fact no crack initiation was seen even after 3M cycles). However, the lifetime of the coarse γ' variant at 90% yield stress is shorter in the uninterrupted test, which shows the high level of scatter in such tests associated with the variable influence of defects such as pore distribution and possibly large favourably oriented grains near the crack initiation sites. It is seen that fatigue lifetime of other Ni-based superalloys at 85% yield stress level in the dog-bone shape samples showed considerable scatter with varying lifetimes of 32255 - 152611 cycles [166]. Such scatter, which was also observed in our study (i.e. 320805 - 483731 cycles at 90% yield stress as seen in Table 4.4), can be ascribed to the microstructural (and defect) variation in the small gauge region of a sample tested in the laboratory in larger plain bend bar and microtensile samples. Crack initiation and short FCG behaviour is closely linked to the local microstructure (i.e. pore and carbide distribution and their local size and shape variation) as described in this study.

The lifetimes of both γ' variants at 110% yield stress are similar and seem to be more significantly linked to the number of cracks and the number of cycles until the first crack is observed. As seen in Figure 4.9, fewer crack initiations and later observation of the first crack in the fine γ'_1 test is associated with enhanced crack initiation resistance and consequently increased lifetime while more cracks were observed and earlier crack observation in the fine γ'_2 test is linked to inferior crack initiation resistance and a reduced lifetime. It should be noted that initiation life was very limited at this higher applied stress level and lifetime data and short fatigue crack behaviour typically do show a lot of scatter.

The fine γ' variant did exhibit relatively more planar slip, which is associated with higher slip reversibility and less intrinsic damage accumulation while the coarse γ' showed a somewhat lower degree of planar slip as represented by HR-DIC and ECCI analysis in section 4.4.1. FCG rate of the

cracks generally shows an increasing trend while fluctuations of FCG rate were seen, with scattered FCG rate observed in both fine and coarse γ' variants at relatively low Δ*K* levels. This scattered data indicates typical features of short crack behaviour at low Δ*K* level where crack growth is considerably influenced by local microstructures (e.g. grain boundaries, grain orientation and precipitates) [31,32]. The slightly accelerated FCG rate of the fine γ' variant in this study is ascribed to the earlier crack coalescence due to cracks forming earlier than in the coarse γ'. Therefore, the decreased lifetime of the fine γ' variant at higher stress levels is ascribed to earlier crack emergence promoting coalescence and enhanced FCG rate while the increased lifetime of the same alloy at lower stress levels is associated with fewer crack initiations which emerged later in the lifetime and therefore delayed crack coalescence events. It can be inferred that the case of slightly improved lifetime of the fine γ' variant is then related to less crack coalescence due to fewer crack initiation sites of fine γ'_1 than seen in the coarse γ' variant. Therefore, it is indicated that the number of crack initiation sites and subsequent crack coalescence events are important in controlling the fatigue lifetime at these stress levels. Further consideration of the effect of γ′ size along with other factors controlling crack initiation process such as defect distributions and sampling, as well as grain size distribution need to be considered as a potential area of future work.

4.4.3 Study of slip trace analysis and strain localisation in the coarse γ′ variant RR1000 alloy at room temperature

The effect of local microstructures (e.g. grain orientation and grain boundary) on crack initiation and short crack growth were investigated by EBSD analysis overlaid with SEM images containing the fatigue crack path, and the strain accumulation in the slip bands were measured by SEM-DIC. Strain developed under the fatigue loading is mainly localised in the slip bands. Slip band cracking in the coarse γ′ variant has initiated along a twin boundary with the highest Schmid factor of activated slip systems as seen in grain 7. It is known that the highest Schmid factor is related to the highest resolved shear stress activating the slip systems and thereby enhanced crack initiation processes [79]. However, as reported in other polycrystalline Ni-based superalloys, crack initiation or propagation process does not always occur with the highest Schmid factor [8]. It is believed that twin boundary can contribute to heterogeneous slip band formation at the matrix and twin, which can result in a high elastic incompatibility stress associated with the discontinuity of stress and displacement at the twin boundary. Slip bands concentrated adjacent to the twin boundary are closely related to a high strain localisation value and consequently an enhanced crack initiation process, which is commonly observed in other Ni-based superalloys [8,166].

Local microstructures predominantly influence primary slip system activation and early stage crack propagation processes. This is linked to the occurrence of a crystallographic zig-zag crack path during short crack propagation. Different orientations of grains accommodating the crack segments experience different Schmid factor related to the resolved shear stress acting on the slip system in terms of the applied tensile stress. Slip trace analysis (Table 4.6) conducted on the grains containing the crack segments indicates cracks are likely to propagate along the slip systems with the highest Schmid factor although some cases observed are not on the highest Schmid factor (possibly linked to the need for crack path contiguity), which is also seen in other polycrystalline Ni based superalloys [167]. It is interesting to note that a decelerated FCG rate after initiation is clearly induced by zig-zag crack path along a grain boundary and a large deflection when the crack propagated into a relatively large grain (Figure 4.15), which results in a clear shielding effect. The crack propagation along the grain boundary may also contribute to decelerated FCG rate due to the more continuous carbide formation on the coarse γ′ variant grain boundary providing a shielding effect.

4.4.4 3D evaluation of internal microstructure and fatigue crack

X-ray CT scanning of a microtensile sample has been carried out to examine the internal microstructure and sub-surface crack growth in RR1000 with coarse γ′ precipitates. The 3D morphology is reconstructed by a series of 2D raw slices. The 3D rendering image described in Figure 4.23 provides information on the pore distribution and 3D crack geometry propagating from the surface of the material slanted at 45^{o} to the loading applied, indicating the initiation occurred along the slip band. It is observed that some part of crack is discontinuous, which can be related to low resolution, manual segmentation process or the sub-surface pores. Pore population size and spatial distribution can contribute to the fatigue crack initiation process. Quantitative analysis of pore volumes shows a low volume fraction of 0.011 % in the scanned area of the coarse γ′ variant due to the advantages of the P/M manufacturing process. It is deduced that the fine γ′ variant will exhibit similar low volume fraction of pores resulting from the same manufacturing process. Although the X-ray scanning results here give limited information on the morphology of multiple short cracks and pore distribution, further investigation of the effects of pore distribution could be considered via finite element analysis of stress evolution [168]. In addition, the crack shape and evolution could be assessed by further scans after applying more loading cycles incrementally, and the evolving 3D morphology of the crack could be examined in terms of the evolving crack tip stress state and associated micromechanics to better understand the early stages of crack growth.

There is a potential resolution limitation of CT which makes it difficult to obtain the true morphology of very fine cracks, particularly near the crack tip where crack opening is small, and the results should be considered in light of this. In this study a submicron resolution of 0.9461 μm was used, which

detect crack openings from ~1 μm and this can be considered at relatively high resolution for a fatigue crack. The match stick sample with a gauge section (less than 0.9 mm x 0.9 mm) was employed in particular to reduce the effects of the high degree of X-ray attenuation found in Ni-based superalloys. Higher resolutions by synchrotron beam line experiments at suitable scan times can enhance the resolution of the crack morphology and is proposed as future work as described in Chapter 8.

4.5 Summary

The effects of microstructure on deformation and fatigue behaviour at room temperature in two γ′ variants of the RR1000 alloy were investigated in this study. Fatigue tests under three point bending with post analysis including a replication method, OM, SEM, EBSD and DIC were conducted. Limited preliminary X-ray CT on microtensile tests have also been assessed. The summary and following conclusions are:

1. Cracks have initiated mainly from slip bands, twin boundaries and pores at the surface or sub-surface followed by crystallographic facet growth in both γ′ variants. Slip trace analysis by EBSD mapping indicates that a twin boundary is a favourable factor in crack initiation with the primary slip system with a relatively high Schmid factor (high resolved shear stress). SEM-DIC analysis showed micro-cracking occurred along the slip band with high strain levels and showed more diffuse strain localisation around the pores, which also promotes crack initiation.
2. The short crack growth after initiation is likely to propagate along the slip system activated with the high Schmid factors in the neighbouring grains. It appears that a zig-zag crack path in the coarse γ′ variant can contribute to partial crack arrest and corresponding decelerated FCG rate due to the intrinsic shielding effect of the crack path.
3. Short FCG rates in both γ′ variants at the higher test stress level (110% yield stress) were scattered, showing typical short crack growth behaviour. Lifetime scatter is closely associated with (1) the number of crack initiation sites (linked to subsequent crack coalescence events, as well as indicating the propensity for crack initiation) and (2) the number of cycles until the first crack is found (also indicating initiation resistance), both of which are important in controlling the fatigue lifetime. This gives rise to the consequently scattered fatigue lifetimes observed in this alloy. A slightly inferior short FCG resistance of the fine γ′ variant is probably related to the frequent crack coalescence events as well as the observed relatively more planar and heterogeneous slip character compared to the coarse γ′ variant.

4. The effect of γ′ size appears to be less important in controlling fatigue lifetimes in these tests, via the classically expected effect of more or less planar slip character affecting either slip band initiation resistance or crack propagation modes. Instead, lifetime is more strongly affected (in these tests) by the number of crack initiation sites (partly linked to initiation resistance) which seems more linked to defect distributions or grain orientation distributions than γ′ size alone. The role of multi-site coalescence in determining lifetime at high stress levels seems to predominate the behaviour seen.
5. 3D evaluation by X-ray CT scan can allow a better understanding of internal microstructure and complex crack morphology. The P/M route used in making these alloys resulted in a low volume fraction of pore distribution in these RR1000 alloy variants. A short fatigue crack propagated from the surface along a slip band slanted at 45°. Further CT scans on the material after more loading cycles offer promise to examine 3D evolution and the effect of pore distributions on further crack initiation processes.

Chapter 5 Fatigue crack initiation behaviour and lifetime at elevated temperature

5.1 Introduction

Chapter 4 has focused on the effect of microstructure on fatigue crack initiation, short FCG mechanisms and lifetime at room temperature where oxidation and creep damages are not taken into account. It is seen that the fatigue mechanisms at room temperature are primarily linked to the synergistic impacts of slip character, grain orientation, the resultant number of crack initiation and resultant crack coalescence events. Primarily, the RR1000 turbine disc alloy is designed to possess excellent mechanical and environmental damage tolerance such as cyclic loading, fatigue, creep and oxidation damages during service in aggressive environments. In such service environments, the microstructural influences now interact with environmental damage as well as slip processes. It is known that oxygen-related damage (i.e. SAGBO [3,113,138–142] and dynamic embrittlement mechanisms [143–146]) result in intergranular cracking at grain boundaries. Moreover, this becomes more pronounced with a continuous precipitate formation at grain boundaries, which gives rise to weakening of overall grain boundary properties [106]. In this chapter, fatigue crack initiation behaviour and lifetime of the alloy at elevated temperatures in air are assessed. In order to understand the effects of oxidising environment on the fatigue mechanism, a trapezoidal waveform loading with a dwell time is introduced at a temperature of 650 ^{o}C. Fatigue tests were carried out under three point bending and trapezoidal waveform loading on PBB samples of both γ′ variants. One fatigue test on a PBB sample of the coarse γ′ variant at 704 ^{o}C was previously carried out by R.Jiang and these results are also discussed and compared to the other testing in the following sections. This chapter will compare the fatigue mechanisms observed at room temperature (detailed in Chapter 4) and also provide a fundamental assessment of fatigue crack initiation mechanisms to connect with the long FCG behaviour at elevated temperature (Chapter 6) in these RR1000 alloy variants.

5.2 Experimental methodology

Fatigue testing at high temperatures and characterisation

A test matrix of the fatigue tests carried out on the RR1000 alloys is presented in Table 5.1. Fatigue tests on both γ′ variants were conducted to examine the effect of these microstructure variations on fatigue crack initiation and lifetime at 650 ºC. The specimen dimension and sample preparation methodology are identical to static isothermal oxidation testing and short FCG tests as described in section 3.3.2 and 4.2.1. In addition, the testing machine and setup are as described in the static isothermal oxidation testing except for the cyclic loading applied as seen in Figure 3.2.

	Fine γ′ variant	Coarse γ′ variant
Uninterrupted	√	√
Interrupted	√	√

Table 5.1: A test matrix of fatigue testing under 90s dwell time at 650 ºC on RR1000 alloys.

Figure 5.1 illustrates a trapezoidal waveform loading adopted in this study in the form of 1-X-1-1, which denotes a 1s ramp from minimum load to maximum load, 'X's dwell time at peak load, a 1s ramp returning back to minimum load and a 1s dwell at minimum load, respectively. In this study, 90s dwell time is introduced at peak load and this loading is referred to 1-'90'-1-1. Fatigue tests were run until the sample failed and then the fracture surface was examined and fatigue crack initiation behaviour assessed (referred to as uninterrupted tests). Some tests were interrupted at certain increments of lifetime to capture and assess crack initiation and short crack propagation stages (interrupted tests). The methodology of the fractography analysis and post-test characterisation were as described in material characterisation (section 3.3) and short fatigue crack test (section 4.2) using OM, JSM 7200F Field emission SEM and Oxford Aztec EDX.

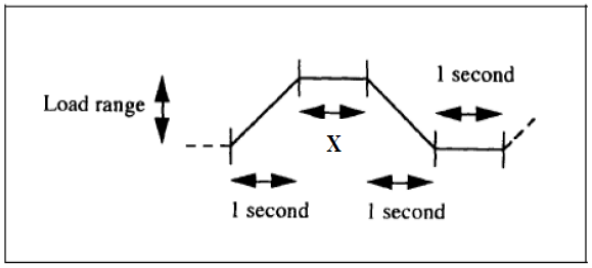

Figure 5.1: A trapezoidal waveform loading of 1s-'X's-1s-1s.

5.3 Results

5.3.1 Uninterrupted tests and fractography

	Fine γ′ variant	Coarse γ′ variant
Lifetime (cycle)	912	982

Table 5.2: Fatigue lifetime of uninterrupted tests at 110% yield stress at 650 ºC.

The lifetimes of uninterrupted tests under a 1-90-1-1 loading at 110% yield stress at 650 ºC on both fine and coarse γ′ variants are represented in Table 5.2. The lifetimes of both γ′ variants showed a LCF lifetime of only around 1,000 cycles compared to the much higher lifetimes (around 2 order of magnitudes) of ~150,000 cycles at high frequency loading and room temperature as seen in Chapter 4. This can be ascribed to significant oxygen-related damage due to the introduction of a dwell time and resultant more diffusion time per cycle at elevated temperature. The lifetime of both γ′ variants are similar although the coarse γ′ variant was expected to have a lower lifetime due to the grain boundary features which had a more continuous carbide formation. This indicates that the crack path around the crack initiation regions of the fine γ′ variant is somewhat angled while that of the coarse γ′ variant seems more perpendicular to the applied tensile axis Figure 5.2 (a) and (b). It also appears that fracture surfaces of both γ′ variants are asymmetric, the fine γ′ variant shows more asymmetric features to some extent as seen in Figure 5.2 (c) and (d). The slightly lower lifetime of the fine γ′ variant may be associated with such asymmetric features (the major crack initiation and a big ratchet mark were slightly more adjacent to an edge region) as seen in the Figure 5.2 (c), which indicates the sample being more compliant and a faster FCG rate (shorter lifetime).

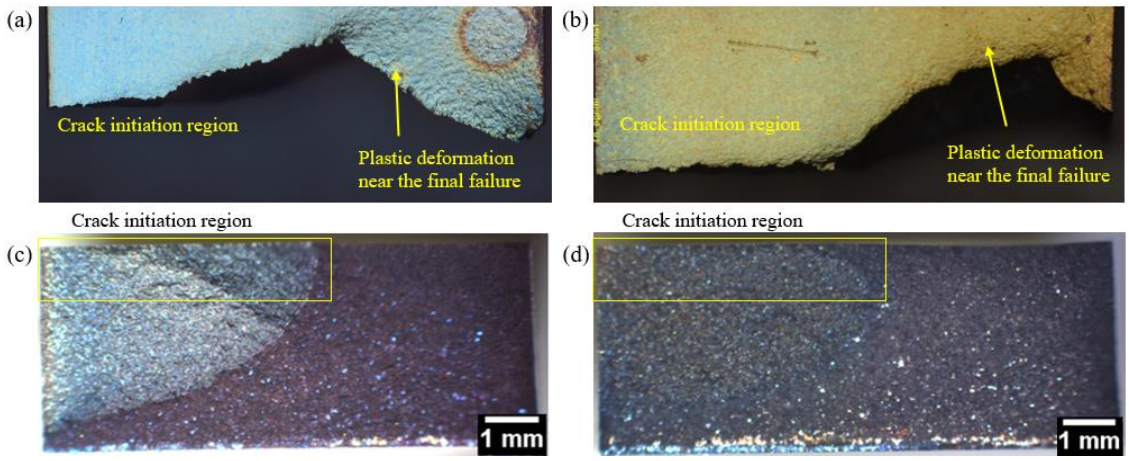

Figure 5.2: OM images at 110% yield stress at 650 ºC showing top surfaces of (a) the fine γ′ variant (b) the coarse γ′ variant; fracture surfaces of (c) the fine γ′ variant (d) the coarse γ′ variant.

Top surfaces of the samples along the primary crack path indicating clear intergranular fracture features of both γ′ variants are seen at higher magnification by OM and SEM in Figure 5.3 and Figure 5.4, respectively. It is interesting to note that grain distribution and slip bands are clearly revealed by the oxidation influences on the surface without any etching process. The significant amount of intergranular cracks and secondary cracks formed along the grain boundaries in both γ′ variants are clearly discerned, which is a distinctive feature of the high temperature fatigue testing. Such high numbers of fatigue cracks give rise to frequent crack coalescence events and consequently accelerated FCG rates, which results in the considerably reduced lifetimes, From the top surface examination, both γ′ variants show a tortuous crack path with a clear intergranular fracture mode although significant plastic deformation occurred near the final failure region. It also appears that many slip bands can be seen particularly near the final failure region, resulting from the high plastic deformation as the crack grew rapidly towards final failure.

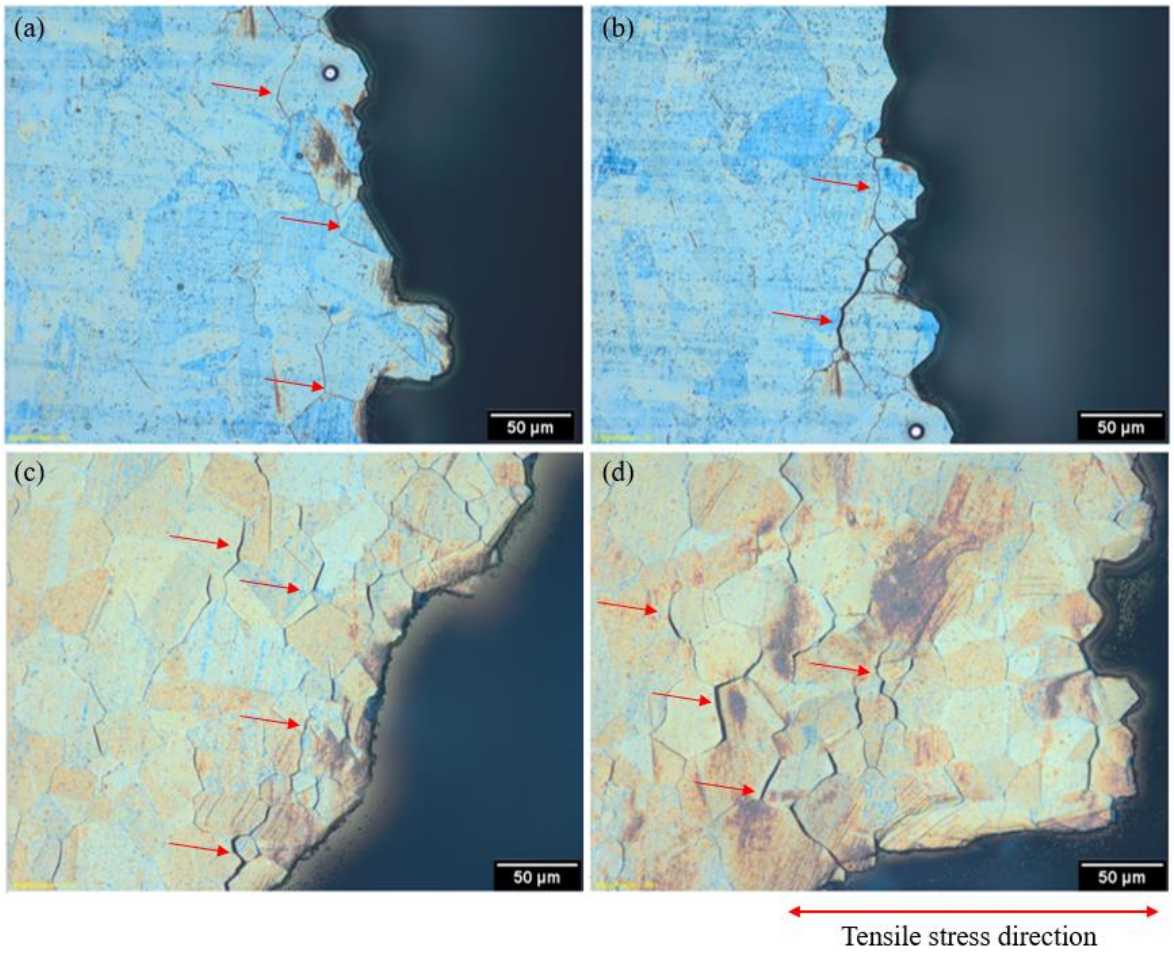

Figure 5.3: OM images of top surface representing plentiful intergranular cracks (marked by arrows) along the main crack path at 110 % yield stress at 650 °C (a) and (b) the fine γ′ variant; (c) and (d) the coarse γ′ variant.

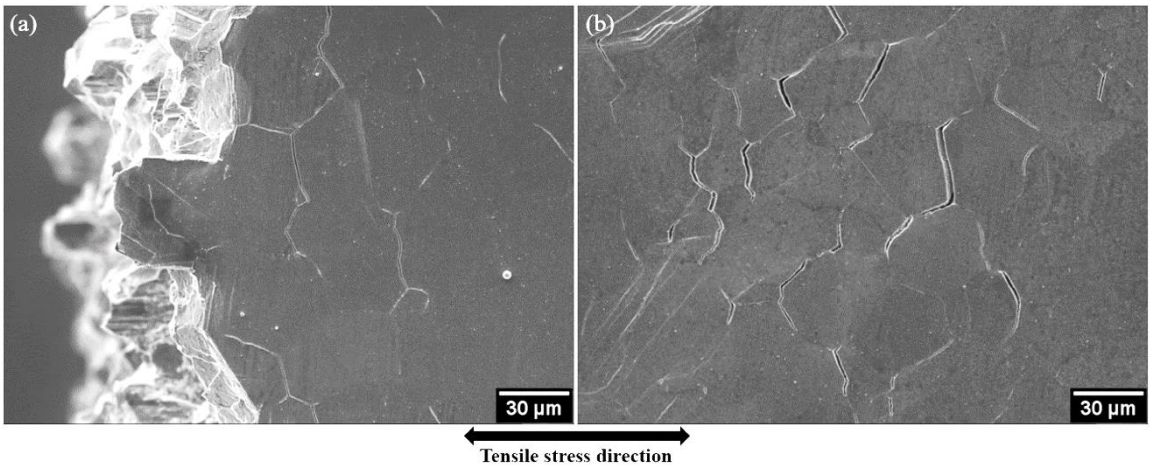

Figure 5.4: SEM images of top surfaces representing plentiful cracks and slip band formation along the main crack path at 110 % yield stress at 650 ^{o}C (a) the fine γ′ variant (b) the coarse γ′ variant.

Figure 5.5 shows fracture surfaces of the fine γ′ variant examined by SEM images based on OM observations. Figure 5.5 (a) and (b) represents the overall fracture surfaces including crack initiation sites, propagation and final failure. At higher magnification, the evidence of multiple crack initiations at surfaces is seen in Figure 5.5 (c), which is validated by a clear ratchet mark (and multiple intergranular crack initiations observed in interrupted tests described in the following section 5.3.2). It is difficult to identify where the first crack has initiated due to the large amount of intergranular crack initiation. It is seen that the intergranular fracture characteristics are dominant when the cracks propagate at 650 ^{o}C with a long dwell while slip band cracking and/or cracks initiating from pores is more dominant at room temperature. An increase in these intergranular failure features is related to the effects of temperature and oxidation damage on grain boundaries assisted by the introduction of a dwell time (accordingly longer diffusion times in each loading cycle) at elevated temperature. As seen in Figure 5.5 (d) and (f), the significant extent of intergranular fracture features and secondary cracks along the grain boundaries are clearly presented.

Such features are also discovered on the top surfaces by SEI and BEI images as seen in Figure 5.6. It appears that thick and bulged grain boundary oxides can be discerned ahead of secondary cracks and ahead of grain boundary cracking. This can be also seen clearly in BEI images. It can be inferred that such oxides are Co-rich oxides as commonly seen in other turbine disc alloys containing a similar Co content to the RR1000 alloy [169]. It is notable that some oxide particles still remain along the crack path as shown in Figure 5.6 (a)-(d). This indicates that grain boundary oxidation is associated with the intergranular cracking. It is also interesting to note that grain boundary cracking propagated through carbides formed at grain boundaries and some remaining particles are seen along the crack path (Figure 5.6 (e)). Some extent of slip bands along the primary crack path are observed near the final failure region due to significant plastic deformation as the crack propagates fast towards final failure as seen in Figure 5.6 (f).

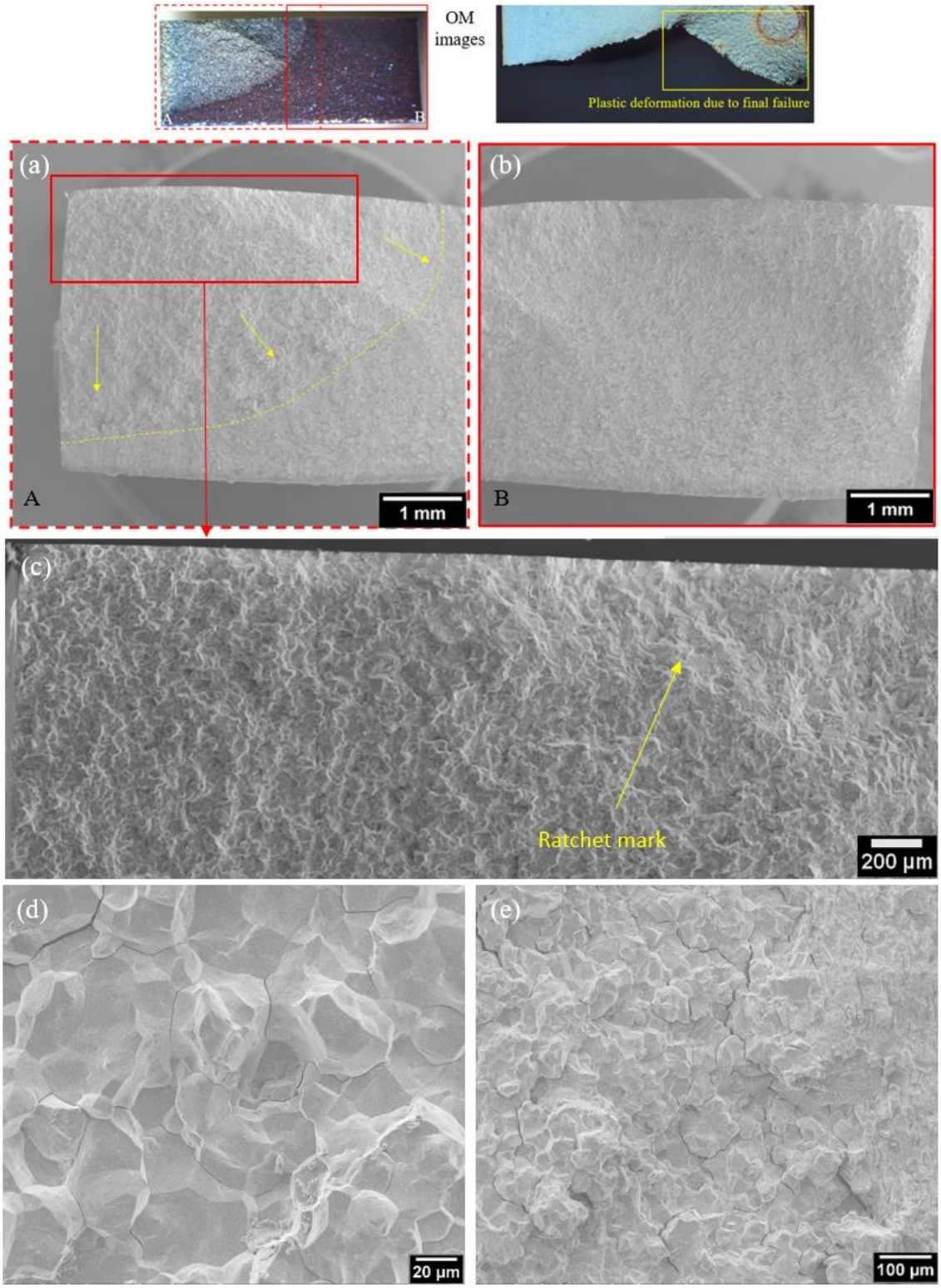

Figure 5.5: Fracture surfaces examined by SEM of the fine γ′ variant (a) region A representing the crack initiation region and intergranular crack growth (b) region B showing the final failure region (c) near the crack initiation sites at higher magnification (d) intergranular FCG (e) extensive secondary cracks near the final failure region.

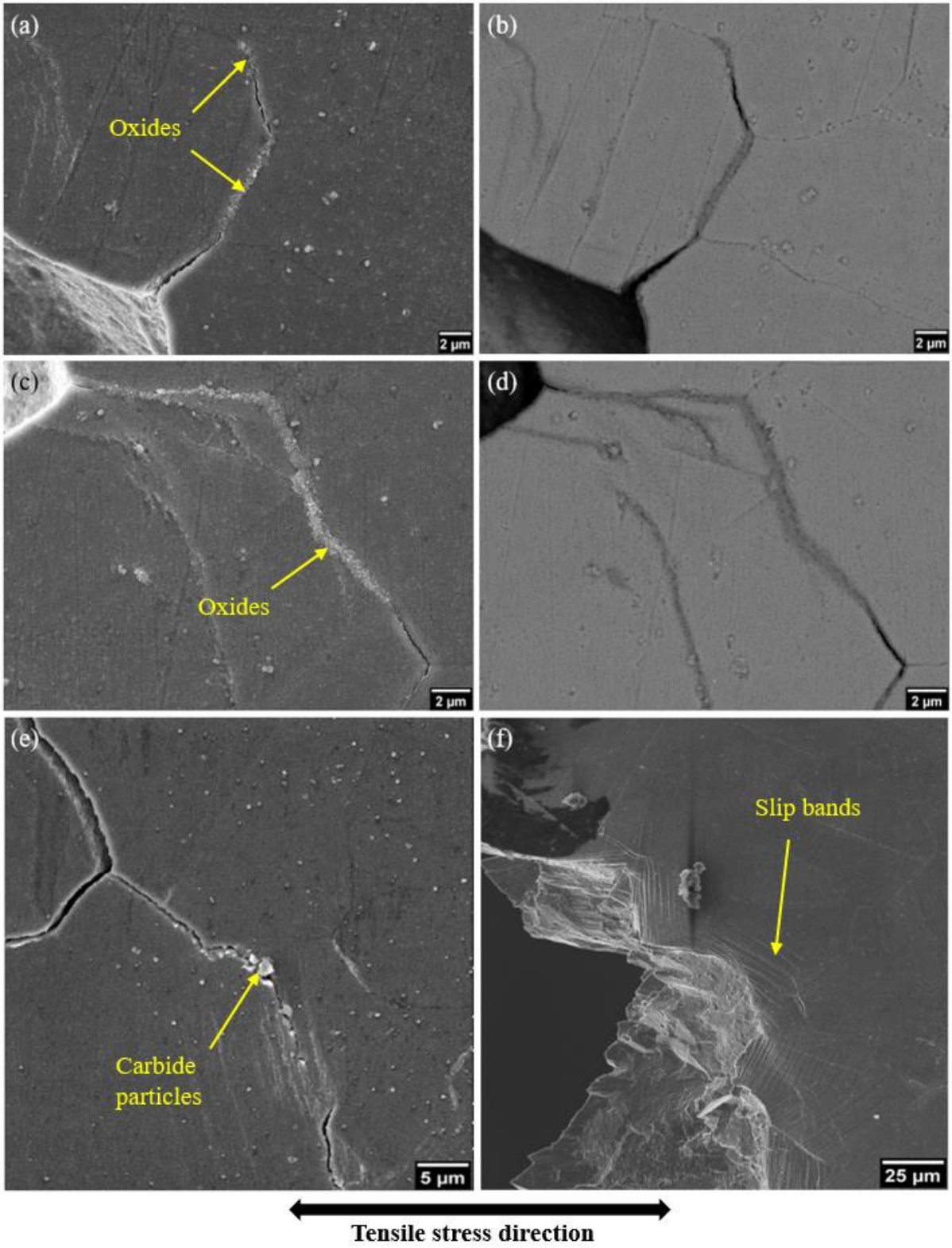

Figure 5.6: SEI images (a) and (b); BEI images (c) and (d) of the fine γ′ variant respectively showing intergranular cracking with bulged oxides at grain boundaries; (e) remaining carbides and oxide particles at grain boundary cracking; (f) slip band formation near the final failure point.

In the coarse γ′ variant, fracture surfaces generally exhibit similar fractography features as the fine γ′ variant. Figure 5.7 (c) shows a multiple crack initiation feature with ratchet marks, which is also validated by the interrupted tests which evidenced a number of intergranular crack initiations. It is worth noting that extensive secondary cracking along the grain boundaries and a detachment of a cluster of grains can be observed on the fracture surface as seen in Figure 5.7 (d), which is associated with an intergranular fracture mode. As marked characteristics of the coarse γ′ variant, particles of carbides at the grain boundary and along the secondary crack path are found in Figure 5.7 (e), which can weaken the grain boundary properties and promote crack initiation at the interface between grain boundary and carbides under oxidising environment.

Top surface examination by SEI and BEI images is also characterised by distinctive intergranular fracture features as presented in Figure 5.8 (a)-(d). It appears that intact oxides are continuously formed along the grain boundary and remaining oxides on the secondary crack path are seen as well. It can be inferred that such intact oxides are formed before crack initiation process and these oxides forming and then cracking contributes to crack initiation. This behaviour is more clearly discerned in the interrupted test in the following section (Figure 5.14 and Figure 5.15). The remaining particles of carbides are also found along the crack path as seen in Figure 5.8 (e). Again extensive slip bands can be discerned near the final failure region due to severe plastic deformation as well as the detachment of a cluster of grains due to significant grain boundary cracking in Figure 5.8 (f). From the top surface assessment, it is interesting to note that the cracks tend to propagate along the grain boundaries in the normal direction to the tensile axis applied in both γ′ variants. The bulged oxides are also apt to be formed in same direction, which may indicate that oxidation process is significantly assisted by the loading applied.

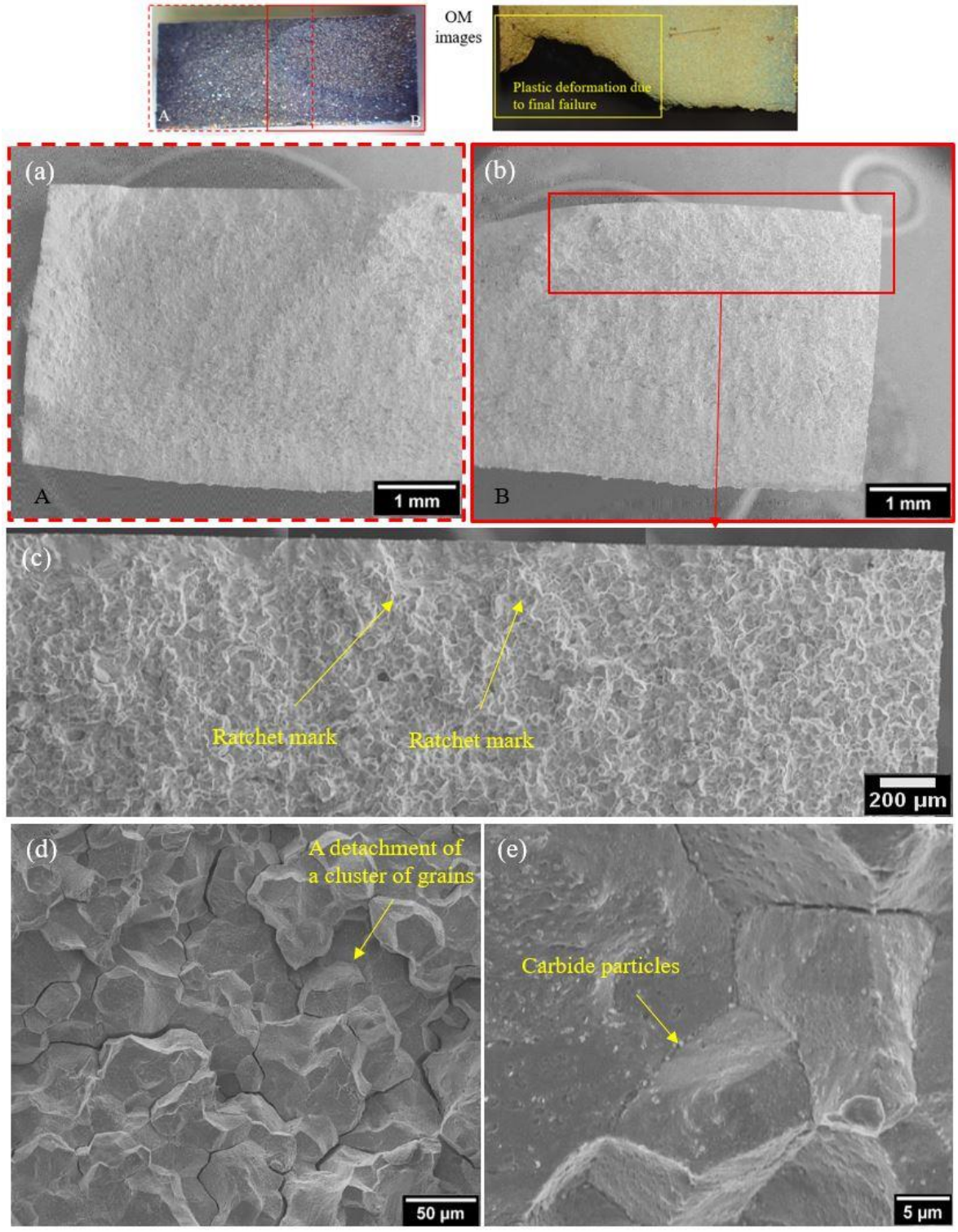

Figure 5.7: Fracture surfaces examined by SEM of the coarse γ′ variant (a) region A indicating the crack initiation region and intergranular crack growth (b) region B showing final failure region (c) near the crack initiation sites at higher magnification (d) significant secondary cracks along the grain boundaries near the final failure region (e) intergranular cracking with some remaining particles at grain boundaries.

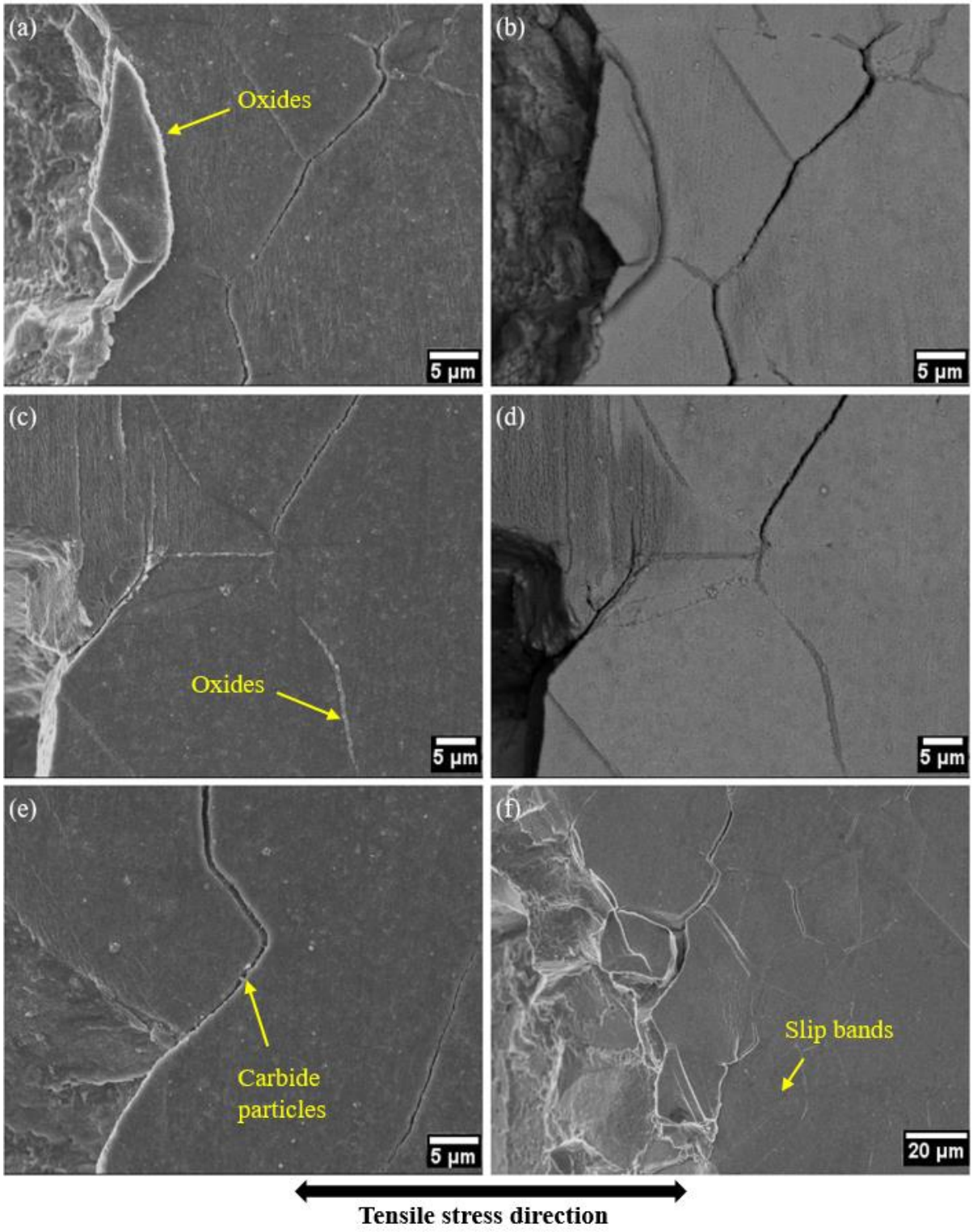

Figure 5.8: SEI images (a) and (b); BEI images (c) and (d) of the coarse γ′ variant respectively showing intergranular cracking with bulged oxides at grain boundaries; (e) some remaining carbides and oxide particles at grain boundary cracking; (f) a detachment of a cluster of grains and some slip band formation near the final failure.

EDX analysis on the bulged oxides which formed along the grain boundaries inclined normal to the applied tensile stress direction was carried out as shown in Figure 5.9 and Figure 5.10. Concentration variation of Ni, Co, Cr, Al, Cr, O is presented based on the content (wt.%) across the grain boundary decorated by oxides. Enrichment in Co and O can be discerned adjacent to the grain boundary along with some content of Cr while the Ni level shows a trend of depletion at the grain boundary. This indicates that the particular bulged oxides at grain boundaries are formed by a Co-rich complex in this alloy under these testing conditions.

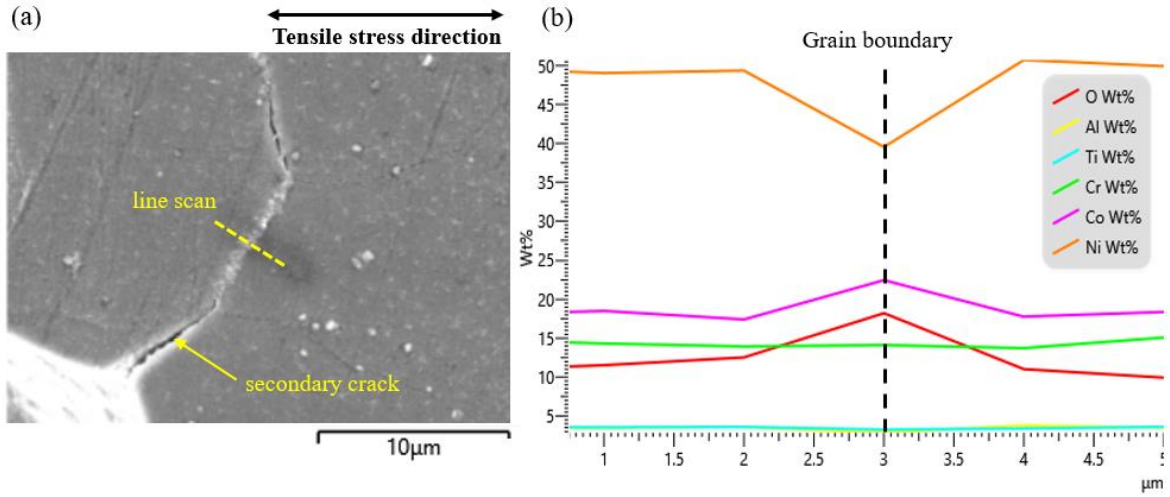

Figure 5.9: EDX analysis of the fine γ′ variant (a) SEM image indicating the line scan across the bulged oxide region by a dashed yellow line (b) compositional profile of EDX line scan showing Co-rich oxides at the grain boundary.

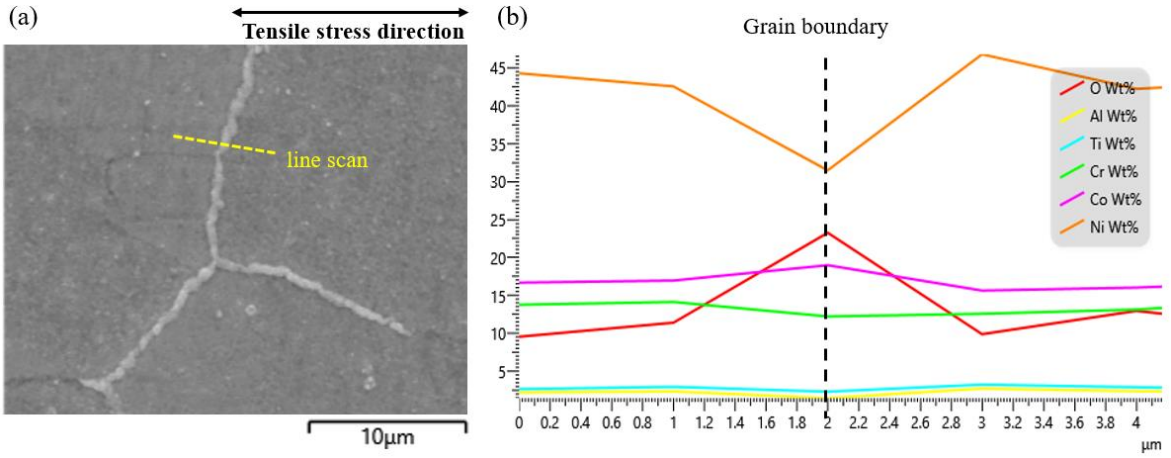

Figure 5.10: EDX analysis of the coarse γ′ variant (a) SEM image indicating the line scan across the bulged oxide region by a dashed yellow line (b) compositional profile of EDX line scan showing Co-rich oxides at the grain boundary.

R.Jiang also conducted a three point bending fatigue testing on the coarse γ′ variant of RR1000 alloys with same dimension of this study at 704°C and a high frequency of 20 Hz. Fractography analysis showed a mixture of transgranular and intergranular propagation modes as seen in Figure 5.11 (a), which is linked to the high loading frequency and consequent insufficient diffusion time although the testing temperature is higher than 650 °C. However, it is still observed that an intergranular crack initiation can be discerned associated with grain boundary oxides as seen in Figure 5.11 (b). It is also seen the oxides are formed along grain boundaries (Figure 5.11 (c)), which can be related to the mixed fracture mode seen under the testing condition provided. Such oxides are likely to be formed normal to the tensile loading applied, indicating that oxide formation can be assisted by the stress/strain applied.

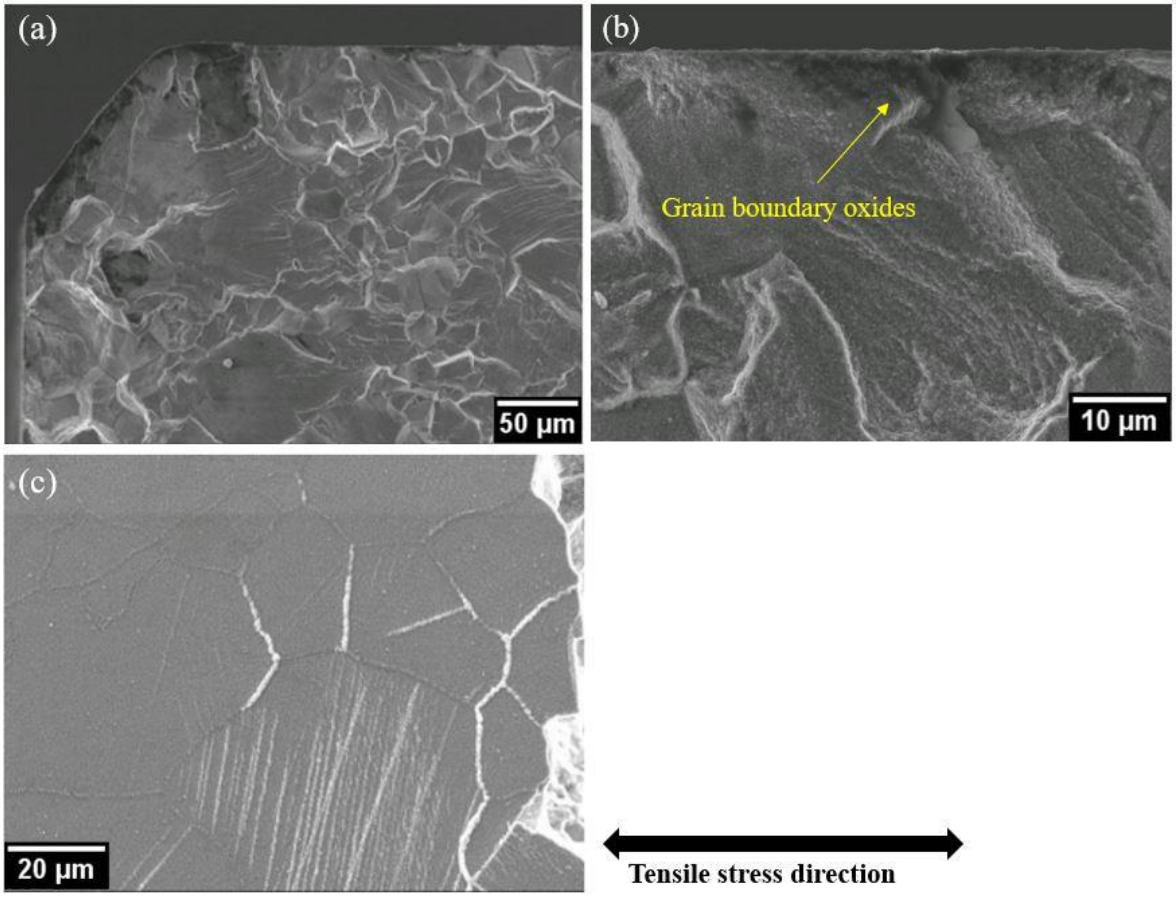

Figure 5.11: SEM images of the coarse γ′ variant at 704 °C and 20 Hz assessed by R.Jiang (a) a mixture of transgranular and intergranular features (b) grain boundary oxides near the surface (c) bulged oxides along the grain boundaries and slip band formation on the top surface.

5.3.2 Interrupted tests

Some of the RR1000 samples were tested at 110 % yield stress under a 1-90-1-1 loading cycle but then interrupted after 250 cycles, which is around a quarter of the expected fatigue lifetime obtained from uninterrupted tests. In the fine γ′ variant, it is observed that only one crack has initiated from

the edge after 250 cycles as seen in Figure 5.12 (a). Afterwards, a further 200 cycles were applied in the fine γ′ variant and crack initiations from other areas were seen at 450 cycles. On the other hand, in the coarse γ′ variant, several cracks at grain boundaries were seen after the first interruption of 250 cycles as seen in Figure 5.12 (b). Applied loading cycles are summarised:

- Fine γ′ variant: 250 cycle – stopped - further 200 cycles (450 cycles in total) - stopped
- Coarse γ′ variant: 250 cycle – stopped

The samples were assessed at higher magnification by SEM. In the fine γ′ variant, it is interesting to note that the crack has initiated from the edge and propagated following a somewhat tortuous crack path along with secondary cracks (Figure 5.13). It is observed that the crack propagated through a carbide formed at grain boundary. At 450 cycles (after further 200 cycles), the crack has propagated more with a high extent of tortuosity and secondary crack formation as shown in Figure 5.14 (a) and (b). Moreover, additional crack initiations at grain boundaries along with oxides formed can be discerned in Figure 5.14 (c) and (d).

In the coarse γ′ variant after 250 cycles applied, several cracks have initiated at grain boundaries along with a continuous oxide formation as well as a crack near the edge. In Figure 5.15 (b), it is noteworthy that one crack has initiated at the interface between the precipitate and grain boundary where stress concentration occurs, which commonly leads to crack initiation in Ni-based superalloys. Grain boundaries of the coarse γ′ variant are heavily described by oxide and carbide formation, which can promote the crack initiation and subsequent propagation. This can be attributed to the more continuous carbide formation along the grain boundaries in the coarse γ′ variant assisted by oxidation damage under 90s dwell time at elevated temperatures.

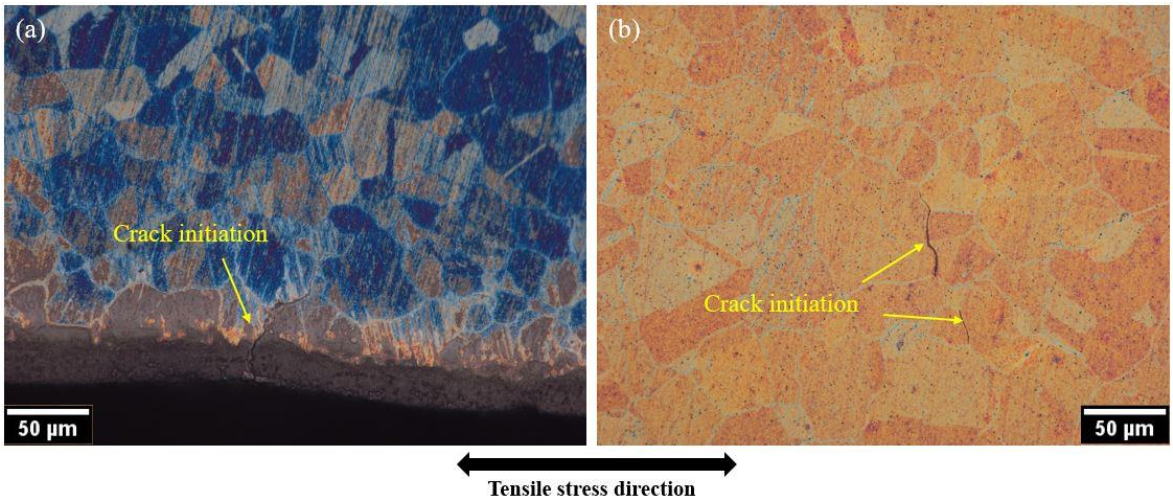

Figure 5.12: OM images of top surfaces at first 250 cycles (a) a crack initiated from the edge interrupted at 250 cycles of the fine γ′ variant (b) cracks at grain boundaries of the coarse γ′ variant.

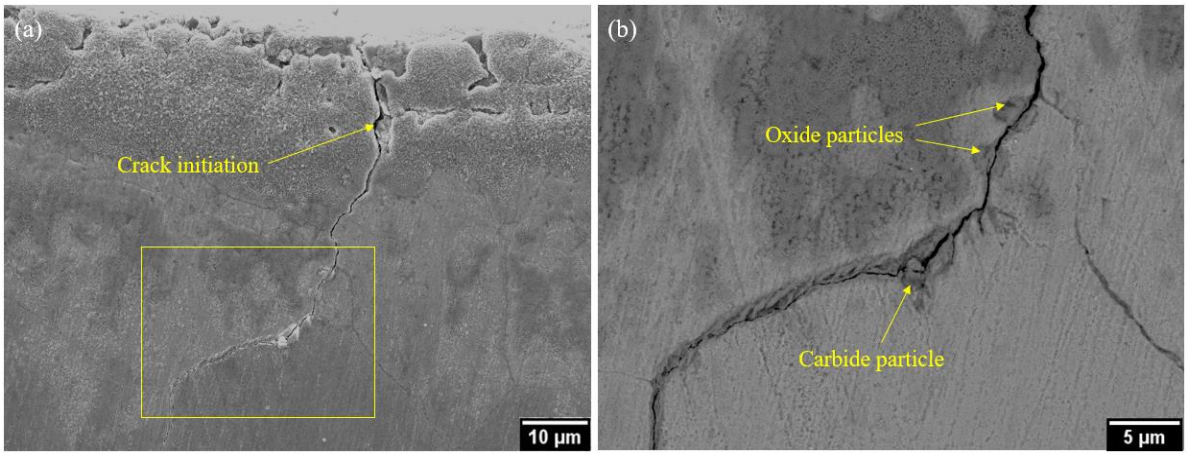

Figure 5.13: (a) SEM images showing the crack initiated from the edge of the fine γ′ variant interrupted at 250 cycles (b) BEI image at higher magnification of short crack path through precipitates of the marked area of image (a).

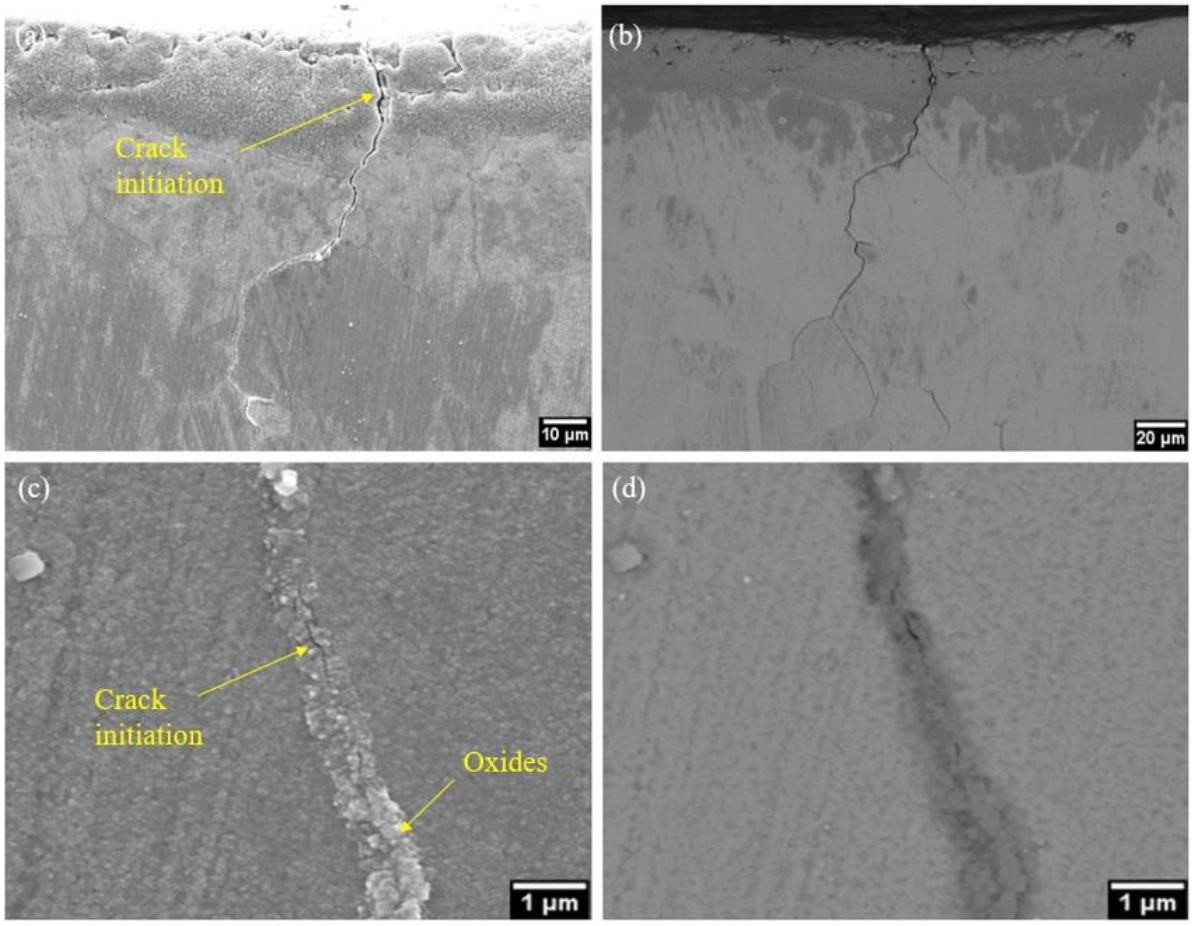

Figure 5.14: (a) SEM images showing the crack initiated from the edge of the fine γ′ variant interrupted at 450 cycles (b) BEI image at higher magnification of short crack path of image (a); (c) SEM image of crack initiation along with oxides formed at grain boundary (d) BEI image of (c) image.

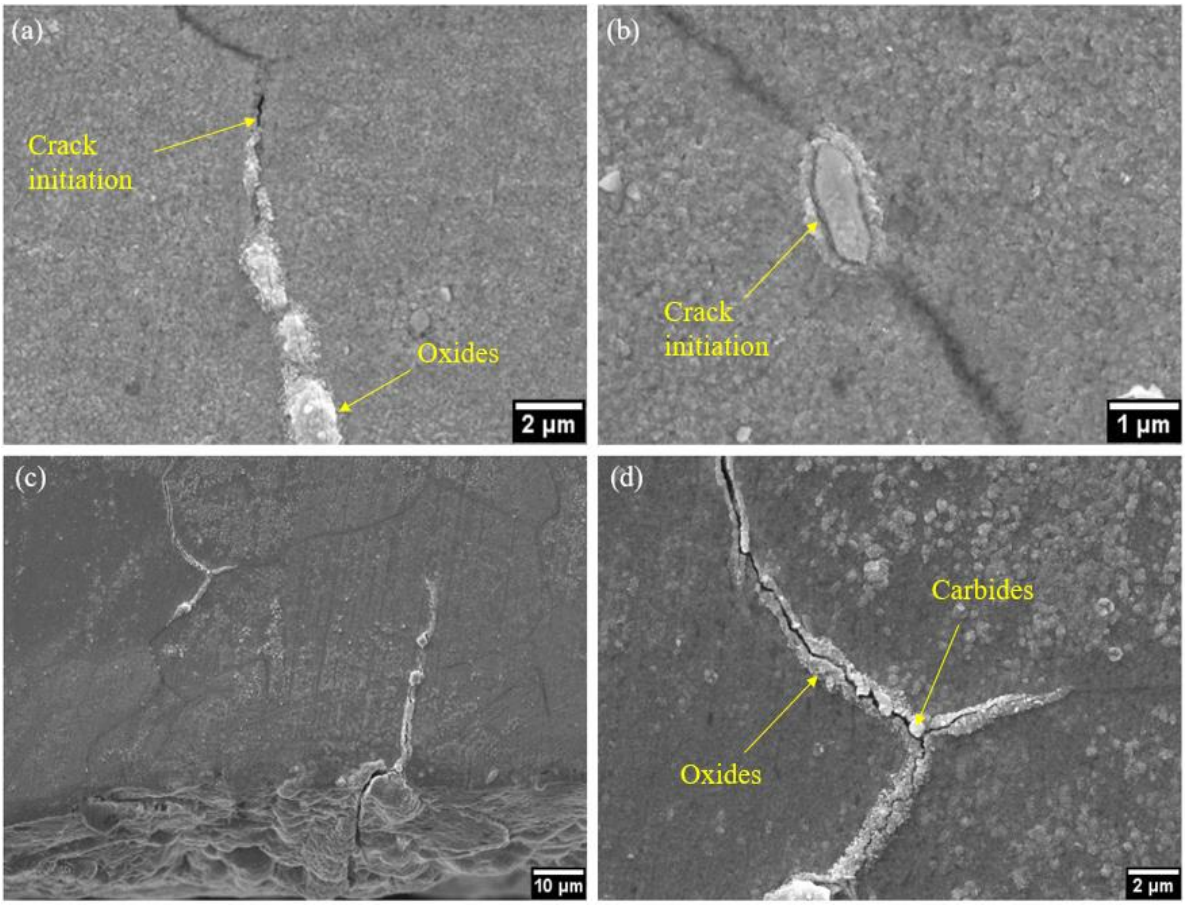

Figure 5.15: SEM images of the coarse γ′ variant interrupted at 250 cycles (a) crack initiation along with oxide formed at grain boundary (b) crack initiation at the interface between carbide and grain boundary (c) grain boundary cracking through carbides and oxides formed at grain boundaries (d) image at higher magnification of (c).

5.4 Discussion

5.4.1 Effect of microstructure and oxidation on fatigue initiation behaviour

It is known that local microstructure exerts a significant influence on fatigue crack initiation and short crack behaviour at room temperature as discussed in Chapter 4. At elevated temperature in air, on the other hands, the effects of temperature and oxidation damage on fatigue behaviour become dominant in conjunction with microstructural influences. Higher temperatures are likely to promote cross slip behaviour or multiple slip processes leading to homogeneous slip and less localised slip. The deformation behaviour of the model microstructure of RR1000 with fine and coarse γ′ precipitates similar to this study tested at somewhat similar elevated temperatures (500 ^{o}C) has been investigated by TEM at the University of Manchester as a part of a collaborative EPSRC project [122]. It should be noted that this allows investigation of the deformation behaviour at elevated

temperatures although it is acknowledged the temperature is lower than those studied this study. In the fine γ′ variant at 500 ºC in Figure 5.16, shearing γ′ was still the dominant dislocation mechanism although some dislocation looping around γ′ particles are also seen, which takes place less at relatively lower temperatures. Coupled dislocations associated with small interparticle spacing can be discerned as well in Figure 5.16 (b).

In terms of the deformation behaviour of the coarse γ′ variant at 500 ºC, dislocations are interrupted and piled up around the γ′ precipitates (Figure 5.17 (a)), which is linked to less localised shear deformation. Dislocation looping around γ′ precipitates is the dominant dislocation mechanism for the coarse γ′ precipitates (the expected dominant dislocation mechanism for coarse γ′ precipitates) although shearing of the γ′ can occur simultaneously at this elevated temperature as shown in Figure 5.17 (b) and (c). From this study at University of Manchester, sheared γ′ particles by a number of slip lines is associated with a fine γ′ precipitate distribution although some dislocation looping can still be activated at the elevated temperature.

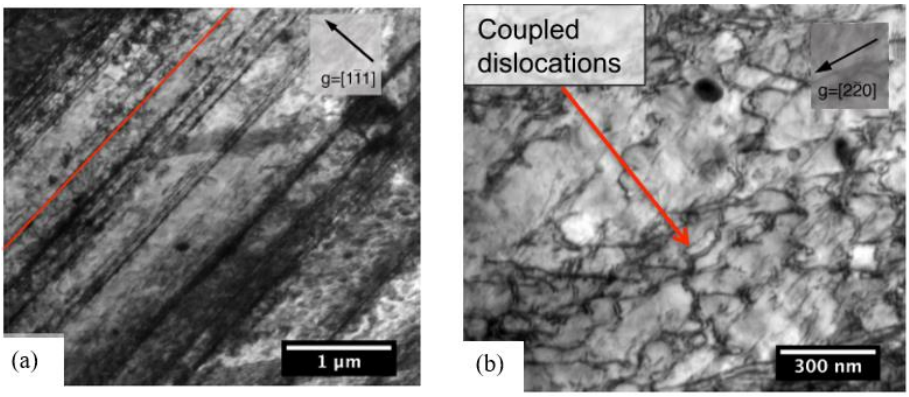

Figure 5.16: TEM images showing the dislocation structures in the fine γ′ variant at 500 ºC (a) red line represent the angle of the shear line (b) coupled dislocations observed [122].

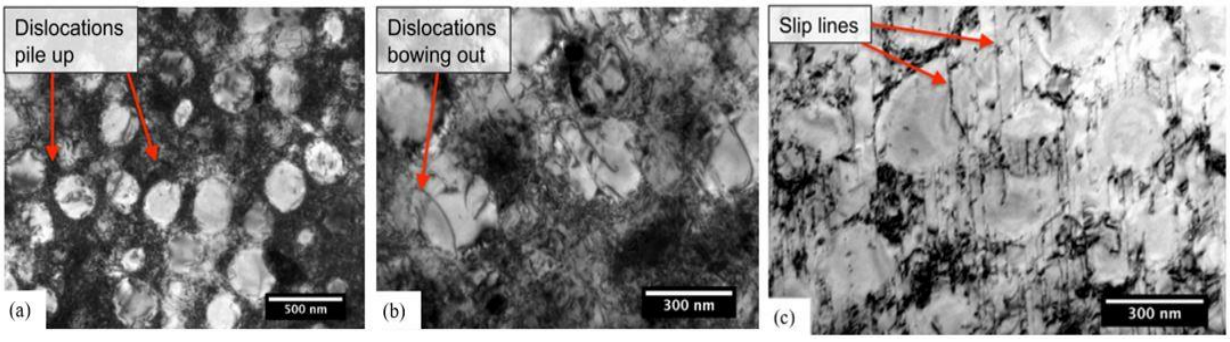

Figure 5.17: TEM images showing the dislocation structures in the coarse γ′ variant at 500 ºC including (a) dislocations pile up (b) dislocations bowing out (c) slip lines [122].

The crack initiation mechanism is apt to transit from slip band cracking at room temperature to intergranular crack initiation at elevated temperature due to the effects of temperature and oxidation damage although some slip band formation can be still observed (especially at high stress or strain levels). As seen in the top surfaces in Figure 5.3 and Figure 5.4, a number of cracks have initiated along grain boundaries all over the breadth of the sample. This can be ascribed to the oxidation damage, such significant grain boundary cracking results in frequent crack coalescence events, which reduces fatigue lives significantly. It is observed in the interrupted tests that a crack has initiated from the interface between a carbide and grain boundary as seen in Figure 5.15 (b). The interface between γ matrix/precipitates is a favourable path for oxidation and stress/strain concentration at elevated temperature while it can act as effective barriers for the crack initiation and propagation at room temperature. It is indicated that the significant volume expansion resulting from oxidation processes (i.e. Nb carbide oxidation) is linked to the subsequent crack initiation at the interface between carbide and matrix. However, the crack initiation from subsurface porosity and crystallographic faceting can be seen even at elevated temperature at low strain level [103,170].

In turbine disc alloys, the oxides that contribute to the intergranular crack initiation differ between alloys and testing conditions. In general, oxide complexes in RR1000 alloys comprise external layers of NiO/CoO and internal layers of Cr_2O_3/TiO_2/Al_2O_3 ahead of the crack tip [140]. The formation of the bulged grain boundary Ni/Co-rich oxides and Cr/Ti/Al oxide intrusion can be seen in turbine disc alloys and this promotes oxide cracking at elevated temperature, which results in intergranular crack initiation [169]. The impingement of slip bands at grain boundaries can be preferential paths for the diffusion of oxygen and oxide forming elements. However, the effect of slip bands on the diffusion seem to be limited at elevated temperature compared to the grain boundaries as the extent of the bulged Ni/Co-rich oxidation is much more marked than any evidence of slip band impingement [109]. In this study, it also appears that bulged oxides on grain boundaries are more frequently seen than slip band formation. It is observed that a Ni/Co-rich oxide formed along grain boundaries and ahead of the crack tip is seen in a RR1000 alloy which has a relatively high amount of Co [140]. Such bulged Ni/Co-rich oxides are normally linked to more mismatch strain and thereby stress concentration, which can promote crack initiation process at grain boundaries and subsequent intergranular FCG behaviour.

5.4.2 Effect of oxidation damage on short crack behaviour and lifetime

In terms of the early stage of crack propagation behaviour at room temperature, transgranular fracture features of slip band cracking with crystallographic facets were dominant. At elevated temperature an intergranular fracture mode seems dominant in the fracture surface (Figure 5.5 and Figure 5.7).

The reduced presence of facets is associated with thermally activated dislocation motion and more cross slip being promoted rather than planar slip at elevated temperatures. It is indicated that the transition from transgranular to intergranular fracture mode occurs in both γ′ variants, assisted by the dwell time and consequent longer diffusion time as temperatures increase. Higher loading frequency without a dwell time leads to mixed transgranular and intergranular fracture features on the fracture surface as seen in Figure 5.11 at 704 °C. This can be attributed to insufficient diffusion time in each loading cycle to induce not fully intergranular fracture due to the higher frequency and consequently limited oxidation damage. When the crack is significantly small, the crack driving force is relatively low, as is the crack advance rate and the fracture mode is more sensitive to the oxidation ahead of the crack tip, temperature and dwell time. This is pertinent to more intergranular fracture modes. On the other hand, as the crack driving force becomes greater (leading to enhanced FCG rates), the diffusion time for oxidation ahead of the crack tip becomes limited for the same increment of crack growth, which usually results in transition back to a more transgranular fracture mode.

Overall, it is seen that fatigue lifetime of both γ′ variants is significantly decreased at elevated temperature compared to lifetime at room temperature as presented in Table 5.2. It was expected that the fine γ′ variant would show the greater lifetime as the coarse γ′ variant exhibits a more continuous carbide distribution on grain boundaries. However, the lifetime was similar in both γ′ variants. This can be ascribed to the fine γ′ variant showing slightly more asymmetrical fracture surfaces and associated cracking, which promotes faster FCG rate and shorten lifetime. At elevated temperatures, the lifetime is closely associated with a significant number of cracks initiating at grain boundaries due to oxidation damage. This is closely linked to frequent crack coalescence events and subsequently accelerated FCG rates, offering significantly reduced lifetimes in both γ′ variants. Crack coalescence takes place even at room temperature, but is less frequent. The number of intergranular cracks is dependent on the degree of oxidation along the grain boundary as well as oxidation of the interface between γ matrix/precipitate. Moreover, a continuous carbide formation is associated with weakening the grain boundary properties and promotes crack initiation and propagation at the interface between carbides and grain boundary assisted by oxidation under cyclic loading. This can contribute to the significantly reduced lifetime of the alloys.

The number of cycles required to observe initial cracks are at around a quarter the lifetime in both γ′ variants at both room and high temperatures (although the crack in the fine γ′ variant initiated from the edge at high temperature). A similar initial crack length at room temperature is observed at 25,000 cycles and 60,000 cycles for the two fine γ′ variants and 45,000 cycles for coarse γ′ variant, which is around 2 orders of magnitude higher than the cycles to first observed crack at high temperature. It should be noted that the loading condition is also different (20Hz and 1-90-1-1 at room and high temperature, respectively). An indicative *da/dN* of the fine γ′ variant is obtained by comparing the crack growth from two observations at 250 cycles (crack ~70μm) and 450 cycles (~150μm) cycles at 650 °C and is estimated as ~0.4 μm/cycles. At similar crack lengths (nominal ΔK levels), testing

at room temperature shows an average *da/dN* of ~0.005 μm/cycle. This indicates that short FCG rate at high temperature is around 2 orders of magnitude higher than the short FCG rate at room temperature, which can be linked to significantly shorter lifetimes at high temperature. The accelerated short FCG rate contributes to the shortened lifetime at high temperature along with plentiful intergranular cracking (and earlier crack initiation) and subsequent crack coalescence events.

5.5 Summary

The effects of microstructure and oxidation on fatigue mechanisms, particularly crack initiation and lifetime, were assessed by three point bending fatigue testing at elevated temperatures. This was compared to the fatigue testing at room temperature and will be further assessed in the next chapter (where long crack behaviour at elevated temperatures is studied in detail). Post analysis of the fatigue tests were carried out by OM, SEM and EDX analysis. The summary and following conclusions are:

1. It is known that the microstructural effects are changed at elevated temperatures due to the significant effects of environment as well as changes in the slip character. It appears that cross slip and less localised slip are promoted with increasing temperatures in both γ′ variants. In the fine γ′ variant, dislocation shearing and heterogeneous slip characteristics are dominant at room temperature whereas some dislocation looping can be activated at elevated temperature. The coarse γ′ variant shows dislocation looping as a main mechanism at elevated temperature while some shearing γ′ can be still activated.
2. In general, the fatigue testing of both γ′ variants under 90s dwell at elevated temperature in air is characterised by intergranular features. A number of fatigue cracks are seen to initiate at grain boundaries with bulged Co-rich oxides at the surface that form at elevated temperatures due to the effects of dwell time (linked to diffusion of oxygen) and resultant oxidation damage. These oxides are associated with enhanced mismatch strain and therefore stress concentration, which can result in oxide cracking. On the other hand, the room temperature testing tends to show more slip band cracking with crystallographic facet and/or porosity crack initiation. It appears that a number of intergranular cracks propagated along oxidised grain boundaries at the surface and result in frequent crack coalescences during propagation. It is noteworthy that fatigue cracks have initiated at the interface between carbide and grain boundary, which results from oxidised carbides and grain boundaries.
3. Fatigue lifetime of both γ′ variants is considerably reduced to the LCF regime at elevated temperature assisted by the loading with a 90s dwell time at elevated temperature compared with the lifetime at room temperature (tested at high frequency). The lifetime of both γ′ variants are similar although the coarse γ′ variant was expected to show a lower lifetime due

to the continuous carbide formation along the grain boundaries. Significantly reduced lifetime is also closely linked to significant intergranular crack initiation and frequent consequent crack coalescence events, which results in enhanced FCG rates. Moreover, the crack initiation between a continuous carbides and grain boundaries promotes accelerated FCG rates and reduced lifetimes.

Chapter 6 Fatigue crack propagation behaviour at high temperatures

6.1 Introduction

After evaluating the crack initiation and short crack regimes at room temperature as discussed in Chapter 4, and the change in such processes at higher temperatures in Chapter 5, in this chapter the long crack propagation regime at higher temperature is next evaluated. The previous chapter offers an insight into the microstructural effects together with oxidation processes (at grain boundaries) on short FCG behaviour. In service, turbine disc components can have defects where a damage tolerant approach is applied, fatigue behaviour is then characterised by FCG rates of long cracks, which is associated with combined influences of microstructure, oxidation and creep processes in an oxidising environment. It is challenging to observe FCG at elevated temperature for naturally occurring small cracks, while the long FCG rates can be evaluated by in-situ mechanical testing approaches at high temperature and allows more detailed comparison of the crack growth mechanisms. Long (through thickness) crack propagation occurs with less irregular and less scattered FCG behaviour compared to the short FCG regime at equivalent ΔK levels. Much more averaged propagation rates can be established and continuous crack length monitoring is also possible. The long FCG regime at high temperature is also influenced by microstructure variations, loading conditions, temperature, test time and the synergistic effects of these.

In this chapter, long FCG tests at elevated temperatures in air have been carried out to investigate the effects of varying γ' size, grain boundary particles, loading frequency (dwell time) and temperatures on FCG behaviour in the model RR1000 alloy systems. The effect of different dwell times has been assessed to evaluate time dependent and cycle dependent fatigue processes using trapezoidal waveform loading in the fatigue tests. The aim is to study the effect of oxygen diffusion time and subsequent oxidation damage in each cycle on FCG behaviour. Testing temperatures have been chosen that represent the more extreme service temperatures for turbine disc applications at 650 ^{o}C and 725 ^{o}C (even higher in recent advanced aeroengine disc alloys). Fatigue tests were also carried out where switching between low and high frequency testing at 650 ^{o}C (referred to as 'block testing') was used to investigate the effect of loading frequency and oxygen related damage ahead of the crack tip, as characterised by the observed transition zone between two frequencies. The testing methodology for each fatigue test and relevant results are discussed in detail in the following section. Much of the work discussed in this chapter has also been published in the following paper:

D. Kim, R. Jiang, A. Evangelou, I. Sinclair, P.A.S. Reed, Effects of γ′ size and carbide distribution on fatigue crack growth mechanisms at 650 °C in an advanced Ni-based superalloy, Int. J. Fatigue. 145 (2021). doi:10.1016/j.ijfatigue.2020.106086.

6.2 Experimental procedure

6.2.1 Fatigue crack propagation tests

	650 °C		**725** °C	
	Fine γ′ variant	Coarse γ′ variant	Fine γ′ variant	Coarse γ′ variant
1-1-1-1	√	√	√	√
1-90-1-1	√	√	√	√
5Hz	√	√	-	-
Block test	√	√	-	-

Table 6.1: The full test matrix conducted for long FCG tests at both 650 °C and 725 °C in air.

A test matrix of experimental tests under a range of testing parameters adopted is represented in Table 6.1. A trapezoidal waveform loading of 1s dwell time at peak load was employed as a baseline test linked to the standard Rolls Royce fatigue testing condition. A longer dwell time of 90s at peak load was employed to assess time dependent crack growth in comparison to the baseline test. Sine waveform loading at a relatively higher frequency of 5Hz was also used to examine cycle dependent crack growth on FCG at 650 °C in air. Tests under a trapezoidal waveform loading with 1s and 90s dwell times were carried out on both γ′ variants at 650 °C and 725 °C while tests at 5 Hz frequency and block tests (alternating between 5Hz and 1-90-1-1) were conducted on both γ′ variants at 650 °C.

Fatigue testing at constant load amplitude at 650 °C and 725 °C

FCG tests at a range of loading frequencies (i.e. 1-1-1-1, 1-90-1-1 and 5Hz) on both γ′ variant alloys have been carried out at constant load amplitude at an R-ratio of 0.1 at test temperatures of 650 °C and 725 °C in air. Single edge-notched bend (SENB) specimens with a dimension of 9.5mm x 9.4mm x 55mm containing a through-thickness notch of around 2.2 mm (a/W = $1/4^{th}$) were employed for the mechanical testing as seen in Figure 6.1. The notches in the specimens were produced by

electrostatic discharge machining (EDM) cutting to induce a stress concentration which can initiate a crack from the notch. Side surfaces of the samples were ground and polished up to 1µm. The fatigue tests on these SENB specimens were performed under three-point bend with a loading span of 40 mm on an Instron 8501 servo-hydraulic testing machine with an ESH Ltd. high temperature chamber attached with four high intensity quartz IR lamps. The temperatures of the specimens were monitored by a Eurotherm 815 thermo-controller and R-type (platinum + 13%rhodium/platinum) thermocouple spot-welded to the specimens which ensured the test temperature was maintained to within ± 1 ^{o}C. The thermocouple was connected in the vicinity of the notch but not on the estimated crack path in order to avoid any damage to the temperature sensing control system. DCPD method was used to monitor long fatigue crack propagation by measuring the change in the resistance of the sample. The SENB sample with the connection of the thermocouple, current wires and four probe wires for DCPD method (two wires for the crack propagation and two wires for the reference) is schematically illustrated in Figure 6.1. The overview of the testing machine with the high temperature chamber and setup of fatigue testing is shown in Figure 6.2.

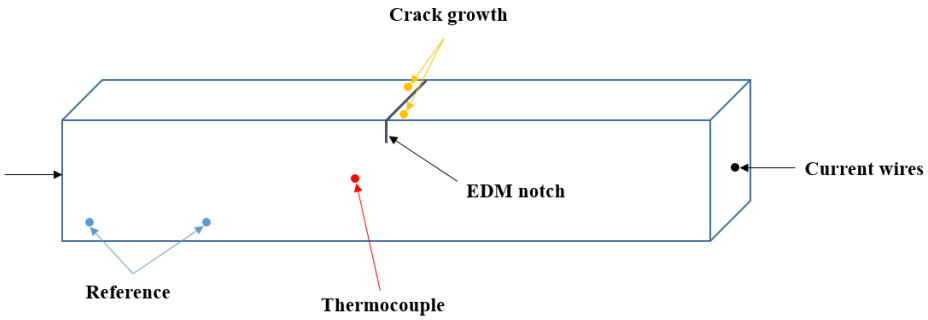

Figure 6.1: A schematic diagram of the setup of high temperature testing with a SENB sample with the wires for the DCPD method and thermocouple.

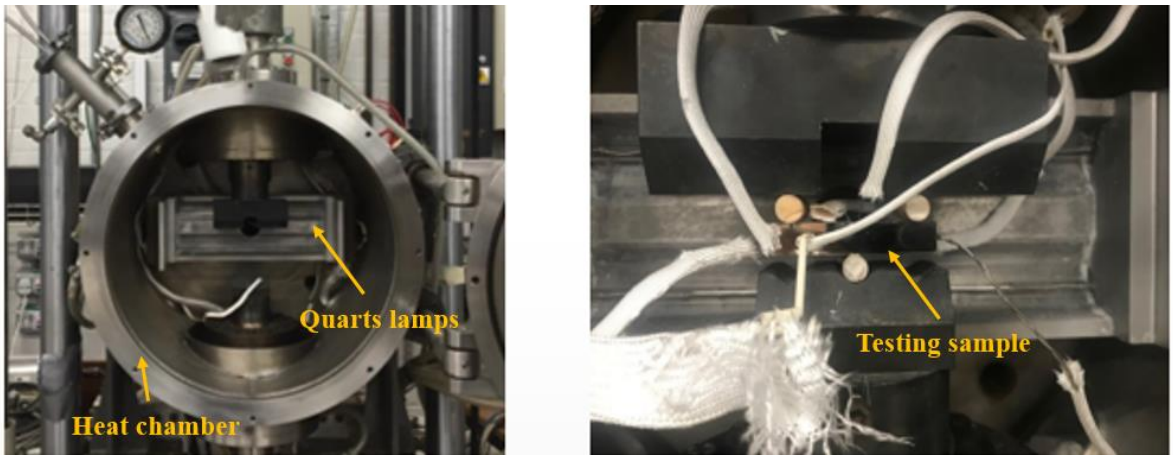

Figure 6.2: A servo-hydraulic testing machine including the setup of a testing sample with all connection in the heat chamber with quarts lamps.

The samples prior to testing were pre-cracked at an initial ΔK level of 20 MPa$\sqrt{m}$ under sine waveform loading, a frequency of 10Hz and R-ratio of 0.1 at room temperature. The pre-cracking routine then employed a load shedding procedure by reducing in steps of 10 % reduction in ΔK level after the crack had grown through at least four monotonic plastic zone sizes at each ΔK level to avoid any overload effects during crack growth. When the pre-cracking process is finished (once the crack had reached a target ΔK level of around 15 MPa$\sqrt{m}$) the chamber was sealed and the specimen was heated up to the test temperatures in the chamber. The samples were held at relatively low load for a few minutes after the set temperature was achieved to ensure temperature homogeneity in the specimens and fatigue testing was started. Each test was run until failure in order to examine fracture surface. The PD value obtained by the DCPD method during the test was calibrated with a noise reduction process by smoothing the data. Crack length with a post-test calibration is calculated based on an experimentally obtained calibration function and the actual crack lengths achieved from fracture surface observation. FCG rate was then derived by using the secant method from the data of calibrated crack length over loading cycle and the crack propagation behaviour was characterised in terms of *da/dN* vs ΔK.

Alternating dwell test (termed as a 'block test') at constant load amplitude at 650 ºC

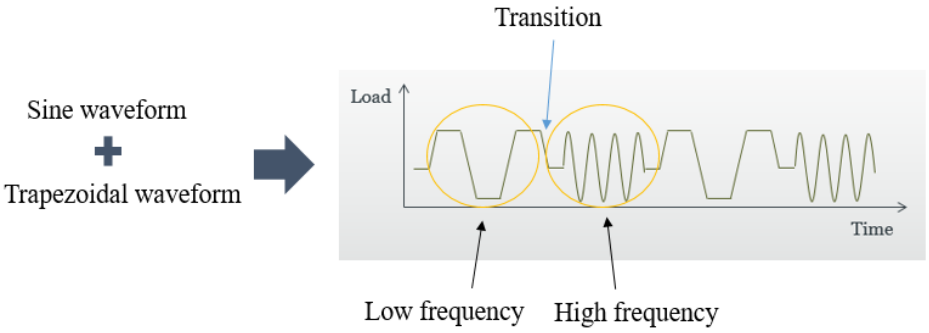

Figure 6.3: A schematic diagram of loading applied for block tests.

In order to investigate the extent of oxygen-related damage zone ahead of the crack tip, two regimes of low and high frequencies were switched between as illustrated in Figure 6.3 via block loadings during the test using the methodology in the references [171,172]. Representative frequencies have been chosen based on FCG mechanisms observed from the long fatigue crack tests at constant load amplitude. Block tests on both γ′ variant alloys were conducted under constant load amplitude (so increasing ΔK) and R-ratio of 0.1. By switching 1-90-1-1 (time dependent crack growth) and 5Hz (cycle dependent crack growth), the transitions between the two frequencies can be characterised in terms of any differences in oxygen related damage ahead of the crack tip and consequent FCG behaviour. Pre-cracking procedure and FCG rate analysis were identical with the earlier described long fatigue crack tests. These tests were halted at the end and held at a sustained load at K_{max} of 21 and 15 MPa$\sqrt{m}$ for around 12 hours for the fine and coarse γ′ alloys respectively and the PD value during this holding time was measured by the DCPD method. After holding the sample for the target

time, the testing was halted and the sample was cut into half for fractography analysis and sample preparation for X-ray CT scans, respectively. An additional crack growth out test (not a block test) of the coarse γ′ variant at 725 ^{o}C was carried out and held at a similar sustained load at 15 MPa$\sqrt{m}$ to compare with the block test at 650 ^{o}C.

6.2.2 Fractography and roughness analysis

Fracture surfaces obtained in a range of fatigue tests were investigated at different Δ*K* levels to understand the fracture mechanisms using a Wild M420 macroscope to obtain mesoscopic images of the overall fracture surface. A JEOL JSM 6500F FEG-SEM was used to examine high magnification images showing typical micromechanistic features at an acceleration voltage of 15kV and WD of around 10 mm. Oxidation features, particularly in relation to grain boundaries, were analysed using both SEI and BEI in the SEM along with the Oxford INCA EDX to analyse chemical composition in AOI.

Fracture roughness analysis on fracture surfaces at varying Δ*K* levels was conducted by Alicona Infinite Focus microscope and the JEOL JSM 6500 FEG-SEM. A topological surface map of images using the Alicona microscope was obtained at x10 magnification. The Alicona microscope provides not only roughness measurements but also pinpoints areas of interest for further fractographic examination by SEM. SEM images were achieved at a magnification of x100 to examine microstructural features and fracture roughness associated with the extent of intergranular fracture mode. Firstly, an image at 0^{o} without tilting should be captured on the AOI and then tilted to -5^{o} and +5^{o} on the same area maintaining same magnification and WD at Δ*K* of 20, 30 and 40 MPa$\sqrt{m}$ on all tested samples for the consistent comparison. These three SEM images were reconstructed into 3D morphology (Figure 6.5) of the fracture surface using the Alicona-MeX software to assess the local surface roughness. The average surface roughness (S_a) and root mean square roughness (S_q) indicative of roughness parameters were obtained to characterise the roughness of the 3D imaged fracture surfaces through the MeX software. A schematic diagram of Alicona microscope and Alicona-MeX is illustrated in Figure 6.4. S_a and S_q are mathematically described as [173]:

$$S_a = \iint_a |Z(x,y)| dxdy \qquad (5.1)$$

$$S_q = \sqrt{\iint_a (Z(x,y))^2 dxdy} \qquad (5.2)$$

where Z (x,y) is the function representing the height of the surface in terms of the best fitting plane.

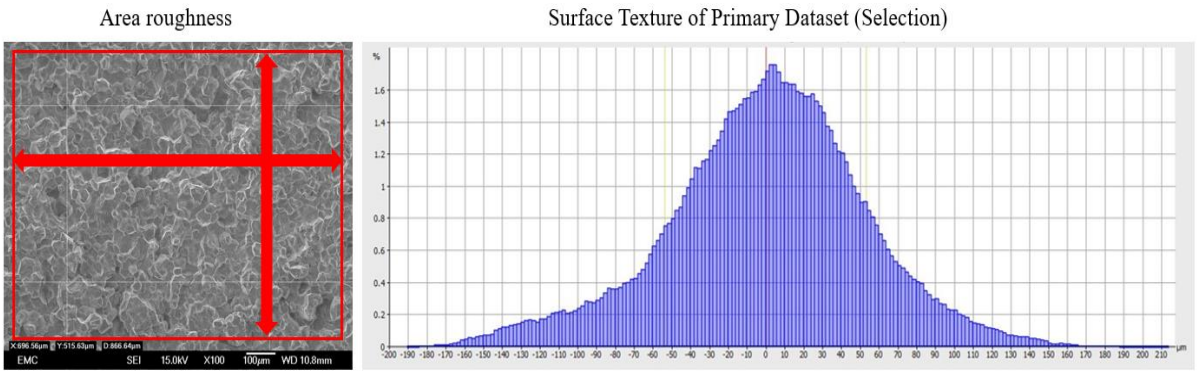

Figure 6.4: An example of the average surface roughness measurement of an AOI.

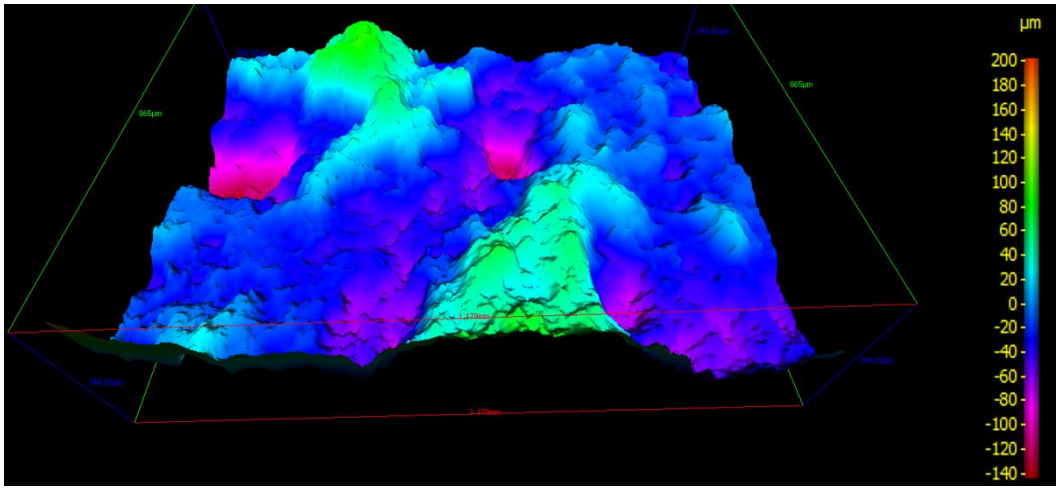

Figure 6.5: An example of 3D morphology of fracture surface reconstructed by SEM-MeX with angles of -5°, 0° and +5°.

6.2.3 Characterisation and statistics of secondary crack length

In order to investigate the interaction between secondary cracks and FCG behaviour on both γ′ variant samples tested at elevated temperatures, the fatigued samples were sectioned as presented in Figure 6.6 using a Mechatome T210 with a diamond cutting wheel. In order to minimise any damage on fracture surface and maintain the edge retention during the sectioning process, a nickel plating process with Watt's solution (500ml H_2O, 150g Nickel sulphate, 20g Nickel chloride, 20g Boric acid) at a temperature range of 40 - 60 °C, using a 99.9 % pure Ni anode, and a current density of 40 mA/cm^2 was carried out for around 30 minutes before sectioning. A diagram for the nickel plating set-up is schematically presented in Figure 6.7. The extracted and plated samples including secondary cracks were then mounted in a conductive Bakelite and ground and polished down to an OPA finish of 0.02 µm to obtain high quality surface condition for microstructural characterisation. The examination of the prepared samples was performed with SEI, BEI using the JEOL FEG-SEM and OM under the same characterisation conditions mentioned in previous sections. EDX examination

was conducted to examine the chemical analysis of the AOI, especially where cracks propagated through grain boundaries and where oxides formed.

Statistics of the secondary crack occurrence on the fracture surfaces of tested samples under different loading conditions at 650 °C was also further analysed to understand the relation between the average secondary crack length and FCG behaviour, to assess the extent of intergranular fracture mode. The average length of secondary cracks was systematically measured by ImageJ software at ΔK level of 20, 30 and 40 MPa$\sqrt{m}$. Images for the analysis were captured by SEM with a magnification of ×100. The fracture surfaces including secondary cracks are observed under higher magnification and the crack lengths were manually measured using the drawing tool of ImageJ software. Some secondary cracks have a branch along the grain boundary particularly in the intergranular fracture mode and they were measured as two individual cracks.

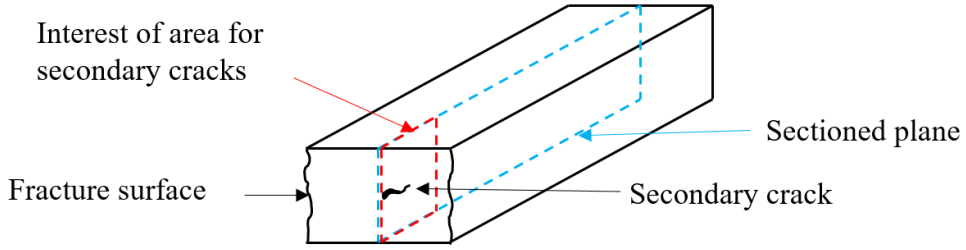

Figure 6.6: Schematic illustration of the sample used for the secondary crack analysis after fatigue testing.

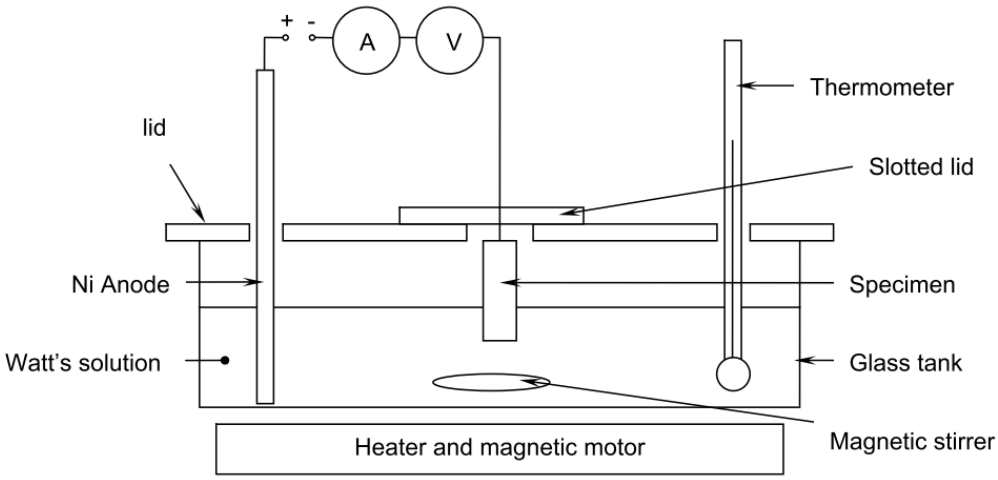

Figure 6.7: A schematic diagram for the Nickel plating set-up [174].

6.2.4 3D evaluation of the crack path by X-ray CT scan

X-ray CT scanning on both γ′ variant samples after the interrupted block tests was carried out to allow 3D analysis of the FCG behaviour. One half of the SENB samples (Figure 6.8) including the notch and fatigue crack path was cut by a diamond cutting wheel to extract a matchstick sample. The sample was then ground to have a small cross section less than ~0.9 mm x 0.9 mm due to the high X-ray attenuation observed in Ni-based superalloys to allow successful CT scanning. The sample was carefully ground to avoid breaking or distorting the extracted sample or to influence the crack path within it, as the sample becomes compliant due to the small dimensions. The Zeiss 160 kVp Versa 510 was used for X-ray CT scanning at the μVIS Imaging Centre of University of Southampton. Figure 6.9 illustrates the set-up for the scanning with the matchstick in the scanning machine. Test parameters are represented in Table 6.2. Four scans on each matchstick sample were conducted to cover the whole crack path including the notch and fatigue crack path with a limited field of view. After the scanning, each scan was stitched using imaging software packages of ImageJ, VGstudio and Avizo. A series of raw 2D slices obtained from the scanning were then processed and reconstructed into 3D morphology by the imaging software.

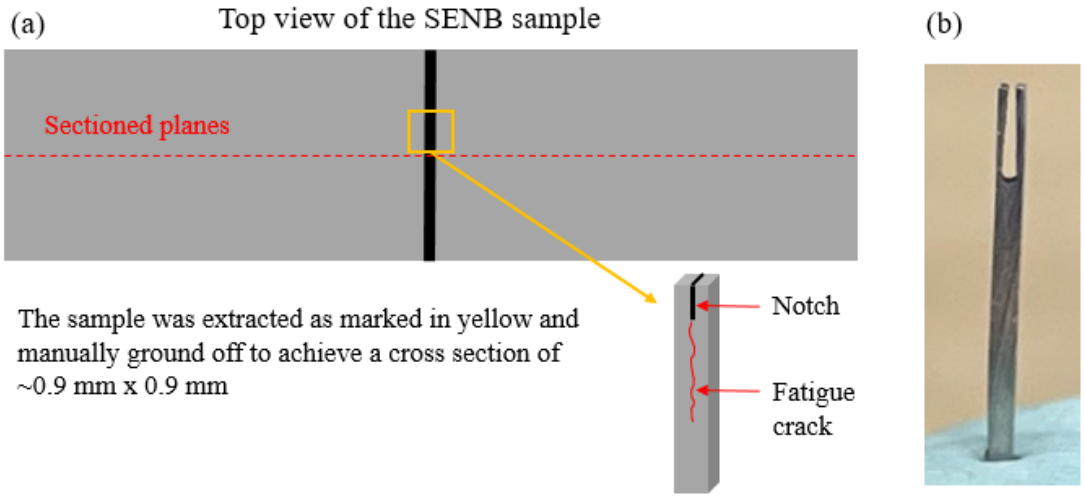

Figure 6.8: (a) A schematic diagram of the sample preparation for X-ray scanning (b) a matchstick sample.

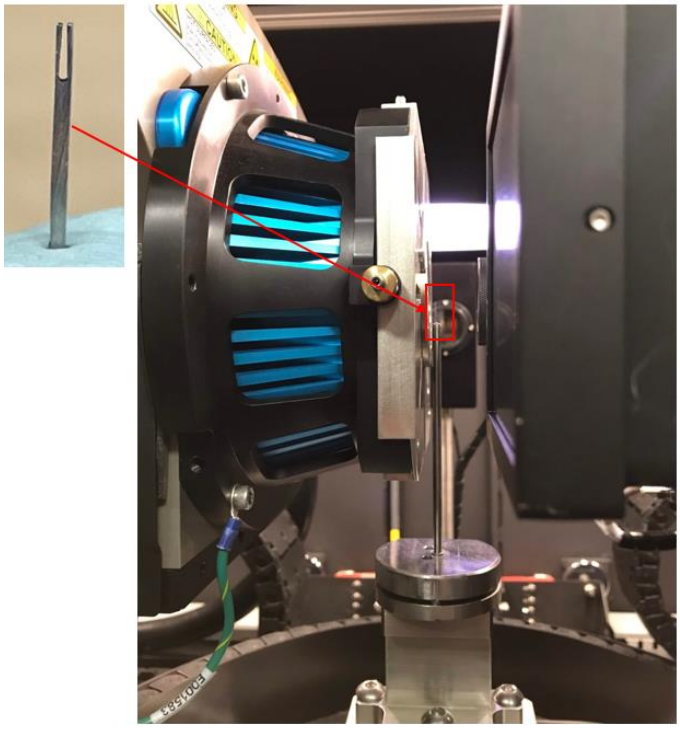

Figure 6.9: Set-up of X-ray CT scanning of the matchstick sample including the notch and fatigue crack path.

Scan parameter	
Voltage	120kV
Power	9W
Pixel size	0.965µm
Exposure time	3s
Binning	X1
Imaging angle range	-180 º to 180 º
Scan time	21 hrs
Number of projection	2701

Table 6.2: Parameters for X-ray CT scanning carried out at University of Southampton.

6.3 Results

6.3.1 Long fatigue crack growth test at elevated temperature (at constant load amplitude, increasing ΔK)

Long FCG rates obtained under the trapezoidal waveform loading with short and long dwell times and under high frequency sinewave form loading were obtained in both fine and coarse γ′ variants at temperatures of **650 ºC** as represented in Figure 6.10 (a). It is important to note that the coarser γ′ variant has not only greater γ′ size but also a more continuous distribution of carbides on grain boundaries. Overall, it is seen that the FCG rates of the coarse γ′ variant are higher than those of the fine γ′ variant at a range of loading frequencies and temperatures. In the fine γ′ variant tested at **650 ºC** as seen in Figure 6.10 (a), it is observed that the FCG rate with a **90s dwell** is approximately one order of magnitude higher than that of a **1s dwell**. On the other hand, the FCG rate of the coarse γ′ variant shows a more pronounced effect of longer dwell time on FCG rate with around two orders higher FCG rate with a **90s dwell** compared to a 1s dwell. Such results indicate that the higher FCG rate at longer dwells can be ascribed to more oxygen related damage due to increased diffusion time for oxidation processes at the crack tip for longer dwell times at peak load and that this is increased in the coarse γ′ variant. At the higher testing frequency of **5Hz**, the FCG rate of the coarse γ′ variant appears to be only slightly higher and the difference of FCG rates between both fine and coarse γ′ variant alloys appears only marginal. In general, it appears that lower frequency testing shows time dependent crack growth behaviour more related to oxidation enhanced mechanisms whereas higher frequency testing exhibits cycle dependent crack growth behaviour. Although creep processes may be linked to enhanced FCG behaviour of Ni-based superalloys, it is observed that the effects on FCG behaviour are limited at lower temperature where disc alloys are used [175] and oxidation processes near the crack tip and along the grain boundary mainly contribute to time dependent FCG behaviour [117,176]. It is also reported that intergranular crack growth behaviour and enhanced FCG rates of RR1000 alloys are mainly influenced by crack tip intergranular oxidation processes in air [117]. However, in future work, it would be interesting to conduct fatigue tests in vacuum to assess the effect of creep processes separately.

FCG rates for the tests carried out on both γ′ variants at **725 ºC** are presented in Figure 6.10. At this temperature, the FCG rate of the fine γ′ variant with a **90s dwell** at **725 ºC** is around two orders of magnitude higher that for a 1s dwell time, which shows a more pronounced difference than seen in the FCG rates at **650 ºC.** This can be ascribed to the marked effect of higher temperature giving rise to more oxidation damage. In the coarse γ′ variant, the FCG rate with **90s dwell** is nearly one order of magnitude higher than the FCG rate with **1s dwell**. It is also interesting to note that the FCG rates of both γ′ variants with a **90s dwell** are quite similar at the higher FCG rates with no distinct difference in the FCG rates between fine and coarse γ′ variants with **90s dwell** time at **725 ºC**. This might be linked to a saturation regime of the FCG rate of these variants under testing conditions

given. The results in the time dependent regime tests may be most associated with the variation in carbide distribution on the grain boundary, which can contribute to variations in the strength of the grain boundary. Moreover, enhanced FCG rates are linked to greater oxygen related damage where testing conditions allow longer diffusion time for oxidation processes at the crack tip per cycle (longer dwells) and with increasing temperature increasing the rate of oxidation. The potential role of creep processes in the time dependent regime can be more clearly separated out in future testing in inert environment/vacuum conditions, which is detailed in the future work section.

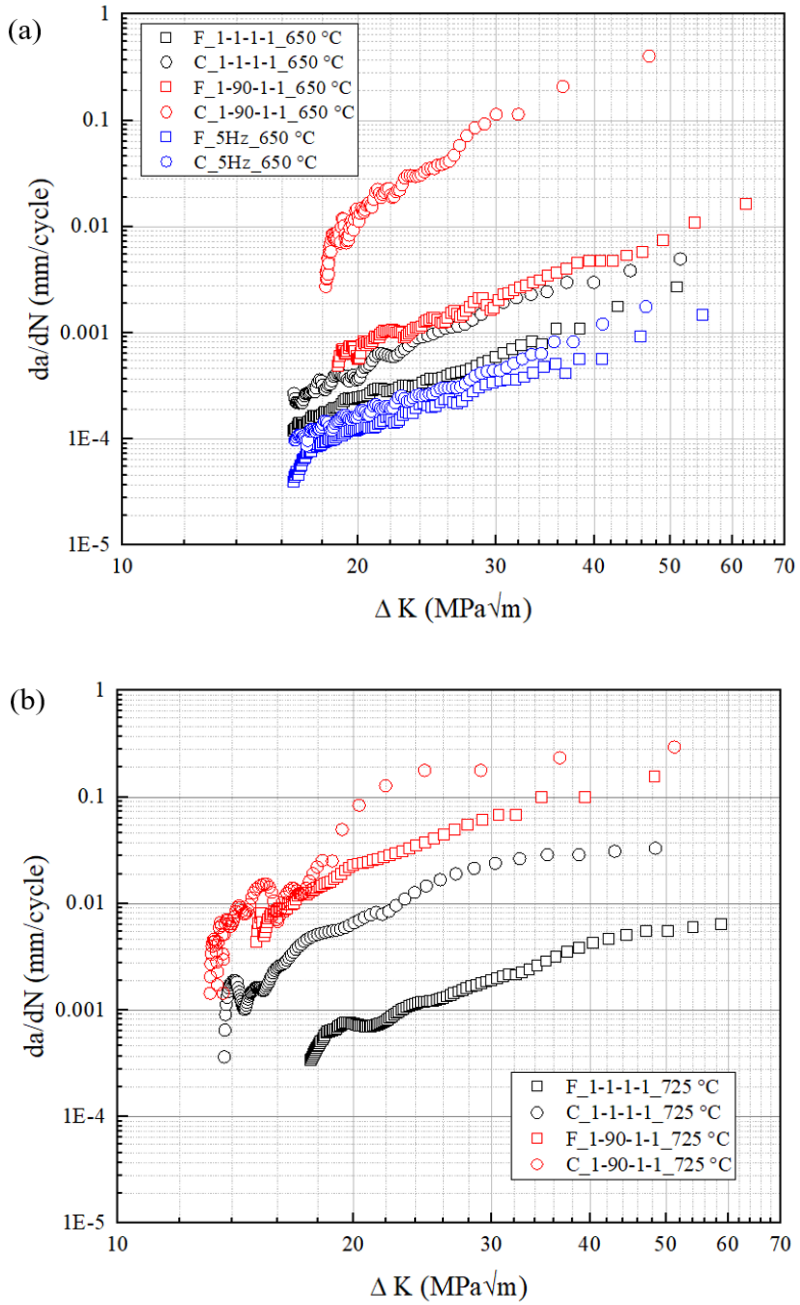

Figure 6.10: FCG rates on fine and coarse γ′ microstructure variants in terms of *da/dN* vs Δ*K* found with different testing frequencies at a temperature of (a) 650 °C and (b) 725 °C.

The FCG rates are compared under similar dwell times to allow comparison between fine and coarse γ′ variants and to see the effect of temperatures more easily in Figure 6.11. It is obvious that a higher temperature gives rise to accelerated FCG rates in both dwell time testing regimes. Under a **1s dwell** time in Figure 6.11 (a), the FCG rate of the coarse γ′ variants at a higher temperature (**725 ºC**) is obviously faster than a lower temperature (**650 ºC)**. Under a **90s dwell** time in Figure 6.11 (b), there was not a noticeable difference of FCG rate between fine and coarse γ′ variant at **725 ºC**, which can be related to the saturation of the oxidation assisted FCG rate.

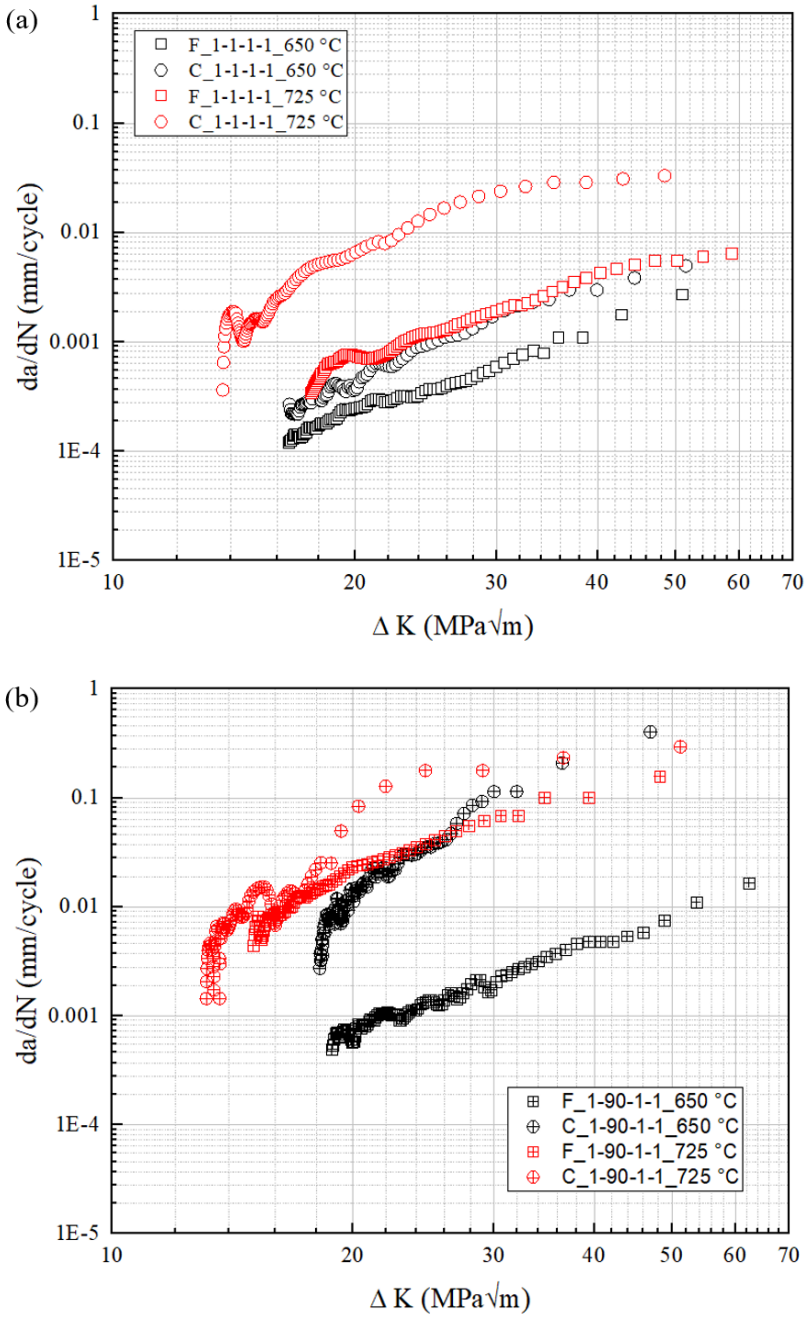

Figure 6.11: FCG rates of fine and coarse γ′ microstructure variants in terms of *da/dN* vs Δ*K* found with different testing frequencies with (a) 1s dwell time and (b) 90s dwell time.

There were several interesting features observed in the raw PD values at the highest FCG rates, just before the final failure in tests with a **90s dwell**. It was found that PD values (corresponding to the crack length) actually decreased somewhat during the dwell period but then experienced a clear jump between each unload/load cycle after the **90s dwell** block as illustrated in Figure 6.12. The jump can be related to fracturing through an embrittled damage zone caused during the dwell due to oxidation processes and this 'oxidation damage zone' ahead of a crack tip can be estimated by the change of PD value. The damage zone associated with enhanced FCG behaviour will be assessed in detail in the following sections through block tests. Discussion of the cause of the decrease in PD during the hold/dwell time of **90s** as the sample approaches to the final failure at relatively high ΔK levels is presented in the following sections.

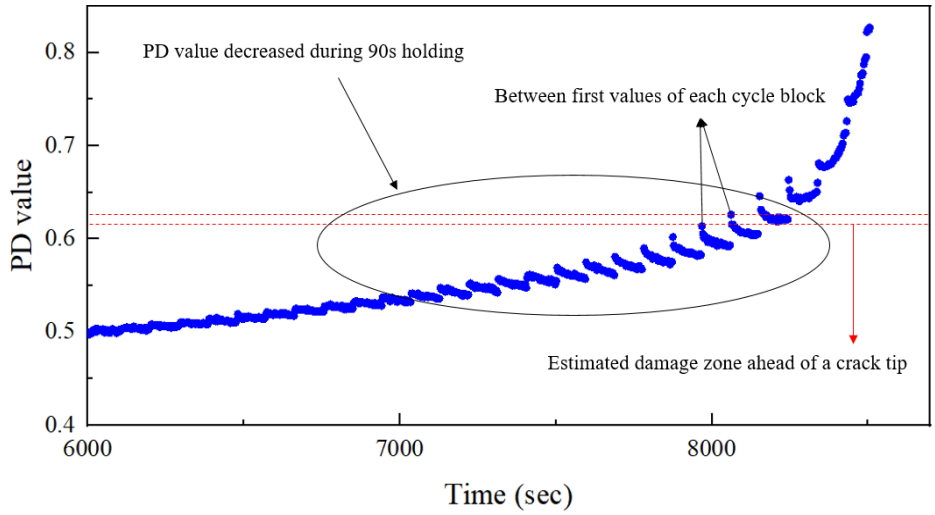

Figure 6.12: PD value over time of 1-90-1-1 at 650 ºC loading showing jumps between blocks of loading cycles at the end of fatigue lifetime.

6.3.2 Fracture surface and roughness analysis

Macroscopic overviews of the fracture surfaces of the RR1000 samples tested at **650 ºC** and **725 ºC** are presented in Figure 6.13 and Figure 6.14, respectively. The fracture surfaces show the areas of the EDM notch, pre-crack (at room temperature), fatigue crack propagation at high temperature and final failure by beach marks, different colours and contrast generated by oxidation processes during the testing. It is found that some fracture surfaces exhibit somewhat asymmetric crack propagation during intergranular high temperature crack growth so that the crack has not propagated uniformly across the breath of the samples with increasing ΔK. It is possible that one side becomes more compliant than the other during crack propagation, which could be attributed to crack coalescence events, more complex intergranular crack paths at one side of the fracture surface at high ΔK level or crack arrest at one edge of the fracture surface.

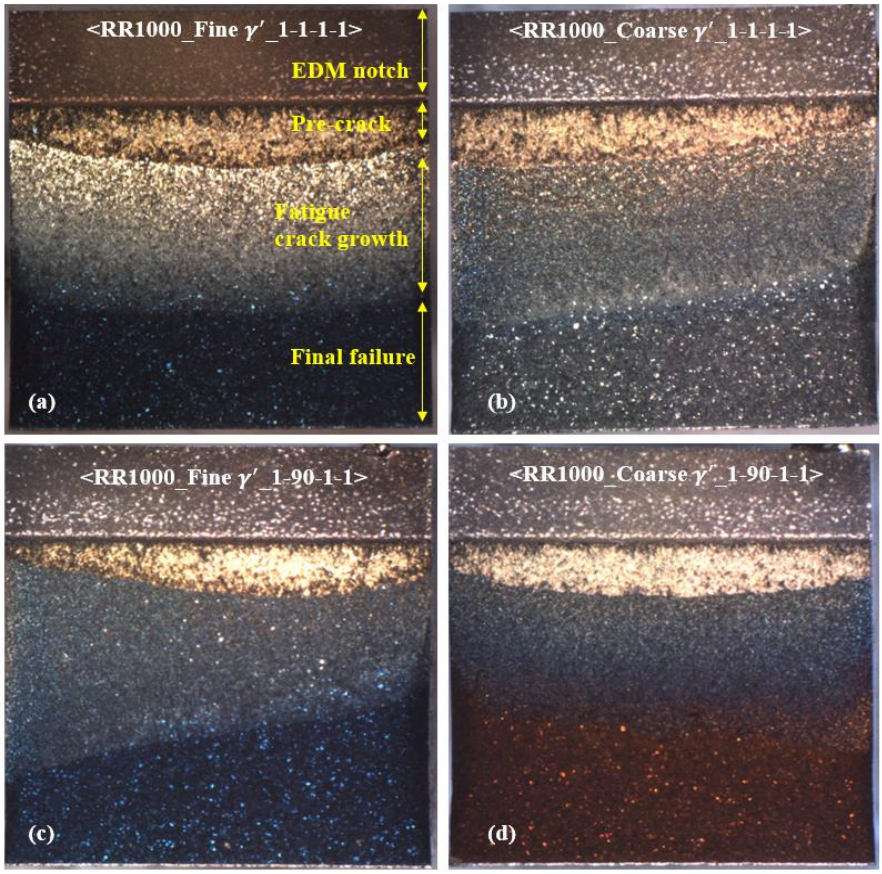

Figure 6.13: An overview of fracture surfaces of RR1000 with (a) fine γ′ and (b) coarse γ′ with a **1s dwell** time; (c) fine γ′ and (d) coarse γ′ with a **90s dwell** time at **650 ºC**, indicating different regions.

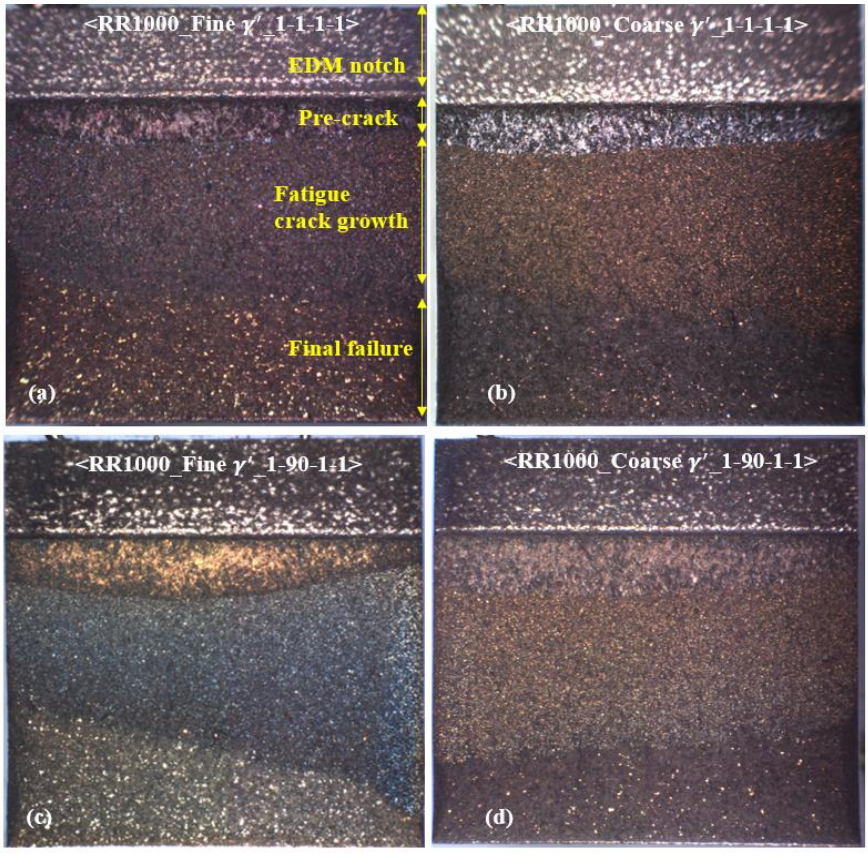

Figure 6.14: An overview of fracture surfaces of RR1000 with (a) fine γ′ and (b) coarse γ′ with a **1s dwell** time; (c) fine γ′ and (d) coarse γ′ with a **90s dwell** time at **725 ºC**, indicating different regions.

The morphology of the fracture surfaces at higher magnification were systematically examined as shown in Figure 6.15-Figure 6.18. Microstructural features and distinct characteristics of the fatigue fracture modes of both fine and coarse γ′ variant alloys are presented as a function of the range of Δ*K* level. At a low Δ*K* level (20 MPa$\sqrt{m}$) in the tests with **a 1s dwell** at **650 ºC**, the fracture surfaces exhibit mixed (both transgranular and intergranular) fracture modes, with more predominant transgranular fracture features in the fine γ′ variant and mainly intergranular fracture features in the coarse γ′ variant as seen in Figure 6.15 (a) and (b), respectively. As the Δ*K* level increases from 30 to 40 MPa$\sqrt{m}$, the fracture mode of the fine γ′ variant becomes significantly more transgranular (Figure 6.15 (c) and (e)). On the other hand, the intergranular fracture mode of the coarse γ′ variant is still evident at Δ*K* levels of 20 and 30 MPa$\sqrt{m}$ but more transgranular fracture features are seen at the higher Δ*K* level of 40 MPa$\sqrt{m}$ (Figure 6.15 (d) and (f)). In other words, the transition from intergranular to more transgranular dominant fracture modes observed as ΔK increases (and the associated *da/dN* levels increase) occurs "earlier" (at a lower Δ*K* level) in the fine γ′ variant than the coarse γ′ variant in the tests with **a 1s dwell** at a temperature of **650 ºC**.

SEI images of the fracture surfaces in Figure 6.16 show the microstructural features at higher magnification in both fine and coarse γ′ variants at varying Δ*K* levels. It is interesting to note that smooth transgranular failure features as well as intergranular secondary cracking are seen (marked by arrows in Figure 6.16 (a) and (c)), which is indicative of a mixed fracture mode of the fine and coarse γ′ variants at relatively low Δ*K*. At the higher Δ*K* level of 30 MPa$\sqrt{m}$, the transgranular fracture mode become evident in the fine γ′ variant as shown in Figure 6.16 (b) while a mixed fracture mode of smooth transgranular and more intergranular features with detachment of a cluster of grains can be discerned in the coarse γ′ variant as seen in Figure 6.16 (d). It is also worth noting that the number of secondary intergranular cracks on the fracture surface increase at higher ΔK levels in the coarse γ′ variant. This can also be associated with the extent of the roughness of the fracture surface, which will be discussed later in this section.

The fracture surfaces in both γ′ variants under **a 90s dwell** testing at **650 ºC** generally exhibit a predominantly intergranular fracture mode with varying Δ*K* levels as described in Figure 6.17. This is ascribed to the effects of longer dwell time (longer diffusion time per cycle) at maximum load and consequent oxygen related damage at grain boundaries ahead of the crack tip. It is noteworthy that the amount of secondary cracks observed on the fracture surfaces have increased with an increasing Δ*K* level. Figure 6.18 illustrates clear intergranular fracture modes with secondary cracking formed along the grain boundary observable. Evidence of particles on the embrittled grain boundary surface is seen at the higher magnification as marked by yellow arrows in Figure 6.18.

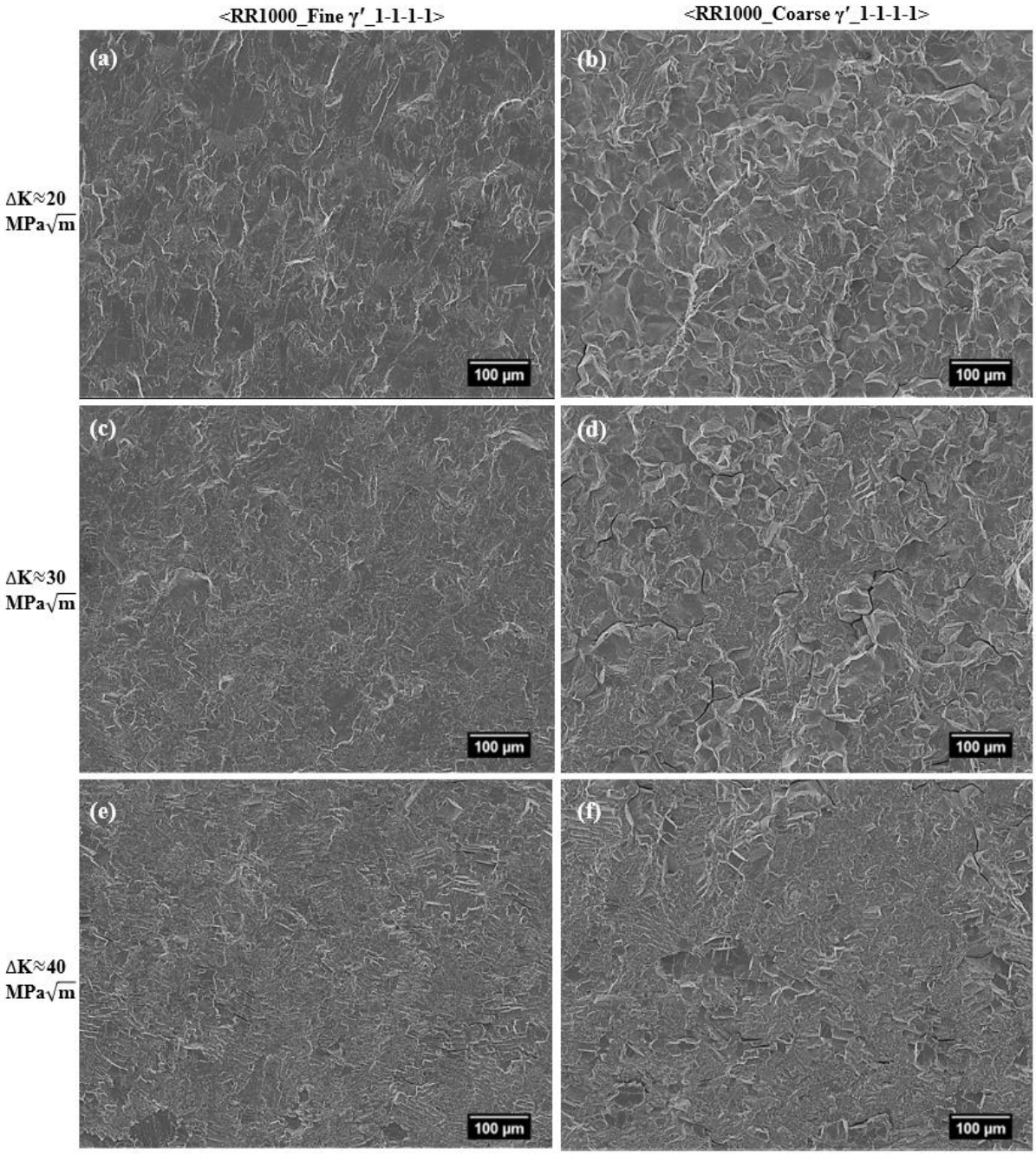

Figure 6.15: Fractography of RR1000 alloys tested with a **1s dwell** time at **650 ºC**; (a) a mixed fracture mode (predominantly transgranular) at low Δ*K* level, (c) and (e) predominantly transgranular fracture mode at increasing Δ*K* level in the fine γ′ microstructure; (b) and (d) a mixed fracture mode (predominantly intergranular) at low and mid Δ*K* level, (f) mostly transgranular fracture mode observed at high Δ*K* level in the coarse γ′ microstructure.

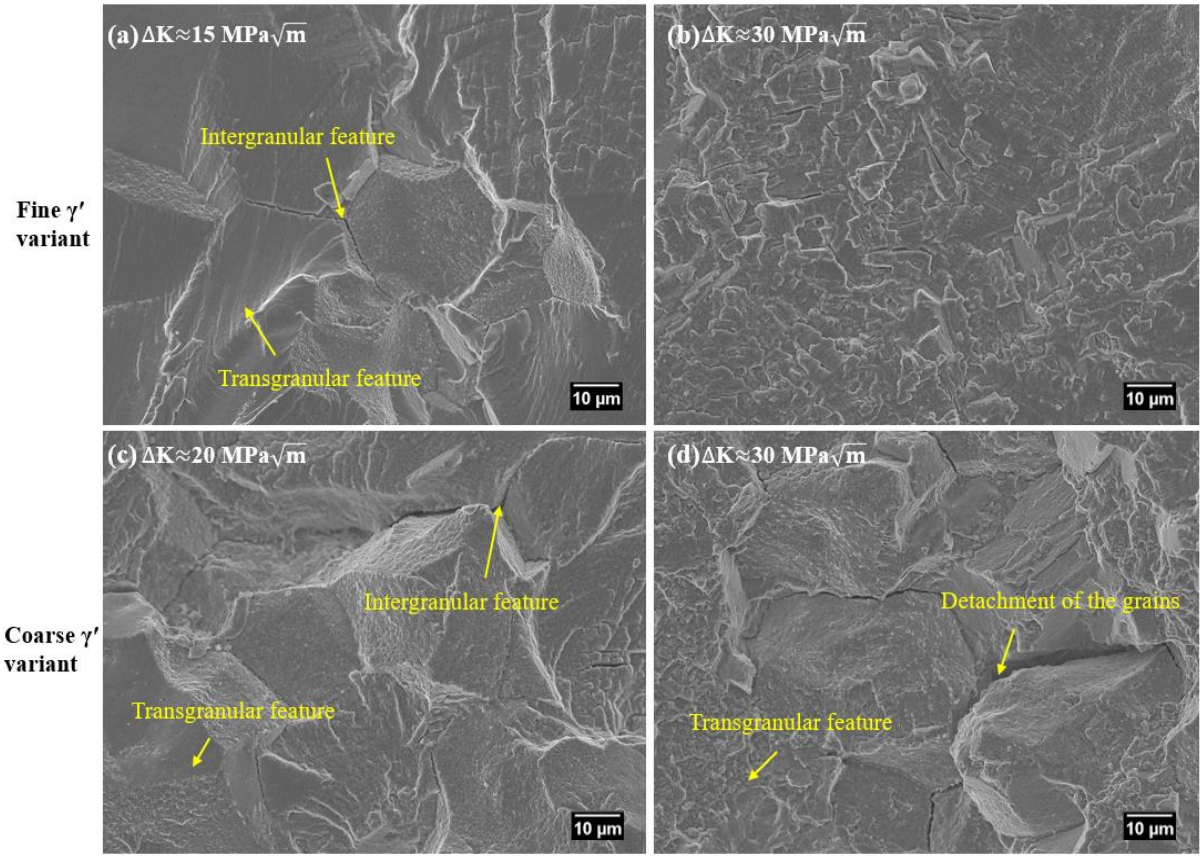

Figure 6.16: Fractography of RR1000 alloys tested with a **1s dwell time** at **650 ºC** at higher magnification; (a) a smooth failure area and intergranular secondary cracking (yellow arrows) feature of the mixed fracture mode at Δ*K* around 15 MPa$\sqrt{m}$ and (b) transgranular features at Δ*K* around 30 MPa$\sqrt{m}$ in the fine γ′ microstructure; (c) and (d) showing a feature of the mixed fracture mode (yellow arrows) at Δ*K* around 20 and 30 MPa$\sqrt{m}$ in the coarse γ′ microstructure.

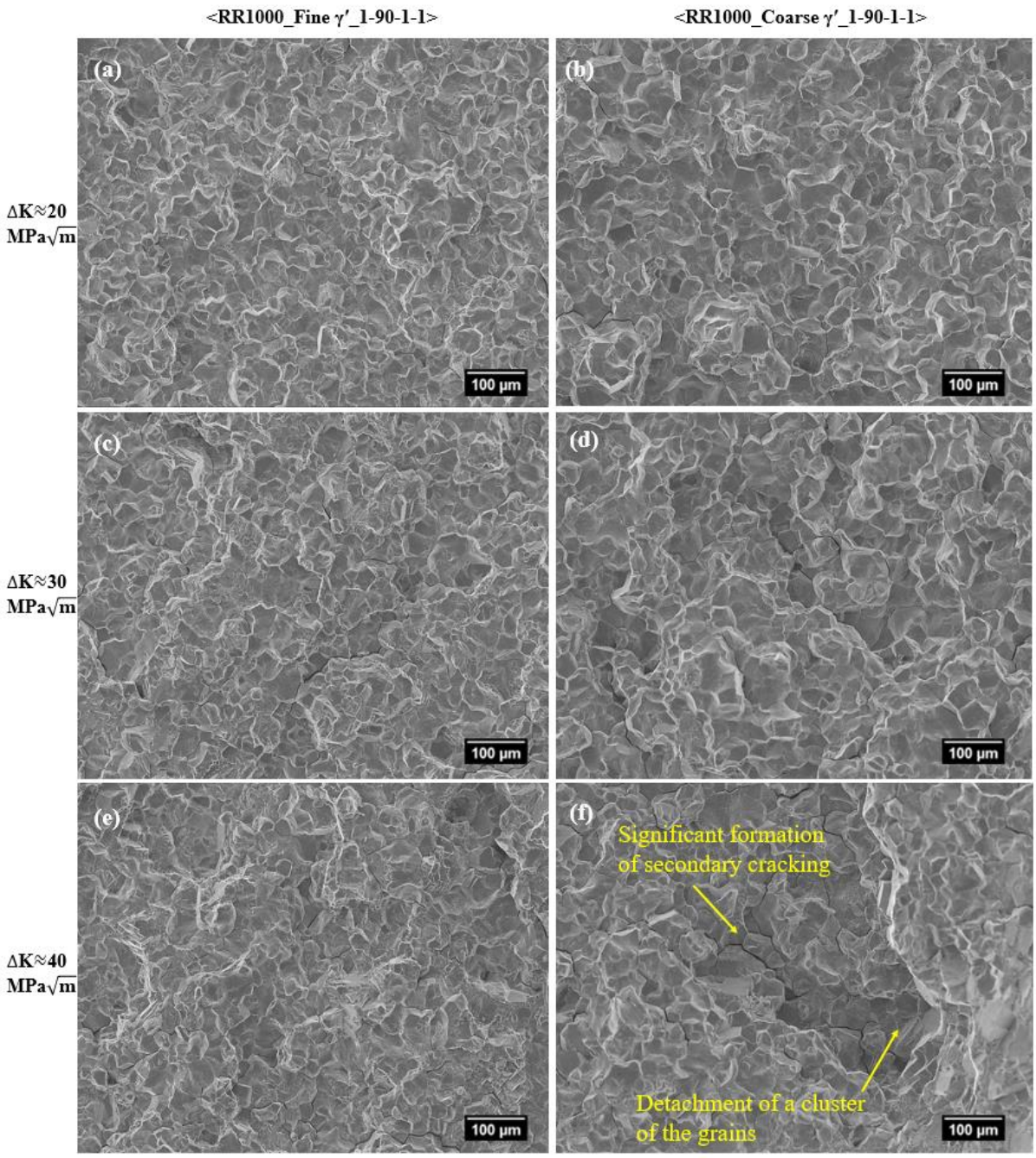

Figure 6.17: Fractography of RR1000 alloys tested with a **90s dwell** time at **650 ºC**; (a), (c) and (e) a predominantly intergranular fracture mode is observed at a range of Δ*K* levels in the fine γ′ microstructure; (b), (d) and (f) a clear intergranular fracture mode is also observed at a range of Δ*K* levels in the coarse γ′ microstructure, showing a dimpled area (yellow arrow) particularly at higher Δ*K*. Note that the formation of secondary cracks seemingly increases with increasing Δ*K* level.

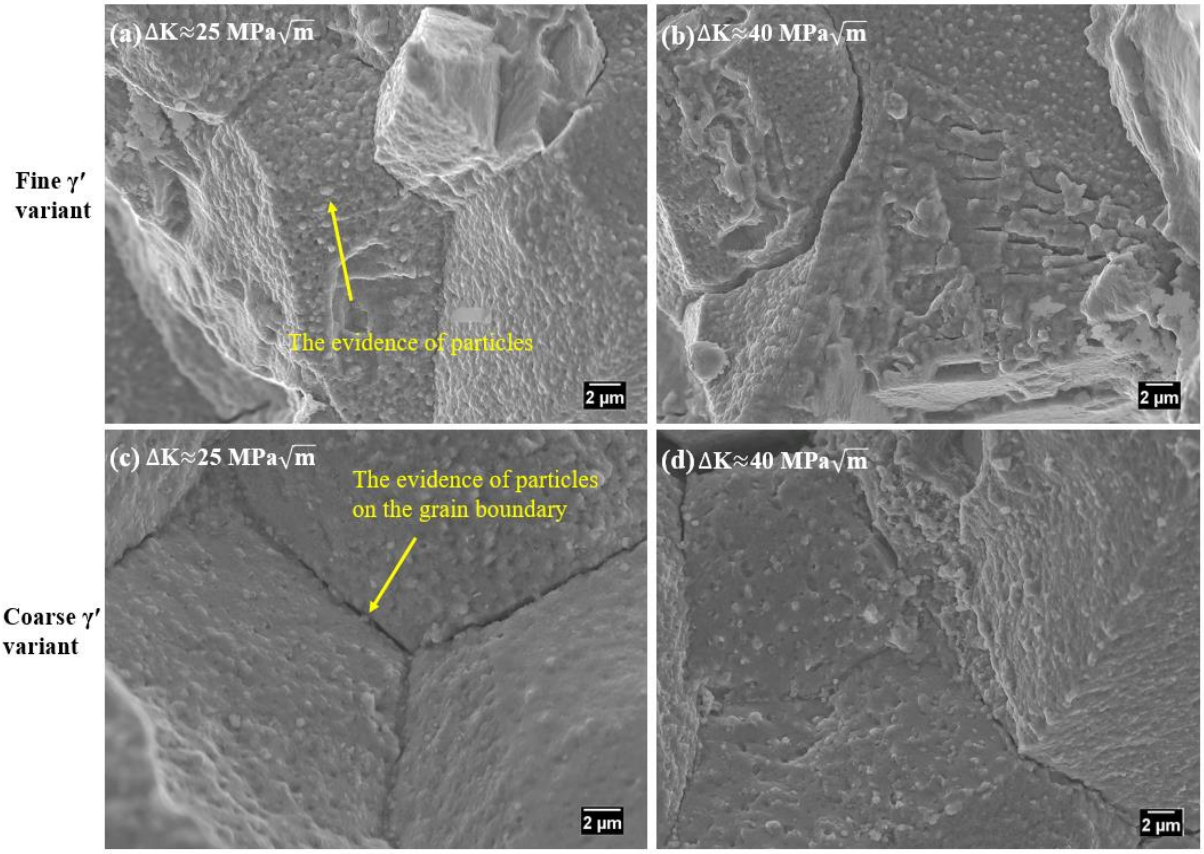

Figure 6.18: Fractography of RR1000 alloys tested with a **90s dwell** time at **650 ºC** at higher magnification; (a) and (b) features of the intergranular fracture mode at Δ*K* around 25 and 40 MPa$\sqrt{m}$ in the fine γ′ microstructure; (c) and (d) features of the intergranular fracture mode at Δ*K* around 25 and 40 MPa$\sqrt{m}$ in the coarse γ′ microstructure.

Figure 6.19-Figure 6.22 delineate the morphology of the fracture surface on both γ′ variants tested with both **1s and 90s dwell time** at **725 ºC.** It is generally seen that an intergranular fracture mode is predominant for both dwell times at a range of Δ*K* level due to the pronounced effects of higher temperature associated with more oxidation damage. As a feature of the intergranular fracture mode, a detachment of a single grain or a cluster of grains is commonly discerned in both γ′ variants with both dwell times, and is even more pronounced at increasing Δ*K* level. However, the fine γ′ variant exhibits a somewhat mixed fracture mode examined at the higher magnification as presented in Figure 6.20 (a) although it appears that an intergranular fracture mode is still dominant. A detachment event occurs more frequently with the evolution of secondary cracks at an increasing Δ*K* level. It is interesting to note that the carbides continuously formed at grain boundaries and particles on the grains (as seen in Figure 6.20 (b) and (c) and Figure 6.22) may be coarsened due to the exposure at high temperature during the testing, which can also promote weakening of the grain boundary and thereby more intergranular fracture mode. Coarsened precipitates and carbides are also seen on the fracture surface on both γ′ variants at **725 ºC**.

It is found that the number of secondary cracks on the fracture surfaces and their length generally have increased especially at increasing Δ*K* level, particularly marked in Figure 6.21 (e) and (f). The extent of secondary cracking can be attributed to the synergistic effects of a dwell time, temperature and grain boundary features, which is associated with the extent of an intergranular fracture mode. The morphology of an intergranular fracture mode and secondary cracking on the fracture surfaces are likely to be similar in both γ′ variants on both **1s** and **90s dwells** while the statistical analysis on secondary cracks will be discussed in a following section.

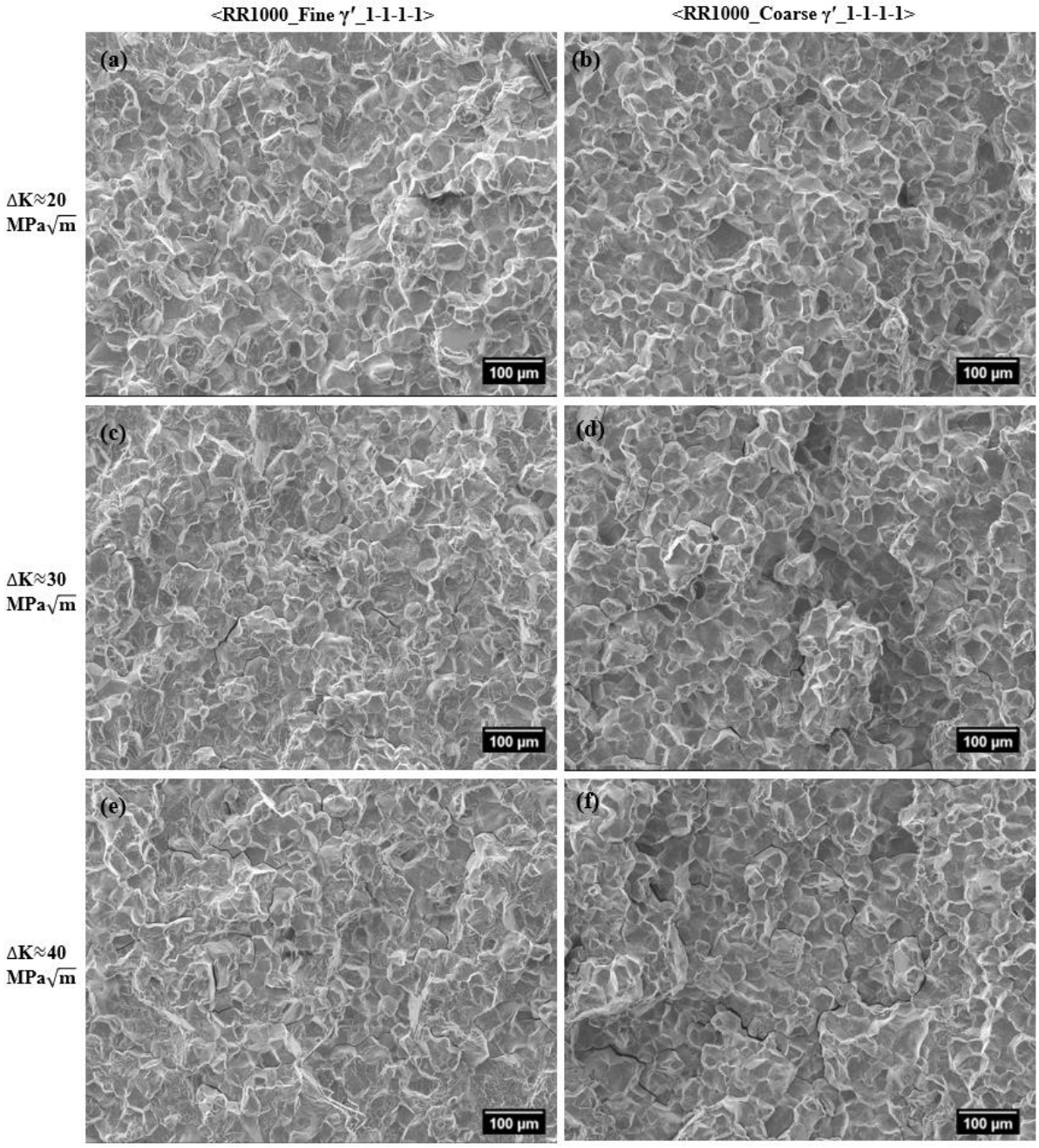

Figure 6.19: Fractography of RR1000 alloys tested with a **1s dwell** time at **725 ºC** of (a) a mixed fracture mode (predominantly intergranular) at low Δ*K* level, (c) and (e) predominantly intergranular fracture mode at increasing Δ*K* level in the fine γ′ microstructure; (b), (d) and (f) predominantly intergranular fracture mode at varying Δ*K* level in the coarse γ′ microstructure.

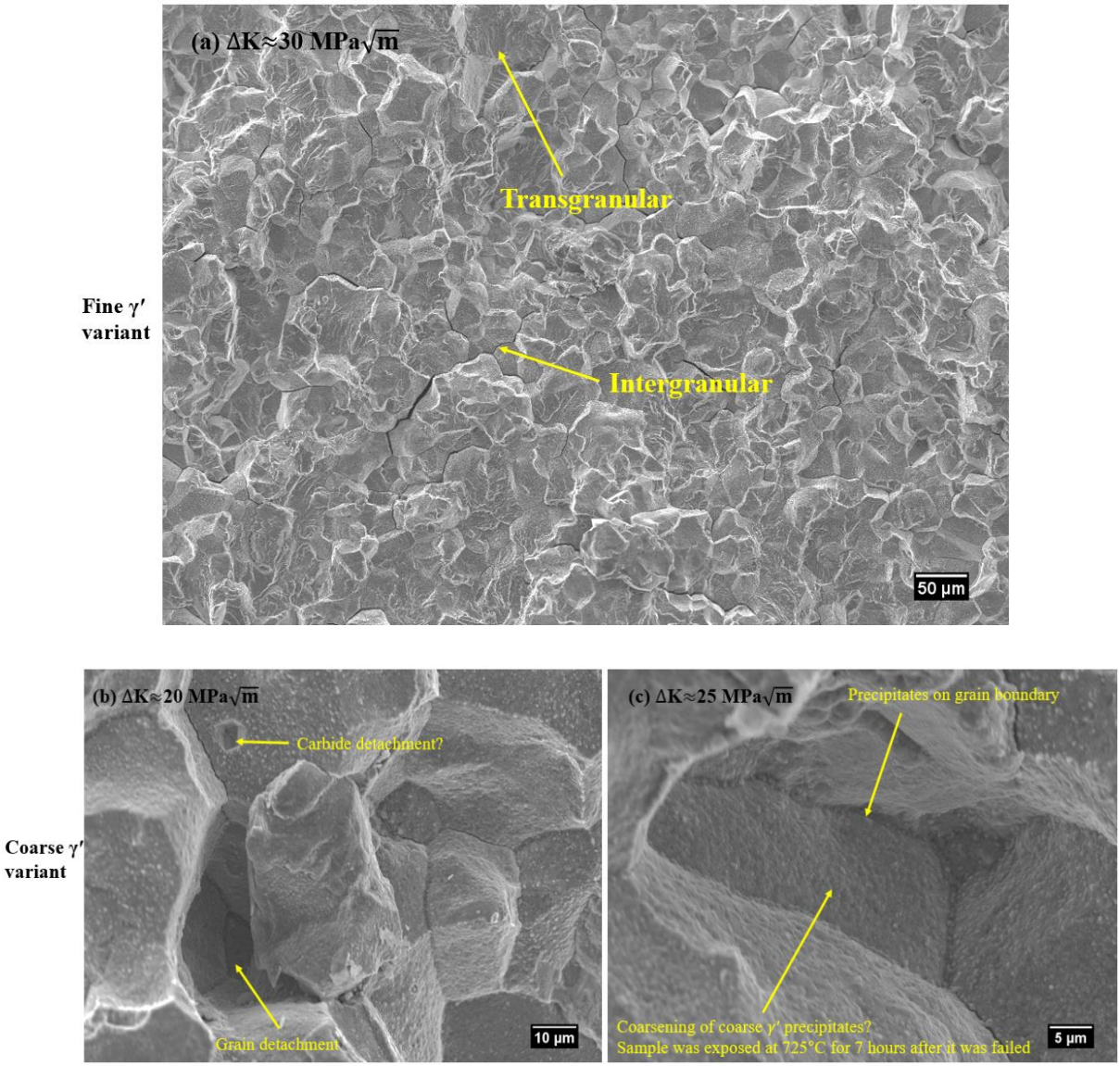

Figure 6.20: Fractography of RR1000 alloys tested with a **1s dwell** time at **725 ºC**. (a) showing a feature of the mixed fracture mode (yellow arrows) at ΔK around 30 MPa$\sqrt{m}$ in the fine γ′ microstructure (b) a detachment of carbide and grain seen at ΔK around 20 MPa$\sqrt{m}$ and (c) continuous carbide distribution on grain boundary and coarsening of precipitates observed on grain boundary at ΔK around 30 MPa$\sqrt{m}$ in the coarse γ′ microstructure;

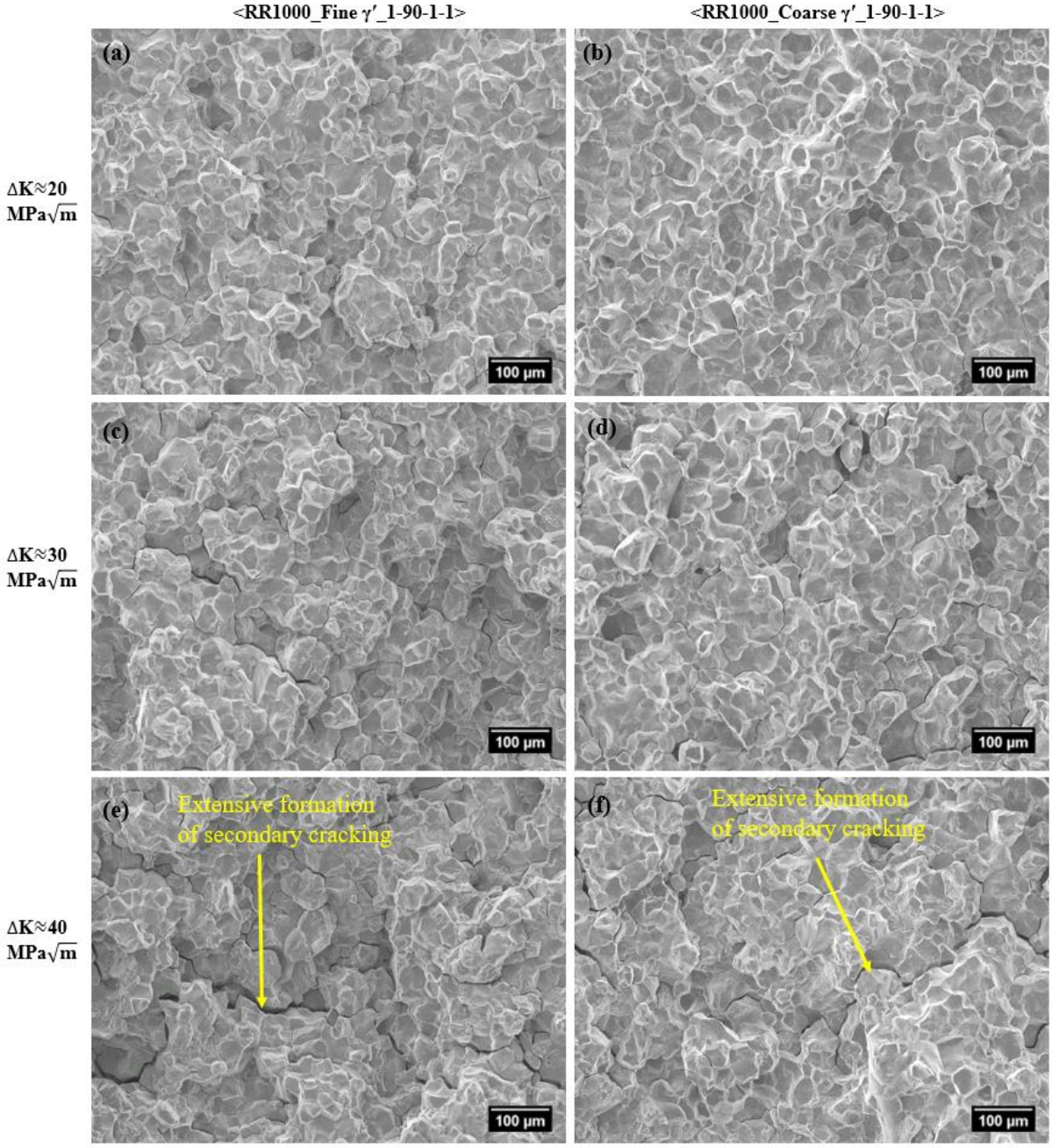

Figure 6.21: Fractography of RR1000 alloys tested with a **90s dwell** time at **725 ºC**; (a), (c) and (e) a predominantly intergranular fracture mode is observed at a range of Δ*K* levels in the fine γ′ microstructure, showing secondary cracks (yellow arrow) particularly at higher Δ*K*; (b), (d) and (f) a intergranular fracture mode is also observed at a range of Δ*K* levels in the coarse γ′ microstructure, showing secondary cracks (yellow arrow) particularly at higher Δ*K*. Note that the formation of secondary cracks seemingly increases with increasing Δ*K* level.

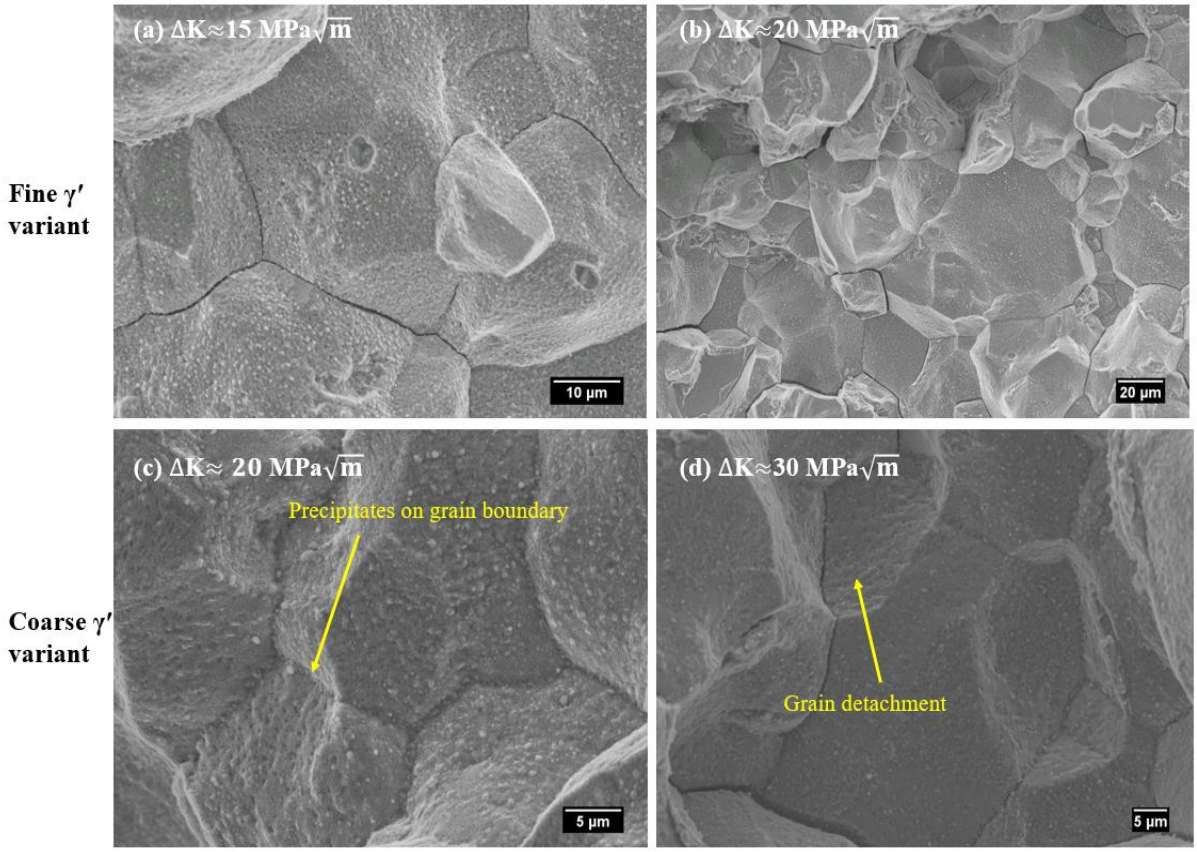

Figure 6.22: Fractography of RR1000 alloys tested with a **90s dwell** time at **725 ºC**. (a) and (b) features of the intergranular fracture mode including secondary cracks at Δ*K* around 15 and 20 MPa$\sqrt{m}$ in the fine γ′ microstructure; (c) and (d) features of the intergranular fracture mode showing continuous carbide formation at grain boundary and a detachment of grain at Δ*K* around 20 and 30 MPa$\sqrt{m}$ in the coarse γ′ microstructure.

Roughness of the fracture surface with a range of loading frequency and temperature in both γ′ variants was investigated at different Δ*K* levels by SEM with Alicona-MeX software and Alicona OM, summarised in Figure 6.23 and Figure 6.24. Figure 6.23 represents the results of roughness obtained by Alicona OM across a wider area covering more of a range of Δ*K* and lower magnification than SEM Alicona-MeX evaluations although it shows similar trends with SEM-Mex analysis. At **650 ºC** under **1s dwell,** it is seen that the fracture surfaces are generally rougher as Δ*K* level increases except for the fine γ′ variant. Here a decrease in S_a (average height of selected area) in the fine γ′ variant is closely associated with the early transition from intergranular to transgranular fracture mode as Δ*K* level increases. However the fracture surface becomes slightly rougher when the Δ*K* level changes from 30 to 40 MPa$\sqrt{m}$, which might result from more secondary crack evolution at higher Δ*K* level. The S_a of the coarse γ′ variant with **a 1s dwell** and the fine γ′ variant with **a 90s dwell** gradually increases with an increasing Δ*K* level, which is also attributed to increasing secondary crack evolution. In the coarse γ′ variant with **a 90s dwell**, the overall roughness of the fracture surface with varying Δ*K* level was higher than that of all other samples and the roughness

significantly increased when ΔK level reached 40 MPa$\sqrt{m}$. This can be ascribed to more secondary crack evolution with longer and tortuous cracks observed with a long dwell time in the coarse γ′ variant. In addition, cavities arising from a single or multiple grain detachment at high ΔK level as seen on the fracture surfaces might further influence the roughness.

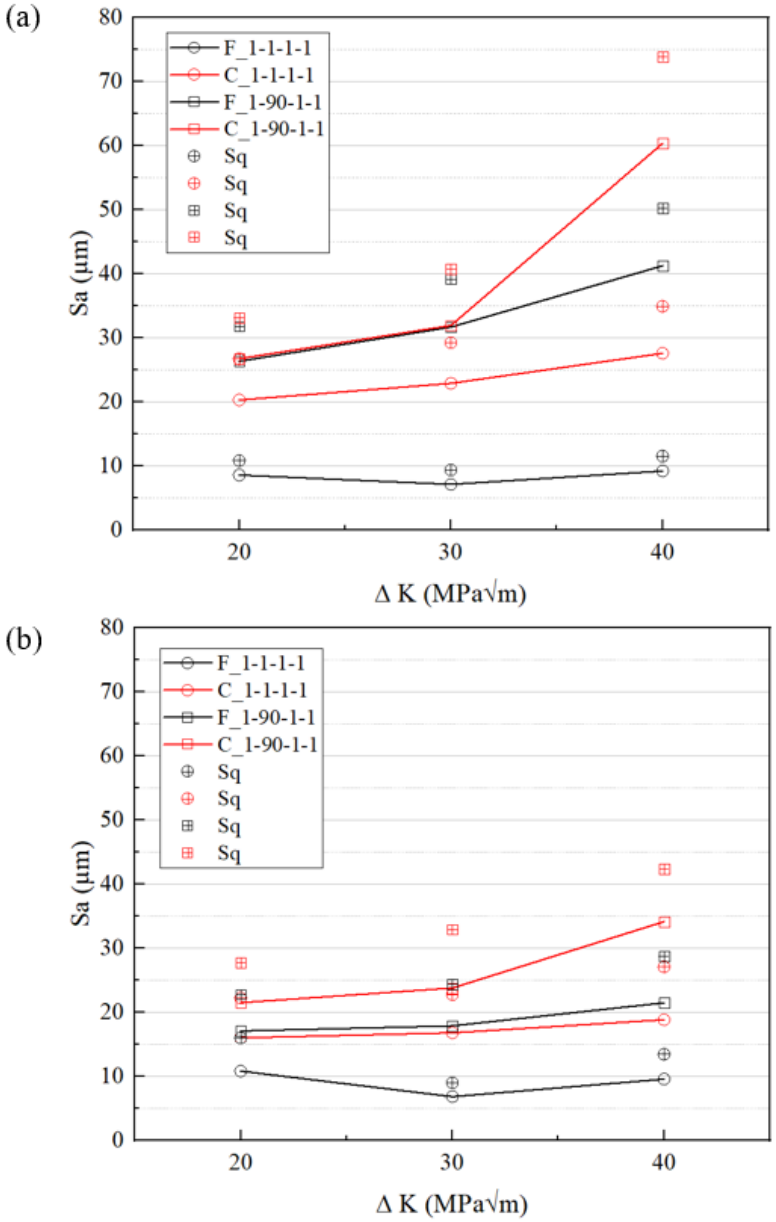

Figure 6.23: S_a and S_q of dwell fatigue tests with a range of loading frequency at **650 ºC** by (a) Alicona optical focussing techniques (b) SEM-MeX.

In order to allow comparison between different temperatures, the roughness was measured by SEM-MeX on both γ′ variants at **725 ºC** as seen in Figure 6.24. In general, the fracture surfaces at **725 ºC** are rougher at varying ΔK levels with a less scattered trend than the results at **650 ºC**. It is worth noting that the highest roughness obtained from a range of testing conditions is between 30-35 µm, which can be associated with the average grain size of the alloys. The roughness of the coarse γ′ variant with a **90s dwell** was expected to be significantly increased due to an enhanced intergranular

fracture mode induced by a combined factors of higher temperature, longer dwell time and continuous carbide distribution on grain boundary. However, it does not increase considerably but exhibits a roughness comparable with the average grain size. This can be ascribed to a saturation of the fracture surface roughness related to 100% intergranular fracture meaning the fracture surface maximum roughness is linked to the grain size of the alloys.

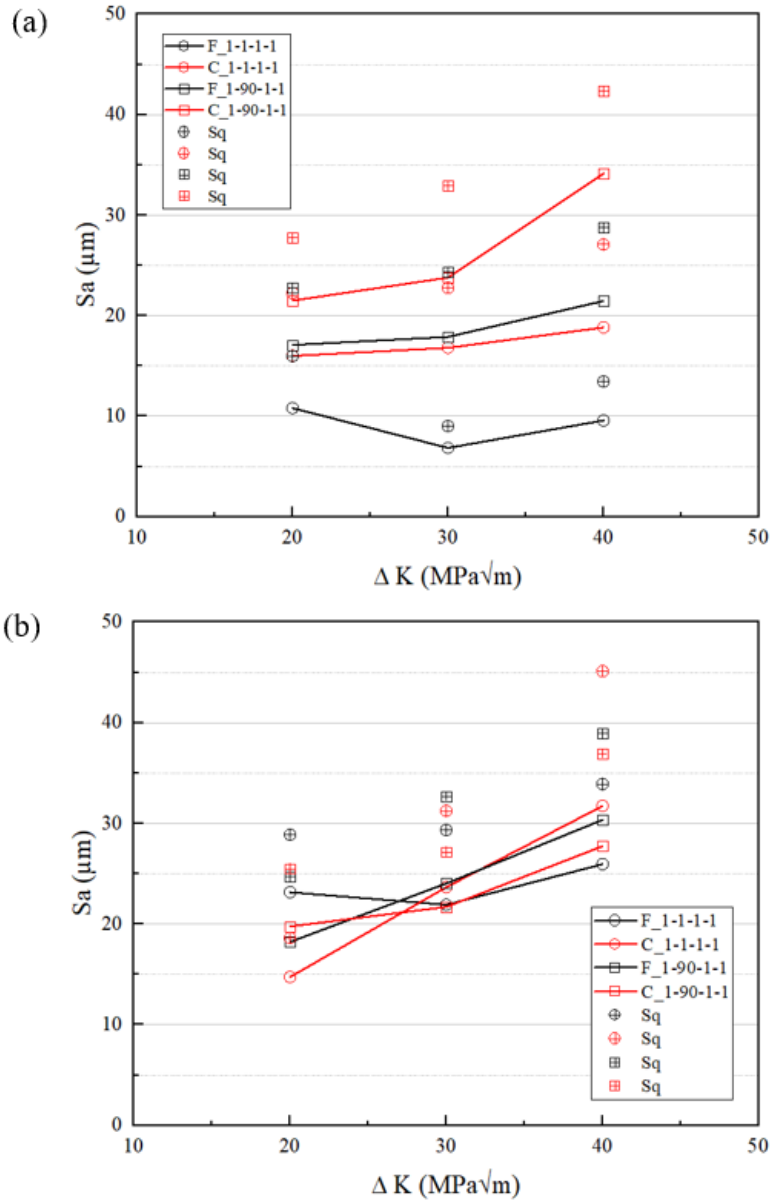

Figure 6.24: Sa and Sq of dwell fatigue tests with a range of loading frequency by SEM-MeX (a) at **650 ºC** and (b) **725 ºC**.

6.3.3 Morphology and statistical analysis on secondary cracks

Morphologies of the secondary cracks of both γ′ variants with testing condition under a **90s dwell** time at **650 ºC** are examined and presented in Figure 6.25-Figure 6.27. In Figure 6.25 (a) and (b), a secondary crack with oxidation that has clearly formed at the grain boundary along the crack path and also ahead of a crack tip in the fine γ' variant, which has propagated and penetrated perpendicular to the fracture surface. The secondary crack observed in the fine γ' variant has propagated along the boundary before being arrested within it. In Figure 6.25 (c) and (d), some voids and porosity also appear to have formed along the secondary crack and near the crack tip of the coarse γ′ variant. EDX mapping has been carried out on the secondary crack of the fine γ′ variant (Figure 6.25 (a)) and the results are shown in Figure 6.26. Oxidation is evident at the grain boundary along the secondary crack and Cr, Ti, Al, Ni, Co oxidation seems dominant across the surface. The oxides formed at the crack tip include external layers of NiO/CoO and internal layers of $Cr_2O_3/TiO_2/Al_2O_3$ in RR1000 alloy [140].

A longer secondary crack penetrating the subsurface behind the fracture surface and propagating along a few grains in the coarse γ′ variant is seen in Figure 6.27. It can be seen that continuously linked microvoids and oxides are formed along the crack path and ahead of the crack tip. This may reflect damage accumulation on the grain boundary or carbides which have fallen out of the grain boundary during oxidation processes or on etching. This is more marked for the coarse γ′ variant which has a more continuous grain boundary carbide distribution. It is also observed that the secondary crack penetrated through the carbide as seen in the vicinity of the beginning of the secondary crack evolution.

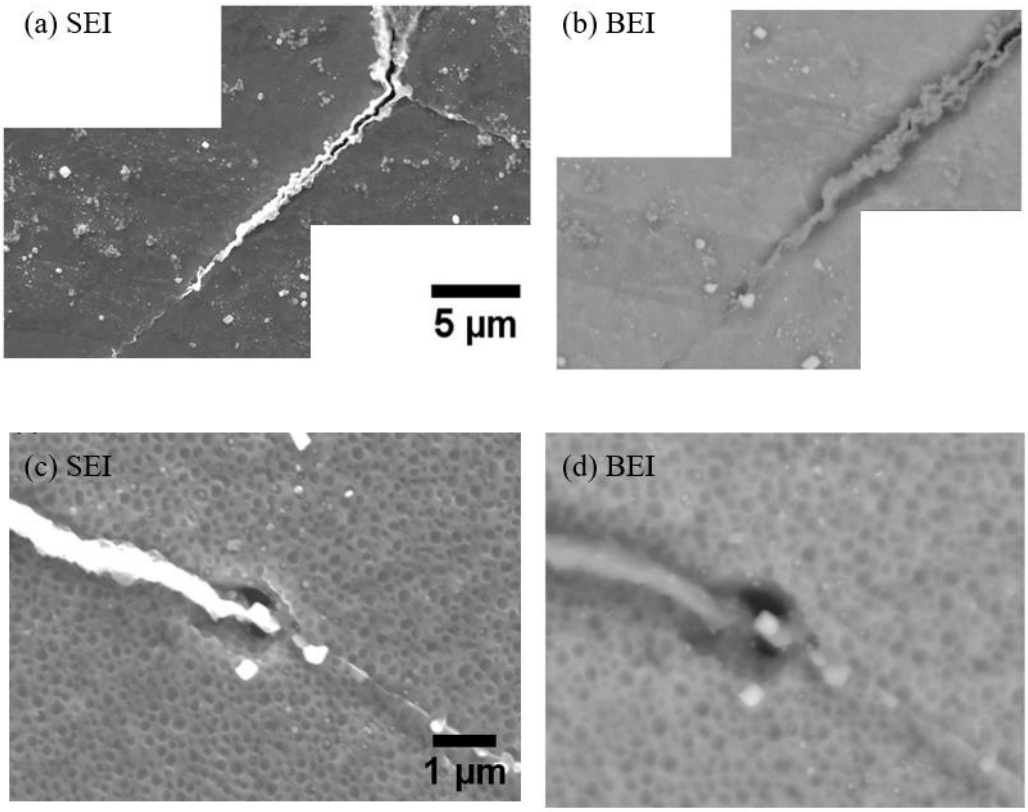

Figure 6.25: Morphology of a secondary crack tip of tests with a **90s dwell** time at **650 ºC** by (a) SEI image (b) BEI image on the fine γ′ variant (c) SEI image (d) BEI image on the coarse γ′ variant.

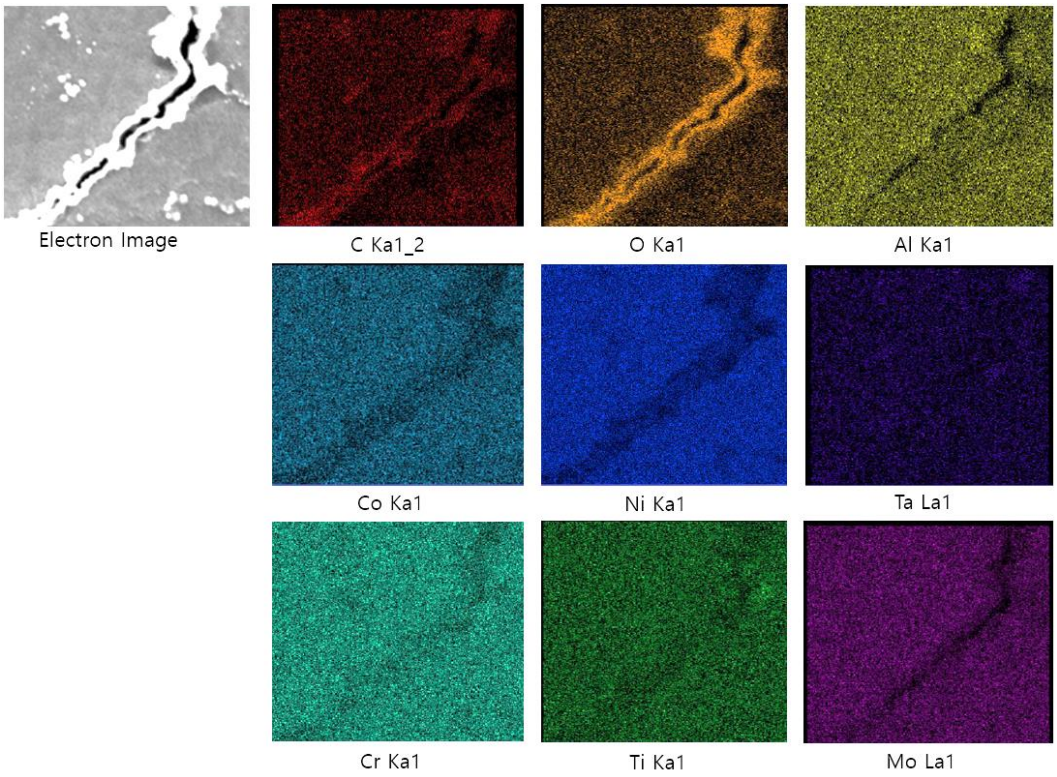

Figure 6.26: EDX mapping on the secondary crack of Figure 6.25 (a) representing the morphology of the oxidation formed along the grain boundary by elemental composition analysis.

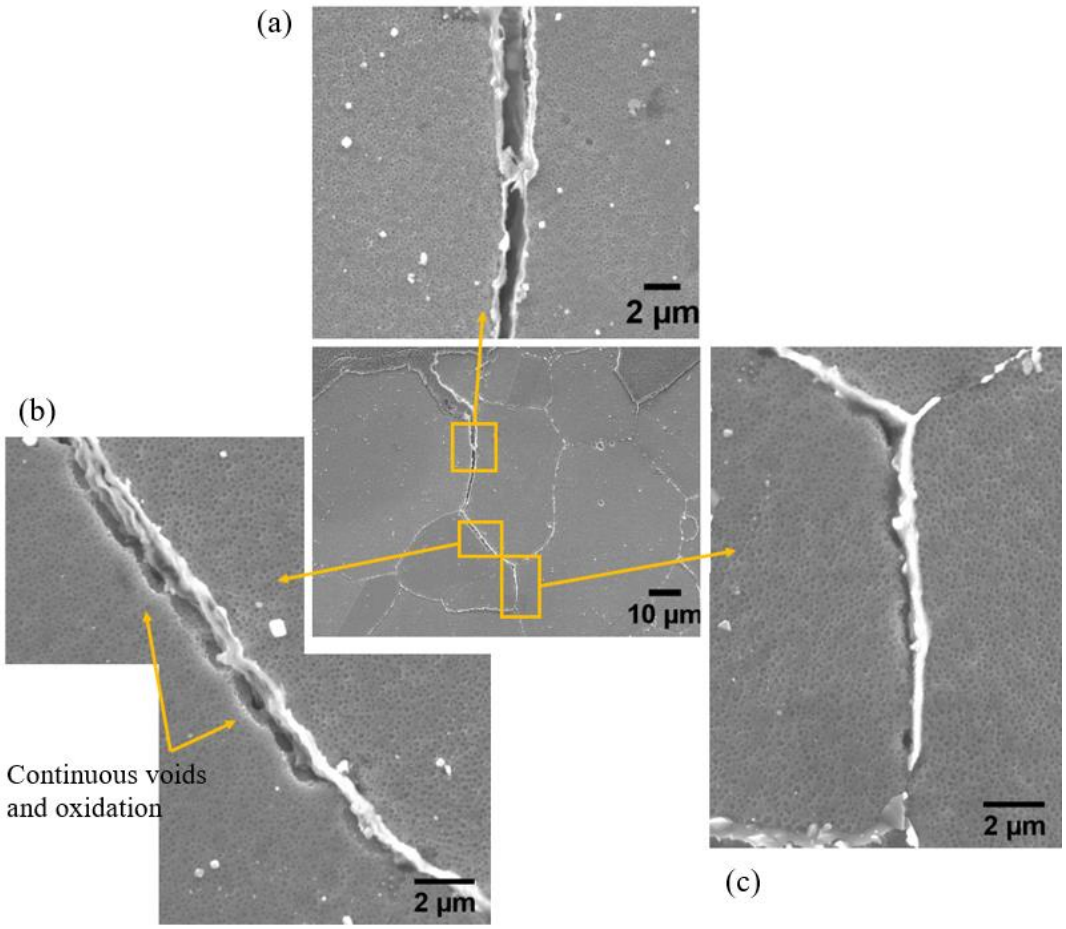

Figure 6.27: Morpholgy of a longer scale of secondary crack, crack tip and γ′ precipitates propagated through a few grains of the coarse γ′ variant tested with a **90s dwell** time at **650 ºC**. (a) secondary crack that seems to penetrate a carbide, (b) crack growth with contiuous formation of voids and oxides and (c) the secondary crack and crack tip area.

The comparison of the average secondary crack length (Figure 6.28) was systematically conducted on the fracture surfaces of both γ′ variants by assessing SEM images at the same magnifications at a range of Δ*K* level at **650 ºC** and **725 ºC**. Examples of the formation of the secondary cracking on the fracture surface are seen in fractography analysis in the previous section. At **650 ºC**, the average length of secondary cracks under both dwell times generally shows an increasing trend with an increasing Δ*K* level except for the case of the fine γ′ variant under a **1s dwell** exhibiting a decreasing trend. This is ascribed to significant oxidation damage on the grain boundary and consequent crack coalescence of the secondary cracks being greater in the coarse γ′ variant with longer dwell time. On the other hand, the apparent transgranular features of the fine γ′ variant with a **1s dwell** at high Δ*K* level gives rise to less occurrence of secondary crack formation. It is interesting to note that the trend of the secondary crack length is comparable with that of the roughness measured by SEM-MeX as shown in Figure 6.24 (a). The average secondary crack length under both dwell times at **725 ºC** appears to be slightly longer than at **650 ºC** while the trend is quite different. It is expected the secondary crack length of the coarse γ′ variant with a **90s dwell** at **725 ºC** will be longer than others due to the synergistic effects of a longer dwell time and continuous carbide distribution at higher

temperature. However, it was only slightly increased at ΔK of 30 MPa$\sqrt{m}$ but decreased back down at a ΔK of 40 MPa$\sqrt{m}$. This can be related to high FCG rate and consequently a shorter diffusion time within a constant crack length increment, which results in less formation of secondary cracks.

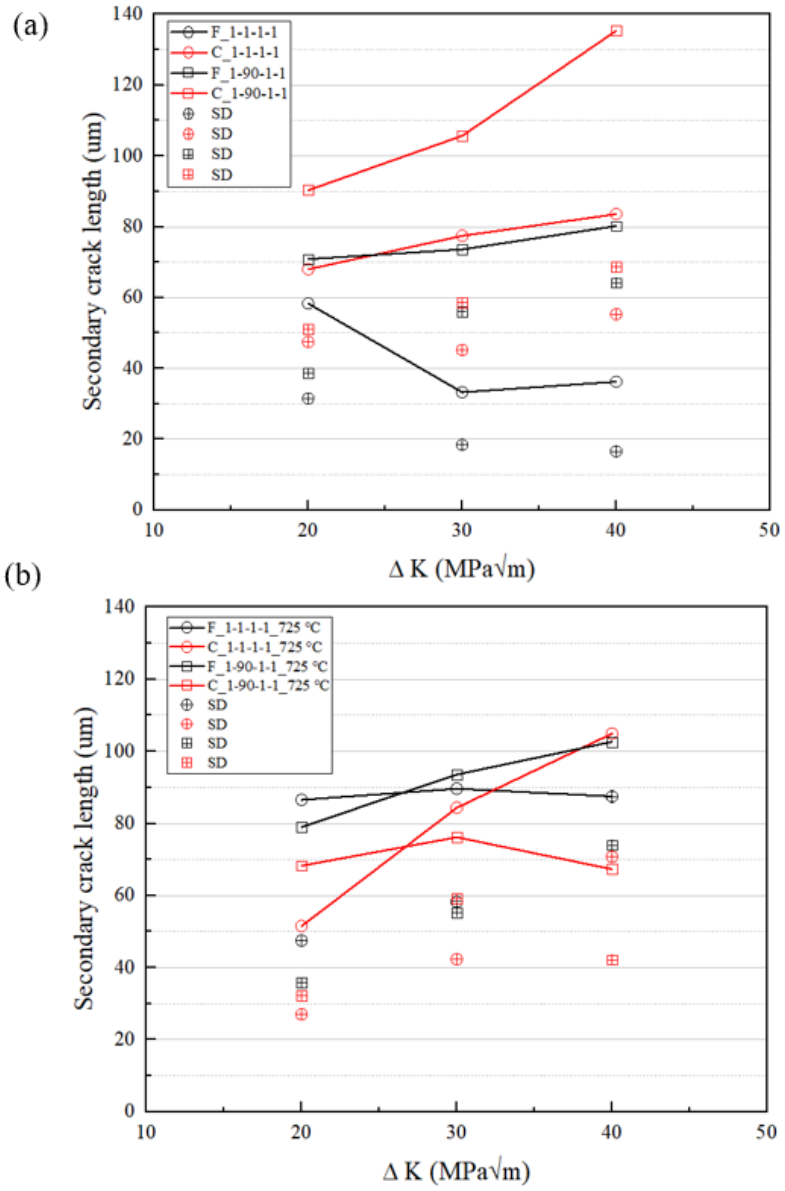

Figure 6.28: Statistic of average secondary crack length of fatigue tests (a) at **650 ºC** (b) at **725 ºC**.

6.3.4 Oxidation damage zone analysis - alternating dwell test (block test)

Alternating dwell tests which were termed as 'block tests' were carried out on both γ′ variant alloys at 650 ºC to examine the damage zone formed during a **90s dwell** time as seen earlier in Figure 6.12 showing the jump of the PD value (corresponding to the crack length) on the unload/reload step. Two

loading frequencies are selected for the block test based on the results from the long FCG tests by showing distinct features of the cycle and time dependent crack growth at frequencies of 5Hz and 1-90-1-1 at 650 ºC, respectively. Figure 6.29 and Figure 6.30 represent the raw PD values of the loading blocks of the frequencies during the tests and the transitions (between low and high frequency regimes) are marked in the figures. It is indicated that the damage zones formed at two transitions of the fine γ′ variant are marginal as seen in zoomed-in graphs of Figure 6.29. On the other hand, the apparent jump of the PD values in the transitions of the coarse γ′ variant is observed when the frequency is changed from a **90s dwell** to a **5 Hz** loading. This is associated with significant microstructural effects of the coarse γ′ variant and the oxidation damage ahead of the crack tip. The damage zone size of the first and second transition of the coarse γ′ variant was estimated by a post calculation and calibration process by transforming the PD values to the actual crack length. The estimated damage zone sizes of 0.04 mm and 0.277 mm at ΔK of 22 and 36 MPa$\sqrt{\text{m}}$ for the first and second transition were respectively obtained. It appears that the damage zone size of the second transition was significantly greater than the first transition as seen in zoomed-in plots in Figure 6.30, which can be ascribed to the higher crack driving force (evidenced by the enhanced FCG rate) at higher ΔK level associated with a larger crack tip damage zone.

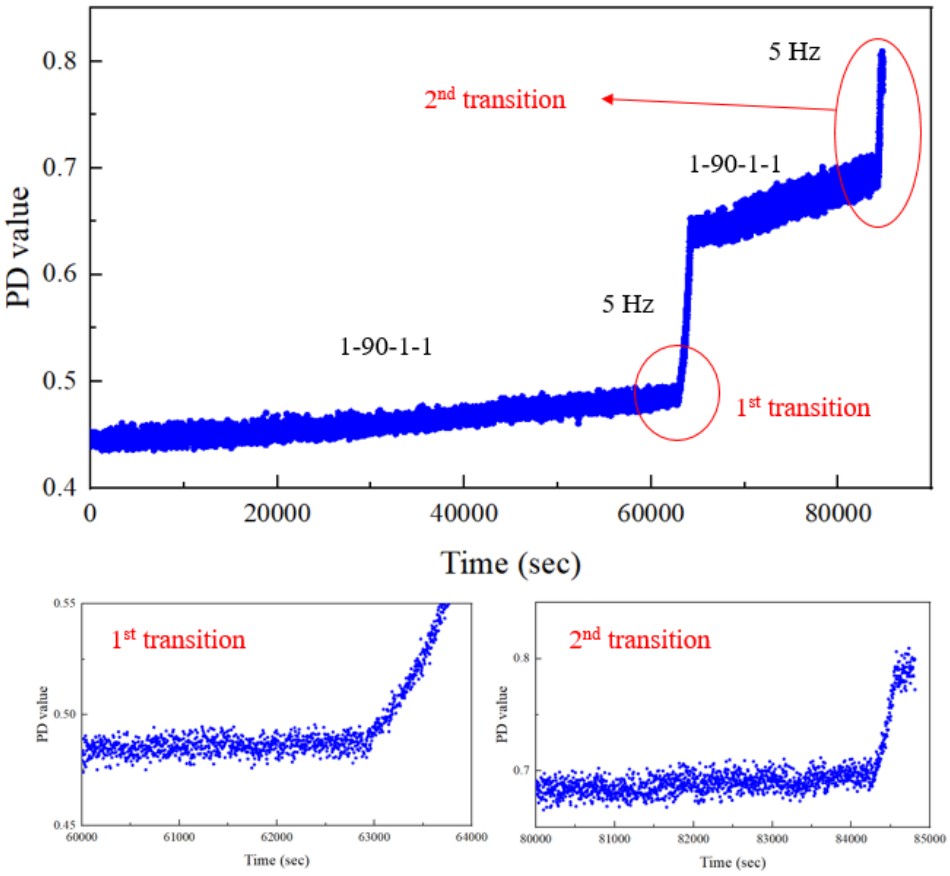

Figure 6.29: PD value over time of the block tests on the fine γ′ variant showing two transitions.

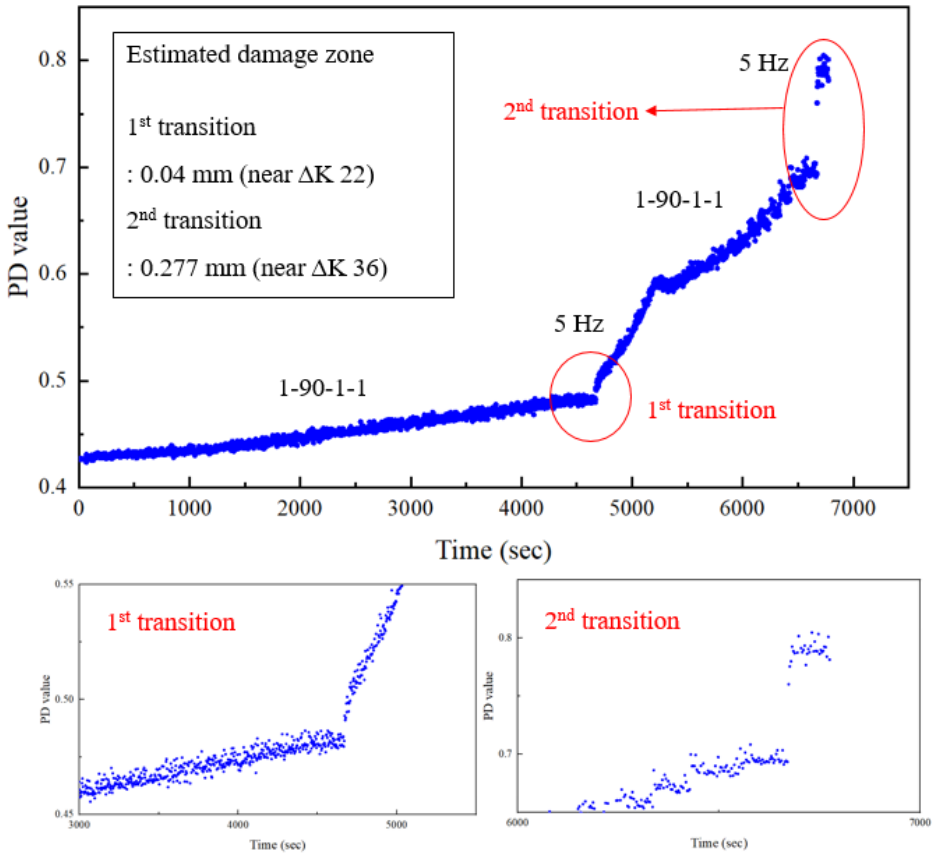

Figure 6.30: PD value over time of the block tests on the coarse γ′ variant showing two transitions.

The FCG rates (*da/dN*) over a range of Δ*K* levels were obtained from the post-test calibration on final fracture surface observations applied to the raw PD values of both γ′ variants as shown in Figure 6.31. The FCG rates of the two different loading frequencies of **1-90-1-1** and **5 Hz** are likely to follow the linear line plotted for each frequency respectively in the steady state, as discovered from the long FCG tests earlier. The two transitions from time to cycle dependent crack growth regime were obtained at Δ*K* levels of around 20 and 30 MPa$\sqrt{m}$ as marked in Figure 6.31. In the first transition (of both γ′ variants), the FCG rate of the subsequent cycle dependent **5Hz** regime is higher than the trend of the steady-state **5Hz** data immediately after switching the frequency from time dependent to cycle dependent crack growth. The cycle dependent FCG rate of both γ′ variants then decreased, possibly due to the fresh crack wake effects caused by the oxidation damage zone and then returned to the expected trend line of the **5Hz** frequency once sufficient cycle dependent crack wake had been developed. In the second transition of the fine γ′ variant, the **5Hz** FCG rate was slower than the steady state **5Hz** trend line and then returned to the expected trend line of cycle dependent crack growth. This can be linked to increased crack wake effects (greater shielding due to prior crack path tortuosity offsetting any oxidation damage ahead of the crack-tip). In the second transition of the coarse γ′ variant, the cycle dependent crack has propagated faster than the expected trend line and shown faster

crack growth at high ΔK levels. This appears to be related to the greater oxidation damage on the grain boundary with a continuous carbide distribution and the concomitant intergranular fracture mode observed in the coarse γ′ variant at higher ΔK levels.

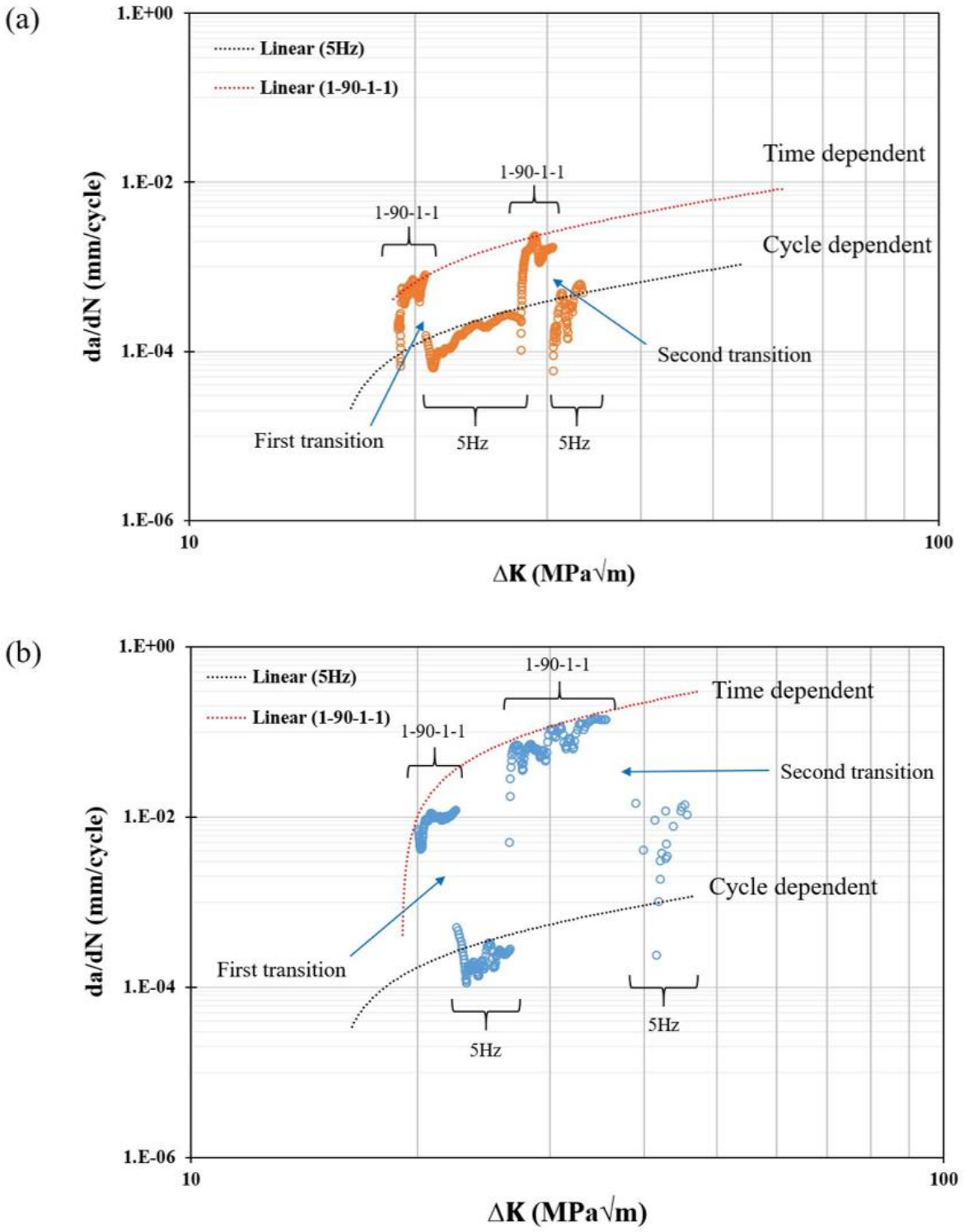

Figure 6.31: FCG rates verses ΔK of the block test of (a) the fine γ′ variant (b) the coarse γ′ variant at 650 ºC.

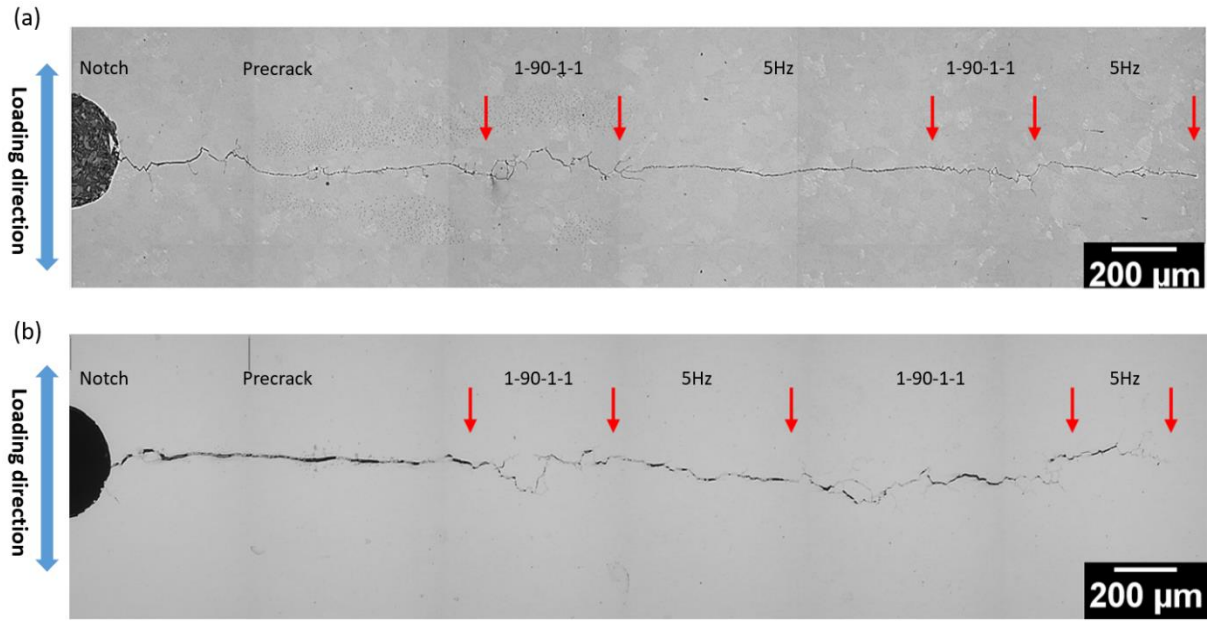

Figure 6.32: Morphology of crack path by OM images (a) the fine γ′ variant and (b) the coarse γ′ variant, showing the time dependent crack growth path is more tortuous than cycle dependent crack growth path.

Figure 6.32 shows the morphology of the crack path in the mid-section of both γ′ variants at **650 ºC**. The crack path includes a pre-crack initiated from the notch perpendicular to the loading direction applied, followed by the fatigue crack propagation of each frequency. The red arrows in the figure point out the start and end of the different regimes of each loading frequency. More tortuous crack growth was observed during time dependent crack growth (**a 90s dwell**), indicating a more intergranular fracture mode caused by oxidation related damage due to the longer dwell time. In terms of the cycle dependent crack growth (**5 Hz**), the crack tends to have a flatter crack path, linked to the features of a transgranular fracture mode. The fracture surfaces of both γ′ alloys of the block tests were examined by optical macroscopy and SEM (Figure 6.33). Macroscopic images are labelled by the different regimes and transition areas were observed with a higher magnification of SEM. Frequencies of **1-90-1-1** and **5 Hz** represent distinct intergranular and transgranular fracture mode respectively as seen in the long crack test at constant load amplitude. The transitions from intergranular to transgranular are clearly seen in Figure 6.33.

It is found that there are some slip bands near the crack tip and cracking along the grain boundary in both γ′ variants by optical microscopic images (Figure 6.34). It is noted that discontinuous cracks on the grain boundary are formed adjacent to the crack tip. However, it was hard to see the oxidation damage in the slip bands with microscopy or SEM analysis due to low resolution while oxidation formation can be examined based on contrast differences in the SEM and EDX work. It would be interesting to conduct further TEM analysis to investigate the effects of oxidation on the slip bands in detail as a future work.

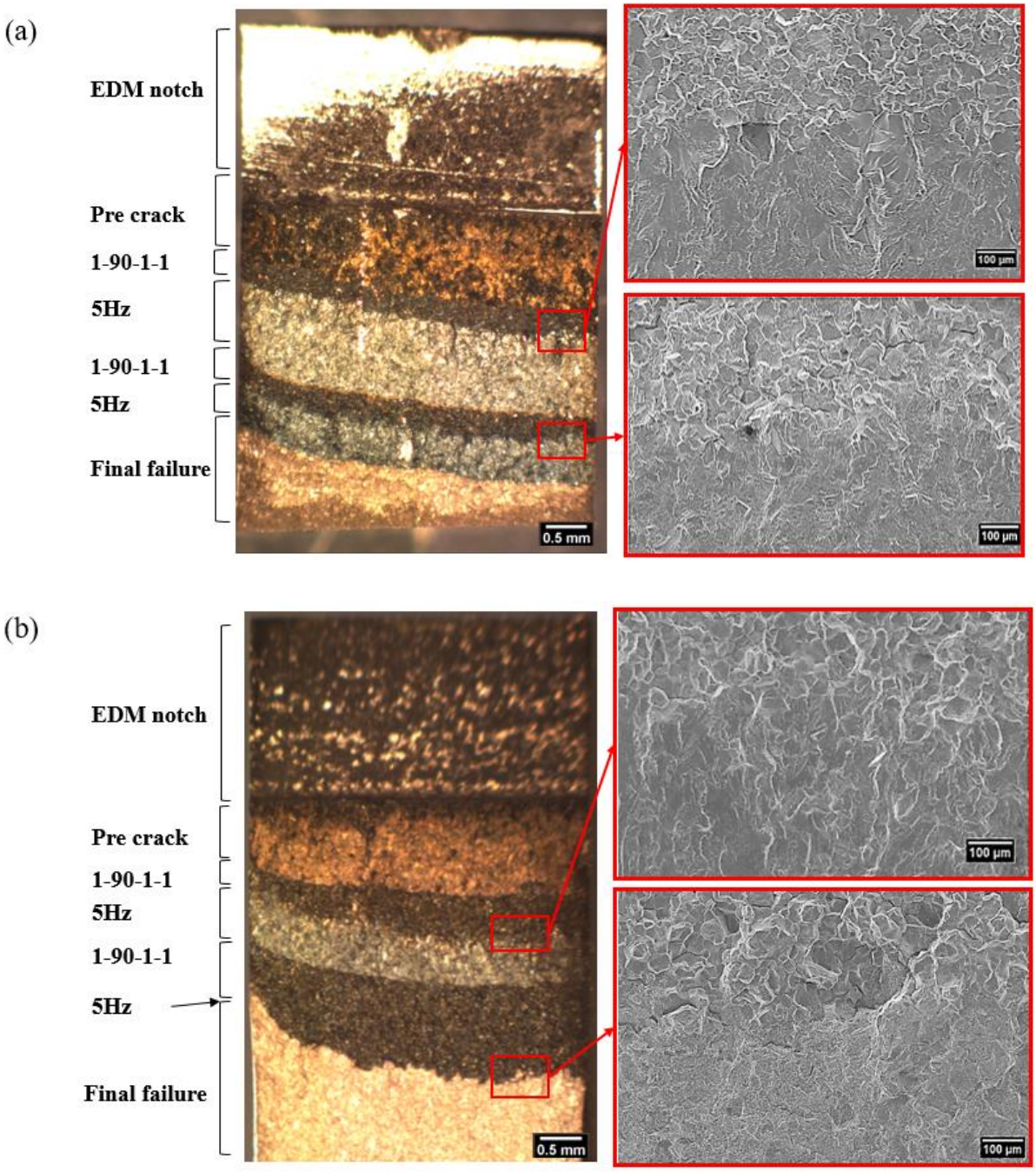

Figure 6.33: Macroscopic images of half of the fracture surface showing the different regimes and associated SEM images of the two transitions of (a) the fine γ′ variant and (b) the coarse γ′ variant.

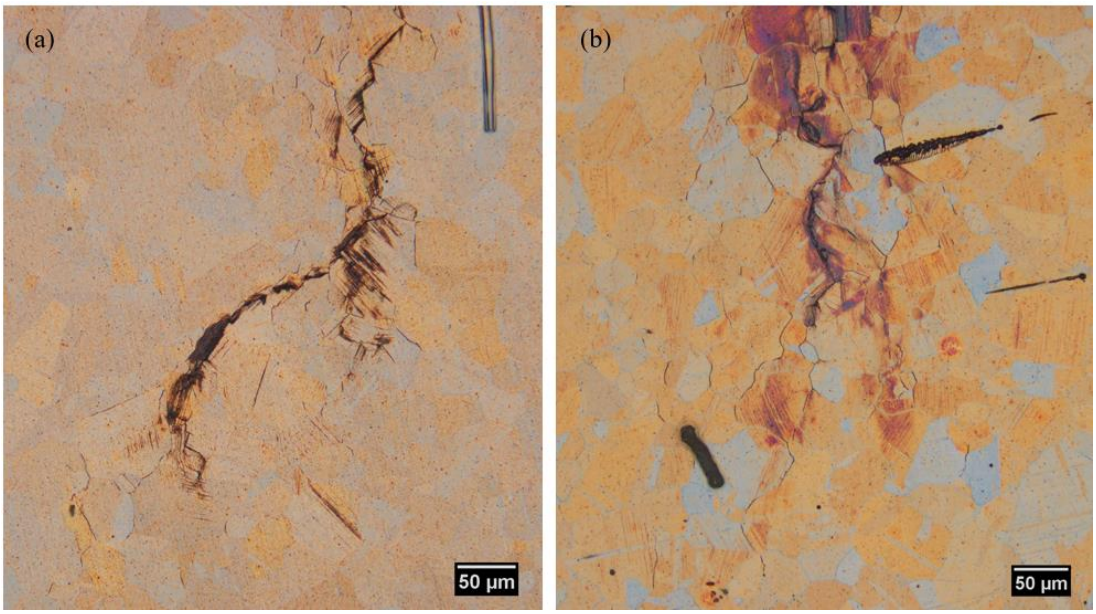

Figure 6.34: A crack tip region showing cracking through the grain boundary after the block test (a) the fine γ′ variant (b) the coarse γ′ variant exhibiting more discontinuous cracks.

Examples of a series of 2D slices including the crack path on the matchsticks of the block tests on both γ′ variants alloys at 650 ºC were obtained by X-ray CT scan as shown in Figure 6.35. The crack path represents the pre-crack from the notch and crack segments of different frequencies. The segments of the pre-crack and **5 Hz** has a relatively flat crack path whilst tortuous crack paths are seen in the **1-90-1-1** loading. It is interesting to note that the secondary crack formation and uncracked ligament by discontinuous cracks can be discerned in the time dependent crack growth regimes, especially at high ΔK level ahead of the crack tip of the coarse γ′ variant during a **90s dwell (**Figure 6.35 (b)).

3D rendering from a series of 2D slices of both γ′ variants is processed and reconstructed by imaging software packages as illustrated in Figure 6.36 and Figure 6.37 with differently angled views, showing overall geometry and roughness of the crack path of each frequency regime. It is indicated that an intergranular fracture mode with a rough crack path is apparent during a **90s dwell** while a transgranular fracture mode with a flatter crack path is dominant in a **5 Hz** frequency. Uncracked ligaments formed by discontinuous cracks in a 3D morphology at the crack tip area are found to be especially marked in the coarse γ′ variant in Figure 6.37. This can be attributed to the effects of noticeable oxidation damage ahead of the crack tip and on grain boundaries with a continuous carbide distribution giving rise to enhanced intergranular FCG behaviour. Discontinuous cracking formed along the grain boundary is also observed by macroscopic images as seen in Figure 6.34. It is seen that the formation of tortuous secondary cracks which have propagated off the direction of the main crack path is captured in the time dependent crack growth regimes at increasing ΔK level as seen in Figure 6.37.

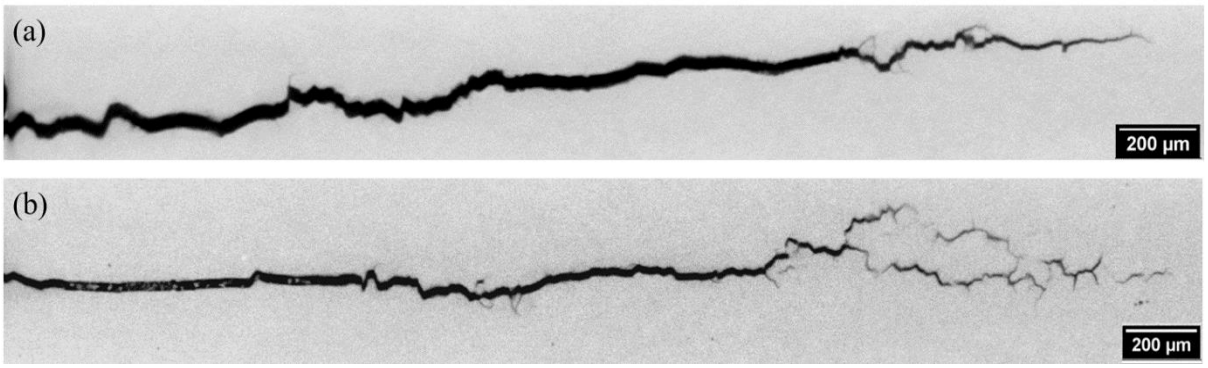

Figure 6.35: Examples of 2D slices obtained from CT scanning showing fatigue crack path of the block tests (a) the fine γ′ variant (b) the coarse γ′ variant.

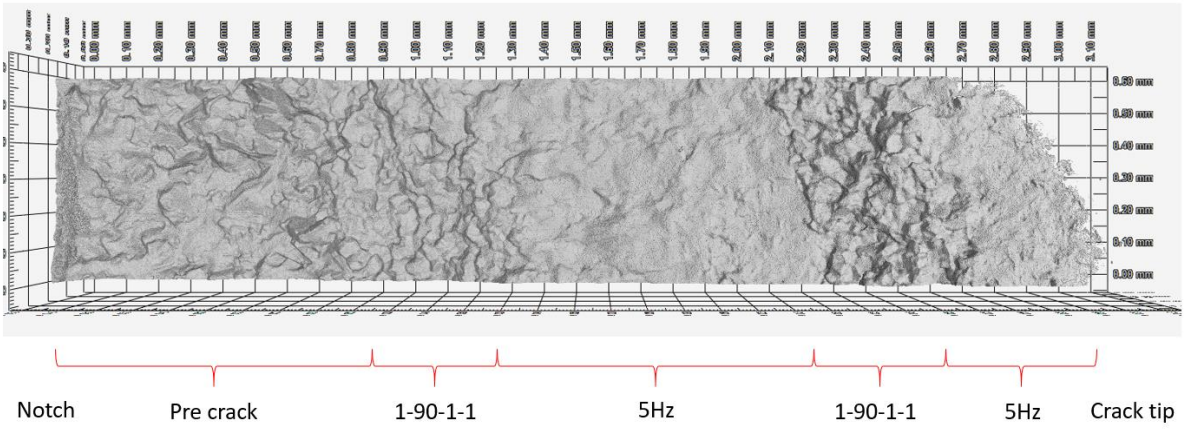

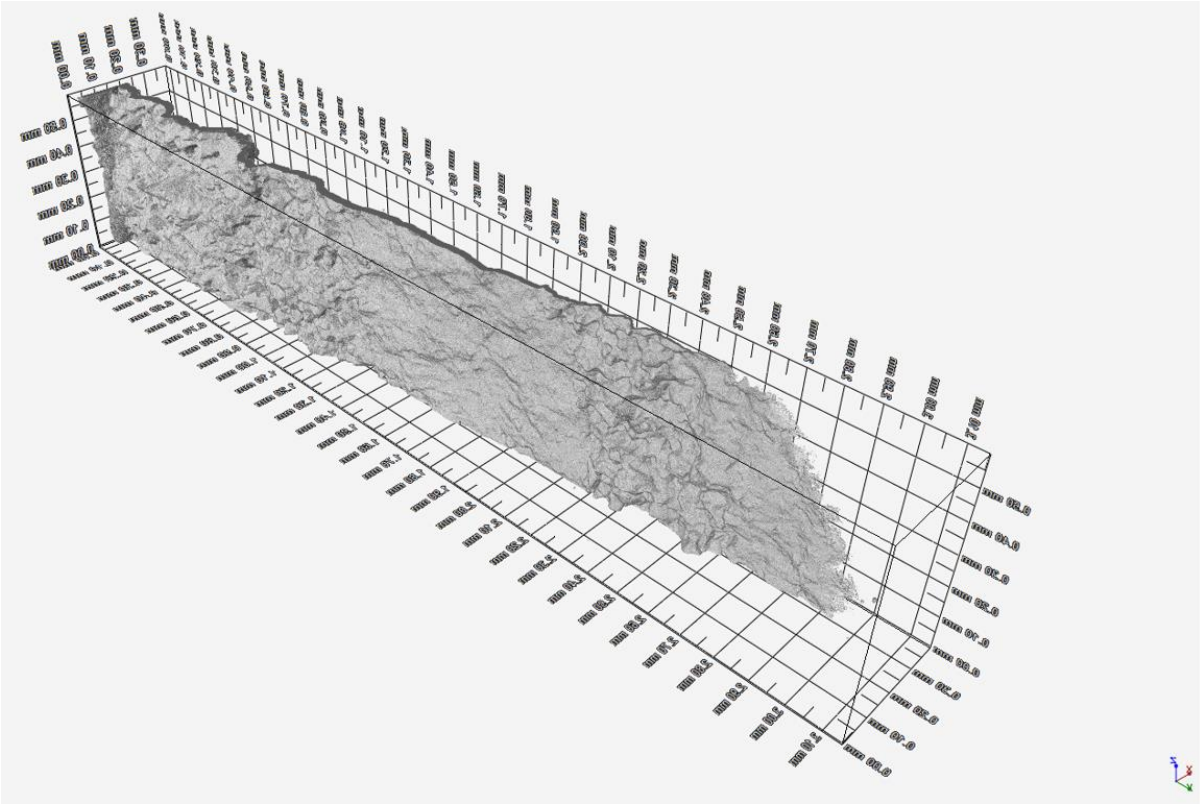

Figure 6.36: 3D morphology of the crack path of the block test on the fine γ′ variant with different angles.

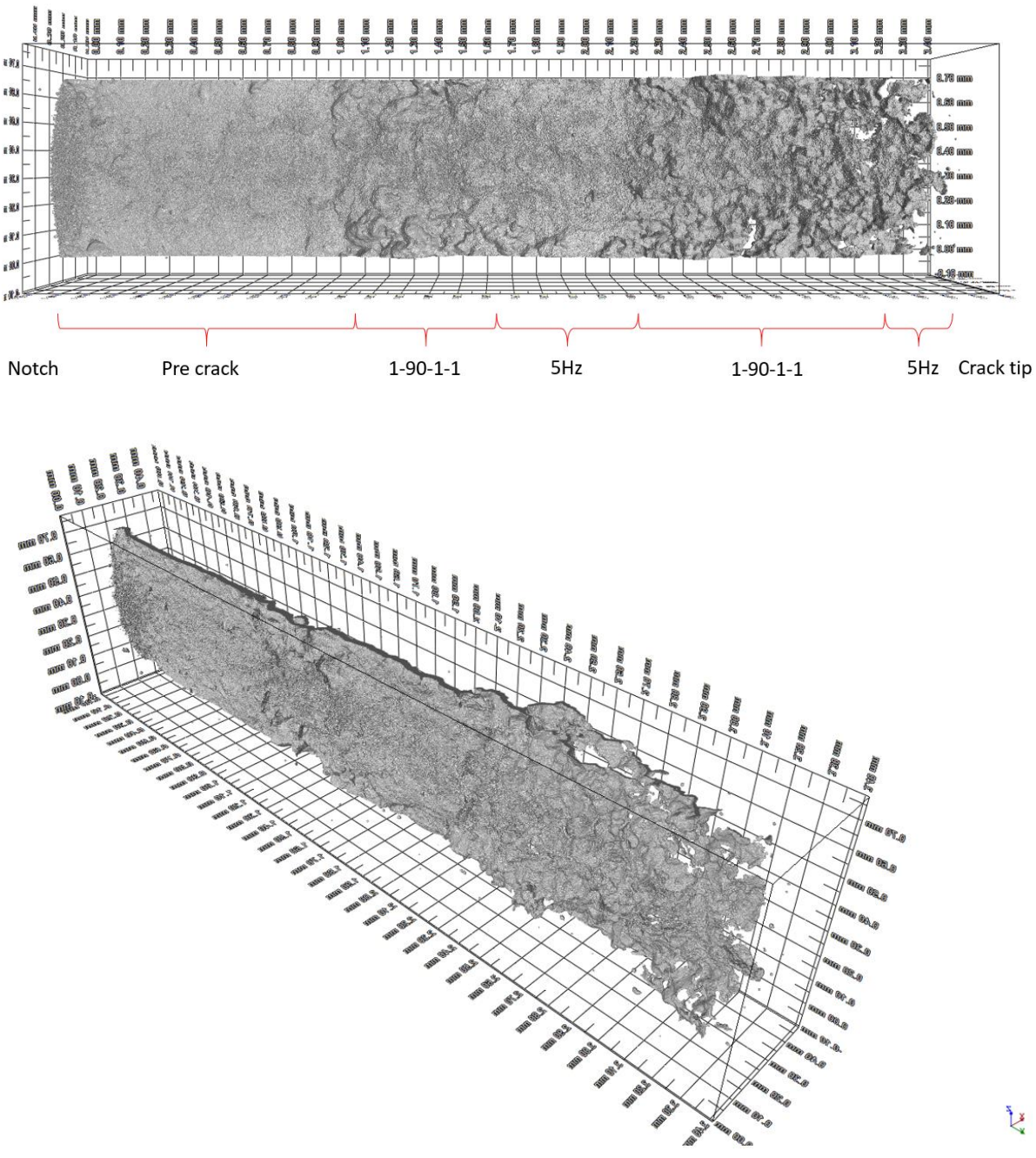

Figure 6.37: 3D morphology of the crack path of the block test on the coarse γ′ variant with different angles.

6.3.5 Loading & reloading / holding time tests at elevated temperatures

Raw PD data of a **90s dwell** on both γ′ variants at **650 ºC** and **725 ºC** was plotted over the testing times as seen in Figure 6.38. Overall, the PD value represents a gradually increasing trend at the beginning of the testing and escalates before the final failure (at high Δ*K* levels). This is pronounced on the test with longer dwell time (**a 90s dwell)** at higher temperature (**725 ºC)** by indicating a surge

of the PD value just before the final failure, which means the crack propagation has accelerated. As briefly mentioned earlier in Figure 6.12, an interesting feature of the PD data was found before the final failure, showing a jump of the PD value between the loading blocks of **1-90-1-1** during unloading and reloading. The crack length was calculated from the raw PD value after a post calibration and plotted over the testing time by focusing on the features in Figure 6.39. It is seen that the crack length of the fine γ′ variant at **650 ºC** has jumped up by each loading block and been sustained during the dwell time while the other figures show decreasing trends of the crack length during the dwell time particularly before the final failure. The decreasing PD propensity during the dwell can result from external or internal factors such as crack closure related to oxidation formed at the crack wake, or stress relaxation allowing crack flanks to touch.

The extent of the crack increase during unloading and reloading near the final failure (assisted by the high crack driving force at high Δ*K* levels) for the **90s dwell** time tests in Figure 6.39 was estimated and compared at different variants and temperatures as presented in Table 6.3 to assess the degree of oxidation damage zone. The increase of the crack length during unloading and reloading is relatively small in the fine γ′ variant at **650 ºC** temperature while a significant crack length increase is seen in the coarse γ′ variant at **725 ºC**. Such results indicate the same dwell time at a lower temperature in the fine γ′ variant exerts relatively less influence in developing the oxidation damage zone and causes relatively less crack propagation on unload/reload. On the other hand, the increase of the crack growth of the coarse γ′ variant with a **90s dwell** time at **725 ºC** was the greatest, which can be closely linked to the synergistic influence of a higher temperature and a continuous carbide distribution on grain boundary.

	Fine γ′ variant	**Coarse γ′ variant**
650 ºC (similar Δ*K* levels)	~0.01 mm (a ~6.1 mm)	~0.1 mm (a ~4.5 mm)
725 ºC (similar Δ*K* levels)	~0.1 mm (a ~6 mm)	~0.2 mm (a ~5 mm)

Table 6.3: A crack growth estimate at similar Δ*K* levels (similar crack length in the same variant) on unloading and reloading step after a **90s dwell** near the final failure in both γ′ variants at 650 ºC and 725 ºC.

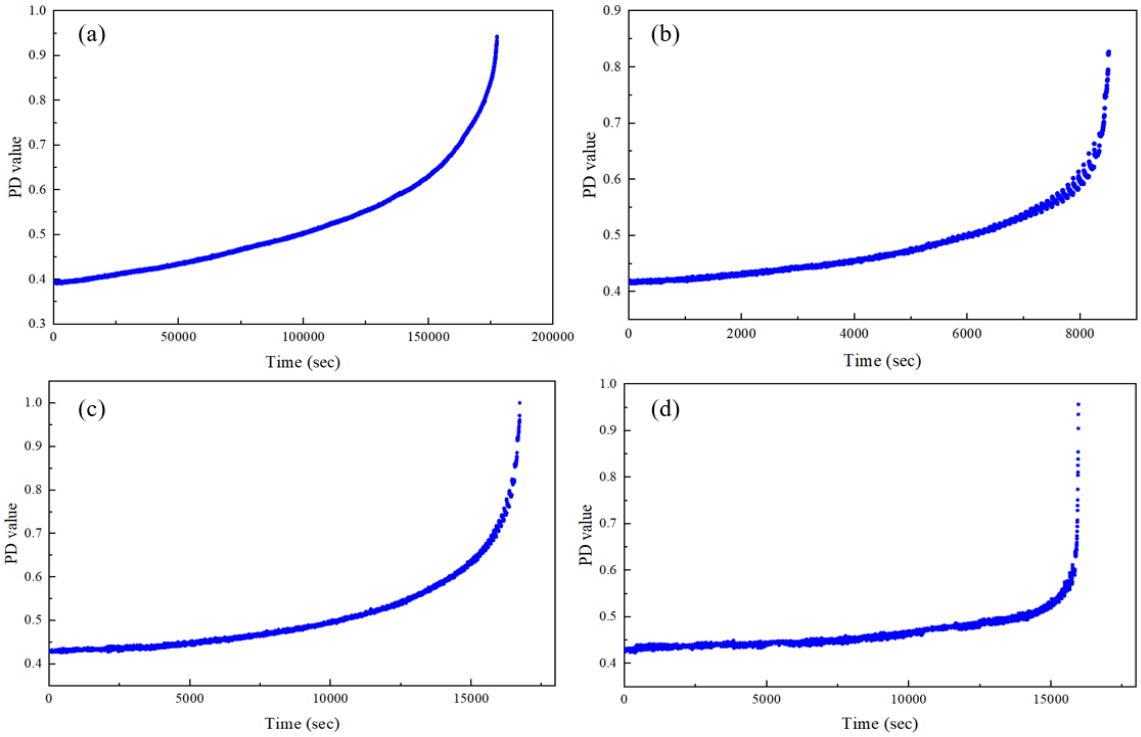

Figure 6.38: PD value vs time of the fatigue tests with a **90s dwell** of (a) the fine γ′ variant (b) the coarse γ′ variant at **650 ºC** and (c) the fine γ′ variant (d) the coarse γ′ variant at **725 ºC**.

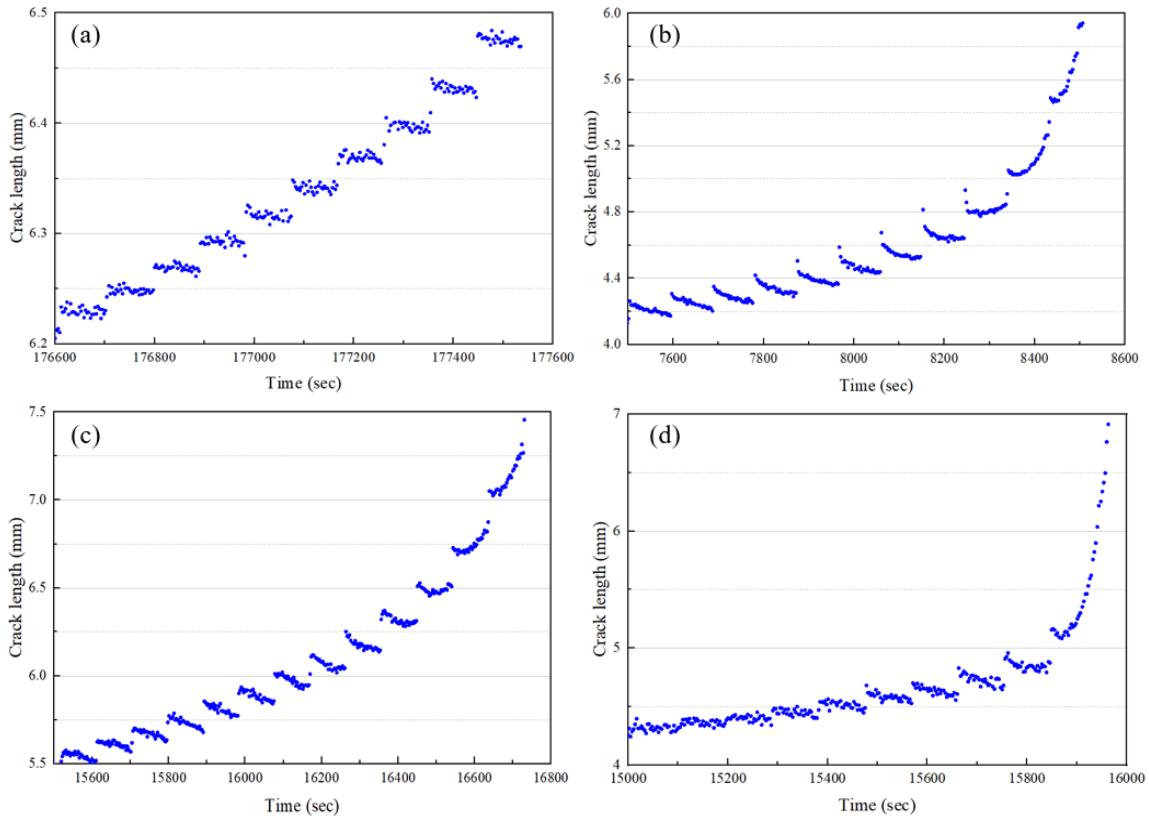

Figure 6.39: Crack length calculated from PD value over time representing loading blocks at the end of the fatigue tests with a **90s dwell** at (a) the fine γ′ variant (b) the coarse γ′ variant at **650 ºC** and (c) the fine γ′ variant (d) the coarse γ′ variant at **725 ºC**.

In order to understand the decrease seen in PD (and so apparently in the crack length during the dwell at maximum load), tests holding the samples at certain K_{max} levels at **650 ºC** and **725 ºC** were carried out and the results are presented in Figure 6.40. The block tests of both γ′ variants were halted at the end of testing and held at K_{max} of 21 and 15 MPa$\sqrt{m}$ for the fine and coarse variants, respectively, for around 12 hours (by holding the sample at constant load). It can be seen that the PD value of the fine γ′ variant remains mostly steady but slightly decreased at the end of the testing time while that of the coarse γ′ variant slightly but gradually decreased over the whole time. This may be associated with the crack closure due to the oxidation formed at the crack wake over time or stress relaxation at the crack tip during the loading applied. Linked to this observation, the observed decrease in the PD value during a **90s dwell** time at higher ΔK levels can be also linked to similar effects on the crack wake with more exposure to the oxidising environment, which is more marked in the coarse γ′ variant. The long holding time constant load test at **725 ºC** on the coarse γ′ variant was also conducted and can be seen in Figure 6.40 (c). This was carried out at the same K_{max} = 15 MPa$\sqrt{m}$ as at **650 ºC** **(**Figure 6.40 (b)) in this variant. Interestingly, the PD value initially slightly decreased then increased until a K_{max} of 16 MPa$\sqrt{m}$ was reached and then slowly increased, as seen during the 90s dwells in Figure 6.39. After a slowly increasing trend, the test has experienced a rapid increase in the PD value from a K_{max} of 20 MPa$\sqrt{m}$ and finally failed.

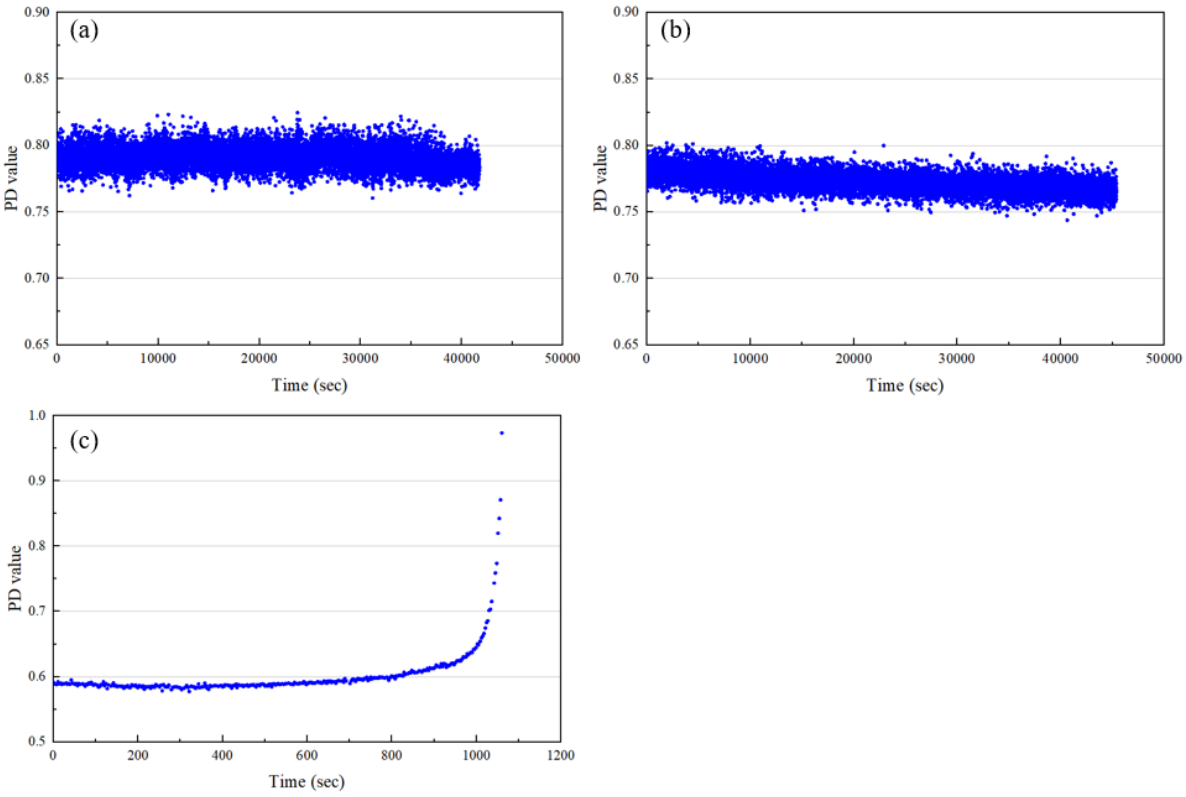

Figure 6.40: PD value vs time for the samples at constant load holding tests (a) the fine γ′ variant holding at K_{max} of 21 MPa$\sqrt{m}$ at 650 ºC (b) the coarse γ′ variant holding at K_{max} of 15 MPa$\sqrt{m}$ at 650 ºC (c) the coarse γ′ variant holding at K_{max} of 15 MPa$\sqrt{m}$ at 725 ºC.

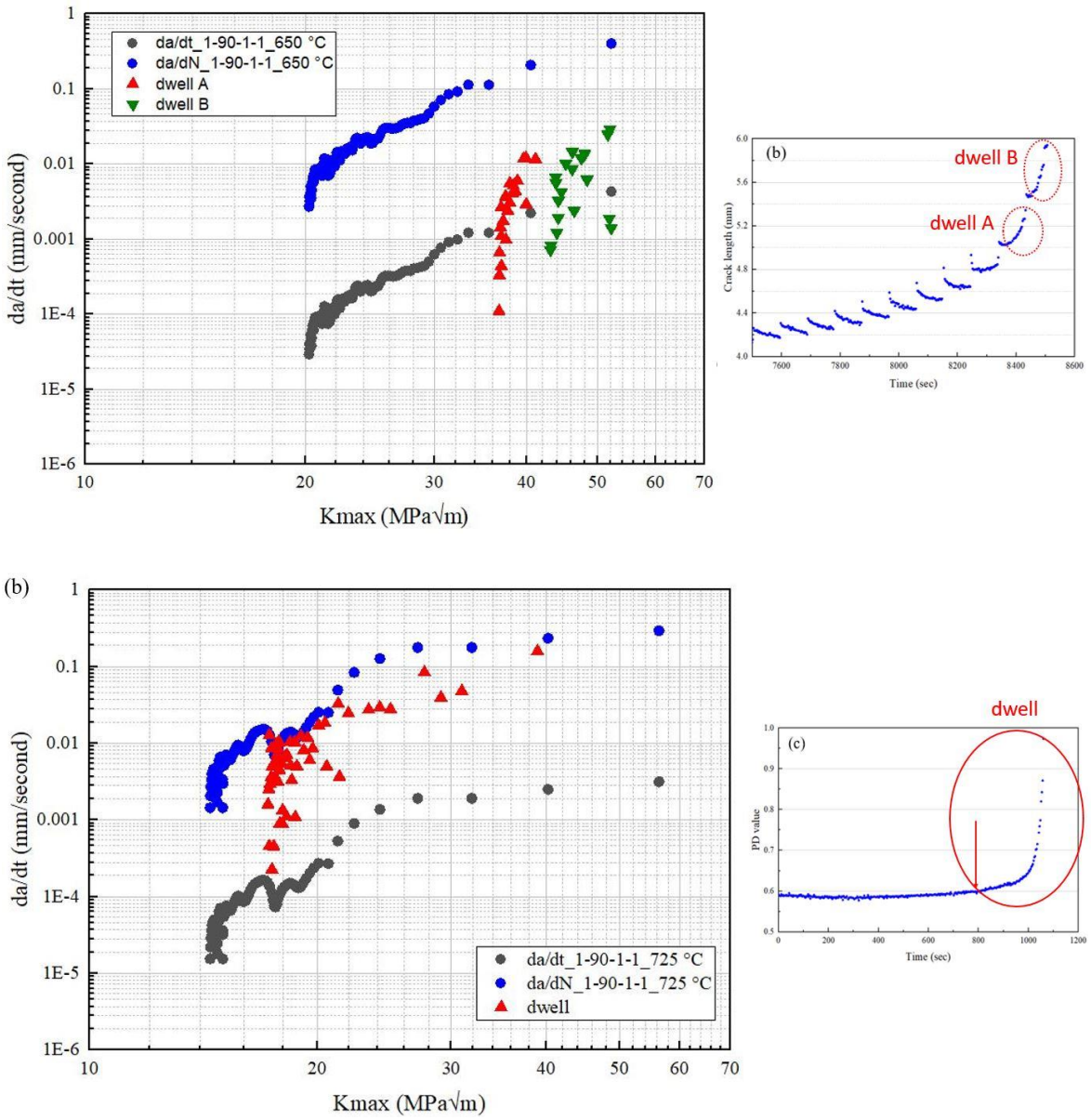

Figure 6.41: *da/dt* vs K_{max} representations in the coarse γ' variant of data from (a) Figure 6.39 (b) at 650ºC and (b) Figure 6.40 (c) at 725ºC, respectively compared to 1-90-1-1 tests at the same temperature.

When *da/dt* rates obtained during separate dwells near to the final failure (at high K_{max} levels) are compared to time dependent representation of crack growth (during the 1-90-1-1 crack growth out), it is seen that *da/dt* during a single dwell seems more scattered as presented in Figure 6.41 (a) (perhaps representing the more averaged *da/dt* calculated as time dependent crack growth in 1-90-1-1 cycling). This is more marked and much faster at higher temperature as seen in Figure 6.41 (b). It is seen that there is transient slower *da/dt* behaviour at the beginning of each dwell and a much more rapid *da/dt* towards the end of a dwell period, as shown in both figures. It can be inferred that time dependent crack growth is slow when "fresh" crack tip material exists right after unload/reloading and the cracking of the prior embrittled zone (by oxidation processes). Then the damage zone at the

crack tip is accelerated in an oxidising environment and *da/dt* increases considerably during extended periods of dwell. In Figure 6.41 (b), *da/dt* of a long term dwell period is comparable with *da/dN* at 725 ^{o}C at higher K_{max} levels (high crack driving force), so effectively two orders of magnitude faster than the da/dt rates observed in individual periods of 90s dwells in a 1-90-1-1 cycle. This indicates a purely time dependent crack growth (i.e. cracking of an embrittled zone caused by oxidation processes during holding at load and/or creep) is progressively much more damaging than when crack advance occurs via cracking of a small region of embrittled zone by unloading and reloading, followed by the formation of a new crack tip embrittled zone. This is difference seen at the higher temperature (725 ^{o}C) and is due to the resultant enhanced oxidation processes (and possible creep) producing a "runaway" damage progression at a crack tip under sustained loading.

6.4 Discussion

6.4.1 Effect of microstructures on fatigue crack propagation behaviour at elevated temperatures

In this study, the FCG rate of the coarse γ′ variant is found to be approximately one to two orders of magnitude higher than that of the fine γ′ variant under a range of testing conditions (i.e. loading frequencies and temperatures). This indicates that microstructural features such as the size of γ′ precipitate and/or carbide distribution on the grain boundary caused by the different heat treatment process exerts a significant influence on FCG behaviour at elevated temperature when time dependent processes predominate. Dislocation behaviour such as cutting or looping of the γ′ precipitate varies with the size of γ′ particles and testing temperature during cyclic deformation, which is linked to the slip character and damage accumulation. It is widely known that finer γ′ precipitates are more likely to be cut by dislocations, which is associated with enhanced resistance to the crack growth resulting from their heterogeneous planar slip behaviour leading to enhanced slip reversibility. The interparticle spacing of fine γ′ precipitates is usually smaller than for coarse γ′ precipitates, promoting the hindrance of dislocation looping. On the other hand, coarse γ′ precipitates are more likely to be looped by dislocations and the resultant homogeneous slip character contributes to enhanced crack growth [49,80]. Cyclic deformation at elevated temperature is associated with more homogeneous slip behaviour exhibiting more cross slip and less planar slip bands, which is linked to reduced slip reversibility and enhanced resistance to slip band crack initiation but reduced FCG resistance. This is more marked in coarser size of γ′ precipitates.

The accelerated FCG rate of the coarse γ′ variant in this study can be related to more homogeneous slip behaviour exhibiting more damage accumulation, but as the crack growth mechanism is intergranular rather than transgranular, the role of slip character in transporting oxygen to the grain

boundary also needs to be considered more in detail. Such penetration of oxygen is associated with the extent of grain boundary oxidation and consequent enhanced intergranular crack growth. Impingement of slip bands on the grain boundary causes local stress concentrations at the boundary. Slip bands can act as preferential paths of oxygen diffusion into material ahead of the crack tip, which makes grain boundaries ahead of the crack tip embrittled. This can result in crack initiation and/or preferential intergranular crack propagation path. The difference of the slip heterogeneity in both γ′ variants in this project may link to different FCG rates in the time dependent regime, but the distinct difference in grain boundary character seems more significant in producing the different time dependent crack growth processes. The related contribution of the difference of the slip character still need to be confirmed.

More grain boundaries can promote enhanced intergranular FCG behaviour as the grain boundary acts as the preferential area for the oxide formation and also has more vacancies and slip band intersections, accelerating oxidation processes. However, the grain size is not a significant variable in this study as the two alloys have similar grain size. It is believed that a more continuous carbide distribution at the grain boundary can weaken grain boundary strength, which accelerates time dependent intergranular processes [104,105,124,136]. As such, the more continuous distribution of carbides on the grain boundary of the coarse γ′ variant appears to significantly contribute to enhanced FCG rate under a range of testing conditions, in comparison to the fine γ′ variant which has discrete carbides on the grain boundaries. The effect of a more continuous carbide distribution on FCG rate is more pronounced with the longer dwell time and higher temperature, which can be ascribed to more diffusion time per cycle and oxidation damage on grain boundaries. The enhanced FCG rate at the second transition in Figure 6.31 (b) can be also related to the effect of such an oxidation process on the grain boundary with a continuous distribution of carbides. However, testing in an inert or vacuum condition would be able to confirm the extent of the effect of carbide distribution the on grain boundary being related to oxidation or creep processes in these alloys.

6.4.2 Effects of dwell time and temperature on fatigue crack propagation behaviour

The effect of the dwell time on FCG behaviour of RR1000 with fine and coarse γ′ distributions at **650 ºC** and **725 ºC** has also been assessed in this study. Dwell time at maximum load and elevated temperatures is usually associated with a complex process of oxygen related damage and/or creep behaviour particularly along the grain boundary [20,137,172]. FCG behaviours of both γ′ variants in this test matrix generally show that an enhanced FCG rate was observed with the longer dwell time of **90s** (lower loading frequency), higher temperature of **725 ºC** and their synergistic effects, with a

more marked propensity of time dependent FCG behaviour. The extent of such FCG rate difference at different frequencies and temperatures can be considered in terms of the size of γ′ precipitates (potentially resulting in different slip characteristics and hence varying ion transportation rates to the grain boundaries to assist short distance and long distance oxidation processes) or the variation in carbide distribution observed along the grain boundaries in the two variants.

It is believed that the enhanced FCG rate with an introduction of a **90s dwell** time in an oxidising environment is mainly ascribed to the oxidation formed ahead of the crack tip along the grain boundary, although grain boundary features and creep processes may also influence FCG behaviour [111,117]. The oxidation along the grain boundary ahead of the crack tip contributes to materials degradation and weakens the strength of the grain boundary, which can result in enhanced intergranular fracture mode. It is also known that the effects of oxidation on FCG behaviour are associated with diffusion time available during the loading cycle, oxygen diffusivity and available diffusion paths on the basis of oxidising species and oxygen diffusion ahead of the crack tip [112]. Therefore, the longer diffusion time of a **90s dwell** and oxygen diffusivity at elevated temperatures in the area of the crack tip are beneficial to an accelerated intergranular FCG rate. It is also found that SAGBO is the main mechanism of intergranular FCG behaviour in the turbine disc alloy RR1000 at elevated temperatures, which is associated with an oxide intrusion forming, consisting of layered oxides in a thermodynamic sequence formed ahead of the propagating crack tip at elevated temperature [140]. Such long diffusion times (**90s**) and oxidation processes contribute to formation of a significant oxidation damage zone (embrittled zone) ahead of the crack tip, which results in the enhanced FCG rate after switching from time dependent to cycle dependent crack growth (in terms of comparison to baseline cycle dependent FCG rate). The more tortuous crack path caused by intergranular FCG behaviour is also ascribed to longer diffusion times and consequent SAGBO. Such crack path tortuosity may also provide a shielding effect at the crack wake and result in decreased FCG rates in subsequent cycle dependent crack growth (compared to the expected baseline). The balance between these two opposing effects needs to be considered further.

It is known that the diffusivity of oxygen and degradation of the grain boundary are promoted at higher temperatures, resulting in enhanced FCG rates and more intergranular fracture modes. Higher temperature exerts a synergistic influence along with dwell time and microstructure on FCG behaviour. In this study, it is seen that higher temperature (**725 ºC**) with shorter dwell time (a **1s dwell**) marginally influenced the FCG rate of the fine γ′ variant while it significantly enhanced the FCG rate of the coarse γ′ variant which is ascribed to the continuous carbide distribution on the grain boundary. Higher temperature (**725 ºC**) with longer dwell time (a **90s dwell**) time has the highest FCG rate in the coarse γ′ variant, but the FCG rate does not increase beyond the FCG rate at **650 ºC** with a **90s dwell** seen in this variant. This can be related to an effective saturation of the FCG rate and relevant oxidation damage that occurs at 90s dwells for these alloys, possibly the SAGBO occurs very easily at both temperatures within the same highly stressed crack tip regime, leaving the ΔK

level as the effective controlling parameter. Higher test temperature is likely to supress planar slip and promote homogeneous slip, which subsequently leads to less localised slip band formation and reduced strain localisation. On the other hand, higher temperature can activate the diffusion path of oxygen on slip bands near the grain boundary and ahead of the crack tip, which can induce more intergranular fracture and time dependent crack growth. Therefore, the transition from a mixed fracture to fully intergranular fracture appears to be discerned at lower ΔK levels at higher temperatures, as observed in the fracture surfaces.

6.4.3 Fracture mechanism assessment by fractography, roughness and secondary crack length

Different types of fracture modes such as transgranular, intergranular or a mixed fracture mode have been observed on the fracture surfaces in this study. It is found that the fatigue fracture mode at lower loading frequency (time dependent crack growth) was predominantly intergranular while a more transgranular fracture mode was observed at higher loading frequency (cycle dependent crack growth) in both γ′ variants tested at elevated temperature. In the tests under a **1s dwell** at **650 ºC**, both γ′ variants showed a mixed trans and intergranular fracture mode indicating simultaneous smooth fracture areas and grain boundary cracking at low ΔK level as seen in Figure 6.15 and Figure 6.16. Transgranular fracture modes appear to be more prominent in the fine γ′ variant whereas intergranular fracture modes are more dominant in the coarse γ′ variant although it did exhibit a mixed fracture mode. Consequently, the transition from a mixed fracture mode to transgranular fracture modes has occurred in both γ′ variants while the transition has occurred earlier (at lower ΔK) in the fine γ′ variant than the coarse γ′ variant. This can result from the effect of the continuous distribution of carbides on the grain boundary and/or more secondary cracks formed due to oxidation damage on grain boundaries in the coarse γ′ variant although dwell time is not likely to be sufficient to cause significant oxidation effects. The transition back to a more transgranular crack growth mode with increasing ΔK level (corresponding to higher FCG rates) as shown in Figure 6.16 has been linked to the mechanical crack driving force outstripping the diffusion assisted time dependent crack tip damage processes and thereby switching back to the propensity of cycle dependent crack growth behaviour. In the tests of both γ′ variants with a **90s dwell** time at **650 ºC**, intergranular crack growth is the main fracture mechanism as seen in Figure 6.17. Similarly, an intergranular fracture mode is the main fracture mechanism in the tests carried out under both **1s** and **90s** dwell times at **725 ºC** due to the noticeable effects of higher temperature and enhanced oxidation damage on FCG behaviour. It is noteworthy that some mixed fracture mode was observed in the fine γ′ variant at low ΔK level at **725 ºC**, which shows that the effect of microstructure (finer γ′, and less continuous carbide

distribution on the grain boundaries) somewhat becomes comparable with the effect of oxidation processes at higher temperature.

The grain boundary character is expected to be closely linked to the intergranular FCG behaviour. As seen in Figure 3.5 and Figure 3.9, a more continuous distribution of carbides is seen on the grain boundary of the coarse γ′ variant, which seems to result in decohesion and microvoid formation on the grain boundary during intergranular crack growth. Damage along the grain boundary of the coarse γ′ variant was also observed in the static load oxidation test held at 90% yield stress at 650 ^{o}C for 10 hours (Figure 3.12). Such damage processes can promote intergranular crack growth and resultant accelerated FCG rates. As seen in Figure 6.27, significant damage including void formation and grain boundary oxidation were observed for the coarse γ′ variant compared to the fine γ′ variant where only oxidation processes were apparent in secondary crack studies.

The roughness on the fracture surface has been assessed systematically to better categorise the fracture mechanisms and associated FCG behaviour under the investigated testing conditions. The roughness of the fracture surface of the fatigue tests is indicative of the degree of the fracture mechanism (transgranular or intergranular or mixed), associated deformation behaviour and the development of crack closure during fatigue testing [115,177]. The extent of the roughness of the fracture surface might be comparable with the grain size relevant to an intergranular fracture while the roughness of a transgranular fracture surface would be expected to be less than the grain size in general. The tests at **725 ºC** indicate that the greatest value of the roughness is likely to be around the grain size (Figure 6.28 (b)), which might result in a saturation of the roughness value. The roughness of the fracture surface measured by SEM images in this study as presented in Figure 6.28 generally indicates that time dependent crack growth (longer dwell time) has a rougher fracture surface than cycle dependent crack growth (shorter dwell time), which is related to an intergranular fracture mode for the former and a mixed fracture mode for the latter. As ΔK level increases, the roughness appears to increase which can result from the formation of significant numbers of secondary cracks along the grain boundary promoting larger scale roughness. The roughness of the coarse γ′ variant with a **90s dwell** time significantly increased with increasing ΔK level, which can be associated with more intergranular fracture mechanisms and increased secondary grain boundary cracking induced by the more continuous distribution of carbides found on the grain boundary in this variant. From these results, it appears that the degree of secondary cracking has a possible correlation with the roughness on the fracture surface and intergranular failure modes. A statistical analysis of secondary cracking is also likely to follow a trend of the roughness. It is worth mentioning that the roughness at high ΔK was somewhat lower than expected perhaps due to fast crack propagation rates not allowing enough diffusion time per cycle for oxidation damage at the crack tip before the crack grows through that region, which will influence the formation and extent of secondary cracking as seen in Figure 6.28 (c).

6.4.4 Oxidation damage ahead of the crack tip

Damage zones ahead of the crack tip were investigated through the block tests to understand the effect of dwell time (frequency) on oxygen related FCG behaviour on both γ′ variants at **650 ºC**. Environmental damage is likely to attack grain boundaries and contribute to enhanced FCG rate under dwell loading condition, which is commonly seen in polycrystalline Ni based superalloy. The pronounced damage zone of the transitions during the block test of the coarse γ′ variant is closely associated with a grain boundary feature and thermal oxidation damage mechanisms. Based on the results in this study and relevant literature, two possible mechanisms of thermal damage oxidation and fatigue causing an oxidation damage zone ahead of the crack tip are SAGBO and/or dynamic embrittlement. The first mechanism (SAGBO) is proposed by diffusion of oxygen and oxides formed at grain boundary due to the action of the local stress applied to accommodate the volume expansion needed for oxide formation. Subsequent crack propagation involves cracking of oxides formed or at the oxide/matrix interface, contributing enhanced intergranular crack growth. The second mechanism (dynamic embrittlement) indicates diffusion of oxygen along preferential path such as slip bands, grain boundaries or γ/γ′ interface. This can result in consequent decohesion at an interface such as the grain boundary (without necessarily forming any oxide). The stress at the crack tip in dynamic embrittlement mechanism plays a role in assisting the diffusion of oxygen along grain boundaries.

In this research, the grain boundary and carbides/grain boundary interface can be easily attacked by environmental damage along with applied stress. The SEM images and EDX analysis indicate the clear oxidation formation along the grain boundary and along the secondary cracks. The continuous carbide distribution (particularly in the coarse γ′ variant) and oxidation formation on the grain boundary and ahead of the crack tip during the longer dwell time simultaneously contribute to time dependent embrittlement and enhanced FCG rates. This is attributed to the main mechanism of intergranular FCG behaviour in the turbine disc alloy RR1000 at elevated temperatures, which is associated with an oxide intrusion forming, consisting of layered oxides in a thermodynamic sequence formed ahead of the propagating crack tip at elevated temperature [140]. When it comes to the extent of oxidation damage linked to the different slip character based on different size of γ′ precipitate, it would be useful to conduct TEM analyses at the crack tip region as a potential piece of future work.

3D evaluation by X-ray CT scan on the fatigue crack path has been carried out to investigate the effect of loading frequency blocks and formation of the oxidation damage zone on FCG behaviour. 3D rendering of the block testing crack paths of both γ′ variants showed the complex morphology of the fatigue crack path including the roughness, secondary crack formation, discontinuous cracks and uncracked bridging ligaments. 3D analysis provides insight into these features. It should be noted that the challenging sample preparation required to have a matchstick with less than ~0.9 mm x 0.9

mm for X-ray CT scanning due to X-ray attenuation effects in P/M Ni-based superalloys limits the region that can be evaluated by this method. The field of view for CT scanning is limited to achieve sufficiently high resolutions and long scanning times are also required. It has been seen that a longer dwell time under an oxidising environment results in rougher and more tortuous crack path by intergranular fracture mode in both γ′ variants at varying Δ*K* levels. This is more marked with the continuous carbide distribution on the grain boundary of the coarse γ′ variant. It is worth noting that more secondary cracks were formed with a tortuous crack path propagating through the grain boundary while the crack path of the high frequency testing block was flat with less secondary crack formation. Moreover, in the coarse γ′ variant (Figure 6.37), discontinuously cracked regions ahead of the crack tip are observed especially at high Δ*K* levels. This can be ascribed to insufficient time for diffusion of oxygen per loading cycle ahead of the crack tip at high Δ*K* level between main crack and secondary cracks. Dynamic embrittlement mechanisms can also weaken grain boundary binding force and thereby significantly increase FCG rates at high Δ*K* levels, which also contributes to insufficient time for oxide formation on the grain boundary. The uncracked ligaments between discontinuous cracks (as seen in Figure 6.37) can be also broken ahead of the crack tip during unloading and reloading with the assistance of high stress/strain and oxygen related damage with a longer dwell time at elevated temperatures [137]. It is probable that the jump of the crack length during the block test observed by the DCPD method (Figure 6.30) occurs when the crack propagated by breaking such embrittled uncracked ligaments at a high overall crack driving force. The uncracked ligament formed during longer dwell time fatigue may be also related to the decrease in PD value observed during dwell, which can result in a complex PD measurement as current can flow through uncracked regions. Extensive secondary cracks over the discontinuous cracking zone are formed away from the main crack path when the fresh crack wake is exposed to oxygen after breaking the uncracked ligaments ahead of the crack tip at high Δ*K* level as presented in 2D and 3D images of the crack path (Figure 6.35 (b) and Figure 6.37).

6.5 Summary

The synergistic interactions between microstructure variation, dwell time (frequency) and temperature on oxidation FCG behaviour at elevated temperatures in model RR1000 alloy variants were evaluated in this chapter. Based on the results and discussion in this chapter, the following conclusions can be made:

1. The coarse γ′ variant, with a more continuous distribution of carbides on the grain boundary, exhibited more damage at the grain boundaries either with or without loading. Associated greater oxidation damage and void formation observed on the grain boundary (on secondary cracks produced under fatigue) contribute to a poor resistance to FCG rate under time dependent conditions in the coarse γ′ variant. Further testing in an inert atmosphere or in

vacuum is proposed as future work to more fully confirm the effects of carbides on the grain boundary and to assess how much this affects oxidation or creep processes during high temperature fatigue in RR1000.

2. The FCG rate is clearly affected by the microstructure of the samples, loading frequency and testing temperature. The fine γ′ variant generally has better resistance to FCG than the coarse γ′ variant at the range of loading frequencies and temperatures studied in these tests. The difference between the two variants in FCG rate became more marked at the longer dwell time of 90s (time-dependent regime) as greater oxidation damage was caused by the longer diffusion time allowed in the longer dwell at maximum load at the crack tip along the grain boundary. Higher temperature and a more continuous heavy carbide distribution on the grain boundary exerts a significant influence on the development of oxidation damage and concomitant enhanced FCG rates. Based on previous TEM characterisation of these model RR1000 γ′ variants in Chapter 5 (slip character at 500 °C has been studied) [122], a precipitate cutting mechanism is still evident with some looping observed in the fine γ′ variant whilst precipitate looping is the dominant mechanism seen in the coarse γ′ variant.
3. Fractographic analysis of both γ′ variants revealed different fracture modes including transgranular, intergranular and a mixed fracture mode. Transgranular fracture modes were more dominant in the fracture surfaces of tests in the fine γ′ microstructure, at lower temperature and higher loading frequency (shorter dwell time). Intergranular fracture modes were more dominant in the tests of the coarse γ′ microstructure (exhibiting a continuous carbide distribution), at higher temperature and lower loading frequency (longer dwell time) due to enhanced oxidation damage processes at maximum load. The transition from a mixed fracture mode to a transgranular one occurs "earlier" in the fine γ′ microstructure at lower temperature and short dwell time as ΔK level increases. This is linked to less time (and propensity) for oxidation damage to occur as well as a discrete carbide distribution along the grain boundary. Higher ΔK level (high mechanical crack driving force) contributes faster *da/dN* allowing less diffusion time per cycle so cycle dependent fatigue outstrips the more limited time dependent processes.
4. Quantitative analysis on the average secondary crack length and fracture surface roughness allows a more precise pinpointing of the degrees of transgranular and intergranular crack growth. As ΔK level increases, average secondary crack length becomes longer and the formation of larger areas of grain detachment on the fracture surface contribute to the higher roughness of the fracture surface. This becomes more pronounced especially in the testing with the coarse γ′ microstructure and higher temperature and longer dwell time, which is attributed to enhanced oxidation damage on the grain boundary and ahead of the crack tip by accelerating intergranular cracking and FCG rate.

5. The extent of oxygen-related damage zone ahead of the crack tip from the block tests on both γ′ variants at 650 °C was assessed. The oxidation damage zone formed at the crack tip during time dependent crack growth enhances FCG rate in both γ′ variants while a slightly delayed shielding effect of crack path tortuosity due to the prior intergranular fracture mode can contribute to subsequent enhanced cyclic FCG resistance. Noticeable damage zone formation in the transitions was observed during the block test of the coarse γ′ variant, which can be ascribed to the effect of a longer dwell time and a continuous carbide distribution. The damage zone is linked to a surge of the crack growth induced by embrittlement cracking.
6. X-ray CT scanning gives a deeper understanding of oxygen enhanced FCG behaviour and complex 3D morphology of the crack path alongside traditional 2D image analysis. The 2D cross section and 3D morphology of the whole crack path indicate that the shorter dwell time test exhibits a relatively flat crack path (transgranular fracture mode) while the longer dwell time test shows more tortuous crack path with an extensive formation of secondary cracks (intergranular fracture mode). It is notable that a discontinuous crack path and uncracked ligaments can be discerned ahead of the crack tip especially in the coarse γ′ variant at high ΔK level. The jumps of the crack length in the transition during the block tests can be ascribed to breaking embrittled zones containing such uncracked ligaments with noticeable oxidation damage in the discontinuous crack zone seen ahead of the crack tip.

Chapter 7 Conclusions

Two variants of the RR1000 alloy have been assessed in this study. Material characterisation has examined critical microstructural features such as γ′ precipitate size, grain distribution and carbide distribution on the grain boundaries, which are tailorable by heat treatment processes. Two microstructural variants containing unimodal fine (~73 nm) and coarse (~161 nm) γ′ precipitate size are produced by non-commercial heat treatment processes, which carefully control the temperatures and cooling processes in the heat treatment processes. It should be noted that the heat treatment, which was targeted at producing two different unimodal γ′ precipitate sizes, also results in different carbide distributions on grain boundaries, where the coarse γ′ variant exhibits a more continuous carbide distribution. The mean grain size of the two variants is similar as they received the same super-solvus solution heat treatment. Overall, the two variants exhibit typical Ni-based superalloy mechanical property characteristics that proof stresses sustain up to a temperature of around 800 ^{o}C, representing a superior high temperature strength. They show similar trends while the fine γ′ variant offers marginally higher strength levels. To examine the effect of elevated temperature on grain boundary character, static isothermal oxidation tests with and without loading were conducted on both γ′ variants. This indicates that the coarse γ′ variant exhibits more defined grain boundaries due to a more continuous carbide distribution and their volume expansion on oxidation is likely to reduce the grain boundary strength. Initially, this study aimed to see the effect of different slip character (hence potentially varying ion transportation rates to the grain boundaries to assist short distance and long distance oxidation processes) linked to different γ′ size distribution at high temperature. However, the effect of continuous carbide distributions along the grain boundaries appears to be more marked at elevated temperatures (affecting both significant intergranular crack initiation and crack growth processes) while slip band cracking is dominant at room temperature in this particular set of alloys studied.

Fatigue crack initiation and short FCG behaviour of both γ′ variant RR1000 alloys at room temperature have been investigated by fatigue testing using three point bending and uniaxial tensile methods. The relevant work reported here has also been compared with previous work by other researchers conducted at the Universities of Southampton and Manchester under a previously completed joint EPSRC programme. In terms of deformation and slip characteristics analysis using HR-DIC and ECCI on these materials conducted at the University of Manchester, it is seen that the fine γ′ variant exhibits more highly planar slip and subsequent heterogeneous slip character which may result in worse crack initiation resistance due to more intense slip band formation while the coarse γ′ variant shows more homogeneous slip character with more and wider slip bands observed.

This indicates that the finer γ′ variant is more likely to exhibit shearing and the coarse γ′ variant is likely to induce more Orowan looping at the same strain level.

At room temperature, fatigue cracks appear to initiate mainly from slip bands, twin boundaries and/or pores at the surface or sub-surface. Fractography shows crystallographic facet features that are indicative of stage-I crack growth in both γ′ variants. SEM-DIC analysis indicates that cracks have initiated at a pore and slip bands with high strain levels and more diffuse strain localisation. It is also seen that slip trace analysis using EBSD mapping shows a crack has initiated from a twin boundary in the grain with a relatively high Schmid factor in relation to the tensile stress axis. The crack has further propagated along the slip systems activated with relatively high Schmid factors of the neighbouring grains. Overall, FCG rates in both γ′ variants show significant scatter at low ΔK level following typical short FCG behaviour. A zig-zag crack path observed in the coarse γ′ variant is associated with the partial crack arrest and thereby decelerated FCG rates, promoting the intrinsic shielding effect during the crack propagation. Such phenomena contribute to the complexity of short FCG behaviour which exhibit significant scatter. It appears that the effect of γ′ size is less important in controlling fatigue lifetimes under given testing conditions, via the classically expected effect of more or less planar slip character affecting either slip band initiation resistance or crack propagation modes. Instead, lifetime is strongly affected by the number of crack initiation sites (partly linked to initiation resistance) which seems more linked to defect distributions or grain orientation distributions than γ′ size alone. The role of multi-site coalescence in determining lifetime at high stress levels seems to predominate the behaviour seen.

3D evaluation of the early stages FCG via X-ray CT scan allows a better understanding of internal microstructure and complex crack morphology together with 2D evaluation. Significant low volume fraction of pore distribution in both γ′ variants is linked to the processing of P/M route of the RR1000 alloys. The crack appears to propagate from the surface along the slip bands slanted at 45^{o}, indicating Stage I faceted crack growth is also occurring sub-surface.

At elevated temperature, the microstructural influences impact alongside the significant effects of temperature and environmental damage. Cross slip and less localised slip characteristics (homogenous slip) appears to be promoted by increasing temperatures in both γ′ variants by TEM observation conducted by University of Manchester. In the fatigue testing under dwell time (linked to diffusion time of oxygen) at 650 ^{o}C, fatigue cracks of both γ′ variants have initiated at grain boundaries with bulged Co-rich oxides at the surface. A number of intergranular cracking events can be seen, which gives rise to frequent crack coalescence events during crack propagation. This results in enhanced FCG rates and consequently a significant decrease in lifetime. Oxides formed along the grain boundaries are associated with local mismatch strain and therefore stress concentration, which can result in oxide cracking. Based on this, the continuous carbide formation along the grain boundaries of the coarse γ′ variant is expected to exhibit a lower lifetime compared to the fine γ′ variant due to volume expansion of oxidised carbides and resultant pronounced crack initiation at the

interface between carbides and grain boundaries. However, in this study, the lifetime of both γ′ variants was similar, which can be attributed to the asymmetrical crack initiation and propagation close to the edge found in the fine γ′ variant, again indicating the importance of initiation site location/frequency and emphasising the stochasticity of these processes.

Long FCG mechanisms at elevated temperatures are controlled by the complexity of microstructure, loading frequency (dwell time) and temperature in this study. Overall, the fine γ′ variant shows a better resistance to FCG than the coarse γ′ variant at a given testing condition (i.e. different temperature and dwell time). The difference between two variants become more marked at longer dwell times, which can be ascribed to greater oxidation damage allowed by longer diffusion times ahead of the crack tip occurring along the grain boundary. The relative contribution of creep processes still needs to be established although it is known that their effects are limited at such relatively low temperatures for turbine disc applications. Moreover, higher temperatures and more continuous carbides on the grain boundaries give significant rises to enhanced intergranular fracture features and corresponding accelerated FCG rates.

Fractography analysis indicates that fracture surfaces of both γ′ variants when testing with shorter dwell time exhibit a mix of transgranular and intergranular fracture, although the transgranular mode becomes more evident at higher ΔK levels. This indicates that the mechanical driving force for cyclic dependent crack growth is outstripping the time dependent crack growth contribution. Under longer dwell time, the intergranular fracture mode is dominant in the both γ′ variants. The fracture surfaces exhibit mainly intergranular fracture features, which results from the longer diffusion time per cycle and resultant enhanced oxidation damage at maximum load. As ΔK level increases, greater average length of secondary cracks along grain boundaries and formation of grain detachment can be seen on the fracture surface, linked to the higher roughness of fracture surface. This is more pronounced in the coarse γ′ variant with a more continuous grain boundary carbide distribution and at higher temperature. Quantification of the average secondary crack length and fracture surface roughness allows a more precise pinpointing of the degrees of transgranular and intergranular crack growth.

The extent of oxidation damage zones formed ahead of the crack tip of both γ′ variants at 650 ^{o}C is further investigated by switching the loading frequencies (aforementioned as block tests). Noticeable damage zone formation in the transitions was observed during the block test of the coarse γ′ variant. The γ′ variants also have quite different grain boundary character, and this is likely to be a significant contributor to their differences in time dependent crack growth processes. The damage zone is linked to a surge of the crack growth induced by embrittlement cracking. 3D evaluation by X-ray CT scanning after the block tests of both γ′ variants at 650 ^{o}C was carried out for a deeper understanding of oxygen enhanced FCG behaviour and complex 3D morphology of the crack path alongside traditional 2D image analysis. The crack path under the shorter dwell time exhibits a relatively flat

crack path (transgranular fracture feature) while the longer dwell time test shows more tortuous crack path and secondary cracks (intergranular fracture feature). As an intergranular fracture feature, a discontinuous crack path and uncracked ligaments can be discerned ahead of the crack tip especially pronounced in the coarse γ′ variant with increasing ΔK levels. The jumps of the crack length in the transition during the block tests can be also ascribed to breaking embrittled zones containing such uncracked ligaments, resulting from oxidation damage in the discontinuous crack zone seen ahead of the crack tip.

In summary, the results from this study can contribute to development of preferential turbine disc alloy microstructural features, through (1) varying deformation behaviour and slip character linked to secondary γ′ size distribution and (2) grain boundary character affecting grain boundary failure mechanisms. In particular, it appears that a more continuous carbide distribution exerts a more critical influence on enhanced FCG rate and resultant reduced lifetime under dwell time loading at elevated temperature in air rather than the effects of varying secondary γ′ size distribution alone. These results can direct appropriate materials optimisation and heat treatment processes (i.e. controlling the size distribution of secondary γ′ and the extent of carbide distribution on grain boundaries), which is directly linked to the performance and fatigue lifetimes of commercial turbine disc alloys. The synergistic effects of microstructure and oxidation processes on fatigue mechanisms of this alloy system in service can be carefully considered in terms of life assessment.

Chapter 8 Future work

8.1 Short fatigue crack growth behaviour at elevated temperature

Short FCG behaviour of both γ′ variants at room temperature is characterised by high resolution analysis techniques such as replica method and EBSD mapping for slip trace analysis in Chapter 4. These analyses offers extensive information including the morphology of crack evolution and effects of microstructure (i.e. γ′ precipitate size and grain orientation) on short FCG mechanisms. Analysis using similar methodologies can be conducted (with considerably more difficulty) to understand the synergistic effects of microstructure and oxidation processes on early crack propagation behaviour at elevated temperature although any replication method is somewhat challenging due to the high test temperature. Fatigue tests on the PBB samples under three point bending method at elevated temperatures to assess the influences of microstructure and oxidation on short FCG and consequent lifetime should be carried out under similar testing conditions as described in Chapter 4 and Chapter 5. The tests could then be interrupted at regular cycle intervals to capture short crack initiation and growth processes by direct SEM and OM observation of the sample surface. This will also investigate the role of oxidation at grain boundaries and interface between carbides and grain boundaries in short FCG behaviour. Although very time consuming, such an approach will yield valuable data. The effects of grain misorientation on short FCG behaviour at elevated temperature could also be examined by EBSD mapping of the area containing short fatigue cracks and neighbouring grains. The results can then be compared along with the roles of oxidation in short FCG behaviour. More challenging in-situ tests of appropriate microtensile samples at elevated temperature in X-ray CT rigs can also be envisaged (see below).

8.2 3D analysis on short and long fatigue crack

X-ray CT scanning was conducted on the microtensile sample of the coarse γ′ variant to assess 3D evaluation on short FCG behaviour and internal microstructure as represented in Chapter 4. The sample contains a short fatigue crack obtained after interrupted uniaxial fatigue testing, especially focussing on the gauge section (~0.9 mm x 0.9 mm) due to high attenuation of Ni-based superalloys. However, the analysis was only carried out after one interruption during the fatigue tests. X-ray CT scans on the sample with further increments of further loading cycles incrementally will allow a better understanding of the 3D morphology and evolution of early crack propagation together with

pore distribution. An extension of this approach to in-situ high temperature testing can also be envisaged, but requires high temperature in-situ rigs [178], some of which are starting to be available at various beam-lines (SPRING 8, DIAMOND etc. [179]). The real challenge here is to define a regime of interest where the data can be reasonably gathered within a typical research programme duration, with sustainable effort. So posing the most effective research question to justify the data-intensive process involved. The use of such data can be linked to 3D image based modelling processes, that account for stress concentration effects of observed defects, but also incorporate appropriate materials responses linked to actual grain morphology and slip systems (e.g. crystal plasticity and discrete dislocation dynamics approaches [180,181].

3D assessment by X-ray CT scan of long FCG behaviour was also conducted on the both γ′ variants after the block tests at 650 ºC as described in the Chapter 6. This provided extensive information such as the tortuosity of crack paths in different loading frequency regimes, secondary crack formation and uncracked ligaments, which is linked to the degree of transgranular or intergranular fracture characteristics. However, it was challenging to quantify the crack path tortuosity and secondary crack and conduct systematic comparison as the loading frequencies and corresponding ΔK level are not constant. Further X-ray CT scans on the both γ′ variants under each loading frequency and/or higher temperature (i.e. 725 ºC) can offer such information to evaluate the extent of intergranular fracture features and the effects of oxidation process under given testing condition. Detailed ex-situ analyses of crack paths and crack-tips of interest may be more amenable in the medium term compared to complex in-situ scanning campaigns, where test conditions are also constrained by sample and scan time requirements.

8.3 The effects of slip character on fatigue behaviour at a range of temperature

γ′ precipitate size affects deformation behaviour and slip character during cyclic loading, which is linked to damage accumulation and crack initiation processes. The assessment of this was carried out as a part of a collaborative research programme under given testing condition in Chapter 4. At elevated temperature, slip bands ahead of the crack tip can act as favourable paths for oxygen diffusion and promote grain boundary degradation, which can result in crack initiation and intergranular crack propagation path. Deformation structure of the model RR1000 alloys was evaluated by TEM analysis at University of Manchester (Chapter 5) at 500 ºC, a temperature that is somewhat lower than the temperature in this study. TEM analysis of slip character at the test temperatures of interest here (650 ºC) would be an area of appropriate future work. Extracting TEM foils ahead of the crack tip after a test hold at certain K_{max} after fatigue testing of both γ′ variant would characterise the deformation behaviour and slip characteristics at elevated temperature in the crack

process zone itself and allow a meaningful mechanism comparison between two variants. Assessing how slip character is associated with transporting oxygen to the grain boundary and consequently the extent of fracture mode (i.e. transgranular or intergranular fracture) at elevated temperature will be of interest in further understanding how the pronounced effects of bulged Co-rich oxides at the grain boundaries are controlled.

8.4 Oxidation ahead of the crack tip and creep damage at elevated temperature

The effects of oxidation on FCG behaviour at elevated temperatures are investigated in Chapter 6. It is seen that the synergistic influences of microstructure, oxidation and temperature impact FCG behaviour. Also, oxidation damage ahead of the crack tip significantly appears to promote intergranular fracture mode at elevated temperature in air. At increasing ΔK levels (increasing FCG rates), mechanical driving crack driving force becomes relatively high compared to oxidation damage, which results in faster *da/dN* and thereby shorter diffusion time within a constant crack length increment. As a consequence, the transition from intergranular fracture to transgranular fracture is apt to occur. Therefore, it should be interesting to evaluate the interaction between mechanical and oxidation damage ahead of the crack tip. This can be conducted by undertaking long FCG tests under a trapezoidal waveform with dwell time (i.e. 90s) using $^{18}O_2$ isotope as a tracer for diffusion at certain ΔK levels [147,182]. The sample after fatigue testing in $^{18}O_2$ rich environment will be sectioned to examine the crack tip region by secondary ion mass spectrometry analysis and therefore reveal the diffusion path of oxygen inside the material. Such characterisation will be assisted by high resolution imaging analysis including SEM and TEM. TEM foils will be prepared from the crack tip using FIB to characterise deformation structure in oxidising environment. EDX analysis will also provide chemical element information ahead of the crack tip, indicating internal oxidation processes. This links to previous work done as part of the collaborative EPSRC programme and would require access to expertise and equipment at the partner institutions.

At elevated temperature, environmental damage in Ni-based superalloys mainly consists of oxidation and creep damage. However, at elevated temperature in air, it is complex to dis-entangle the respective role of them in fatigue mechanisms although it is known than creep damage of RR1000 alloy is limited in an oxidising environment. Therefore, it should be interesting to conduct fatigue testing on this alloy under vacuum or inert environment conditions at elevated temperature (where effects of oxidation are absent) to explicitly investigate the effects of oxidation and creep on fatigue crack initiation and propagation. Experimental tests would then be comparable to short and long

fatigue crack tests in Chapter 5 and Chapter 6, respectively. The results could then be characterised by high resolution imaging analysis including OM, SEM, EBSD and TEM in order to systematically conduct a comparison with the results from the tests under an oxidising environment as reported in Chapter 5 and 6. FCG rates of the tests under vacuum or inert environment conditions could also be compared to those of the tests in air to assess the role of oxidation and creep on the FCG mechanism.

8.5 Effects of γ′ precipitate and carbide distribution

To further understand the effect of the distribution of γ′ precipitates and grain boundary carbides on slip character and fatigue mechanisms, Inconel 690 that is a solid solution strengthened Ni-based superalloy without γ′ precipitates can be studied. Table 8.1 represents the alloying composition of the alloy. As with the other variants, a carbide distribution along the grain boundary can be varied based on heat treatment process (i.e. achieving a continuous and discrete distribution or absence of carbide distribution). Figure 8.1 represent one example of Inconel 690 alloys exhibiting the microstructural features of no distribution of γ′ precipitates and carbides on the grain boundaries as seen in Table 8.2. Experimental tests and characterisation could be identical to this study and systematically compared with the results of the RR1000 alloys. It is expected that the absence of γ′ precipitates of the alloy will provide information about the relative importance of their effects on slip characteristics and fatigue mechanism at a range of temperatures. The grain boundary carbide variations available will also make a useful comparison with the RR1000 system, particularly of interest in an oxidising environment.

C	Si	Mn	S	P	Cr	Fe	Al	Ti	N	O	Ni
0.16	0.047	0.01	0.0005	0.002	29.36	9.62	0.24	0.2	0.001	0.0014	Bal.

Table 8.1: Composition of Inconel 690 alloy (wt.%).

	Heat treatment	Microstructural feature
Inconel 690 alloy	Solid solution	- no distribution of γ′ precipitate - no grain boundary carbides - average grain size of around 30 μm

Table 8.2: Heat treatment and microstructural characters of Inconel 690 alloy (solid solution heat treatment containing 100 ppm N: 1050 ^{o}C/8 min followed by water quench).

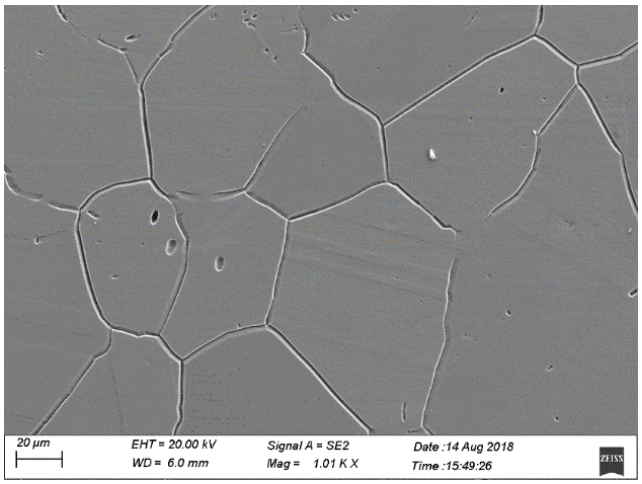

Figure 8.1: Microstructure of Inconel 690 alloys showing grain boundary (no carbide distribution) [183].

Appendix A Evaluation of stress intensity factor range Δ*K*

A semi-elliptic crack in a plate subject to bending condition is schematically illustrated in Fig A1.1 and the parameters needed for calculation of Δ*K* are present in terms of Scott and Thorpe's review [161].

Δ*K* for a semi elliptic crack can be calculated by equation:

$$\Delta \mathrm{k} = M_{f(\frac{\pi}{2})}[1 - 1.36\left(\frac{a}{t}\right)\left(\frac{a}{c}\right)^{0.1}]\frac{\sigma_b}{E(K)}\sqrt{\pi a}$$

Equation A1

Where the front face correction factor $M_{f(\frac{\pi}{2})}$:

$$M_{f(\frac{\pi}{2})} = 1.13 - 0.07(\frac{a}{c})^{0.5}$$

Equation A2

And the elliptic integral of the second kind *E(K)* can be described as:

$$E(K) = [1 + 1.47\left(\frac{a}{c}\right)^{1.64}]^{0.5}$$

Equation A3

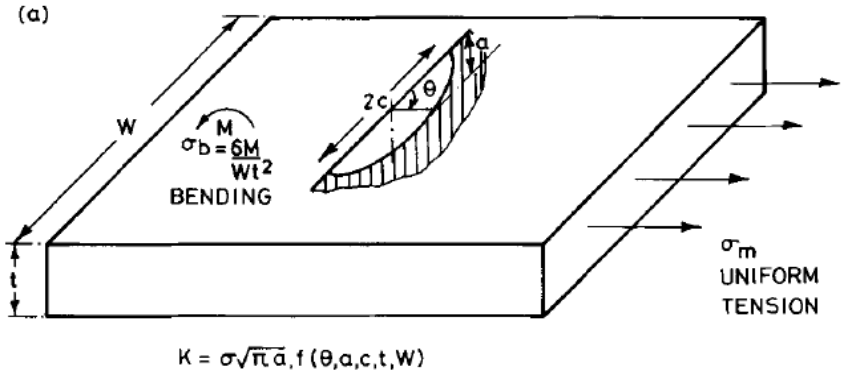

Figure A1.1 A semi- elliptic crack in a plate

The finite area correction for bending case is expressed:

$$B_w = 1 + \frac{F\left(\frac{a}{c}\right)G\left(\frac{c}{w}\right)H(\frac{a}{t})}{(0.2745)^2}$$

Equation A4

Where $F\left(\frac{a}{c}\right), G\left(\frac{c}{w}\right), H(\frac{a}{t})$ are polynomial functions:

$$\mathrm{F}\left(\frac{a}{c}\right) = 0.38 - 0.141\left(\frac{a}{c}\right) - 0.366\left(\frac{a}{c}\right)^2 + 0.569\left(\frac{a}{c}\right)^3 - 0.248\left(\frac{a}{c}\right)^4$$

Equation A5

$$\mathrm{G}\left(\frac{a}{w}\right) = -0.0239 + 1.434\left(\frac{a}{w}\right) - 2.984\left(\frac{a}{w}\right)^2 + 7.822\left(\frac{a}{c}\right)^3$$

Equation A6

$$\mathrm{H}\left(\frac{a}{t}\right) = -0.0113 + 0.323\left(\frac{a}{t}\right) + 0.749\left(\frac{a}{t}\right)^2 - 0.535\left(\frac{a}{t}\right)^3$$

a is crack depth at the notch root and *c* is half length of a crack. *t* denotes the thickness of a sample. In terms of an aspect ratio a/c, ΔK calculation in this research presume a/c is 1.

List of References

[1] M. Yuri, K. Tsukagoshi, S. Hada, J. Masada, E. Ito, Development of 1600 °C-Class High-efficiency Gas Turbine for Power Generation Applying J-Type Technology, Mitsubishi Heavy Ind. Tech. Rev. 50 (2013) 1–10. https://www.mhi-global.com/company/technology/review/pdf/e491/e491018.pdf.

[2] S. Candel, N. Docquier, Combustion control and sensors: a review, Prog. Energy Combust. Sci. 28 (2002) 107–50. doi:10.1016/S0360-1285(01)00009-0.

[3] A. Pineau, S.D. Antolovich, High temperature fatigue of nickel-base superalloys - A review with special emphasis on deformation modes and oxidation, Eng. Fail. Anal. 16 (2009) 2668–2697. doi:10.1016/j.engfailanal.2009.01.010.

[4] Reed. R. C., Superalloys: Fundamentals and applications, Cambridge University Press, 2006.

[5] J.Y. Guedou, J.C. Lautridou, Y. Honnorat, N18, Powder metallurgy superalloy for disks: Development and applications, J. Mater. Eng. Perform. 2 (1993) 551–556. doi:10.1007/BF02661740.

[6] S.D. Antolovich, Microstructural aspects of fatigue in Ni-base superalloys, Philos. Trans. R. Soc. A Math. Phys. Eng. Sci. 373 (2015) 1–36. doi:10.1098/rsta.2014.0128.

[7] R.E. Loge, Evolution of microstructure and twin density during thermomechanical processing in a c - c ’ nickel-based superalloy, 60 (2012) 5056–5066. doi:10.1016/j.actamat.2012.06.028.

[8] R. Jiang, N. Karpasitis, N. Gao, P.A.S. Reed, Effects of microstructures on fatigue crack initiation and short crack propagation at room temperature in an advanced disc superalloy, Mater. Sci. Eng. A. 641 (2015) 148–159. doi:10.1016/j.msea.2015.05.065.

[9] H.T.Pang, Effect of microstructure variation on turbine disc fatigue lives, University of Southampton, 2003.

[10] M.C. Hardy, B. Zirbel, G. Shen, R. Shankar, Developing damage tolerance and creep resistance in a high strength nickel alloy for disc applications, Superalloys 2004. (2004) 83–90. doi:10.7449/2004/Superalloys_2004_83_90.

[11] T.M. Pollock, A. Van Der Ven, The evolving landscape for alloy design, MRS Bull. 44 (2019) 238–246. doi:10.1557/mrs.2019.69.

[12] Y. GU, C. CUI, Y. YUAN, Z. ZHONG, RESEARCH PROGRESS IN A HIGH PERFORMANCE CAST and WROUGHT SUPERALLOY FOR TURBINE DISC APPLICATIONS, Acta Metall. Sin. 51 (2015) 1191–1206. doi:10.11900/0412.1961.2015.00442.

[13] I. Bantounas, B. Gwalani, T. Alam, R. Banerjee, D. Dye, Elemental partitioning, mechanical and oxidation behaviour of two high-γ ′ W-free γ/γ ′ polycrystalline Co/Ni superalloys, Scr. Mater. 163 (2019) 44–50. doi:10.1016/j.scriptamat.2018.12.025.

[14] P.A.J. Bagot, O.B.W. Silk, J.O. Douglas, S. Pedrazzini, D.J. Crudden, T.L. Martin, M.C. Hardy, M.P. Moody, R.C. Reed, An Atom Probe Tomography study of site preference and partitioning in a nickel-based superalloy, Acta Mater. 125 (2017) 156–165. doi:10.1016/j.actamat.2016.11.053.

[15] Jena, Role of Alloying Elements for Nickel Superalloys, 19 (1984) 3121–3139. doi:10.1007/BF00549796.

[16] R.Bowman, Superalloys: A Primer and History, Miner. Met. Mater. Soc. (2000). https://www.tms.org/meetings/specialty/superalloys2000/superalloyshistory.html.

[17] N.E.P. D.V.V.Satyanarayana, Aerospace Materials and Material Technologies, Volume 1: Aerospace Material Technologies, 2017. doi:10.1007/978-981-10-2134-3.

[18] Y. Yuan, Y.F. Gu, T. Osada, Z.H. Zhong, T. Yokokawa, H. Harada, Deformation mechanisms in a new disc superalloy at low and intermediate temperatures, Scr. Mater. 67 (2012) 137–140. doi:10.1016/j.scriptamat.2012.03.042.

[19] H.K.D.H. Bhadeshia, Superalloys, (2003). https://www.phase-trans.msm.cam.ac.uk/2003/nickel.html.

[20] H.Y. Li, J.F. Sun, M.C. Hardy, H.E. Evans, S.J. Williams, T.J.A. Doel, P. Bowen, Effects of microstructure on high temperature dwell fatigue crack growth in a coarse grain PM nickel based superalloy, Acta Mater. 90 (2015) 355–369. doi:10.1016/j.actamat.2015.02.023.

[21] Y.Q. Chen, E. Francis, J. Robson, M. Preuss, S.J. Haigh, Compositional variations for small-scale gamma prime (γ′) precipitates formed at different cooling rates in an advanced Ni-based superalloy, Acta Mater. 85 (2015) 199–206. doi:10.1016/j.actamat.2014.11.009.

[22] T.M. Pollock, S. Tin, Nickel-based superalloys for advanced turbine engines: Chemistry, microstructure, and properties, J. Propuls. Power. 22 (2006) 361–374. doi:10.2514/1.18239.

[23] E. Cadel, D. Lemarchand, S. Chambreland, D. Blavette, Atom probe tomography investigation of the microstructure of superalloys N18, 50 (2002) 957–966.

[24] D. Hull, D.J. Bacon, Introduction to dislocations, Elsevier, 2011.

[25] B. Reppich, Some new aspects concerning particle hardening mechanisms in γ' precipitating Ni-base alloys -I. Theoretical concept, Acta Metall. 30 (1982) 87–94.

[26] P.M. Kelly, The quantitative relationship between micro-structure and properties in two-phase alloys, Int. Met. Rev. 18 (1973) 31.

[27] B.R.P.S.G. Wehner, Some new aspects concerning particle hardening mechanisms in γ' precipitating nickel-base alloys - II. Experiments, Acta Metall. 30 (1982) 95–104.

[28] K. Yashiro, F. Kurose, Y. Nakashima, K. Kubo, Y. Tomita, H.M. Zbib, Discrete dislocation dynamics simulation of cutting of γ′ precipitate and interfacial dislocation network in Ni-based superalloys, Int. J. Plast. 22 (2006) 713–723. doi:10.1016/j.ijplas.2005.05.004.

[29] W. Huther, B. Reppich, Interaction of dislocations with coherent, stress-free ordered particles, Zeitschrift Fur Met. 69 (1978) 628–634.

[30] D. Raynor, J.M. Silcock, Strengthening mechanisms in γ′ precipitating alloys, Met. Sci. J. 4 (1970) 121–130.

[31] L.M. Brown, R.K. Ham, Dislocation-particle interactions, Strength. Methods Cryst. (1971) 9–135.

[32] E. Nembach, E. Nembach, Particle strengthening of metals and alloys, Wiley New York, 1997.

[33] G. Gottstein, Physical Foundation of Material Science, 2004. doi:10.1038/282346b0.

[34] B.H. Kear, Dislocation configurations in plastically deformed polycrystalline Cu3Au alloys, FRANKLIN INST PHILADELPHIA PA LABS FOR RESEARCH AND DEVELOPMENT, 1961.

[35] S. Takeuchi, E. Kuramoto, Temperature and orientation dependence of the yield stress in Ni {in3} Ga single crystals, Acta Metall. 21 (1973) 415–425.

[36] C.T.E.M.A. URER, Primary and Secondary Melt 3 Processing—Superalloys, Superalloys, Supercompos. Superceram. (2012) 49.

[37] W. min GUO, J. tao WU, F. ge ZHANG, M. han ZHAO, Microstructure, Properties and Heat Treatment Process of Powder Metallurgy Superalloy FGH95, J. Iron Steel Res. Int. 13 (2006) 65–68. doi:10.1016/S1006-706X(06)60097-6.

[38] S.A. Croxall, M.C. Hardy, H.J. Stone, P.A. Midgley, The 3D microstructure of RR1000 nickel-base superalloy : a FIB-SEM dual-beam approach, Eur. Microsc. Confrence. (2012) 1–2. doi:10.1002/9781118686768.ch33.

[39] J. Coakley, H. Basoalto, D. Dye, Coarsening of a multimodal nickel-base superalloy, Acta Mater. 58 (2010) 4019–4028. doi:10.1016/j.actamat.2010.03.017.

[40] G. Lvov, V.I. Levit, M.J. Kaufman, Mechanism of primary MC carbide decomposition in Ni-base superalloys, Metall. Mater. Trans. A Phys. Metall. Mater. Sci. 35 A (2004) 1669–1679. doi:10.1007/s11661-004-0076-x.

[41] M.J. Donachie, S.J. Donachie, Superalloys: a technical guide, ASM international, 2002.

[42] R.J. Mitchell, J.A. Lemsky, R. Ramanathan, H.Y. Li, K.M. Perkins, L.D. Connor, Process Development & Microstructure & Mechanical Property Evaluation of a Dual Microstructure Heat Treated Advanced Nickel Disc Alloy, Superalloys 2008 (Eleventh Int. Symp. (2008) 347–356. doi:\url{10.7449/2008/Superalloys{\textunderscore }2008{\textunderscore }347{\textunderscore }356}.

[43] T.P. Gabb, P.T. Kantzos, J. Telesman, J. Gayda, C.K. Sudbrack, B. Palsa, Fatigue resistance of the grain size transition zone in a dual microstructure superalloy disk, Int. J. Fatigue. 33 (2011) 414–426. doi:10.1016/j.ijfatigue.2010.09.022.

[44] J. Gayda, T.P. Gabb, P.T. Kantzos, The effect of dual microstructure heat treatment on an advanced nickel-base disk alloy, Superalloys 2004. (2004) 323–329. doi:10.7449/2004/Superalloys_2004_323_329.

[45] T.P. Gabb, J. Gayda, J. Telesman, A. Garg, N. Glenn, B. Rd, The Effects of Heat Treatment and Microstructure Variations on Disk, Superalloys 2008. (2008) 121–130. doi:10.7449/2008/Superalloys_2008_121_130.

[46] T. Osada, Y. Gu, N. Nagashima, Y. Yuan, T. Yokokawa, H. Harada, Optimum microstructure combination for maximizing tensile strength in a polycrystalline superalloy with a two-phase structure, Acta Mater. 61 (2013) 1820–1829. doi:10.1016/j.actamat.2012.12.004.

[47] J. Telesman, T. Gabb, A. Carg, P. Bonacuse, J. Gayda, Effect of Microstructure on Time Dependent Fatigue Crack Growth Behavior In a P/M Turbine Disk Alloy, Superalloys 2008. (2008) 807–816. doi:10.7449/2008/Superalloys_2008_807_816.

[48] R.J. Mitchell, M.C. Hardy, M. Preuss, S. Tin, Development of γ′ morphology in P/M rotor disc alloys during heat treatment, Proc. Int. Symp. Superalloys. (2004) 361–370. doi:10.7449/2004/superalloys_2004_361_370.

[49] H.T. Pang, P.A.S. Reed, Fatigue crack initiation and short crack growth in nickel-base

turbine disc alloys - The effects of microstructure and operating parameters, Int. J. Fatigue. 25 (2003) 1089–1099. doi:10.1016/S0142-1123(03)00146-4.

[50] A. J Knowles, L. Reynolds, V. A Vorontsov, D. Dye, A nickel based superalloy reinforced by both Ni3Al and Ni3V ordered-fcc precipitates, Scr. Mater. 162 (2019) 472–476. doi:10.1016/j.scriptamat.2018.12.013.

[51] H.E. Boyer, Fatigue Testing, Stress. 1 (1986) 0.

[52] S. Suresh, Fatigue of Materials, 2nd ed., Cambridge University Press, 1998.

[53] U. Krupp, Fatigue crack propagation in metals and alloys: microstructural aspects and modelling concepts, John Wiley & Sons, 2007.

[54] O.H. Basquin, The exponential law of endurance tests, Proc. Annu. Meet. ASTM. 10 (1919) 625.

[55] L.E. Coffin, The Problem of Thermal Stress Fatigue in Austenitic Steels at Elevated Temperatures, Proc. Symp. Eff. Cycl. Heat. Stress. Met. Elev. Temp. ASTM STP 1 (1954) 31.

[56] S.S. Manson, Behaviour of materials under conditions of thermal stress, NACA Rep. 1170. (1954).

[57] S.H. Nahm, C.M. Suh, M.W. Jung, J.Y. Kim, C.H. Yang, Application of damage tolerance approach for turbine disk life extension, Int. J. Mod. Phys. B. 17 (2003) 1916–1921. doi:10.1142/s0217979203019873.

[58] T.. Anderson, Anderson, Ted L. Fracture mechanics: fundamentals and applications, CRC press, 2017.

[59] M.H. El Haddad, K.N. Smith, T.H. Topper, Fatigue Crack Propagation of Short Cracks, J. Eng. Mater. Technol. 101 (1979) 42. doi:10.1115/1.3443647.

[60] W. Devenport, Fracture toughness testing (ESM Laboratory Course Notes), (2006). http://www.dept.aoe.vt.edu/~devenpor/aoe3054/manual/expt5/index.html.

[61] T. Broom, R.K. Ham, The hardening and softening of metals by cyclic stressing, Proc. R. Soc. London. Ser. A. Math. Phys. Sci. 242 (1957) 166–179.

[62] B.H. Choe, H.C. Lee, Cyclic softening and hardening behavior of a nickel-base superalloy, Scr. Metall. Mater. 32 (1995) 1283–1287. doi:10.1016/0956-716X(94)00018-D.

[63] F.D. León-Cázares, F. Monni, T. Jackson, E.I. Galindo-Nava, C.M.F. Rae, Stress response and microstructural evolution of nickel-based superalloys during low cycle fatigue: Physics-based modelling of cyclic hardening and softening, Int. J. Plast. 128 (2020). doi:10.1016/j.ijplas.2020.102682.

[64] V.S. Sarma, M. Sundararaman, K.A. Padmanabhan, Effect of γ′ size on room temperature low cycle fatigue behaviour of a nickel base superalloy, Mater. Sci. Technol. 14 (1998) 669–675. doi:10.1179/mst.1998.14.7.669.

[65] B.A. Lerch, N. Jayaraman, S.D. Antolovich, A STUDY OF FATIGUE DAMAGE MECHANISMS IN {WASPALOY} FROM 25 TO 800 \textdegree{C}, Mater. Sci. Eng. 66 (1984) 151–166.

[66] K. Gopinath, A.K. Gogia, S. V. Kamat, R. Balamuralikrishnan, U. Ramamurty, Low cycle fatigue behaviour of a low interstitial Ni-base superalloy, Acta Mater. 57 (2009) 3450–

3459. doi:10.1016/j.actamat.2009.03.046.

[67] K. Wang, H. Jing, L. Xu, Y. Han, L. Zhao, K. Song, Cyclic response and dislocation evolution of a nickel-based superalloy under low cycle fatigue deformation, Mater. Sci. Eng. A. 814 (2021) 141225. doi:10.1016/j.msea.2021.141225.

[68] R.E. Stoltz, A.G. Pineau, Dislocation-Precipitate Interaction and Cyclic Stress-Strain Behavior of a γ′ Strengthened Superalloy, Mater. Sci. Eng. 34 (1978) 275–284.

[69] J. Gayda, R. V. Miner, The effect of microstructure on 650°C fatigue crack growth in P/M astroloy, Metall. Trans. A. 14 (1983) 2301–2308. doi:10.1007/BF02663305.

[70] F.D. León-Cázares, R. Schlütter, T. Jackson, E.I. Galindo-Nava, C.M.F. Rae, A multiscale study on the morphology and evolution of slip bands in a nickel-based superalloy during low cycle fatigue, Acta Mater. 182 (2020) 47–59. doi:10.1016/j.actamat.2019.10.033.

[71] B. Max, B. Viguier, E. Andrieu, J.M. Cloue, A Re-examination of the Portevin-Le Chatelier Effect in Alloy 718 in Connection with Oxidation-Assisted Intergranular Cracking, Metall. Mater. Trans. A Phys. Metall. Mater. Sci. 45 (2014) 5431–5441. doi:10.1007/s11661-014-2508-6.

[72] R.W. Hayes, W.C. Hayes, On the mechanism of delayed discontinuous plastic flow in an age-hardened nickel alloy, Acta Metall. 30 (1982) 1295–1301.

[73] S. Stanzl-Tschegg, H. Mughrabi, B. Schoenbauer, Life time and cyclic slip of copper in the VHCF regime, Int. J. Fatigue. 29 (2007) 2050–2059. doi:10.1016/j.ijfatigue.2007.03.010.

[74] M.D. Sangid, The physics of fatigue crack initiation, Int. J. Fatigue. 57 (2013) 58–72. doi:10.1016/j.ijfatigue.2012.10.009.

[75] Donny, Fracture mechanis, (2019). https://blog.naver.com/rossie999.

[76] P. Lukáš, L. Kunz, Role of persistent slip bands in fatigue, Philos. Mag. 84 (2004) 317–330. doi:10.1080/14786430310001610339.

[77] S.G.S. Raman, K.A. Padmanabhan, Fatigue, 16 (1994) 209–215.

[78] P.A.S. Reed, Fatigue crack growth mechanisms in superalloys: overview, Mater. Sci. Technol. 25 (2009) 258–270. doi:10.1179/174328408X361463.

[79] J. Miao, T.M. Pollock, J. Wayne Jones, Crystallographic fatigue crack initiation in nickel-based superalloy René 88DT at elevated temperature, Acta Mater. 57 (2009) 5964–5974. doi:10.1016/j.actamat.2009.08.022.

[80] H.T. Pang, P.A.S. Reed, Effects of microstructure on room temperature fatigue crack initiation and short crack propagation in Udimet 720Li Ni-base superalloy, Int. J. Fatigue. 30 (2008) 2009–2020. doi:10.1016/j.ijfatigue.2008.01.001.

[81] J. Miao, T.M. Pollock, J. Wayne Jones, Microstructural extremes and the transition from fatigue crack initiation to small crack growth in a polycrystalline nickel-base superalloy, Acta Mater. 60 (2012) 2840–2854. doi:10.1016/j.actamat.2012.01.049.

[82] Z.F. Zhang, Z.G. Wang, Comparison of fatigue cracking possibility along large- and low-angle grain boundaries, Mater. Sci. Eng. A. 284 (2000) 285–291. doi:10.1016/S0921-5093(00)00796-6.

[83] W.H. Kim, C. Laird, Crack nucleation and stage I propagation in high strain fatigue—I. Microscopic and interferometric observations, Acta Metall. 26 (1978) 777–787.

[84] W.H. Kim, C. Laird, Crack nucleation and stage I propagation in high strain fatigue—II. Mechanism, Acta Metall. 26 (1978) 789–799.

[85] P. Peralta, C. Laird, Compatibility stresses in fatigued bicrystals: Dependence on misorientation and small plastic deformations, Acta Mater. 45 (1997) 5129–5143. doi:10.1016/S1359-6454(97)00184-5.

[86] Z.F. Zhang, Z.G. Wang, Fatigue-cracking characteristics of a copper bicrystal when slip bands transfer through the grain boundary, Mater. Sci. Eng. A. 343 (2003) 308–313. doi:10.1016/S0921-5093(02)00389-1.

[87] Z.J. Zhang, P. Zhang, L.L. Li, Z.F. Zhang, Fatigue cracking at twin boundaries: Effects of crystallographic orientation and stacking fault energy, Acta Mater. 60 (2012) 3113–3127. doi:10.1016/j.actamat.2012.02.016.

[88] D.L. Davidson, R.G. Tryon, M. Oja, R. Matthews, K.S. Ravi Chandran, Fatigue crack initiation in WASPALOY at 20 °C, Metall. Mater. Trans. A Phys. Metall. Mater. Sci. 38 A (2007) 2214–2225. doi:10.1007/s11661-007-9178-6.

[89] C.J. Mcmahon, L.F. Coffin, McMahon-Coffin1970_Article_MechanismsOfDamageAndFractureI.pdf, I (1970) 3443–3450.

[90] S. Cruchley, H.Y. Li, H.E. Evans, P. Bowen, D.J. Child, M.C. Hardy, The role of oxidation damage in fatigue crack initiation of an advanced Ni-based superalloy, Int. J. Fatigue. 81 (2015) 265–274. doi:10.1016/j.ijfatigue.2015.08.016.

[91] U. Krupp, H.J. Christ, Internal corrosion of engineering alloys: Experiment and computer simulation, J. Phase Equilibria Diffus. 26 (2005) 487–493. doi:10.1007/s11669-005-0040-5.

[92] C.F. Miller, G.W. Simmons, R.P. Wei, Evidence for internal oxidation during oxygen enhanced crack growth in P/M Ni-based superalloys, Scr. Mater. 48 (2003) 103–108. doi:10.1016/S1359-6462(02)00355-X.

[93] A. Karabela, L.G. Zhao, J. Tong, N.J. Simms, J.R. Nicholls, M.C. Hardy, Effects of cyclic stress and temperature on oxidation damage of a nickel-based superalloy, Mater. Sci. Eng. A. 528 (2011) 6194–6202. doi:10.1016/j.msea.2011.04.029.

[94] T. Connolley, P.A.S. Reed, M.J. Starink, Short crack initiation and growth at 600 °C in notched specimens of Inconel718, 340 (2003).

[95] T. Connolley, INITIATION AND GROWTH OF SHORT CRACKS IN U-NOTCH BEND SPECIMENS OF SUPERALLOY IN718 DURING HIGH TEMPERATURE LOW CYCLE FATIGUE, Univ. Southampt. (2001).

[96] J. Luo, P. Bowen, Small and long fatigue crack growth behaviour of a PM Ni-based superalloy, Udimet 720, Int. J. Fatigue. 26 (2004) 113–124. doi:10.1016/S0142-1123(03)00139-7.

[97] Y. Gao, J.S. Stölken, M. Kumar, R.O. Ritchie, High-cycle fatigue of nickel-base superalloy René 104 (ME3): Interaction of microstructurally small cracks with grain boundaries of known character, Acta Mater. 55 (2007) 3155–3167. doi:10.1016/j.actamat.2007.01.033.

[98] J.C. Healy, L. Grabowski, C.J. Beevers, Short Fatigue Crack Growth in a Nickel Base Superalloy at Room and Elevated Temperature, Int J. Fatigue. 2 (1991) 1183–1196.

[99] M. Goto, D.M. Knowles, Initiation and propagation behaviour of microcracks in Ni-base superalloy Udimet 720 LI, Eng. Fract. Mech. 60 (1998) 1–18. doi:10.1016/S0013-7944(98)00003-4.

[100] R. Jiang, F. Pierron, S. Octaviani, P.A.S. Reed, Characterisation of strain localisation processes during fatigue crack initiation and early crack propagation by SEM-DIC in an

advanced disc alloy, Mater. Sci. Eng. A. 699 (2017) 128–144. doi:10.1016/j.msea.2017.05.091.

[101] A. Pineau, D.L. McDowell, E.P. Busso, S.D. Antolovich, Failure of metals II: Fatigue, Acta Mater. 107 (2016) 484–507. doi:10.1016/j.actamat.2015.05.050.

[102] R. Jiang, S. Everitt, N. Gao, K. Soady, J.W. Brooks, P.A.S. Reed, Influence of oxidation on fatigue crack initiation and propagation in turbine disc alloy N18, Int. J. Fatigue. 75 (2015) 89–99. doi:10.1016/j.ijfatigue.2015.02.007.

[103] H.T. Pang, P.A.S. Reed, Microstructure effects on high temperature fatigue crack initiation and short crack growth in turbine disc nickel-base superalloy Udimet 720Li, Mater. Sci. Eng. A. 448 (2007) 67–79. doi:10.1016/j.msea.2006.11.016.

[104] W. bin Ma, G. quan Liu, B. fu Hu, Y. wen Zhang, J. tao Liu, Effect of Hf on carbides of FGH4096 superalloy produced by hot isostatic pressing, Mater. Sci. Eng. A. 587 (2013) 313–319. doi:10.1016/j.msea.2013.05.015.

[105] J. Hou, J.X. Dong, Z.H. Yao, H. Jiang, M.C. Zhang, Influences of PPB, PPB affect zone, grain boundary and phase boundary on crack propagation path for a P/M superalloy FGH4096, Mater. Sci. Eng. A. 724 (2018) 17–28. doi:10.1016/j.msea.2018.03.066.

[106] D. Kim, R. Jiang, A. Evangelou, I. Sinclair, P.A.S. Reed, Effects of γ′ size and carbide distribution on fatigue crack growth mechanisms at 650 °C in an advanced Ni-based superalloy, Int. J. Fatigue. 145 (2021). doi:10.1016/j.ijfatigue.2020.106086.

[107] T. Zhang, J. Jiang, B.A. Shollock, T. Ben Britton, F.P.E. Dunne, Slip localization and fatigue crack nucleation near a non-metallic inclusion in polycrystalline nickel-based superalloy, Mater. Sci. Eng. A. 641 (2015) 328–339. doi:10.1016/j.msea.2015.06.070.

[108] W.Z. Abuzaid, M.D. Sangid, J.D. Carroll, H. Sehitoglu, J. Lambros, Slip transfer and plastic strain accumulation across grain boundaries in Hastelloy X, J. Mech. Phys. Solids. 60 (2012) 1201–1220. doi:10.1016/j.jmps.2012.02.001.

[109] R. Jiang, Study of Fatigue Crack Initiation and Propagation Mechanisms in an Advanced Ni-based Superalloy: Effects of Microstructures and Oxidation, Univ. Southampt. (2015). http://www.ncbi.nlm.nih.gov/pubmed/25652998.

[110] Z. Alam, D. Eastman, G. Weber, S. Ghosh, K. Hemker, Microstructural aspects of fatigue crack initiation and short crack growth in René 88DT, Proc. Int. Symp. Superalloys. 2016-Janua (2016) 561–568. doi:10.1002/9781119075646.ch60.

[111] R. Jiang, D. Proprentner, M. Callisti, B. Shollock, X.T. Hu, Y.D. Song, P.A.S. Reed, Role of oxygen in enhanced fatigue cracking in a PM Ni-based superalloy: Stress assisted grain boundary oxidation or dynamic embrittlment?, Corros. Sci. 139 (2018) 141–154. doi:10.1016/j.corsci.2018.05.001.

[112] R. Jiang, P.A.S. Reed, Critical assessment 21: Oxygen-assisted fatigue crack propagation in turbine disc superalloys, Mater. Sci. Technol. (United Kingdom). 32 (2016) 401–406. doi:10.1080/02670836.2016.1148227.

[113] R. Jiang, S. Everitt, M. Lewandowski, N. Gao, P.A.S. Reed, Grain size effects in a Ni-based turbine disc alloy in the time and cycle dependent crack growth regimes, Int. J. Fatigue. 62 (2014) 217–227. doi:10.1016/j.ijfatigue.2013.07.014.

[114] K. Sadananda, P. Shahinian, The effect of environment on the creep crack growth behavior several structural alloys, Mater. Sci. Eng. 43 (1980) 159–168. doi:10.1016/0025-5416(80)90143-3.

[115] F. V. Antunes, A. Ramalho, J.M. Ferreira, Identification of fatigue crack propagation modes

by means of roughness measurements, Int. J. Fatigue. 22 (2000) 781–788. doi:10.1016/S0142-1123(00)00048-7.

[116] J. Tong, J. Byrne, Effects of frequency on fatigue crack growth at elevated temperature, Fatigue Fract. Eng. Mater. Struct. 22 (1999) 185–193. doi:10.1046/j.1460-2695.1999.00160.x.

[117] D.M. Knowles, D.W. Hunt, The influence of microstructure and environment on the crack growth behavior of powder metallurgy nickel superalloy RR1000, Metall. Mater. Trans. A Phys. Metall. Mater. Sci. 33 (2002) 3165–3172. doi:10.1007/s11661-002-0302-3.

[118] F. Schulz, H.Y. Li, H. Kitaguchi, D. Child, S. Williams, P. Bowen, Influence of Tertiary Gamma Prime (γ′) Size Evolution on Dwell Fatigue Crack Growth Behavior in CG RR1000, Metall. Mater. Trans. A Phys. Metall. Mater. Sci. 49 (2018) 3874–3884. doi:10.1007/s11661-018-4779-9.

[119] B. Lawless, S.D. Antolovich, C. Bathias, B. Boursier, The effect of microstructure on the fatigue crack propagation and overload behavior of Waspaloy at room temperature, Fract. Interact. Microstruct. Mech. Mech. Warrendale, PA TMSAIME. (1985) 285–301.

[120] C.P. Blankenship Jr, E. Hornbogen, E.A. Starke Jr, Predicting slip behavior in alloys containing shearable and strong particles, Mater. Sci. Eng. A. 169 (1993) 33–41.

[121] J.-O. Nilsson, Influence of dislocation–precipitate interaction on low cycle fatigue resistance of Alloy 800 at 600° C, Met. Sci. 18 (1984) 351–356.

[122] E.M. Knoche, Influence of the precipitate size on the deformation mechanisms in two nickel-base superalloys, The University of Manchester, 2011.

[123] K. MacIejewski, H. Ghonem, Influence of continuum precipitates on intergranular fatigue crack growth of a P/M nickel-based superalloy, Mater. Sci. Eng. A. 560 (2013) 439–449. doi:10.1016/j.msea.2012.09.088.

[124] L.N. Zhang, P. Wang, J.X. Dong, M.C. Zhang, Microstructures' effects on high temperature fatigue failure behavior of typical superalloys, Mater. Sci. Eng. A. 587 (2013) 168–178. doi:10.1016/j.msea.2013.08.065.

[125] J. Reuchet, L. Remy, High temperature low cycle fatigue of MAR-M 509 superalloy I: The influence of temperature on the low cycle fatigue behaviour from 20 to 1100°C, Mater. Sci. Eng. 58 (1983) 19–32. doi:10.1016/0025-5416(83)90134-9.

[126] J. Byrne, R. Hall, L. Grabowski, Elevated temperature fatigue crack growth under dwell conditions in Waspaloy, Int. J. Fatigue. 19 (1997) 359–367. doi:10.1016/S0142-1123(97)00056-X.

[127] H. Loyer-Danflou, M. Marty, A. Walder, J. Mendez, P. Violan, The effect of environment and structure on creep fatigue crack propagation in a P/M astroloy, Le J. Phys. IV. 3 (1993) C7-359.

[128] T. Isomoto, N.S. Stoloff, Effect of microstructure and temperature on high cycle fatigue of powder metallurgy Astroloy, Mater. Sci. Eng. A. 124 (1990) 171–181.

[129] D. Turan, D. Hunt, D.M. Knowles, Dwell time effect on fatigue crack growth of RR1000 superalloy, Mater. Sci. Technol. 23 (2007) 183–188. doi:10.1179/174328407x154257.

[130] J.J. Moverare, D. Gustafsson, Hold-time effect on the thermo-mechanical fatigue crack growth behaviour of Inconel 718, Mater. Sci. Eng. A. 528 (2011) 8660–8670. doi:10.1016/j.msea.2011.08.027.

[131] R.P. Wei, Z. Huang, Influence of dwell time on fatigue crack growth in nickel-base superalloys, Mater. Sci. Eng. A. 336 (2002) 209–214. doi:10.1016/S0921-5093(01)01957-8.

[132] H. Yang, R. Bao, J. Zhang, L. Peng, B. Fei, Crack growth behaviour of a nickel-based powder metallurgy superalloy under elevated temperature, Int. J. Fatigue. 33 (2011) 632–641. doi:10.1016/j.ijfatigue.2010.11.003.

[133] J. Tong, S. Dalby, J. Byrne, M.B. Henderson, M.C. Hardy, Creep, fatigue and oxidation in crack growth in advanced nickel base superalloys, Int. J. Fatigue. 23 (2001) 897–902. doi:10.1016/S0142-1123(01)00049-4.

[134] G. Onofrio, G.A. Osinkolu, M. Marchionni, Fatigue crack growth of UDIMET 720 Li superalloy at elevated temperature, Int. J. Fatigue. 23 (2001) 887–895. doi:10.1016/S0142-1123(01)00053-6.

[135] M.R. Winstone, K.M. Nikbin, G.A. Webster, Modes of failure under creep/fatigue loading of a nickel-based superalloy, J. Mater. Sci. 20 (1985) 2471–2476. doi:10.1007/BF00556076.

[136] R.P. Wei, C. Miller, Z. Huang, G.W. Simmons, D.G. Harlow, Oxygen enhanced crack growth in nickel-based superalloys and materials damage prognosis, Eng. Fract. Mech. 76 (2009) 715–727. doi:10.1016/j.engfracmech.2008.09.003.

[137] R. Jiang, D.J. Bull, D. Proprentner, B. Shollock, P.A.S. Reed, Effects of oxygen-related damage on dwell-fatigue crack propagation in a P/M Ni-based superalloy: From 2D to 3D assessment, Int. J. Fatigue. 99 (2017) 175–186. doi:10.1016/j.ijfatigue.2017.03.003.

[138] L. Viskari, M. Hörnqvist, K.L. Moore, Y. Cao, K. Stiller, Intergranular crack tip oxidation in a Ni-base superalloy, Acta Mater. 61 (2013) 3630–3639. doi:10.1016/j.actamat.2013.02.050.

[139] H.E. Evans, H.Y. Li, P. Bowen, A mechanism for stress-aided grain boundary oxidation ahead of cracks, Scr. Mater. 69 (2013) 179–182. doi:10.1016/j.scriptamat.2013.03.026.

[140] H.S. Kitaguchi, H.Y. Li, H.E. Evans, R.G. Ding, I.P. Jones, G. Baxter, P. Bowen, Oxidation ahead of a crack tip in an advanced Ni-based superalloy, Acta Mater. 61 (2013) 1968–1981. doi:10.1016/j.actamat.2012.12.017.

[141] R. Molins, G. Hochstetter, J.C. Chassaigne, E. Andrieu, Oxidation effects on the fatigue crack growth behaviour of alloy 718 at high temperature, Acta Mater. 45 (1997) 663–674. doi:10.1016/S1359-6454(96)00192-9.

[142] A.A.N. Németh, D.J. Crudden, D.E.J. Armstrong, D.M. Collins, K. Li, A.J. Wilkinson, C.R.M. Grovenor, R.C. Reed, Environmentally-assisted grain boundary attack as a mechanism of embrittlement in a nickel-based superalloy, Acta Mater. 126 (2017) 361–371. doi:10.1016/j.actamat.2016.12.039.

[143] D. Bika, C.J. McMahon, A model for dynamic embrittlement, Acta Metall. Mater. 43 (1995) 1909–1916. doi:10.1016/0956-7151(94)00387-W.

[144] J.A. Pfaendtner, J.J. McMahon, Oxygen-induced intergranular cracking of a Ni-base alloy at elevated temperatures - An example of dynamic embrittlement, Acta Mater. 49 (2001) 3369–3377. doi:10.1016/S1359-6454(01)00005-2.

[145] U. Krupp, W.M. Kane, C. Laird, C.J. McMahon, Brittle intergranular fracture of a Ni-base superalloy at high temperatures by dynamic embrittlement, Mater. Sci. Eng. A. 387–389 (2004) 409–413. doi:10.1016/j.msea.2004.05.053.

[146] U. Krupp, K. Wackermann, H.J. Christ, M.H. Colliander, K. Stiller, Intergranular Oxidation Effects During Dwell-Time Fatigue of High-Strength Superalloys, Oxid. Met. 88 (2017) 3–14. doi:10.1007/s11085-016-9707-z.

[147] B.J. Foss, M.C. Hardy, D.J. Child, D.S. McPhail, B.A. Shollock, Oxidation of a Commercial Nickel-Based Superalloy under Static Loading, Jom. 66 (2014) 2516–2524. doi:10.1007/s11837-014-1196-4.

[148] S.Y. Yu, H.Y. Li, M.C. Hardy, S.A. McDonald, P. Bowen, Mechanisms of dwell fatigue crack growth in an advanced nickel disc alloy RR1000, MATEC Web Conf. 14 (2014) 03002. doi:10.1051/matecconf/20141403002.

[149] M. Herbig, A. King, P. Reischig, H. Proudhon, E.M. Lauridsen, J. Marrow, J.Y. Buffire, W. Ludwig, 3-D growth of a short fatigue crack within a polycrystalline microstructure studied using combined diffraction and phase-contrast X-ray tomography, Acta Mater. 59 (2011) 590–601. doi:10.1016/j.actamat.2010.09.063.

[150] S. Dezecot, J.Y. Buffiere, A. Koster, V. Maurel, F. Szmytka, E. Charkaluk, N. Dahdah, A. El Bartali, N. Limodin, J.F. Witz, In situ 3D characterization of high temperature fatigue damage mechanisms in a cast aluminum alloy using synchrotron X-ray tomography, Scr. Mater. 113 (2016) 254–258. doi:10.1016/j.scriptamat.2015.11.017.

[151] J. Rannou, N. Limodin, J. Réthoré, A. Gravouil, W. Ludwig, M.C. Baïetto-Dubourg, J.Y. Buffière, A. Combescure, F. Hild, S. Roux, Three dimensional experimental and numerical multiscale analysis of a fatigue crack, Comput. Methods Appl. Mech. Eng. 199 (2010) 1307–1325. doi:10.1016/j.cma.2009.09.013.

[152] E.N. Landis, D.T. Keane, X-ray microtomography, Mater. Charact. 61 (2010) 1305–1316. doi:10.1016/j.matchar.2010.09.012.

[153] M. Hassanipour, S. Watanabe, K. Hirayama, H. Toda, K. Uesugi, A. Takeuchi, Short crack growth behavior and its transitional interaction with 3D microstructure in Ti-6Al-4V, Mater. Sci. Eng. A. 738 (2018) 229–237. doi:10.1016/j.msea.2018.09.073.

[154] W. Schaef, M. Marx, H. Vehoff, A. Heckl, P. Randelzhofer, A 3-D view on the mechanisms of short fatigue cracks interacting with grain boundaries, Acta Mater. 59 (2011) 1849–1861. doi:10.1016/j.actamat.2010.11.051.

[155] L. Salvo, M. Suéry, A. Marmottant, N. Limodin, D. Bernard, 3D imaging in material science: Application of X-ray tomography, Comptes Rendus Phys. 11 (2010) 641–649. doi:10.1016/j.crhy.2010.12.003.

[156] E. Maire, P.J. Withers, Quantitative X-ray tomography, Int. Mater. Rev. 59 (2013) 1–43. doi:10.1179/1743280413y.0000000023.

[157] S. Birosca, J.Y. Buffiere, F.A. Garcia-Pastor, M. Karadge, L. Babout, M. Preuss, Three-dimensional characterization of fatigue cracks in Ti-6246 using X-ray tomography and electron backscatter diffraction, Acta Mater. 57 (2009) 5834–5847. doi:10.1016/j.actamat.2009.08.009.

[158] D.P. Naragani, P.A. Shade, P. Kenesei, H. Sharma, M.D. Sangid, X-ray characterization of the micromechanical response ahead of a propagating small fatigue crack in a Ni-based superalloy, Acta Mater. 179 (2019) 342–359. doi:10.1016/j.actamat.2019.08.005.

[159] A. Harte, Private communication, (2018).

[160] R.J. Mitchell, C.M.F. Rae, S. Tin, Grain boundary transformations during isothermal exposure of powder metallurgy nickel base superalloys for turbine disc applications, Mater. Sci. Technol. 21 (2005) 125–132. doi:10.1179/174328405X16261.

[161] P.M. Scott, T.W. Thorpe, A critical review of crack tip stress intensity factors for semi elliptical cracks, Fatigue Eng. Mar´terials Strukt. 4 (1981) 291–309.

[162] P. Villechaise, L. Sabatier, J.C. Girard, On slip band features and crack initiation in fatigued 316L austenitic stainless steel: Part 1: Analysis by electron back-scattered diffraction and atomic force microscopy, Mater. Sci. Eng. A. 323 (2002) 377–385. doi:10.1016/S0921-5093(01)01381-8.

[163] P.A.S. Jiang, R. Reed, Private communication for EPSRC project, 2017.

[164] A. Harte, M. Atkinson, A. Smith, C. Drouven, S. Zaefferer, J. Quinta da Fonseca, M. Preuss, The effect of solid solution and gamma prime on the deformation modes in Ni-based superalloys, Acta Mater. 194 (2020) 257–275. doi:10.1016/j.actamat.2020.04.004.

[165] A. Harte, Imaging and quantifying deformation patterns in Ni-base superalloys, 2016.

[166] R.R. Stephens, L. Grabowski, D.W. Hoeppner, The effect of temperature on the behaviour of short fatigue cracks in Waspaloy using an in situ SEM fatigue apparatus, Int. J. Fatigue. 15 (1993) 273–282. doi:10.1016/0142-1123(93)90376-2.

[167] R. Jiang, Y.D. Song, P.A. Reed, Fatigue crack growth mechanisms in powder metallurgy Ni-based superalloys—A review, Int. J. Fatigue. 141 (2020) 105887. doi:10.1016/j.ijfatigue.2020.105887.

[168] Y. Liu, M. Kang, Y. Wu, M. Wang, M. Li, J. Yu, H. Gao, J. Wang, Crack formation and microstructure-sensitive propagation in low cycle fatigue of a polycrystalline nickel-based superalloy with different heat treatments, Int. J. Fatigue. 108 (2018) 79–89. doi:10.1016/j.ijfatigue.2017.10.012.

[169] R. Jiang, N. Gao, P.A.S. Reed, Influence of orientation-dependent grain boundary oxidation on fatigue cracking behaviour in an advanced Ni-based superalloy, J. Mater. Sci. 50 (2015) 4379–4386. doi:10.1007/s10853-015-8992-2.

[170] T.P. Gabb, J. Gayda, J. Telesman, P.T. Kantzos, Thermal and Mechanical Property Characterization of the Advanced Disk Alloy LSHR - Technical Memorandum, (2005) 82. http://gltrs.grc.nasa.gov.

[171] A. Evangelou, K.A. Soady, S. Lockyer, N. Gao, P.A.S. Reed, On the mechanism of oxidation-fatigue damage at intermediate temperatures in a single crystal Ni-based superalloy, Mater. Sci. Eng. A. 742 (2019) 648–661. doi:10.1016/j.msea.2018.10.095.

[172] D. Gustafsson, J.J. Moverare, S. Johansson, K. Simonsson, M. Hörnqvist, T. Mnsson, S. Sjöström, Influence of high temperature hold times on the fatigue crack propagation in Inconel 718, Int. J. Fatigue. 33 (2011) 1461–1469. doi:10.1016/j.ijfatigue.2011.05.011.

[173] 3D S Parameters - Height (Amplitude) Parameters, Michigan Metrology, LLC, (2010). https://www.michmet.com/3d_s_height_parameters.htm.

[174] S. Everitt, Developments in advanced high temperature disc and blade materials for aero-engine gas turbine application, University of Southampton, 2012.

[175] H.M. Lu, T.J. Delph, D.J. Dwyer, M. Gao, R.P. Wei, Environmentally-enhanced cavity growth in nickel and nickel-based alloys, Acta Mater. 44 (1996) 3259–3266. doi:10.1016/1359-6454(95)00405-X.

[176] E. Andrieu, R. Molins, H. Ghonem, A. Pineau, Intergranular crack tip oxidation mechanism in a nickel-based superalloy, 154 (1992) 21–28.

[177] A. Shyam, W.W. Milligan, Effects of deformation behavior on fatigue fracture surface morphology in a nickel-base superalloy, Acta Mater. 52 (2004) 1503–1513. doi:10.1016/j.actamat.2003.11.032.

[178] Y. Wang, X. Xu, W. Zhao, N. Li, S.A. McDonald, Y. Chai, M. Atkinson, K.J. Dobson, S.

Michalik, Y. Fan, P.J. Withers, X. Zhou, T.L. Burnett, Damage accumulation during high temperature fatigue of Ti/SiCf metal matrix composites under different stress amplitudes, Acta Mater. 213 (2021). doi:10.1016/j.actamat.2021.116976.

[179] Y.G. Tan, D.J. Bull, R. Jiang, A. Evangelou, S. Chaudhuri, S. Octaviani, F. Pierron, N. Gao, H. Toda, I. Sinclair, P.A.S. Reed, Data rich imaging approaches assessing fatigue crack initiation and early propagation in a DS superalloy at room temperature, Mater. Sci. Eng. A. 805 (2021) 140592. doi:10.1016/j.msea.2020.140592.

[180] P. Zhang, S. Lu, K.P. Baxevanakis, L.G. Zhao, T.Y. Yu, R.X. Zhou, A framework of modelling slip-controlled crack growth in polycrystals using crystal plasticity and XFEM, J. Phys. Conf. Ser. 1885 (2021). doi:10.1088/1742-6596/1885/4/042014.

[181] B. Lin, M. Huang, L. Zhao, A. Roy, V. Silberschmidt, N. Barnard, M. Whittaker, G. McColvin, 3D DDD modelling of dislocation–precipitate interaction in a nickel-based single crystal superalloy under cyclic deformation, Philos. Mag. 98 (2018) 1550–1575. doi:10.1080/14786435.2018.1447159.

[182] F.B. Ismail, V.A. Vorontsov, T.C. Lindley, M.C. Hardy, D. Dye, B.A. Shollock, Alloying effects on oxidation mechanisms in polycrystalline Co–Ni base superalloys, Corros. Sci. 116 (2017) 44–52. doi:10.1016/j.corsci.2016.12.009.

[183] R. Jiang, Private communication for Inconel 690, 2019.